

<sup>1</sup> Observation of the Higgs boson in the  $WW^*$   
<sup>2</sup> channel and search for Higgs boson pair  
<sup>3</sup> production in the  $b\bar{b}b\bar{b}$  channel with the  
<sup>4</sup> ATLAS detector

<sup>5</sup> A DISSERTATION PRESENTED  
<sup>6</sup> BY  
<sup>7</sup> TOMO LAZOVICH  
<sup>8</sup> TO  
<sup>9</sup> THE DEPARTMENT OF PHYSICS

<sup>10</sup> IN PARTIAL FULFILLMENT OF THE REQUIREMENTS  
<sup>11</sup> FOR THE DEGREE OF  
<sup>12</sup> DOCTOR OF PHILOSOPHY  
<sup>13</sup> IN THE SUBJECT OF  
<sup>14</sup> PHYSICS

<sup>15</sup> HARVARD UNIVERSITY  
<sup>16</sup> CAMBRIDGE, MASSACHUSETTS  
<sup>17</sup> MAY 2016

<sup>18</sup> ©2016 – TOMO LAZOVICH

<sup>19</sup> ALL RIGHTS RESERVED.

20      **Observation of the Higgs boson in the  $WW^*$  channel and search  
 21      for Higgs boson pair production in the  $b\bar{b}b\bar{b}$  channel with the  
 22      ATLAS detector**

23      ABSTRACT

24      This dissertation presents two studies: the observation and measurement of the Higgs boson in the  
 25       $H \rightarrow WW^* \rightarrow \ell\nu\ell\nu$  channel at  $\sqrt{s} = 7$  TeV and  $\sqrt{s} = 8$  TeV and a search for Higgs pair pro-  
 26      duction in the  $HH \rightarrow b\bar{b}b\bar{b}$  channel at  $\sqrt{s} = 13$  TeV with the ATLAS detector in  $pp$  collisions at the  
 27      Large Hadron Collider.

28      First, the discovery of a particle consistent with the Higgs in  $4.8 \text{ fb}^{-1}$  at  $\sqrt{s} = 7$  TeV and  $5.8 \text{ fb}^{-1}$  at  
 29       $\sqrt{s} = 8$  TeV is discussed. Then, the measurement of the Higgs boson signal strength and cross section  
 30      in both the gluon fusion and vector boson fusion (VBF) production modes using  $20.3 \text{ fb}^{-1}$  of  $\sqrt{s} =$   
 31       $8$  TeV data combined with  $4.8 \text{ fb}^{-1}$  of  $7$  TeV data is shown. The combined signal strength is measured  
 32      to be  $\mu = 1.09^{+0.23}_{-0.21}$ . The total observed significance of the  $H \rightarrow WW^*$  process is observed to be  
 33       $6.1\sigma$  (with  $5.8\sigma$  expected). Advanced methods for background reduction and estimation, particularly in  
 34      same-flavor lepton final states, are shown. The VBF signal strength is measured to be  $\mu_{\text{VBF}} = 1.27^{+0.53}_{-0.45}$   
 35      with an observed significance of  $3.2\sigma$  (with  $2.7\sigma$  expected). In the VBF channel, a selection requirement  
 36      based method, the precursor to the final multivariate technique used for the result, is detailed.

37      Finally, a search for Higgs pair production in the  $b\bar{b}b\bar{b}$  final state with  $3.2 \text{ fb}^{-1}$  at  $\sqrt{s} = 13$  TeV  
 38      is presented. A particular focus is placed on a tailored signal region for resonant production of Higgs  
 39      pairs at high masses, utilizing novel techniques in object reconstruction to increase signal acceptance in  
 40      boosted final state topologies. No significant excesses are observed, and upper limits on cross sections are  
 41      placed for spin-2 Randall Sundrum gravitons (RSG) and narrow spin-0 resonances. The cross section of  
 42       $\sigma(pp \rightarrow G_{\text{KK}}^* \rightarrow hh \rightarrow b\bar{b}b\bar{b})$  with  $k/\bar{M}_{\text{Pl}} = 1$  is constrained to be less than  $70 \text{ fb}$  for masses in the  
 43      range  $600 < m_{G_{\text{KK}}^*} < 3000 \text{ GeV}$ . For the RSG model with  $k/\bar{M}_{\text{Pl}} = 2$ , cross sections limits between  
 44       $40 \text{ fb}$  and  $200 \text{ fb}$  are set for the mass range of  $500 < m_{G_{\text{KK}}^*} < 3000 \text{ GeV}$ . The cross section upper  
 45      limits for  $\sigma(pp \rightarrow H \rightarrow hh \rightarrow b\bar{b}b\bar{b})$  ranges from  $30$  to  $300 \text{ fb}$  in the mass range of  $500 < m_H <$   
 46       $3000 \text{ GeV}$ .

# Contents

47

48	o INTRODUCTION	I
49	I Theoretical and Experimental Background	5
50	I.1 THE PHYSICS OF THE HIGGS BOSON	6
51	I.1.1 The Standard Model of Particle Physics	6
52	I.1.2 Electroweak Symmetry Breaking and the Higgs	8
53	I.1.3 Higgs Boson Production and Decay	II
54	I.1.4 Higgs Pair Production in the Standard Model	15
55	I.1.5 Higgs Pair Production in Theories Beyond the Standard Model	16
56	I.1.6 Conclusion	21
57	2 THE ATLAS DETECTOR AND THE LARGE HADRON COLLIDER	22
58	2.1 The Large Hadron Collider	23
59	2.2 The ATLAS Detector	25
60	2.3 The ATLAS Muon New Small Wheel Upgrade	36
61	2.4 Object Reconstruction in ATLAS	40
62	II Observation and measurement of Higgs boson decays to $WW^*$ in LHC	
63	Run I at $\sqrt{s} = 7$ and 8 TeV	49
64	3 $H \rightarrow WW^* \rightarrow \ell\nu\ell\nu$ ANALYSIS STRATEGY	50
65	3.1 Introduction	50
66	3.2 The $H \rightarrow WW^* \rightarrow \ell\nu\ell\nu$ signal in ATLAS	51
67	3.3 Background processes	52
68	3.4 Shared signal region selection requirements	56
69	3.5 Background reduction in same-flavor final states	58
70	3.6 Parameters of interest and statistical treatment	64
71	4 THE DISCOVERY OF THE HIGGS BOSON AND THE ROLE OF THE $H \rightarrow WW^* \rightarrow \ell\nu\ell\nu$ CHANNEL	
72	4.1 Introduction	70

74	4.2	Data and simulation samples . . . . .	71
75	4.3	$H \rightarrow WW \rightarrow e\nu\mu\nu$ search . . . . .	71
76	4.4	$H \rightarrow \gamma\gamma$ search . . . . .	76
77	4.5	$H \rightarrow ZZ \rightarrow 4\ell$ search . . . . .	77
78	4.6	Combined results . . . . .	79
79	4.7	Conclusion . . . . .	81
80	5	OBSERVATION OF VECTOR BOSON FUSION PRODUCTION OF $H \rightarrow WW^* \rightarrow \ell\nu\ell\nu$ . . . . .	83
81	5.1	Introduction . . . . .	83
82	5.2	Data and simulation samples . . . . .	84
83	5.3	Object selection . . . . .	88
84	5.4	Analysis selection . . . . .	91
85	5.5	Background estimation . . . . .	99
86	5.6	Systematic uncertainties . . . . .	110
87	5.7	Results . . . . .	114
88	6	COMBINED RUN I $H \rightarrow WW^* \rightarrow \ell\nu\ell\nu$ RESULTS . . . . .	119
89	6.1	Introduction . . . . .	119
90	6.2	Results of dedicated gluon fusion $H \rightarrow WW^* \rightarrow \ell\nu\ell\nu$ search . . . . .	120
91	6.3	Signal strength measurements in ggF and VBF production . . . . .	122
92	6.4	Measurement of Higgs couplings to vector bosons and fermions . . . . .	125
93	6.5	Higgs production cross section measurement . . . . .	126
94	6.6	Conclusion . . . . .	127
95	III	Search for Higgs pair production in the $HH \rightarrow b\bar{b}b\bar{b}$ channel in LHC	
96		Run 2 at $\sqrt{s} = 13$ TeV . . . . .	129
97	7	SEARCH FOR HIGGS PAIR PRODUCTION IN BOOSTED $b\bar{b}b\bar{b}$ FINAL STATES . . . . .	130
98	7.1	Introduction . . . . .	130
99	7.2	Motivation . . . . .	131
100	7.3	Data and simulation samples . . . . .	133
101	7.4	Event reconstruction and object selection . . . . .	135
102	7.5	Event selection . . . . .	138
103	7.6	Data-driven background estimation . . . . .	141
104	7.7	Systematic uncertainties . . . . .	147
105	7.8	Results . . . . .	150

<sup>106</sup>	<b>8 COMBINED LIMITS FROM BOOSTED AND RESOLVED SEARCHES</b>	<sup>152</sup>
<sup>107</sup>	<b>8.1 Introduction</b> . . . . .	<sup>152</sup>
<sup>108</sup>	<b>8.2 Resolved results</b> . . . . .	<sup>153</sup>
<sup>109</sup>	<b>8.3 Search technique and results</b> . . . . .	<sup>153</sup>
<sup>110</sup>	<b>8.4 Limit setting</b> . . . . .	<sup>154</sup>
<sup>111</sup>	<b>IV Looking ahead</b>	<sup>158</sup>
<sup>112</sup>	<b>9 CONCLUSION</b>	<sup>159</sup>
<sup>113</sup>	<b>APPENDIX A OPTIMIZATION OF <math>b</math>-TAGGING WORKING POINT IN <math>X \rightarrow HH \rightarrow b\bar{b}b\bar{b}</math></b>	
<sup>114</sup>	<b>SEARCH</b>	<sup>161</sup>
<sup>115</sup>	<b>APPENDIX B <math>b</math>-TAGGING EFFICIENCY AT HIGH <math>p_T</math></b>	<sup>163</sup>
<sup>116</sup>	<b>REFERENCES</b>	<sup>172</sup>

# Listing of figures

118	1.1	The particles of the Standard Model and their properties[1]. . . . .	7
119	1.2	The four most common Higgs boson production modes at the LHC: (a) gluon-gluon fu- sion, (b) vector boson fusion, (c) $W/Z + H$ production, (d) $t\bar{t}H$ production . . . . .	II
120	1.3	Higgs production cross sections as a function of center of mass energy ( $\sqrt{s}$ ) at a $pp$ collider[2]. . . . .	12
121	1.4	Higgs boson branching ratios as a function of $m_H$ [2]. . . . .	14
122	1.5	The two leading diagrams for Standard Model di-Higgs production at the LHC: (a) box di- agram, (b) Higgs self coupling . . . . .	16
123	1.6	Diagrams with new vertices for non-resonant Higgs pair production arising in composite Higgs models . . . . .	17
124	1.7	Generic Feynman diagram for resonant Higgs pair production in BSM theories . . . . .	18
125	1.8	Branching ratios for a spin-2 Randall-Sundrum graviton as a function of mass computed in MadGraph with the CP3-Origins implementation [3, 4] . . . . .	18
126	1.9	$\sigma \times BR(HH)$ for RSG as a function of mass computed in MadGraph with the CP3-Origins implementation [3, 4] . . . . .	19
127	1.10	RSG width as a function of mass computed in MadGraph with the CP3-Origins implemen- tation [3, 4] . . . . .	20
128	1.11	Branching ratios for heavy Higgs $H$ in Type I (left) and Type II (right) 2HDM models with $\tan \beta = 1.5$ and $\cos(\beta - \alpha) = 0.1(0.01)$ for Type I (Type II). [5] . . . . .	21
129	2.1	A schematic view of the LHC ring [6] . . . . .	23
130	2.2	A full diagram of the ATLAS detector [7] . . . . .	26
131	2.3	The ATLAS coordinate system . . . . .	27
132	2.4	Layout of the ATLAS Inner Detector system [8] . . . . .	28
133	2.5	Layout of the ATLAS calorimeter system [7] . . . . .	30
134	2.6	Layout of the ATLAS muon system [7] . . . . .	32
135	2.7	Predicted field integral as a function of $ \eta $ for the ATLAS magnet system [7] . . . . .	34
136	2.8	ATLAS trigger rates for Level-1 triggers as a function of instantaneous luminosity in 2012 and 2015 operation. These are single object triggers for electromagnetic clusters (EM), muons (MU), jets (J), missing energy (XE), and $\tau$ leptons (TAU). The threshold of the trigger is given in the name in GeV. [9] . . . . .	35
137	2.9	Instantaneous luminosity as a function of time for data recorded by ATLAS at different cen- ter of mass energies [10, 11] . . . . .	36

149	2.10	MDT tube hit (solid) and segment (dashed) efficiency as a function of hit rate per tube [12]	38
150	2.11	Trigger rate as a function of $p_T$ threshold with and without the NSW upgrade [12] . . . . .	38
151	2.12	Illustrations of the geometry (left) and operating principle (right) of the micromegas detector [12] . . . . .	39
153	2.13	Geometry of the sTGC detector [12] . . . . .	40
154	2.14	Illustration of particle interactions in ATLAS [13] . . . . .	41
155	2.15	Electron performance: (a) reconstruction efficiency as a function of electron $E_T$ [14] (b) energy resolution in simulation as a function of $ \eta $ for different energy electrons [15] . . . . .	42
157	2.16	Muon performance: (a) reconstruction efficiency as a function of muon $p_T$ (b) dimuon mass resolution as a function of average $p_T$ [16] . . . . .	44
159	2.17	Jet energy response after calibration as a function of true $p_T$ in simulation [17] . . . . .	45
160	2.18	Light jet rejection (1/efficiency) vs. $b$ -jet efficiency for MV1 and its input algorithms (a) [18] and MV2 (b) [19] in simulated $t\bar{t}$ events. The numbers in the algorithm names in (b) refer to the fraction of charm events used in the MV2 training. . . . .	46
163	2.19	Resolution of $E_T^{\text{miss}}$ components as a function of $\sum E_T$ before pileup suppression with different pileup techniques [20] . . . . .	48
165	3.1	Branching ratios for a $WW$ system. $q$ refers to quarks. $\ell$ can be either an electron or muon, and the leptonic branching ratios of the $\tau$ are included. For example, the $\ell\nu qq$ final state includes one $W$ decaying to $e\nu$ , $\mu\nu$ , or $\tau\nu$ . $\tau_h$ refer to hadronic decays of the $\tau$ . . . . .	52
166	3.2	Feynman diagram for Standard Model $WW$ production . . . . .	53
169	3.3	Feynman diagrams for top pair production (left) and $Wt$ production (right) . . . . .	54
170	3.4	An example Feynman diagram of $W + \text{jets}$ production . . . . .	54
171	3.5	An example Feynman diagram of $Z + \text{jets}$ production . . . . .	55
172	3.6	An illustration of the unique analysis signal regions[21] . . . . .	56
173	3.7	A graphical illustration of the $E_{T,\text{rel}}^{\text{miss}}$ calculation . . . . .	58
174	3.8	Predicted backgrounds (compared with data) as a function of $n_j$ (a and b) and $n_b$ (c) . . . . .	59
175	3.9	An event display of a $Z/\gamma^* + \text{jets}$ event illustrating the effect of pileup interactions . . . . .	60
176	3.10	The RMS of different missing transverse momentum definitions as a function of the average number of interactions per bunch crossing . . . . .	61
177	3.11	The difference between the true and reconstructed values of the missing transverse momentum (a) and $m_T$ (b) in a gluon fusion signal sample . . . . .	62
180	3.12	Comparison of $f_{\text{recoil}}$ distributions for $Z/\gamma^* + \text{jets}$ , $H \rightarrow WW^*$ , and other backgrounds with real neutrinos. . . . .	63
182	3.13	Signal significance as a function of required value for $f_{\text{recoil}}$ and $p_{T,\text{rel}}^{\text{miss}(\text{trk})}$ in the ggF $H \rightarrow WW^*$ with $n_j = 0$ . . . . .	64

184	4.1	Jet multiplicity distribution in data and MC after applying lepton, jet, and $E_{\text{T},\text{rel}}^{\text{miss}}$ selections.	
185		The $WW$ and top backgrounds have been normalized using control samples, and the hashed	
186		band indicates the total uncertainty on the prediction. [22] . . . . .	72
187	4.2	Comparison of $m_{\text{T}}$ between data and simulation in the $n_j = 0$ $WW$ (a) and $n_j = 1$	
188		top (b) control samples [22] . . . . .	74
189	4.3	$m_{\text{T}}$ distribution in the $H \rightarrow WW \rightarrow e\nu\mu\nu n_j \leq 1$ channels for 8 TeV data[22]. . . . .	76
190	4.4	Diphoton mass spectrum in 7 and 8 TeV data. Panel a) shows the unweighted data distri-	
191		bution superimposed on the background fit, while panel c) shows the data where each event	
192		category is weighted by its signal to background ratio. Panels b) and d) show the respective	
193		distributions with background subtracted[22]. . . . .	77
194	4.5	Four lepton invariant mass spectrum ( $m_{4\ell}$ ) in 7 and 8 TeV data compared to background	
195		estimate. A 125 GeV SM Higgs signal is shown in blue[22]. . . . .	78
196	4.6	Local $p_0$ distribution as a function of hypothesized Higgs mass for the $H \rightarrow ZZ^* \rightarrow 4\ell$	
197		(a), $H \rightarrow \gamma\gamma$ (b), and $H \rightarrow WW^* \rightarrow \ell\nu\ell\nu$ (c) channels. Dashed curves show expected	
198		results, while solid curves show observed. Red curves are from 7 TeV data, blue curves from	
199		8 TeV, and black curved combined[22]. . . . .	80
200	4.7	Combined 95% CL limits (a), local $p_0$ values (b), and signal strength measurement (c) as a	
201		function of Higgs mass[22]. . . . .	81
202	4.8	Comparison of measured signal strength $\mu$ for a 126 GeV Higgs in the 7 and 8 TeV datasets[22].	82
203	4.9	Two dimensional likelihood as a function of signal strength $\mu$ and Higgs mass $m_H$ [22]. . . . .	82
204	5.1	A comparison of the subleading lepton $p_{\text{T}}$ spectrum between VBF $H \rightarrow WW^*$ production	
205		and $t\bar{t}$ background . . . . .	85
206	5.2	Leading jet $\eta$ in VBF $H \rightarrow WW^*$ (red) and $t\bar{t}$ (black) . . . . .	93
207	5.3	Distributions of (a) $m_{jj}$ , (b) $\Delta y_{jj}$ , (c) $C_{\ell 1}$ , and (d) $\sum m_{\ell j}$ , for the VBF analysis. The top	
208		panels compare simulation and data, while the bottom panels show normalized distributions	
209		for all background processes and signal[21]. . . . .	95
210	5.4	A cartoon of the $WW$ final state. Momenta are represented with thin arrows, spins with thick	
211		arrows. [21] . . . . .	96
212	5.5	Event display of a VBF candidate event[21]. . . . .	97
213	5.6	Distributions of $m_{\ell\ell}$ (top left), $\Delta\phi_{\ell\ell}$ (top right), and $m_{\text{T}}$ (bottom), Higgs topology vari-	
214		ables used in the selection requirements of the cut-based signal region and as inputs to the	
215		BDT result. These are plotted after all of the BDT pre-training selection cuts[21]. . . . .	100
216	5.7	Distributions of $m_{jj}$ (top left), $\Delta y_{jj}$ (top right), $\sum C_{\ell}$ (bottom), VBF topology variables	
217		used in the selection requirements of the cut-based signal region and as inputs to the BDT	
218		result. These are plotted after all of the BDT pre-training selection cuts[21]. . . . .	101
219	5.8	Distributions of $m_{jj}$ (a) and $O_{\text{BDT}}$ (b) in the VBF $n_b = 1$ top CR [21]. . . . .	103

220	5.9	Comparison of $m_{jj}$ shape in a same flavor $Z \rightarrow \ell\ell$ control region and the VBF cut-based signal region. . . . .	105
221	5.10	General illustration of the ABCD region definitions for $Z/\gamma^* \rightarrow \ell\ell$ background estimation. . . . .	106
222	5.11	Distribution of $m_{T2}$ in the $WW$ validation region of the VBF analysis[21]. . . . .	107
223	5.12	Extrapolation factors for the $W + \text{jets}$ estimate derived for muons (a) and electrons (b) as a function of lepton $p_T$ [21]. . . . .	109
224	5.13	Background composition in final VBF signal region[21]. . . . .	110
225	5.14	Variations in the top background extrapolation factor in the cut-based analysis due to PDF uncertainties, binned in $m_T$ . . . . .	112
226	5.15	Variations in the top background extrapolation factor in the cut-based analysis due to QCD scale uncertainties, binned in $m_T$ . . . . .	113
227	5.16	Postfit distributions in the cut-based VBF analysis. Panel (a) shows the one-dimensional $m_T$ distribution, while (b) shows the data candidates split into the bins of $m_T$ and $m_{jj}$ used in the final fit[21]. . . . .	116
228	5.17	Postfit distributions in the BDT VBF analysis[21]. . . . .	117
229	5.18	Overlap between cut-based and BDT VBF signal region candidates in the $m_{jj}$ - $m_T$ plane. .	117
230	6.1	Post-fit $m_T$ distribution in the $n_j \leq 1$ regions[21]. . . . .	121
231	6.2	Best fit signal strength $\hat{\mu}$ as a function of hypothesized $m_H$ [21]. . . . .	123
232	6.3	Local $p_0$ as a function of $m_H$ [21]. . . . .	123
233	6.4	Likelihood as a function of $\mu_{\text{VBF}}/\mu_{\text{ggF}}$ [21]. . . . .	124
234	6.5	Likelihood scan as a function of $\mu_{\text{VBF}}$ and $\mu_{\text{ggF}}$ [21]. . . . .	125
235	6.6	Likelihood scan as a function of $\kappa_F$ and $\kappa_V$ [21]. . . . .	126
236	6.7	Comparison of signal strength measurements in different Higgs decay channels on ATLAS[23].	128
237	7.1	Parton luminosity ratios as a function of resonance mass $M_X$ for 13/8 TeV and 7/8 TeV [24].	131
238	7.2	Summary of $HH$ branching ratios [25]. . . . .	132
239	7.3	Minimum $\Delta R$ between $B$ decay vertices for different RSG masses in a $G_{\text{KK}}^* \rightarrow HH \rightarrow 4b$ sample with $c = 1$ . . . . .	133
240	7.4	Trigger efficiency for events passing all signal region selections as a function of mass in $G_{\text{KK}}^* \rightarrow HH \rightarrow 4b$ samples with $c = 1$ [26]. In the trigger names, “j” refers to a jet or jets. “ht” refers to $H_T$ , the scalar sum of transverse momenta in the event. “bloose” refers to a loose $b$ -tagging requirement applied to the jet. “aior” refers to anti- $k_T$ jets with $R = 1.0$ . The numbers at the end are the thresholds on the given quantity in GeV. . . . .	135
241	7.5	Comparison of untrimmed and trimmed jet masses for large radius jets in a RSG sample with $m_{G_{\text{KK}}^*} = 1$ TeV. JES (JMS) refers to the standard jet energy (mass) scale calibration for ATLAS [17].	136

255	7.6 Efficiency of finding two $b$ -jets from each Higgs in an RSG event using calorimeter jets with $R = 0.3$ or different track jet radii [27] . . . . .	137
256	7.7 Illustration of the boosted selection requirements on Higgs candidates. Each large-radius calorime- ter jet (Higgs candidate) must contain two track jets . . . . .	139
257	7.8 Acceptance $\times$ efficiency as a function of mass for (a) RSG and (b) narrow heavy scalar sig- nal models [28]. . . . .	140
258	7.9 Efficiency of requiring 3 or 4 $b$ -tagged track jets vs. RSG mass. The efficiency quoted is rel- ative to the previous selection requirements (rather than an absolute efficiency). . . . .	141
259	7.10 $M_J^{\text{sublead}}$ vs. $M_J^{\text{lead}}$ in a 2 $b$ -tag data sample. The signal region is defined by the inner black contour ( $X_{hh} < 1.6$ ) and the sideband region is defined by the outer contour ( $R_{hh} >$ 35.8 GeV). The region between the black contours is the control region. The mass region which is enriched in $t\bar{t}$ background is also shown for illustration. [28] . . . . .	143
260	7.11 An illustration of the data-driven background estimation technique for the boosted anal- ysis . . . . .	144
261	7.12 Leading large-R jet mass in the 3 $b$ (a) and 4 $b$ (b) sideband regions. The multijet and $t\bar{t}$ back- grounds are estimated using the data-driven methods described above. Because their normal- izations are derived in the sideband region, the total background normalization is constrained by default to match the normalization of the data [28]. . . . .	145
262	7.13 Di-jet invariant mass ( $M_{2,J}$ ) in the 3 $b$ (a) and 4 $b$ (b) control regions. The multijet and $t\bar{t}$ back- grounds are estimated using the data-driven methods described above [28]. . . . .	146
263	7.14 Di-jet invariant mass ( $M_{2,J}$ ) in the 3 $b$ (a) and 4 $b$ (b) signal regions. The multijet and $t\bar{t}$ back- grounds are estimated using the data-driven methods described above. In the 3 $b$ region, a graviton signal with $m_{G_{\text{KK}}^*} = 1.8$ TeV and $c = 1$ is overlaid, with the cross section mul- tiplied by a factor of 50 so that the signal is visible. In the 4 $b$ region, signals with $m_{G_{\text{KK}}^*} =$ 1.0 TeV and $m_{G_{\text{KK}}^*} = 1.5$ TeV are overlaid, both with $c = 1$ and the yields multiplied by factors of 2 and 5 respectively [28]. . . . .	151
264		
265	8.1 Di-jet invariant mass ( $M_{2,J}$ ) in the resolved signal region. Agraviton signal with $m_{G_{\text{KK}}^*} =$ 800 GeV and $c = 1$ is overlaid. [28]. . . . .	154
266	8.2 Expected and observed upper limit as a function of mass for $G_{\text{KK}}^*$ in the RSG model with (a) $c = 1$ and (b) $c = 2$ , as well as (c) $H$ with fixed $\Gamma_H = 1$ GeV, at the 95% confidence level in the $CL_s$ method. [28] . . . . .	157
267		
268	A.1 Estimated significance as a function of signal mass for RSG $c = 1$ models in the 3 $b$ (a) and 4 $b$ (b) regions for different $b$ -tagging efficiency working points . . . . .	162
269		

# Listing of tables

288

289	1.1	Production cross sections for a 125 GeV Higgs boson at $\sqrt{s} = 8$ TeV with scale and PDF uncertainties [2]. . . . .	13
290	1.2	Branching ratios for a 125 GeV Higgs boson[2]. . . . .	15
291	1.3	Possible channels for Higgs searches. Checkmarks denote the most sensitive production modes [29]. . . . .	15
292			
293			
294	1.4	Production cross sections for pair production of a 125 GeV Higgs boson at $\sqrt{s} = 14$ TeV with total uncertainty [30]. The uncertainties include QCD scale and PDF variations as well as uncertainties on $\alpha_S$ . . . . .	16
295			
296			
297	2.1	Evolution of LHC machine conditions [31, 32] . . . . .	25
298	2.2	Performance requirements for the ATLAS detector [7]. . . . .	37
299	2.3	Signal efficiencies for $WH$ production with $H \rightarrow b\bar{b}$ and $H \rightarrow WW^* \rightarrow \mu\nu qq$ under different trigger configurations [12]. . . . .	40
300			
301	3.1	A summary of backgrounds to the $H \rightarrow WW^* \rightarrow \ell\nu\ell\nu$ signal . . . . .	55
302			
303	4.1	Monte carlo generators used to model signal and background for the Higgs search[22]. . . . .	71
304	4.2	Normalization factors (ratio of data and MC yields in a control sample) for the Standard Model $WW$ and top backgrounds in the $H \rightarrow WW^* \rightarrow \ell\nu\ell\nu$ analysis [22]. Only statistical uncertainties are shown. . . . .	74
305			
306	4.3	Data and expected yields for signal and background in the final $H \rightarrow WW^* \rightarrow \ell\nu\ell\nu$ signal region. Uncertainties shown are both statistical and systematic. [22] . . . . .	75
307			
308	4.4	Summary of the expected and observed significance and measured signal strengths in the combined 7 and 8 TeV datasets for the Higgs discovery analysis[22]. . . . .	79
309			
310	5.1	Single lepton triggers used for electrons and muons. A logical “or” of the triggers listed for each lepton type is taken. Units are in GeV, and the $i$ denotes an isolation requirement in the trigger. . . . .	85
311			
312			
313	5.2	Di-lepton triggers used for different flavor combinations. The two thresholds listed refer to leading and sub-leading leptons, respectively. The di-muon trigger only requires a single lepton at level-i. . . . .	85
314			
315			

316	5.3	Trigger efficiency for signal events and relative gain of adding a dilepton trigger on top of the single lepton trigger selection. The first lepton is the leading, while the second is the sub-leading. Efficiencies shown here are for the ggF signal in the $n_j = 0$ category but are comparable for the VBF signal. . . . .	86
317			
318	5.4	Monte Carlo samples used to model the signal and background processes[21]. . . . .	87
319			
320	5.5	$p_T$ dependent isolation requirements for muons. Muons are required to have the amount of calorimeter or track based cone sums be less than this fraction of their $p_T$ . . . . .	89
321			
322	5.6	$p_T$ dependent requirements for electrons. Electrons are required to have the amount of calorimeter or track based cone sums be less than this fraction of their $E_T$ . . . . .	90
323			
324	5.7	Event selection for the $n_j \geq 2$ VBF analysis in the 8 TeV cut-based analysis[21]. . . . .	98
325			
326	5.8	Top normalization factors computed at each stage of the cut-based selection. Uncertainties are statistical only. . . . .	102
327			
328	5.9	Top normalization factors computed for each bin of $O_{\text{BDT}}$ . Uncertainties are statistical only. . . . .	102
329			
330	5.10	$Z/\gamma^* \rightarrow \tau\tau$ correction factors for the VBF cut-based analysis. Uncertainties are statistical only. . . . .	105
331			
332	5.11	$Z/\gamma^* \rightarrow \ell\ell$ normalization factors for cut-based and BDT analyses. Uncertainties are statistical only. . . . .	107
333			
334	5.12	Systematic uncertainties for various processes in the cut-based VBF analysis, given in units of % change in yield. Values are given for the low $m_{jj}$ signal region. . . . .	III
335			
336	5.13	Composition of the post-fit uncertainties (in %) on the total signal ( $N_{\text{sig}}$ ), total background ( $N_{\text{bkg}}$ ), and individual background yields in the VBF analysis[21]. . . . .	114
337			
338	5.14	Event selection for the VBF BDT analysis. The event yields in (a) are shown after the pre-selection and the additional requirements applied before the BDT classification (see text). The event yields in (b) are given in bins in $O_{\text{BDT}}$ after the classification[21]. . . . .	115
339			
340	6.1	All signal regions definitions input into final statistical fit[21]. . . . .	120
341	6.2	Post-fit yields in the different ggF and VBF dedicated signal regions[21]. . . . .	121
342			
343	7.1	Summary of requirements on objects used in the $X \rightarrow HH \rightarrow b\bar{b}b\bar{b}$ search . . . . .	138
344	7.2	Effect of boosted selection on data, RSG signal models, $t\bar{t}$ , and $Z+\text{jets}$ . The numbers from simulation are normalized with the MC generator cross section and do not take into account the data driven estimates described in section 7.6 [33]. . . . .	142
345			
346	7.3	Mass region definitions used for background estimation . . . . .	143
347	7.4	Parameters derived for exponential fit to background $M_{2J}$ shape in the 3 $b$ and 4 $b$ signal regions [33] . . . . .	146
348			
349	7.5	The number of events in data and predicted background events in the boosted 3-tag and 4-tag sideband and control regions. The uncertainties shown are statistical only. [28] . . . . .	147
350			

351	7.6	Summary of systematic uncertainties in the total background and signal event yields (expressed in %) in the boosted 3-tag and 4-tag signal regions. Systematic uncertainties on the signal normalization are shown for models with $m_{G_{\text{KK}}^*} = 1.5 \text{ TeV}$ and both $c = 1$ and $c = 2$ as well as a narrow width heavy scalar. . . . .	149
352	7.7	Alternate fit functions used to model the $M_{JJ}$ distribution in the QCD multijet background. In the equations, $x = M_{JJ}/\sqrt{s}$ . . . . .	150
353	7.8	Observed yields in the 3-tag and 4-tag signal regions for the boosted analysis compared to the predicted number of background events Errors correspond to the total uncertainties in the predicted event yields. The yields for a graviton with $m_{G_{\text{KK}}^*} = 1 \text{ TeV}$ and $c = 1$ are also shown. [28] . . . . .	151
354			
355	8.1	Observed yields in the resolve selection 4-tag signal region compared to the predicted num- ber of background events Errors correspond to the total uncertainties in the predicted event yields. The yields for a graviton with $m_{G_{\text{KK}}^*} = 800 \text{ GeV}$ and $c = 1$ are also shown. [28] . .	153
356			
357			
358			
359			
360			
361			
362			
363			



# Acknowledgments

366 I have been a member of the Harvard ATLAS group for many years now, first as an undergraduate  
 367 and then as a graduate student. As a result, I have had the privilege of interacting with many amazing  
 368 people there over the years and have accumulated a large list of folks to thank.

369 First and foremost, I must thank the two people who have effectively been my academic parents since  
 370 I started in the Harvard group: Joao Guimaraes da Costa and Melissa Franklin. Melissa Franklin and  
 371 Joao Guimaraes da Costa. They have both been so important to both my academic and personal devel-  
 372 opment that I can't even put one before the other. Joao has been an excellent PhD advisor, showing me  
 373 how to look at the big picture and helping me navigate the sometimes complicated politics of ATLAS.  
 374 He got me started on my first projects with ATLAS as a young college sophomore before there was even  
 375 beam in the LHC (go cosmic ray muons!). He has also been a constant source of advice and support,  
 376 even when we have been on different continents. Melissa gave me my start in HEP as a summer student  
 377 on CDF and has been an unbelievable mentor throughout my time at Harvard. I still remember our  
 378 weekly chalkboard particle physics lessons after that first summer. She also graciously took me on as a  
 379 co-advisee after Joao moved on to his new position at IHEP. I am incredibly lucky to have had both of  
 380 them as advisors.

381 Another mentor who was essential to my development as a graduate student is Paolo Giromini. His  
 382 uncanny knowledge and intuition about detectors is unmatched and I am very grateful to have had  
 383 the chance to work with him on the micromegas for the ATLAS New Small Wheel upgrade project. I  
 384 owe essentially all my practical knowledge about detectors (and building things in general) to him. I also  
 385 appreciated his unique sense of humor which made sometimes difficult tasks much easier to get through.

386 I am grateful to John Huth and Masahiro Morii for their helpful advice as the other professors in the  
 387 Harvard ATLAS group as well. I especially thank John for helping me get started on the micromegas  
 388 trigger project and being a great professor to TF particle physics for.

389 I also owe enormous thanks to Hugh Skottowe, the postdoc that I worked most closely with in my  
 390 early years as a graduate student. He was always able to help me through complicated tasks in everything  
 391 from writing code to understanding difficult physics concepts. I particularly enjoyed walking down to  
 392 his office in Palfrey at random times and talking through whatever problem I was tackling on that day.

393 Alex Tuna, the second postdoc that I worked closely with at Harvard, deserves great thanks as well.  
 394 He helped me push through to the end of my graduate career and offered great advice along the way.

395 Being at Harvard, I have seen an incredible array of graduate students graduate before me: Ben Smith,  
 396 Verena Martinez Outschoorn, Srivas Prasad, Michael Kagan, Giovanni Zevi Della Porta, Laura Jeanty,  
 397 Kevin Mercurio, William Spearman, and Andy Yen. I want to thank them all for showing me what a

398 good physicist looks like and for patiently answering my questions and offering insightful advice about  
399 physics and life.

400 Getting through graduate school would not have been possible without the support and friendship  
401 of the other students in our group. Thanks to Emma Tolley for geeking out with me about cool com-  
402 puting stuff, going to taste delicious beers with me, and helping start the Palfrey tradition of Taco Tues-  
403 days. Thanks to Brian Clark for being a great friend and housing companion both in Kirkland House  
404 and in our tiny summer apartment in Geneva (and thanks to his partner Allison Goff for the same rea-  
405 sons!). Thanks to Siyuan Sun for giving me my first aikido lesson and always being there for great con-  
406 versations, big and small. Tony (Baojia) Tong deserves special recognition for working with me on the  
407  $4b$  analysis and putting up with my sometimes strange requests (and giving me rides to the Val Thoiry  
408 Migros so I wouldn't have to pay exorbitant Geneva grocery prices!). Stephen Chan is probably the only  
409 student in the group who both understands my references to the Sopranos and makes some of his own.  
410 To the younger graduate students - Karri Di Petrillo, Jennifer Roloff, Julia Gonski, and Ann Wang - I  
411 want to say thank you for making the group a fun and lively place to be and giving all of us energy that  
412 the older graduate students like myself can sometimes lack.

413 I'd like to thank Annie Wei and Gray Putnam, the two undergraduates I have worked with as a gradu-  
414 ate student. Their unbelievable intuition and quickness in picking up difficult particle physics concepts  
415 is inspiring.

416 I would also like to thank all of the postdocs that I have interacted with in my time in the Harvard  
417 group: Kevin Black, Alberto Belloni (who would always ask me "Do you have it?"...I can now say that  
418 I do!), Shulamit Moed, Corrinne Mills, Geraldine Conti, David Lopez Mateos, Chris Rogan, Valerio  
419 Ippolito, and Stefano Zambito.

420 There are many people on ATLAS who have helped me get to this point as well. In the  $WW$  group,  
421 I have to thank Jonathan Long, Joana Machado Miguens, Ben Cerio, Philip Chang, Bonnie Chow,  
422 Richard Polifka, Heberth Torres, Tae Min Hong, and Jennifer Hsu for being wonderful colleagues and  
423 making the entire analysis run smoothly. In the  $4b$  group, I have to thank Qi Zeng, Tony Tong, Alex  
424 Tuna, Michael Kagan, Max Bellomo, John Alison, and Patrick Bryant.

425 Kirkland House was my home for the last three years of graduate school and was an wonderful envi-  
426 ronment and support system. I want to thank my fellow tutors, especially Brian Clark and Allison Goff  
427 (again), Zach Abel, Kelly Bodwin, Alex Lupsasca, John and Pam Park, Luke and Erin Walczewski, and  
428 Philip Gant for their friendship and support. I also want to thank Kate Drizos Cavell, Bob Butler, and  
429 the Faculty Deans Tom and Verena Conley.

430 There are still a few friends that haven't been covered yet and deserve great thanks. Jake Connors and  
431 Meredith MacGregor have been absolutely wonderful friends and I thank them in particular for the  
432 many home-cooked meals and great conversations we've had in their apartment. Nihar Shah has been  
433 my friend and confidant since we were both wee freshmen in Harvard Yard. Gareth Kafka, though he  
434 sits on the "neutrino" side of Palfrey House, has made days there more fun and has also been an enthusi-

435 astic participant in the Palfrey Taco Tuesdays.

436 Being at Harvard necessarily means having to navigate through bureaucracy at some point or another.  
437 I thank Lisa Cacciabaudo, Carol Davis, and Jacob Barandes for always having open doors and being the  
438 most kind, helpful people in the Physics department.

439 I thank Venky Narayananamurti for putting on a great SPU course that I was proud to be a part of and  
440 TF for. I'd also like to thank Jim Waldo for offering me much advice about working in Computer Science  
441 and giving me a fun data project to be a part of in my free time.

442 I grew up in a very tight knit Serbian community on the south side of Chicago which helped make  
443 me the person I am today. I would like to thank all of the people at St. Simeon Mirotochivi Serbian  
444 Orthodox Church who have always been sources of enthusiasm and support in my life.

445 I would not be here without the unconditional love and constant support and encouragaement of my  
446 family. To my pokojni Dendas Branko and Miloje, my pokojni Baba Milka, and my Baba Desa, I want to  
447 say thank you for instilling in me at an early age the love of curiosity and storytelling that I have carried  
448 throughout my life. To my sister Angelina, I want to say thank you for always loving me and being my  
449 partner in crime throughout our childhoods. To my parents, Miroljub and Nada, Tata and Mama, I  
450 really cannot express how grateful I am to you and how much I owe you. As I look back now I see how  
451 I am a combination of both of your best qualities and every day I am in situations where I understand  
452 more and more the lessons you made sure to teach me and the sacrifices you made to make sure I got the  
453 best possible education. I love you all.

454 Finally, I have to thank my soul mate, the one person in my life who understands me more than any-  
455 one else, my fiancee Kelly Brock. You are my sounding board, my support system, my cheerleader (fig-  
456 uratively and literally!), my best friend, my role model, and my everything. I would not have gotten  
457 through graduate school without you and my life would not be the same without you. I cannot wait to  
458 start our new lives together as the married doctors, tackling whatever comes our way with the same zeal  
459 with which we tackled graduate school. I love you with all my heart and soul.

# 0

460

461

## Introduction

462 The Higgs boson is often described as one of the cornerstones of the Standard Model. Since the con-  
463 ception of the Higgs mechanism as the source of electroweak symmetry breaking in the early 1960s,  
464 countless collider experiments have searched for this elusive particle. This dissertation presents multi-  
465 ple studies of the Higgs boson with the ATLAS detector at the Large Hadron Collider (LHC).

466 One of the first priorities of the early LHC was the search for the Higgs boson. This search was first  
467 tackled in three main channels:  $H \rightarrow \gamma\gamma$ ,  $H \rightarrow ZZ^*$ , and  $H \rightarrow WW^*$ . Each channel has its own  
468 merits, but the  $WW^*$  is particularly suited to searching over a wide range of masses. The  $H \rightarrow WW$   
469 branching ratio is large and it is the primary decay channel above the  $2m_W$  mass threshold.

470 While the rate of events produced in  $H \rightarrow WW^*$  is large, the channel poses some challenges. First,  
471 the most common mode of study for this channel is  $H \rightarrow WW^* \rightarrow \ell\nu\ell\nu$ . With neutrinos in the  
472 final state, it is not possible to fully reconstruct the invariant mass of the parent Higgs like the  $\gamma\gamma$  and  
473  $ZZ \rightarrow 4\ell$  channels. Second, the final state topology is mimicked by a wide variety of backgrounds that

474 need to be properly estimated. This means tailored selection requirements for background reduction  
475 and robust background estimation techniques must both be developed.

476 In 2012, the ATLAS and CMS experiments announced the discovery of a new particle consistent with  
477 the Higgs boson [22, 34]. In ATLAS, this discovery was made with  $4.8 \text{ fb}^{-1}$  collected at  $\sqrt{s} = 7 \text{ TeV}$   
478 and  $5.8 \text{ fb}^{-1}$  at  $\sqrt{s} = 8 \text{ TeV}$ . The  $H \rightarrow WW^* \rightarrow \ell\nu\ell\nu$  analysis played an important role in this  
479 discovery. After the discovery, measurement of the properties of the newly discovered particle and con-  
480 firmation of its consistency with the Standard Model Higgs were the main priorities. The  $WW^*$  chan-  
481 nel is also uniquely suited to these types of measurements. Because of its good rate, it offers some of the  
482 best cross section measurements available among the various Higgs decay modes. It is also suited for  
483 measurement of multiple Higgs production modes, like the vector boson fusion (VBF) mode, where in-  
484 coming quarks radiate  $W/Z$  bosons which fuse to make a Higgs. In VBF production with the  $WW^*$   
485 decay channel, the coupling of the Higgs to the  $W$  boson is present in both the production and decay  
486 which allows for more precise measurements of this coupling than other channels which rely on gluon  
487 fusion production (where gluons couple to the Higgs through a top loop in the production). The mea-  
488 surement of VBF carries the additional challenge that its cross section is an order of magnitude smaller  
489 than that of gluon fusion, meaning that the large branching ratio to  $WW^*$  offers an additional advan-  
490 tage in isolating this production mode. In the final ATLAS Run 1 results, combining  $20.3 \text{ fb}^{-1}$  taken at  
491  $\sqrt{s} = 8 \text{ TeV}$  with the  $4.8 \text{ fb}^{-1}$  collected at  $\sqrt{s} = 7 \text{ TeV}$ , the  $WW^*$  channel achieved its first observa-  
492 tion of VBF production of the Higgs.

493 After Run 1 of the LHC, with the existence of the Higgs now firmly established, the focus shifted to  
494 searches for physics beyond the Standard Model. In particular, searches for high mass resonances benefit  
495 from the LHC's increase to  $\sqrt{s} = 13 \text{ TeV}$  in Run 2. The newly discovered Higgs can be used as a tool  
496 in these searches. Higgs pair production in the Standard Model has a low cross section that requires large  
497 datasets (on the order of the LHC's lifetime) for full measurement. However, new physics can modify  
498 this cross section, especially new resonances which decay to two Higgs bosons. A search for Higgs pair  
499 production in the  $HH \rightarrow b\bar{b}b\bar{b}$  final state was performed with  $3.2 \text{ fb}^{-1}$  collected with ATLAS at  $\sqrt{s} =$   
500  $13 \text{ TeV}$  in 2015.

501 This dissertation begins by discussing the discovery of the Higgs and the role of the  $H \rightarrow WW^* \rightarrow$   
502  $\ell\nu\ell\nu$  channel. It then discusses the first observation of the VBF production mode in  $H \rightarrow WW^* \rightarrow$   
503  $\ell\nu\ell\nu$  with the full ATLAS Run 1 dataset, as well as the final combined Run 1 measurements from this  
504 channel. Finally, it presents a search for Higgs pair production in the  $HH \rightarrow b\bar{b}b\bar{b}$  channel. It is orga-  
505 nized into four parts.

506 Part 1 presents the theoretical and experimental background required for the subsequent parts. Chap-  
507 ter 1 gives an overview of Higgs physics, particularly single and double Higgs production in the Standard  
508 Model and beyond. Chapter 2 presents details regarding the Large Hadron Collider and the ATLAS  
509 experiment. The evolution of machine conditions, descriptions of the ATLAS sub-detectors, and an  
510 overview of object reconstruction in ATLAS are all shown. A brief interlude on the ATLAS Muon New  
511 Small Wheel upgrade is also given, as this upgrade has been a focus of my graduate work and will have  
512 important impact on ATLAS' ability to study the Higgs at the High Luminosity LHC.

513 Part 2 discusses the observation and measurement of the Higgs in the  $H \rightarrow WW^* \rightarrow \ell\nu\ell\nu$   
514 channel in the ATLAS Run 1 dataset at  $\sqrt{s} = 7$  and 8 TeV. Because I worked in this channel from  
515 before the discovery through to the final analysis of the Run 1 dataset, Part 2 is organized in such a way  
516 to allow easy presentation of multiple analyses on different subsets of the full Run 1 dataset. Chapter 3  
517 presents a general overview of the  $H \rightarrow WW^*$  analysis strategy and defines many of the variables and  
518 common elements used in the rest of Part 2. Chapter 4 presents the discovery of the Higgs boson, fo-  
519 cusing on the role of the  $WW^*$  channel in this discovery. Chapter 5 presents the first observation of the  
520 VBF production mode of the Higgs in the  $WW^*$  channel, a study which was done on the full Run 1  
521 ATLAS dataset. In this chapter, the focus is mainly on the selection cut-based VBF analysis. The cut-  
522 based analysis was an important first step to the final VBF result which used a Boosted Decision Tree  
523 (BDT). Where appropriate, connections between the cut-based and BDT analyses are shown and their  
524 compatibility is discussed. Finally, the VBF analysis was an important input into the combined Run 1  
525  $H \rightarrow WW^* \rightarrow \ell\nu\ell\nu$  result, which used both the gluon fusion and VBF channels in a combined  
526 fit to infer properties of the Higgs, including its couplings to the gauge bosons and its production cross  
527 section. This is the topic of Chapter 6.

528        Part 3 presents a search for Higgs pair production in the  $HH \rightarrow b\bar{b}b\bar{b}$  channel. Chapter 7 presents  
529        an overview of this search in the boosted regime, where the Higgs pairs are the result of the decay of a  
530        heavy resonance. Chapter 8 shows the combined results between the boosted regime and the resolved  
531        regime, which is sensitive to lower mass resonances and non-resonant Higgs pair production. Finally,  
532        Part 4 presents a conclusion and brief outlook of future Higgs physics with ATLAS.

<sup>533</sup>

## Part I

<sup>534</sup>

## Theoretical and Experimental Background

# 1

535

536

## The Physics of the Higgs Boson

537 This chapter presents an overview of the Standard Model of Particle Physics and in particular the physics  
538 of the Higgs boson. First, a brief overview of the Standard Model and its history are presented. Then, a  
539 description of the Higgs mechanism of electroweak symmetry breaking is given. Next, the physics of sin-  
540 gle Higgs boson production and decay is described. The Standard Model also allows for production of  
541 two Higgs bosons and this is detailed as well. Finally, di-Higgs production in two beyond the Standard  
542 Model (BSM) theories - Randall-Sundrum gravitons (RSG) and Two Higgs Doublet Models (2HDM) -  
543 is shown.

### 544 1.1 THE STANDARD MODEL OF PARTICLE PHYSICS

545 The Standard Model (SM) of Particle Physics is a quantum field theory describing the fundamental  
546 particles of nature and the forces that govern their interactions. Several comprehensive treatments of  
547 the SM already exist in the literature[1, 29, 35–38] and this section will not rehash those. Rather, this

548 section presents a brief overview of the SM particles and forces in order to define them for subsequent  
 549 discussions.

550 The Standard Model consists of two primary categories of fundamental particles: fermions (spin 1/2  
 551 particles) and bosons (integer spin particles). The SM also describes three forces: electromagnetism, the  
 552 weak nuclear force, and the strong nuclear force. Gravity is not included in the theory and is largely irrele-  
 553 vant at the scales currently probed by collider experiments. Within the fermions, there are both quarks  
 554 (which interact via all three forces) and the leptons. The charged leptons interact via electromagnetic and  
 555 weak interactions, while neutrinos (neutral leptons) interact only via the weak force. Within the bosons,  
 556 there are the  $W^\pm$  and  $Z$  bosons (the mediators of the weak force), the gluon ( $g$ , the mediator of the  
 557 strong force), and the photon ( $\gamma$ ), the mediator of the electromagnetic force. Finally, there is the Higgs  
 558 boson, a fundamental spin-0 particle resulting from the Higgs mechanism of electroweak symmetry  
 559 breaking. Figure 1.1 summarizes the fermions and bosons of the SM.

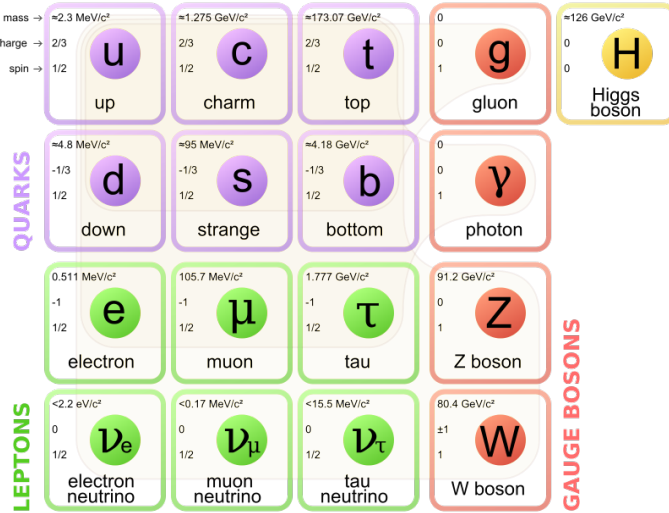


Figure 1.1: The particles of the Standard Model and their properties[1].

560 The Standard Model coalesced into a unified theoretical framework in the 1960s through the work of  
 561 Glashow, Weinberg, Salam, and others on the theory of electroweak interactions[39–42]. This theory  
 562 characterized both the electromagnetic and weak interactions as unified under a single gauge symme-  
 563 try group, namely  $SU(2) \times U(1)$ . At low enough energy scales (on the order of the  $W$  and  $Z$  masses,  
 564 the electroweak symmetry is broken, as evidenced by the fact that the weak bosons have mass while the

565 photon does not. The discovery of the Higgs boson in 2012 confirmed the Higgs mechanism as the most  
 566 likely candidate for this electroweak symmetry breaking[22, 34]. The electroweak theory is then com-  
 567 bined with the theory of quantum chromodynamics (which models the strong sector as a non-Abelian  
 568  $SU(3)$  gauge group) to form the complete SM[43].

## 569 1.2 ELECTROWEAK SYMMETRY BREAKING AND THE HIGGS

570 In the Standard Model Lagrangian, it is difficult to include mass terms for the  $W$  and  $Z$  bosons without  
 571 breaking the fundamental gauge symmetry of the Lagrangian. A traditional mass term does not preserve  
 572 the  $SU(2) \times U(1)$  symmetry. Additionally, scattering of massive  $W$  and  $Z$  bosons violate unitarity  
 573 and these diagrams diverge at high energy scales. In the 1960s, Higgs, Brout, Englert, Guralnik, Kibble,  
 574 and Hagen developed a mechanism for spontaneous symmetry breaking via the addition of a complex  
 575 scalar doublet to the SM. Three of the four real degrees of freedom of this complex field would go to the  
 576 longitudinal modes of the  $W^\pm$  and  $Z$ , thus allowing them to have mass[44–47]. The remaining degree  
 577 of freedom would manifest as an additional scalar, known now as the Higgs boson.

578 The mechanism works by introducing a Lagrangian for the newly introduced field that still respects  
 579 the symmetry of the Standard Model inherently, but with a minimum at a non-zero vacuum expecta-  
 580 tion value for the field. In this minimum of the potential, the electroweak symmetry is broken. Specifi-  
 581 cally, consider a complex scalar doublet  $\Phi$  with four degrees of freedom, as shown in equation 1.1.

$$\Phi = \begin{pmatrix} \phi^+ \\ \phi^0 \end{pmatrix} = \frac{1}{\sqrt{2}} \begin{pmatrix} \phi_1^+ + i\phi_2^+ \\ \phi_1^0 + i\phi_2^0 \end{pmatrix} \quad (1.1)$$

582 The minimal potential of a self-interacting Higgs that still respects the SM symmetry is given in equa-  
 583 tion 1.2.

$$V(\Phi) = \mu^2 \Phi^\dagger \Phi + \lambda (\Phi^\dagger \Phi)^2 \quad (1.2)$$

584 If the  $\mu^2$  term of this potential is positive, then the potential has a minimum at  $\Phi = 0$  and the SM

<sup>585</sup> symmetry is preserved. However, if instead  $\mu^2 < 0$ , then the minimum is at a finite value of  $\Phi$ , namely

$$\Phi_{\min} = \frac{1}{\sqrt{2}} \begin{pmatrix} 0 \\ v \end{pmatrix} \quad (1.3)$$

<sup>586</sup> where  $v = \sqrt{\mu^2/\lambda}$ . Because this is the location of the minimum, it corresponds to the vacuum expecta-  
<sup>587</sup> tion value for the field ( $\langle \Phi \rangle = \Phi_{\min}$ ). The excitations of the Higgs can then be parameterized as

$$\Phi = \frac{1}{\sqrt{2}} \begin{pmatrix} 0 \\ v + H \end{pmatrix} \quad (1.4)$$

<sup>588</sup> The full scalar Lagrangian, including the kinetic term, is then given as

$$\mathcal{L}_s = (D^\mu \Phi)^\dagger (D_\mu \Phi) - V(\Phi) \quad (1.5)$$

<sup>589</sup> where the covariant derivative is defined as

$$D_\mu = \partial_\mu + \frac{ig}{2} \tau^a W_\mu^a + ig' Y B_\mu \quad (1.6)$$

<sup>590</sup> and  $W^1, W^2, W^3$  and  $B$  are the  $SU(2)$  and  $U(1)$  gauge fields of the electroweak theory, respectively.  $g$   
<sup>591</sup> and  $g'$  are the corresponding coupling constants. With the scalar Lagrangian in place, the physical gauge  
<sup>592</sup> fields can then be written as

$$W_\mu^\pm = \frac{1}{\sqrt{2}} (W_\mu^1 \mp i W_\mu^2) \quad (1.7)$$

<sup>593</sup>

$$Z_\mu = \frac{-g' B_\mu + g W_\mu^3}{\sqrt{g^2 + g'^2}} \quad (1.8)$$

<sup>594</sup>

$$A_\mu = \frac{g B_\mu + g' W_\mu^3}{\sqrt{g^2 + g'^2}} \quad (1.9)$$

<sup>595</sup> Equation 1.7 corresponds to the charged  $W^+$  and  $W^-$  bosons, equation 1.8 corresponds to the neutral

596  $Z$  boson, and equation 1.9 corresponds to the neutral photon. The masses of the particles also arise from  
 597 the Lagrangian. The photon has zero mass, while the masses of the  $W$  and  $Z$  bosons are given in equa-  
 598 tion 1.10.

$$\begin{aligned} M_W^2 &= \frac{1}{4}g^2v^2 \\ M_Z^2 &= \frac{1}{4}(g^2 + g'^2)v^2 \end{aligned} \quad (1.10)$$

599 The fermion masses also arise through a coupling with the Higgs via the Yukawa interaction (for a de-  
 600 tailed description, see [38]). In this case the coupling between the Higgs and the fermions goes as

$$g_{Hf\bar{f}} = \frac{m_f}{v} \quad (1.11)$$

601 The full Lagrangian of Higgs interactions can be written as

$$\mathcal{L}_{\text{Higgs}} = -g_{Hf\bar{f}}\bar{f}fH + \frac{g_{HHH}}{6}H^3 + \frac{g_{HHHH}}{24}H^4 + \delta_V V_\mu V^\mu \left( g_{HVV}H + \frac{g_{HHVV}}{2}H^2 \right) \quad (1.12)$$

602 with

$$\begin{aligned} g_{HVV} &= \frac{2m_V^2}{v} & g_{HHVV} &= \frac{2m_V^2}{v^2} \\ g_{HHH} &= \frac{3m_H^2}{v} & g_{HHHH} &= \frac{3m_H^2}{v^2} \end{aligned} \quad (1.13)$$

603 Here,  $V$  refers to the  $W^\pm$  and  $Z$ , and  $\delta_W = 1$  while  $\delta_Z = 1/2$ . Phenomenologically, there are a few  
 604 features of this Lagrangian that are useful to note. First, note that the Higgs mass is a free parameter  
 605 of the theory that must be determined experimentally. Second, note that the coupling of the Higgs to  
 606 the vector bosons and fermions scales with the masses of these particles, a fact that is important when  
 607 considering both the production and decays of the particle. Also note that the branching ratio of the  
 608 Higgs to  $W$  bosons will be twice that of the branching ratio to  $Z$  if the Higgs mass is large enough to  
 609 produce the particles on shell because of the extra symmetry factor associated with the  $W$  coupling.  
 610 Finally, note the presence of the cubic and quartic Higgs self interaction terms, which can lead to final  
 611 states with multiple Higgs bosons produced.

612 1.3 HIGGS BOSON PRODUCTION AND DECAY

613 This section discusses the properties of Higgs production and decay mechanisms. The details presented  
614 here will focus on the properties of a 125 GeV Higgs boson, as this is the mass closest to that of the  
615 newly discovered Higgs.

616 1.3.1 HIGGS PRODUCTION

617 The Higgs is produced by four main production modes at the Large Hadron Collider - gluon-gluon  
618 fusion (ggF), vector boson fusion (VBF), associated production with a  $W$  or  $Z$  boson, or associated  
619 production with top quarks ( $t\bar{t}H$ ). Figure 1.2 shows the Feynman diagrams for these four modes.

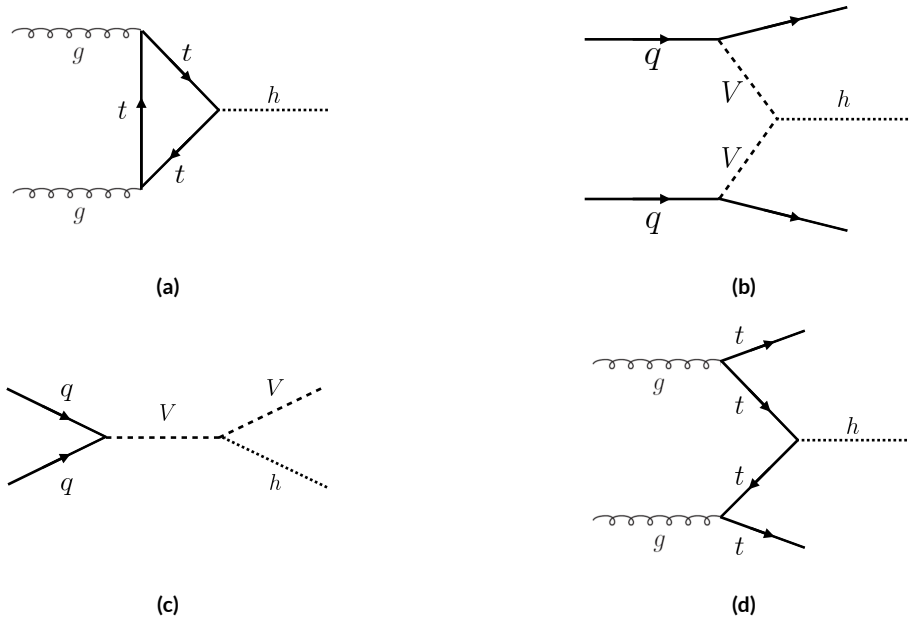
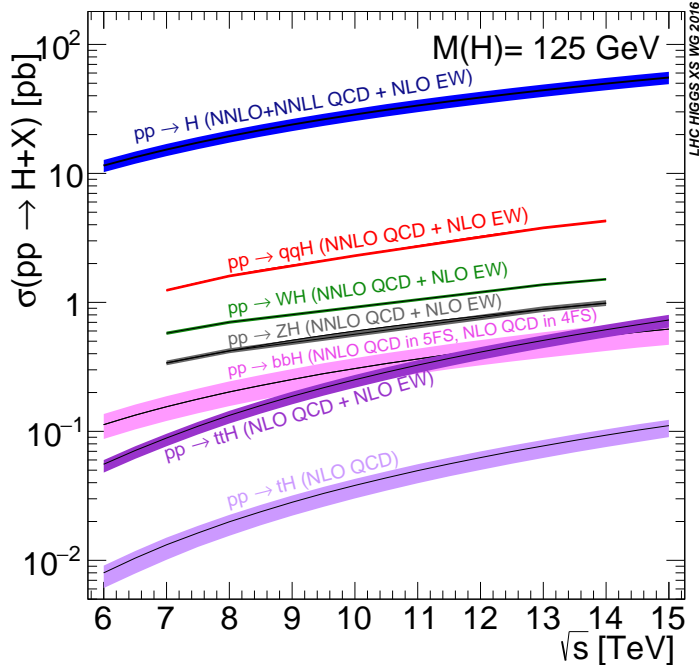


Figure 1.2: The four most common Higgs boson production modes at the LHC: (a) gluon-gluon fusion, (b) vector boson fusion, (c)  $W/Z + H$  production, (d)  $t\bar{t}H$  production

620 In gluon-gluon fusion, gluons from the incoming protons fuse via a top-quark loop to produce a  
621 Higgs. The top quark is the dominant contribution in the loop due to its heavy mass and the fact that  
622 the Higgs-fermion coupling constant scales with fermion mass. In vector boson fusion, the incoming  
623 quarks each radiate a  $W$  or  $Z$  boson which fuse to produce the Higgs. This production mode results in  
624 a final state with a Higgs boson and two additional jets which tend to be forward because they carry the

625 longitudinal momentum of the incoming partons. The Higgs can also be produced in association with a  
 626  $W$  or  $Z$  boson. The  $W/Z$  is produced normally and then radiates a Higgs (this mode is also sometimes  
 627 known as “Higgs-strahlung”). Finally, the Higgs can be produced in association with two top quarks.  
 628 Each incoming gluon splits into a  $t\bar{t}$  pair, and one of the top pairs combines to create a Higgs.

629 Figure 1.3 shows the production cross section for a 125 GeV Higgs boson in each of these modes at a  
 630  $pp$  collider as a function of center of mass energy.



**Figure 1.3:** Higgs production cross sections as a function of center of mass energy ( $\sqrt{s}$ ) at a  $pp$  collider[2].

631 In figure 1.3, note that gluon fusion has the largest cross section, while VBF is the second largest at  
 632 approximately a factor of 10 smaller. The figure also includes the less commonly studied  $b\bar{b}H$  and  $tH$   
 633 modes. The  $b\bar{b}H$  and  $tH$  modes are not studied as commonly as  $t\bar{t}H$  due to the larger background con-  
 634 tributions and lower cross sections, respectively. At  $\sqrt{s} = 8$  TeV, ggF production of a 125 GeV Higgs  
 635 has a cross section of 19.47 pb, while VBF has a cross section of 1.601 pb[2]. The cross sections of all  
 636 of the main Higgs production modes at this center of mass energy, as well as their uncertainties from  
 637 varying the renormalization and factorization scales and PDFs, are summarized in table 1.1 for a 125 GeV  
 638 Higgs.

Production mode	$\sigma$ ( pb)	QCD scale uncert. (%)	PDF + $\alpha_s$ uncert. (%)
Gluon fusion	19.47	+7.3 / - 8.0	3.1
Vector boson fusion	1.601	+0.3 / - 0.2	2.2
$WH$	0.7026	+0.6 / - 0.9	2.0
$ZH$	0.4208	+2.9 / - 2.4	1.7
$t\bar{t}H$	0.1330	+4.1 / - 9.2	4.3
$b\bar{b}H$	0.2021	+20.7 / - 22.3	
$tH$ ( $t$ -channel)	0.01869	+7.3 / - 16.5	4.6
$tH$ ( $s$ -channel)	$1.214 \times 10^{-3}$	+2.8 / - 2.4	2.8

**Table 1.1:** Production cross sections for a 125 GeV Higgs boson at  $\sqrt{s} = 8$  TeV with scale and PDF uncertainties [2].

### 639 1.3.2 HIGGS BRANCHING RATIOS

640 The fact that the Higgs couples more strongly to more massive particles is crucial for understanding its  
 641 branching ratios. The width for Higgs decays to fermions is given in equation 1.14 [29].

$$\Gamma(H \rightarrow f\bar{f}) = \frac{N_c \sqrt{2} G_F m_f^2 m_H}{8\pi} \quad (1.14)$$

642 In this case,  $N_c$  is the number of colors,  $G_F$  is the Fermi constant,  $m_f$  is the mass of the fermion, and  
 643  $m_H$  is the mass of the Higgs. Note that the width scales with the square of the fermion mass. (This also  
 644 assumes that the Higgs mass is large enough to decay with both the fermions on shell.)

645 The decay width to  $WW$  is given in equation 1.15 [29].

$$\Gamma(H \rightarrow W^+W^-) = \frac{\sqrt{2} G_F M_W^2 m_H}{16\pi} \frac{\sqrt{1-x_W}}{x_W} (3x_W^2 - 4x_W + 4) \quad (1.15)$$

646 where  $m_W$  is the mass of the  $W$  and  $x_W = 4M_W^2/m_H^2$ . To get the branching ratio to  $ZZ$ , the  
 647 equation is divided by 2 to account for identical particles in the final state, and  $x_W$  is replaced with  
 648  $x_Z = 4M_Z^2/m_H^2$ . This is shown in equation 1.16 [29].

$$\Gamma(H \rightarrow ZZ) = \frac{\sqrt{2} G_F M_Z^2 m_H}{32\pi} \frac{\sqrt{1-x_Z}}{x_Z} (3x_Z^2 - 4x_Z + 4) \quad (1.16)$$

649 These formulas can also be visualized as a function of Higgs mass. Figure 1.4 shows the branching

650 ratios as a function of the Higgs mass.

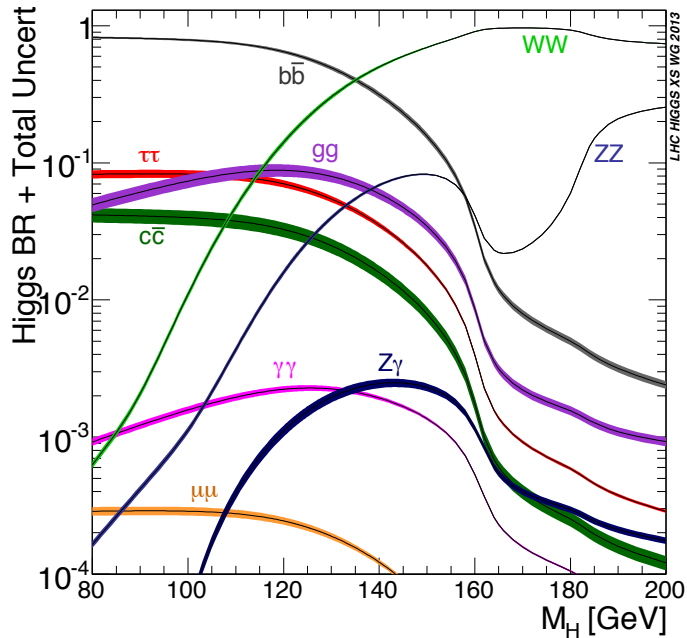


Figure 1.4: Higgs boson branching ratios as a function of  $m_H$  [2].

651 There are a few interesting features to note in this figure. First, note that at high Higgs masses, once  
 652 on-shell production of both  $W$  and  $Z$  bosons is possible, these two decays are the dominant ones due to  
 653 the large masses of the  $W/Z$ . Also note that the branching ratio to  $W$ s is twice that of  $Z$ s at these large  
 654 masses due to the  $\delta_V$  symmetry factor noted previously. At 125 GeV, the Higgs is accessible through  
 655 many different decay modes. The largest branching ratio is the decay  $H \rightarrow b\bar{b}$  at 58.24% [2]. This  
 656 branching is larger than the  $WW/ZZ$  decays because one of the two bosons must be produced off-  
 657 shell for  $m_H = 125$  GeV. The second largest branching ratio is to  $WW^*$  at 21.37 % (before taking  
 658 into account the branching ratios of the  $W$ ). Table 1.2 summarizes the branching ratios for a 125 GeV  
 659 Higgs. Note that there is in fact a Higgs branching ratio to  $\gamma\gamma$  even though photons are massless. This  
 660 decay happens through a loop (the largest contributions to the loop are top and  $W$ ) which suppresses  
 661 the branching ratio.

662 Note that the branching ratios alone do not tell the full story of which Higgs channels are the most  
 663 sensitive. For example, a  $H \rightarrow b\bar{b}$  search in gluon fusion production is incredibly difficult due to the

Decay	Branching ratio (%)
$b\bar{b}$	58.24
$WW^*$	21.37
$gg$	8.187
$\tau\tau$	6.272
$c\bar{c}$	2.891
$ZZ^*$	2.619
$\gamma\gamma$	0.2270
$Z\gamma$	0.1533
$\mu\mu$	0.02176

**Table 1.2:** Branching ratios for a 125 GeV Higgs boson[2].

large QCD dijet background at the LHC. However, in associated production of the Higgs, where a  $W$  or  $Z$  gives additional final state particles that can be used to reduce background, a search for  $H \rightarrow b\bar{b}$  can be sensitive. The combinations of production and decay modes that are most commonly studied are summarized in table 1.3 [29].

Decay	Inclusive (incl. ggF)	VBF	$WH/ZH$	$t\bar{t}H$
$H \rightarrow \gamma\gamma$	✓	✓	✓	✓
$H \rightarrow b\bar{b}$			✓	✓
$H \rightarrow \tau^+\tau^-$		✓		
$H \rightarrow WW^* \rightarrow \ell\nu\ell\nu$	✓	✓	✓	
$H \rightarrow ZZ \rightarrow 4\ell$	✓			
$H \rightarrow Z\gamma \rightarrow \ell\ell\gamma$	very low			

**Table 1.3:** Possible channels for Higgs searches. Checkmarks denote the most sensitive production modes [29].

#### 1.4 HIGGS PAIR PRODUCTION IN THE STANDARD MODEL

The Standard Model also allows for processes that produce two Higgs bosons in the final state, known as Higgs pair production or di-Higgs production. The two main production mechanisms are shown in figure 1.5.

The two diagrams in figure 1.5 interfere destructively with one another, resulting in a low overall cross section for di-Higgs production at the LHC. Nevertheless, Higgs pair production is quite interesting to study because it gives direct access to the  $\lambda$  parameter of the Higgs potential, also known as the Higgs self

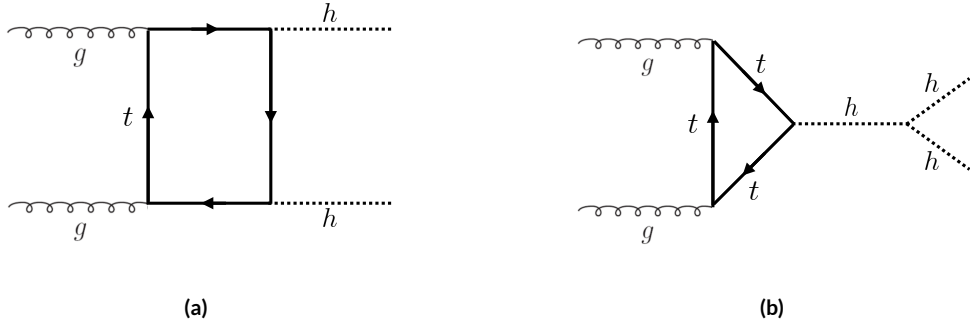


**Figure 1.5:** The two leading diagrams for Standard Model di-Higgs production at the LHC: (a) box diagram, (b) Higgs self coupling

coupling. The diagram in figure 1.5(b) is sensitive to this coupling through the triple Higgs vertex.

One can substitute the gluon fusion production of diagram 1.5(b) with any of the other production modes previously discussed. These other modes do not suffer from interference with the box diagram in figure 1.5(a) due to the presence of additional particles in the final state. They still have a lower cross section than the gluon fusion mode, however. The cross sections for di-Higgs production in the different modes, as well as their uncertainties, are shown in table 1.4 [30]. These are shown for  $\sqrt{s} = 14$  TeV as the higher center of mass energy is more sensitive to this process. Note that the scale of cross section quoted is now in fb rather than pb.

Production mode	$\sigma$ (fb)	Total uncert. (%)
Gluon fusion	33.89	+37.2 / - 27.8
Vector boson fusion	2.01	+7.6 / - 5.1
$W H H$	0.57	+3.7 / - 3.3
$Z H H$	0.42	+7.0 / - 5.5
$t\bar{t}H$	1.02	-

**Table 1.4:** Production cross sections for pair production of a 125 GeV Higgs boson at  $\sqrt{s} = 14$  TeV with total uncertainty [30]. The uncertainties include QCD scale and PDF variations as well as uncertainties on  $\alpha_S$ .

682

## 1.5 HIGGS PAIR PRODUCTION IN THEORIES BEYOND THE STANDARD MODEL

The Standard Model Higgs pair production cross section is rather small, and datasets on the scale of the full lifetime of the LHC will be required to obtain sensitive measurements of the Higgs self-coupling.

686 However, the discovery of the Higgs also gives particle physicists a new tool that can be exploited in the  
 687 search for new physics beyond the Standard Model. In particular, Higgs pair production is a promising  
 688 channel in the search for new physics. The cross section for di-Higgs production can be altered through  
 689 both resonant and non-resonant production of Higgs pairs. In non-resonant production, di-Higgs pro-  
 690 duction vertices can arise from the presence of a new strong sector and additional colored particles[48–  
 691 50]. Figure 1.6 shows examples of the types of vertices that can arise. In the resonant case, new heavy  
 692 particle can decay to Higgs pairs. Such new particles can include heavy Higgs bosons arising in two  
 693 Higgs doublet models (2HDM) or Higgs portal models as well as heavy gravitons in Randall-Sundrum  
 694 theories[3, 5, 48, 51–55]. Figure 1.7 shows a generic diagram for a heavy resonance decaying to two Higgs  
 695 bosons. In the 2HDM,  $X$  corresponds to the heavy CP-even scalar  $H$ . In the Randall-Sundrum model,  
 696  $X$  corresponds to a heavy spin-2 graviton  $G$ .

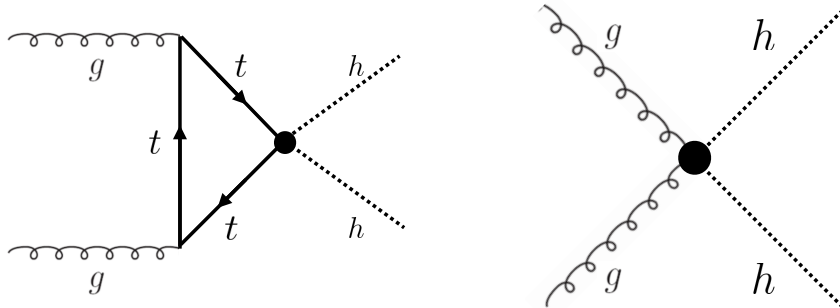


**Figure 1.6:** Diagrams with new vertices for non-resonant Higgs pair production arising in composite Higgs models

697 The next sections provide more detail on the phenomenology of resonant Higgs production in  
 698 Randall-Sundrum and 2HDM models, as these models will later be tested in a dedicated search for reso-  
 699 nant production of boosted Higgs pairs.

### 700 1.5.1 RANDALL-SUNDRUM GRAVITONS

701 The Randall-Sundrum model is a proposed solution to the hierarchy problem that posits a five-dimensional  
 702 warped spacetime that contains two branes: one where the force of gravity is very strong and a second  
 703 brane at the TeV scale corresponding to the known Standard Model sector [51]. In the theory, the  
 704 branes are weakly coupled and the graviton probability function drops exponentially going from the

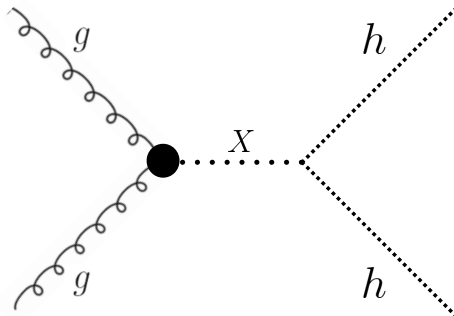


**Figure 1.7:** Generic Feynman diagram for resonant Higgs pair production in BSM theories

705 gravity brane to the SM brane, rendering gravity weak on the SM brane. The experimental consequence  
 706 of this theory is a tower of widely spaced (in mass) Kaluza-Klein graviton resonances. In theories where  
 707 the fermions are localized to the SM brane, production of gravitons from fermion pairs is suppressed  
 708 and the primary mode of production is gluon fusion[3]. These gravitons have a substantial branching  
 709 fraction to Higgs pairs, ranging from 6.43% for gravitons with a mass of 500 GeV to 7.66% at 3 TeV.  
 710 Figure 1.8 shows the branching ratios of the spin-2 Randall Sundrum graviton (RSG) as a function of its  
 711 mass. The predominant decays are to  $t\bar{t}$  above the mass threshold for that channel.

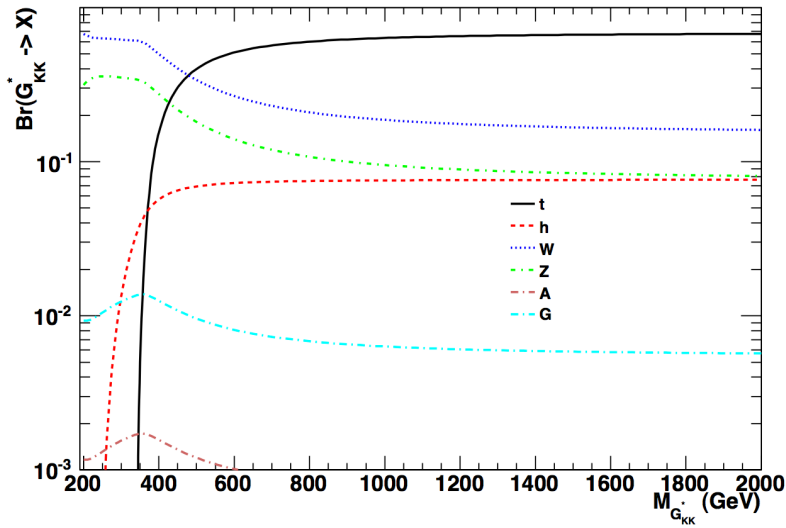


**Figure 1.8:** Branching ratios for a spin-2 Randall-Sundrum graviton as a function of mass computed in MadGraph with the CP3-Origins implementation [3, 4]

712 These models have two free parameters - the mass of the graviton and a curvature parameter  $k$ . Typ-

713 ically, rather than  $k$ , the theory is parameterized using  $c \equiv k/\bar{M}_{\text{pl}}$ , where  $\bar{M}_{\text{pl}}$  is the reduced Planck  
 714 mass. The cross section for production of the RSG decreases as a function of mass and is strongly depen-  
 715 dent on the gluon PDF. The increase in center of mass energy from 8 to 13 TeV in LHC Run 2 greatly  
 716 increases the cross section at higher mass. Figure 1.9 shows the cross section as a function of graviton  
 717 mass at  $\sqrt{s} = 13$  TeV for RSG models with  $c = 1.0$  and  $c = 2.0$ .

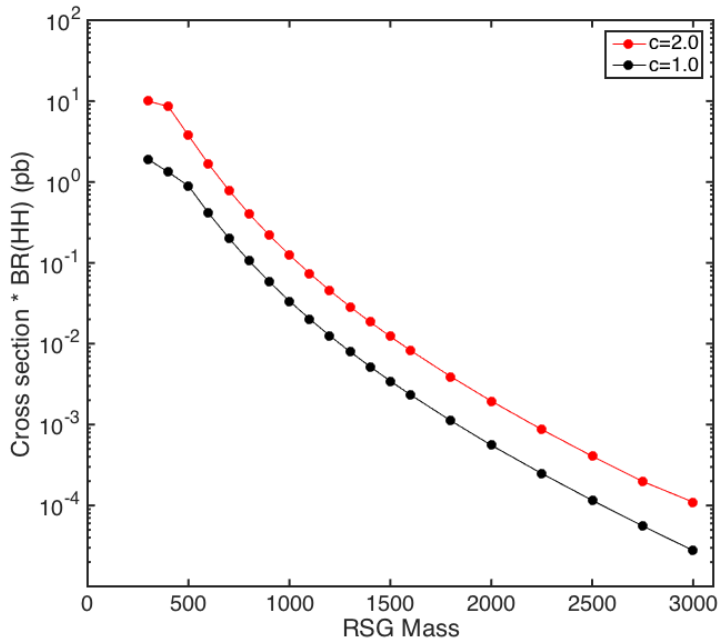


**Figure 1.9:**  $\sigma \times \text{BR}(HH)$  for RSG as a function of mass computed in MadGraph with the CP3-Origins implementation [3, 4]

718 Another interesting feature of the theory is that the width of the graviton increases with both  $c$  and  
 719  $m_G$ . Figure 1.10 shows the graviton width for both  $c = 1.0$  and  $c = 2.0$  as a function of mass. In  
 720  $c = 1.0$ , the width starts at 8.365 GeV for a mass of 300 GeV and increases to 187.2 GeV at a mass of  
 721 3 TeV. Similarly, with  $c = 2.0$ , the width starts at 33.46 GeV for  $m_G = 300$  GeV and increases to  
 722 748.8 GeV at a mass of 3 TeV.

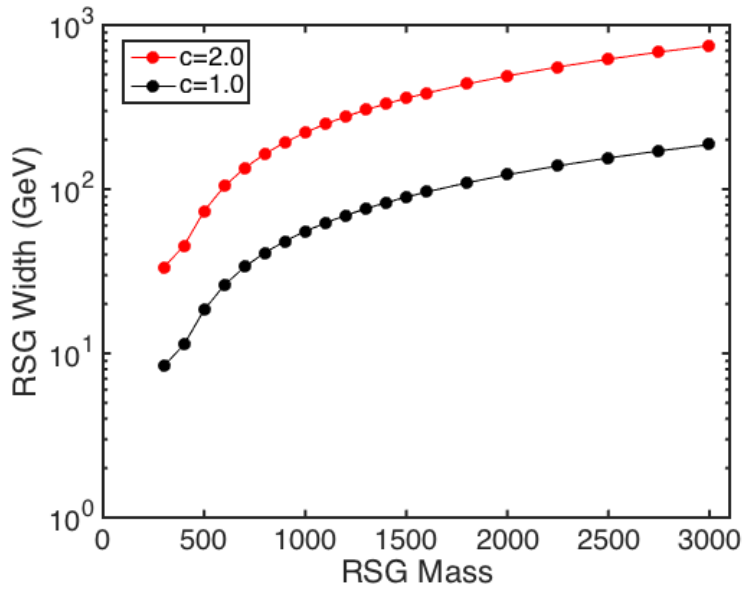


Figure 1.10: RSG width as a function of mass computed in MadGraph with the CP3-Origins implementation [3, 4]

### 723 1.5.2 TWO HIGGS DOUBLET MODELS

724 In Two Higgs Doublet Models (2HDM), a second complex scalar doublet is added to SM[5, 53, 54]. In  
 725 this case, all four degrees of freedom in the second doublet correspond to new particles, meaning that  
 726 there are five total scalars from the two Higgs doublets -  $h$  (light CP-even Higgs),  $H$  (heavy CP-even  
 727 Higgs),  $A$  (heavy CP-odd Higgs), and  $H^\pm$  (charged Higgs). The model is parameterized by two main  
 728 parameters. The first,  $\tan \beta \equiv \frac{v_2}{v_1}$ , is the ratio of the vacuum expectation values of the two Higgs dou-  
 729 blets (where  $v_1$  corresponds to the  $v$  in the SM Higgs model described above). The second parameter  
 730 is  $\alpha$ , a mixing angle between the heavy and light Higgs fields. Models are also often parameterized with  
 731  $\cos(\beta - \alpha)$  rather than  $\alpha$  directly. The limit where  $\cos(\beta - \alpha) = 0$  is called the alignment limit, and  
 732 it is in this limit that the light Higgs  $h$  has the same couplings as a Standard Model Higgs.

733 2HDM models are usually separated into two main types - Type I and Type II. In Type I models, the  
 734 charged fermions only couple to the second Higgs doublet, leading to a fermiophobic light Higgs. In  
 735 Type II models, up-type quarks couple to the first doublet while down-type quarks couple to the second  
 736 doublet. One specific realization of a Type II 2HDM is the Minimal Supersymmetric Standard Model  
 737 (MSSM).

738 Resonant di-Higgs production in this model can proceed through decays of the heavy CP-even Higgs  
 739  $H \rightarrow hh$ . The branching ratio for  $H \rightarrow hh$  depends on the model type as well as the values of  $\tan \beta$   
 740 and  $\cos(\beta - \alpha)$ . Figure 1.11 shows the branching ratios as a function of the mass of the heavy scalar  $H$  for  
 741 both Type I and Type II models. Depending on the type of model  $hh$  can be a substantial fraction of the  
 742 decays of  $H$ .

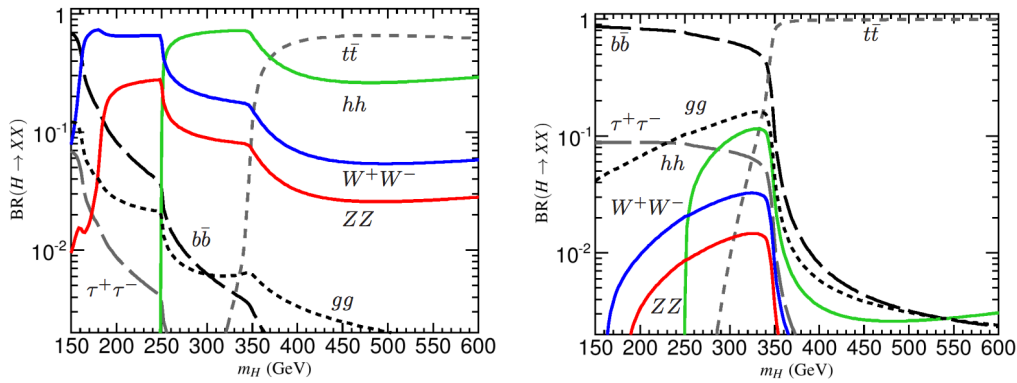


**Figure 1.11:** Branching ratios for heavy Higgs  $H$  in Type I (left) and Type II (right) 2HDM models with  $\tan \beta = 1.5$  and  $\cos(\beta - \alpha) = 0.1$  (Type I) ( $0.01$  for Type II). [5]

## 743 1.6 CONCLUSION

744 Studying the Higgs sector is essential for understanding the details of how mass arises in the Standard  
 745 Model and how the electroweak symmetry is broken. The discovery of the Higgs boson also opens the  
 746 door for its use as a tool to search for new physics, and Higgs pair production is an ideal candidate for  
 747 this study. Even if no BSM physics is found in Higgs pair production, searches for Higgs pairs will put  
 748 constraints on the Higgs self coupling and thus further knowledge of the Standard Model and the details  
 749 of the Higgs potential.

*This is some random quote to start off the chapter.*

Firstname lastname

# 2

750

751

752

## The ATLAS detector and the Large Hadron Collider

753 This chapter presents an overview of the experimental systems used to conduct the measurements pre-  
754 sented in this thesis. First, a brief overview of the accelerator, the Large Hadron Collider, will be given.  
755 In this section, the accelerator conditions relevant to data-taking are presented as well. Next, an overview  
756 of the ATLAS experiment is given. The basics of each sub-detector's role are summarized, as well as the  
757 details of the datasets accumulated. Then, a brief interlude on the ATLAS Muon New Small Wheel up-  
758 grade is presented. While this new detector does not have a direct impact on any of the datasets taken  
759 so far, it will have an impact on future analyses and the work done on it is briefly summarized here. Fi-  
760 nally, an overview of object reconstruction in ATLAS is given. While the details of all of the algorithms  
761 will not be presented in detail, aspects of the reconstruction performance such as object resolutions are  
762 shown as these are relevant to the two studies presented later in this thesis.

763 2.1 THE LARGE HADRON COLLIDER

764 The Large Hadron Collider (LHC) is a proton-proton collider at the CERN laboratory in Geneva,  
765 Switzerland[56]. It is designed for a maximum collision center of mass energy of  $\sqrt{s} = 14 \text{ TeV}$  and  
766 has a circumference of 26.7 kilometers. Four main experiments are located at the interaction points (IP)  
767 of the accelerator: ATLAS (A Toroidal LHC ApparatuS), CMS (the Compact Muon Solenoid), ALICE  
768 (A Large Ion Collider Experiment), and LHCb [7, 57–59]. The studies performed in this thesis were all  
769 completed with the ATLAS detector.

770 Figure 2.1 shows a schematic of the LHC ring and the various experiments.

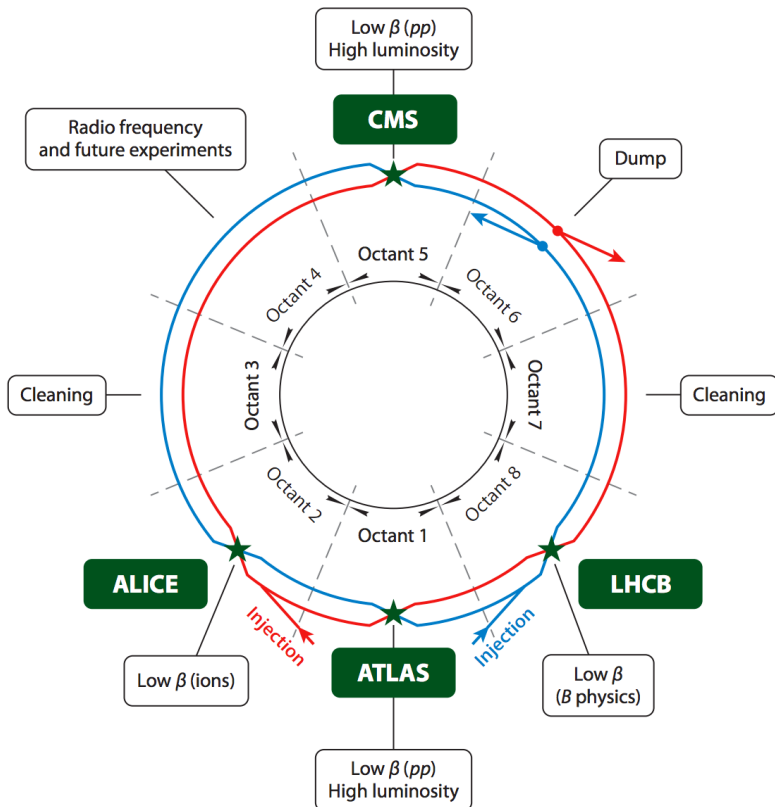


Figure 2.1: A schematic view of the LHC ring [6]

771 One of the most interesting features of the LHC is in its magnet design. Because the tunnel does not  
772 have room for separate superconducting magnets for each of the beam pipes, the LHC employs a twin-  
773 bore magnet design. Each magnet must hold an 8.3 Tesla magnetic field in order to bend the proton

774 beams at  $\sqrt{s} = 14$  TeV. The superconducting magnets are cooled to a temperature of 1.9 Kelvin with  
 775 superfluid helium.

776 **2.1.1 INSTANTANEOUS LUMINOSITY**

777 The rate of physics events expected from the accelerator is dependent on the instantaneous luminosity  
 778 of the machine and the cross section of the physics process,  $R_{\text{events}} = L\sigma$ . Here,  $R_{\text{events}}$  is the number  
 779 of events per second,  $L$  is the instantaneous luminosity of the machine, and  $\sigma$  is the cross section for the  
 780 physics process being measured. The instantaneous luminosity of the LHC is determined by numerous  
 781 factors related to machine conditions. Equation 2.1 gives the equation for instantaneous luminosity of  
 782 Gaussian beam profile [6].

$$L = \frac{N_b^2 n_b f_{\text{rev}} \gamma_r}{4\pi \epsilon_n \beta^*} F \quad (2.1)$$

783 The LHC collides protons in bunches, and in the above equation  $N_b$  is the number of protons per  
 784 bunch while  $n_b$  is the number of bunches per beam. Nominally, the LHC can hold up to 2808 pro-  
 785 ton bunches.  $f_{\text{rev}}$  is the revolution frequency.  $\epsilon_n$  is the normalized transverse beam emittance, a mea-  
 786 surement of the average spread of the particles position-momentum space which has the dimension of  
 787 length.  $\beta^*$  is the value of the *beta* function for the beam at the interaction point. It relates the emmi-  
 788 tance to the Gaussian width of the beam with  $\sigma_{\text{beam}} = \sqrt{\epsilon \cdot \beta}$ .  $F$  is a reduction factor that corrects for  
 789 the fact that the beams are colliding at an angle at the IP.

790 Another way of writing the instantaneous luminosity is shown in equation 2.2. In this case, the in-  
 791 stantaneous luminosity is written as the ratio of the rate of inelastic collisions with the inelastic cross  
 792 section[60].

$$L = \frac{R_{\text{inel}}}{\sigma_{\text{inel}}} = \frac{\mu n_b f_{\text{rev}}}{\sigma_{\text{inel}}} \quad (2.2)$$

793 In this case,  $\mu$  is the average number of interactions per bunch crossing in the accelerator.  $\mu$  is a useful  
 794 parameter for characterizing the amount of activity recorded in an experiment. As the instantaneous

795 luminosity and thus  $\mu$  increase, there are more interactions per bunch crossing and more activity in the  
 796 detector. This is often characterized with  $\langle \mu \rangle$ , the measured per bunch crossing  $\mu$  value averaged over  
 797 all bunch crossings. The interactions inside each bunch crossing that are not the main physics process of  
 798 interest are often referred to as “pileup” interactions, and  $\langle \mu \rangle$  is a measurement of the level of pileup in  
 799 the detector.

### 800 2.1.2 EVOLUTION OF MACHINE CONDITIONS

801 This thesis uses datasets taken at three different center of mass energies:  $\sqrt{s} = 7$  TeV data taken in the  
 802 year 2011,  $\sqrt{s} = 8$  TeV data taken in the year 2012, and  $\sqrt{s} = 13$  TeV dataa taken in the year 2015. In  
 803 addition to increasing center of mass energy, the instananeous luminosity and parameters that determine  
 804 it were evolving. Table 2.1 summarizes that machine conditions in each of these datasets.

	2011	2012	2015	Design
$\sqrt{s}$ [ TeV]	7	8	13	14
Number of bunches	1380	1380	1825	2808
Max. protons per bunch	$1.45 \times 10^{11}$	$1.7 \times 10^{11}$		$1.15 \times 10^{11}$
Bunch spacing [ns]	50	50	25	25
Max. instantaneous luminosity [ $\text{cm}^{-2}\text{s}^{-1}$ ]	$3.7 \times 10^{33}$	$7.7 \times 10^{33}$	$5 \times 10^{33}$	$10^{34}$
$\beta^*$ [m]	1.0	0.6	0.8	0.55
$\langle \mu \rangle$	11.6	20.7	13.7	-

Table 2.1: Evolution of LHC machine conditions [31, 32]

## 805 2.2 THE ATLAS DETECTOR

806 The ATLAS detector is a multi-purpose particle detector experiment at the LHC’s Point 1 [7]. It has  
 807 nearly  $4\pi$  coverage in solid angle around the interaction point. It consists of an inner detector for mea-  
 808 suring charged particles, electromagnetic and hadronic calorimeters, and a muon spectrometer. Fig-  
 809 ure 2.2 gives an overview of the detector.

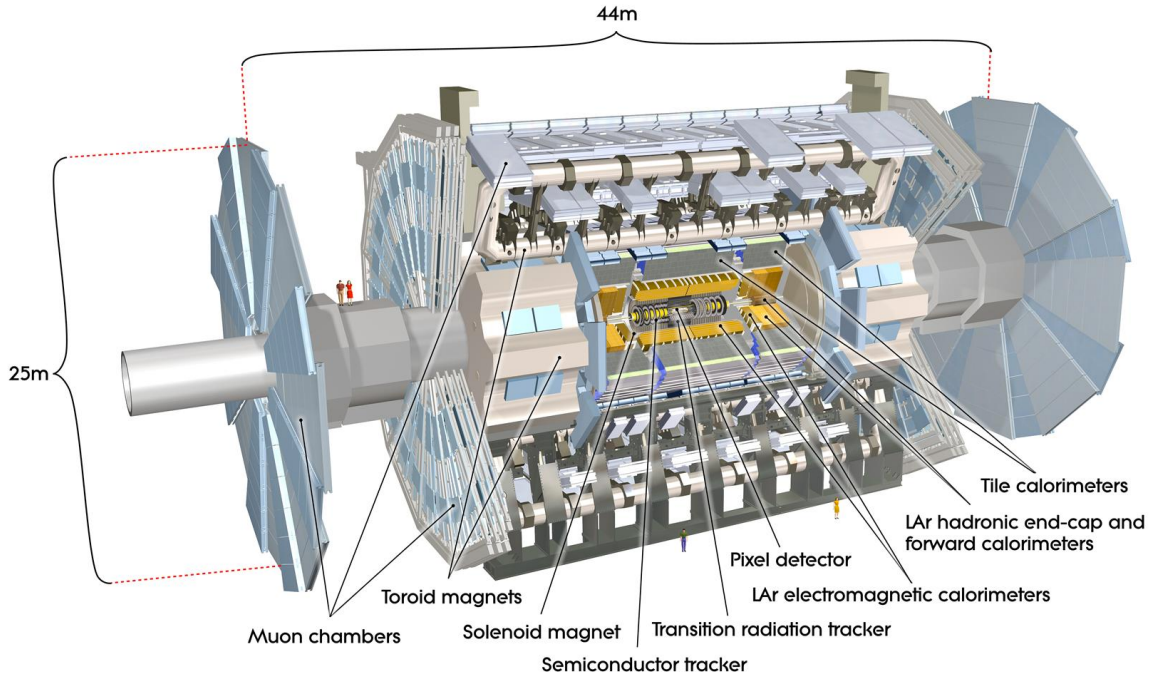


Figure 2.2: A full diagram of the ATLAS detector [7]

### 810 2.2.1 COORDINATE SYSTEM

811 Before defining the properties of the individual detectors, it is important to establish the coordinate  
 812 system used. Figure 2.3 shows a schematic of the coordinate system. The azimuthal plane (perpendicular  
 813 to the beam line) is defined as the  $x$ - $y$  plane. The angle in this plane is referred to as  $\phi$ . The angle relative  
 814 to the beam axis is referred to as  $\theta$ . Rather than using  $\theta$  directly as a coordinate, the experiment often  
 815 uses the pseudorapidity  $\eta$ .  $\eta$  is defined in equation 2.3.

$$\eta = \ln \left( \tan \left( \frac{\theta}{2} \right) \right) \quad (2.3)$$

816 Pseudorapidity is the massless approximation of rapidity, the angle used to parameterize boosts in  
 817 special relativity. This is important for two reasons. First, it means that differences in  $\eta$  are Lorentz in-  
 818 variant. Second, particle production is roughly constant in pseudorapidity. Particles with  $\eta$  close to zero  
 819 are referred to as “central”, while those at high  $|\eta|$  are called “forward”. In general, two main detector

820 topologies can be seen in figure 2.2. There are “barrel” elements, which surround the beam line cylind-  
 821 drically and are in the central region of the detector. In the forward region, there are “endcap” regions  
 822 which are arranged as disks perpendicular to the beam line.

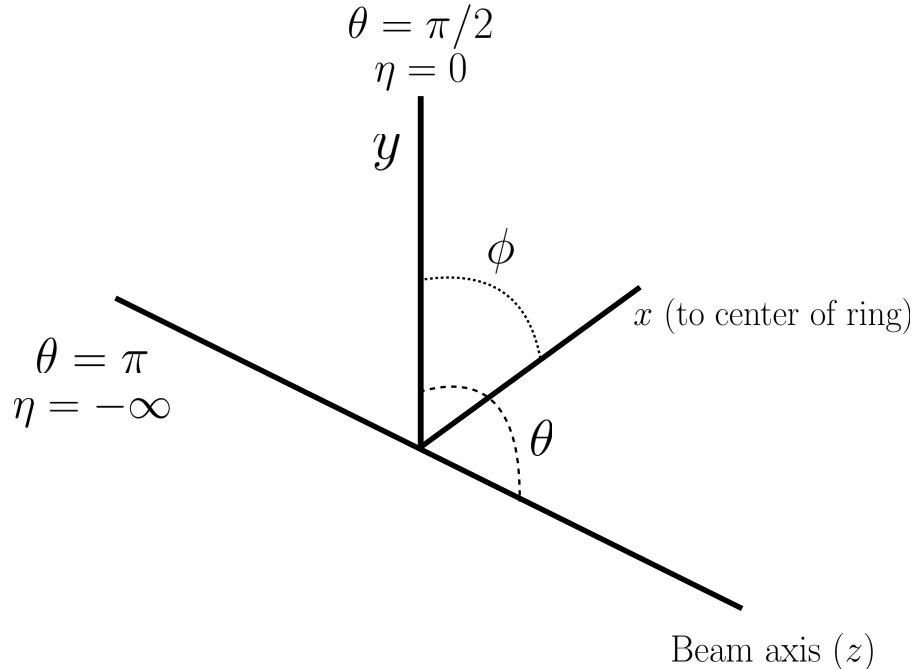


**Figure 2.3:** The ATLAS coordinate system

### 823 2.2.2 INNER DETECTOR

824 The ATLAS Inner Detector (ID) system is built for precision tracking of charged particles. It covers the  
 825 range  $|\eta| < 2.5$ . In this range, approximately 1000 particles are generated every bunch crossing in the  
 826 detector. This requires having fine granularity to achieve the resolutions required for good momentum  
 827 measurement and vertex reconstruction.

828 The ID consists of three sub-components: the pixel detector, semiconductor tracker (SCT), and trans-  
 829 sition radiation tracker (TRT). It is surrounded by a solenoid providing a 2 T axial magnetic field which  
 830 bends particles in the transverse plane to allow for momentum measurement. Figure 2.4 shows the layout  
 831 of each of these components.

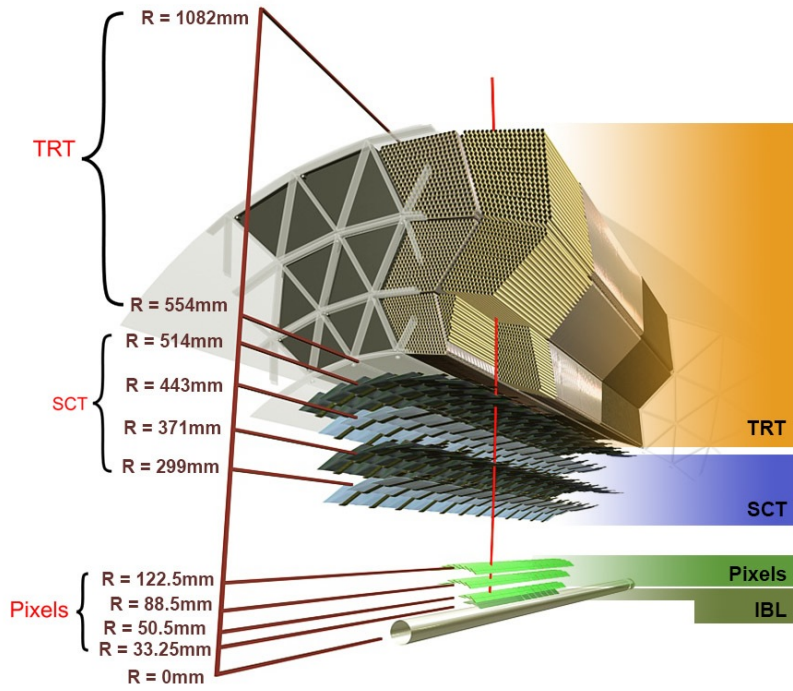


Figure 2.4: Layout of the ATLAS Inner Detector system [8]

### 832 PIXEL DETECTOR

833 The pixel detector is the first detector particles traverse after being generated in proton collisions and is  
 834 the most granular detector. Its operation is crucial for precision tracking and vertex reconstruction as  
 835 well as higher level object reconstruction like tagging of jets from  $b$ -quarks. The basic sensing element in  
 836 this subdetector is a silicon pixel detector. The operating principle for the silicon pixels is that of a  $p$ - $n$   
 837 junction. When a charged particle passes through, it creates electron-hole pairs that are then separated  
 838 by the electric field. The sensors are  $250 \mu\text{m}$  thick and use oxygenated  $n$ -type wafers with readout pixels  
 839 on the  $n^+$  side of the detector [7]. Overall, the pixel detector has 1744 sensors and 80.4 million readout  
 840 channels.

841 In the barrel region, the pixel detector has three concentric layers of sensors surrounding the beam-  
 842 line. In the endcap region, it consists of disks perpendicular to the beam axis. The detector is segmented  
 843 in the  $R$ - $\phi$  plane and in  $z$ . Usually, three pixel layers are crossed by a charged particle track. The intrinsic  
 844 accuracies of the sensors are  $10 \mu\text{m}$  in  $R$ - $\phi$  and  $115 \mu\text{m}$  in  $z$  (or  $R$  for the endcap).

845    **INSERTABLE B-LAYER**

846    In Run 2, a new innermost pixel layer, known as the insertable B-layer (IBL), was added to the Inner  
847    Detector [61]. This layer was added to cope with the higher luminosities planned in LHC Run 2 and  
848    at the high luminosity HL-LHC. Additionally it improves tracking position resolution which in turn  
849    improves the vertexing and  $b$ -tagging capabilities in ATLAS. The detector sits directly on a new beam  
850    pipe, only 33.25 mm away from the collision points in the azimuthal plane.

851    **SEMICONDUCTOR TRACKER (SCT)**

852    The semiconductor tracker (SCT) consists of silicon microstrips and comprises the next four layers of  
853    the ID. This sub-detector has 6.4cm long sensors that are daisy-chained into strips with a strip pitch of  
854     $80 \mu\text{m}$  [7]. Some of the strips have a small stereo angle to allow for measurement of both angular coor-  
855    dinates. In total there are 6.3 million readout channels. The intrinsic accuracies are  $17 \mu\text{m}$  in  $R\text{-}\phi$  and  
856     $580 \mu\text{m}$  in  $z$  (or  $R$  in the endcap).

857    **TRANSITION RADIATION TRACKER (TRT)**

858    The transition radiation tracker (TRT) serves two purposes. First, it consists of 4mm diameter straw  
859    tubes filled with a 70/27/3% gas mixture of xenon, carbon dioxide, and oxygen to provide tracking of  
860    charged particles. Particles typically have 36 TRT straw tube hits per track. The material in between  
861    the straws is designed to induce transition radiation which can be useful for particle identification. As  
862    particles pass between media with different dielectric constants, they emit transition radiation that can  
863    cause additional showers in the TRT. In particular it is useful for discrimination between electrons and  
864    pions or other charged hadrons, as the amount of transition radiation is proportional to the Lorentz  
865    factor of the particle.

866    **2.2.3 CALORIMETERS**

867    The calorimeter system consists of two main sub-components: a fine granularity electromagnetic calorime-  
868    ter tailored for the measurement of photons and electrons and multiple coarser hadronic calorimeters

869 dedicated to the measurement of hadronic showers [7]. The calorimeter system has broader coverage  
870 than the inner detector, covering the region out to  $|\eta| < 4.9$ . It is also designed to deliver good contain-  
871 ment of showers so as to limit leakage into the muon system. Figure 2.5 shows the layout of the calorime-  
872 ter system.

873 Both the electromagnetic and hadronic calorimeters are sampling calorimeters. They alternate active  
874 material for energy measurement with passive material for energy absorption. The materials used for  
875 each purpose vary based on the type of calorimeter and its location in the detector.

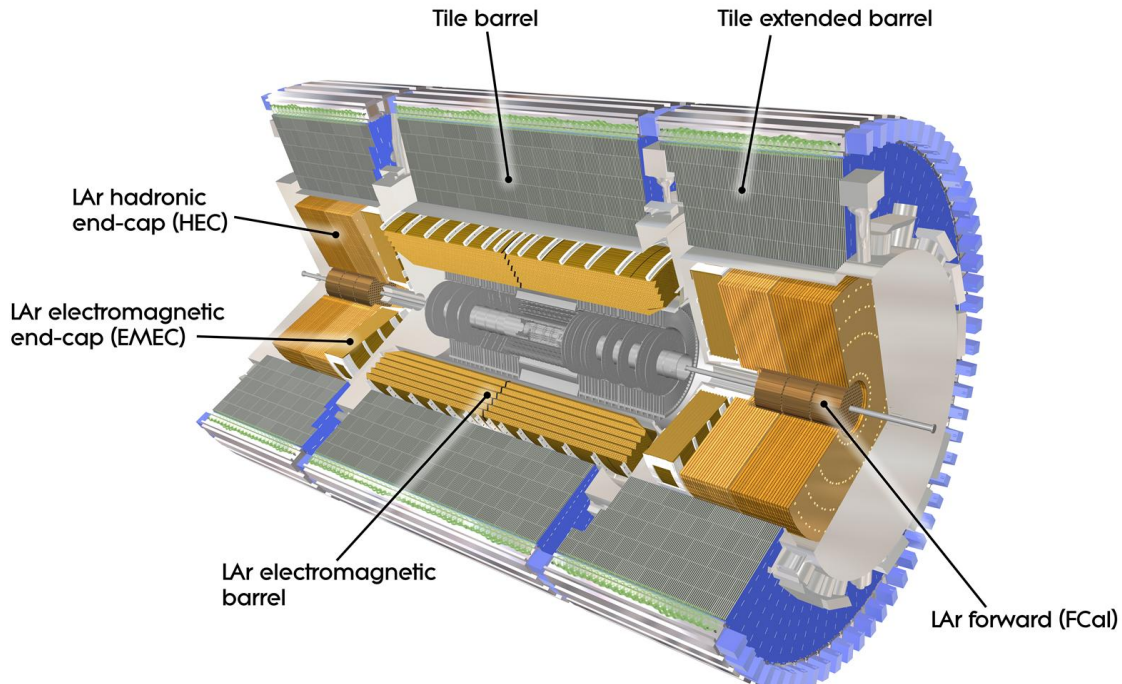


Figure 2.5: Layout of the ATLAS calorimeter system [7]

876 ELECTROMAGNETIC CALORIMETER

877 The electromagnetic calorimeter (EM calorimeter) use liquid Argon (LAr) as its active material and lead  
878 as its passive material. It is arrange in an accordion geometry to increase the absorption area while still  
879 allowing it to have no azimuthal cracks (complete symmetry in  $\phi$ ). The EM calorimeter is divided into a

880 barrel portion that extends to  $|\eta| < 1.475$  and an endcap portion going from  $1.375 < |\eta| < 3.2$ . The  
881 region where these two units overlap is called the “transition region”.

882 In order to provide good containment the calorimeter depth must be optimized. Typically, for elec-  
883 tromagnetic calorimeters the depth is measured in radiation lengths. In general, the intensity of a par-  
884 ticle beam attenuates exponentially in distance with a constant equal to the radiation length. That is,  
885  $I(x) = I_0 e^{-x/X_0}$ , where  $I$  is the intensity,  $x$  is the distance traveled, and  $X_0$  is the radiation length.  
886 The ATLAS EM calorimeter is designed to have  $> 22$  radiation lengths in the barrel and  $> 24$  in the  
887 endcap [7].

888 **HADRONIC CALORIMETERS**

889 There are three types of hadronic calorimeters present in ATLAS: the tile calorimeter (TileCal), hadronic  
890 endcap (HEC), and forward calorimeter (FCal). Each one is optimized for stopping of hadronic showers  
891 and the materials chosen are specific to their placement in the detector.

892 The TileCal is a scintillating tile calorimeter placed directly outside the EM calorimeter. It uses steel as  
893 the absorber and plastic scintillator tiles as the active material. It has coverage in the barrel at  $|\eta| < 1.0$   
894 and in the “extended barrel” region of  $0.8 < |\eta| < 1.7$ .

895 The HEC had two wheels perpendicular to the beam line per endcap and is located directly behind  
896 the EM calorimeter endcap modules. The HEC covers the region from  $1.5 < |\eta| < 3.2$ , overlapping  
897 slightly with both the tile calorimeter and the forward calorimeter. Like the EM calorimeter, it uses liq-  
898 uid Argon as the active material, but it uses copper as the absorber.

899 The FCal covers the most forward regions of the calorimeter system, extending to the region of  $3.1 <$   
900  $|\eta| < 4.9$ . It again uses liquid argon as its active material. For absorber, it consists of an innermost  
901 module made of copper followed by a module made of tungsten.

902 The hadronic equivalent of radiation length is called the interaction length and is denoted as  $\lambda$ . In the  
903 barrel, the hadronic calorimeter depth is approximately  $9.7\lambda$ , while in the endcap is is  $10\lambda$ . The outer  
904 supports contribute an additional  $1.3\lambda$ . This is been shown to be sufficient to limit punch-through of  
905 showers to the muon system [7].

906 2.2.4 MUON SPECTROMETER

907 The muon spectrometer is dedicated to measuring the momentum and position of muons. It consists  
908 of tracking and trigger chambers which are unique in the barrel and endcap regions. The magnetic field  
909 for bending of muons is provided by a system of three large air-core toroid magnets (from which ATLAS  
910 derives its name.) These magnets provide 1.5 to 5.5 Tm of bending power at  $0 < |\eta| < 1.4$  and approx-  
911 imately 1 to 7.5 Tm in the endcap region of  $1.6 < |\eta| < 2.7$ . The entire muon system covers the range  
912  $0 < |\eta| < 2.7$ . Monitored drift tubes (MDTs) are used for tracking in the barrel and the two outer  
913 layers of the endcap, while cathode strip chambers (CSCs) are used to provide tracking in the innermost  
914 endcap wheel. In the barrel, resistive plate chambers (RPCs) are used as trigger chambers while thin gap  
915 chambers (TGCs) are used in the endcap. Figure 2.6 shows the layout of the ATLAS muon system. The  
916 entire muon system is designed with the specification of providing a 10% momentum resolution for a  
917 1 TeV muon.

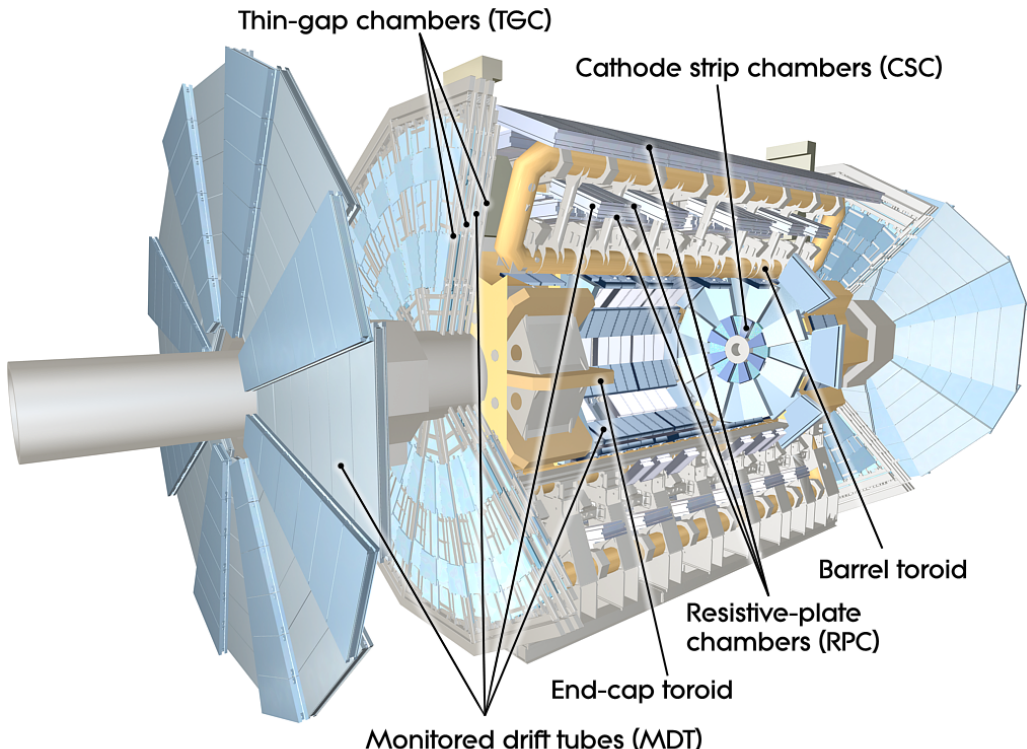


Figure 2.6: Layout of the ATLAS muon system [7]

918 MONITORED DRIFT TUBES (MDTs)

919 The monitored drift tubes (MDTs) are aluminum 3cm diameter tubes filled with a 93/7 % mixture of  
920 Argon and CO<sub>2</sub>, with trace amounts of water. As a charged particle traverses the tube, it ionizes the gas  
921 and the ions drift to a wire at the center of the tube. The radial distance of traversal of the particle in the  
922 tube is determined by the drift time of the electrons, allowing for fine position resolution. The tubes  
923 have an average resolution of 80  $\mu\text{m}$  per tube and a maximum drift time of approximately 700ns. The  
924 tubes are oriented so that they give precision measurement in  $\eta$  and run along  $\phi$ . They cover  $|\eta| < 2.7$ ,  
925 except in the innermost layer of the endcap where they only go to  $|\eta| < 2.0$  [7].

926 CATHODE STRIP CHAMBERS (CSCs)

927 The cathode strip chambers cover a narrow window of the innermost endcap region at  $2.0 < |\eta| <$   
928 2.7. In this region the background rates in the cavern are particularly high and the CSCs are designed  
929 to handle these higher rates. The CSCs are multiwire proportional chambers with wires pointing in  
930 the radial direction (away from the beam pipe). The wire serves as an anode and there are two types of  
931 segmented cathode strip, one perpendicular to the wires which gives the precision measurement and one  
932 parallel which provides the transverse coordinate. It has an 80/20 gas mixture of Argon and CO<sub>2</sub> [7].

933 RESISTIVE PLATE CHAMBERS (RPCs)

934 The resistive plate chambers (RPCs) are gaseous electrode-plate detectors covering the region  $|\eta| <$   
935 1.05. They consist of two resistive plates separated by a distance of 2 mm. The gas mixture used is a  
936 94.7/5/0.3% mixture of C<sub>2</sub>H<sub>2</sub>F<sub>4</sub>, Iso-C<sub>4</sub>H<sub>10</sub>, and SF<sub>6</sub>. It has readout strips with a pitch of 23-35 mm  
937 for both  $\eta$  and  $\phi$  measurement and thus provides measurement of the azimuthal coordinate in the barrel  
938 that the MDTs do not. The thin gas gap allows for a quick response time which makes it ideal for use in  
939 the trigger. There are three layers of RPCs which are referred to as the three trigger stations. They allwo  
940 for both a low  $p_T$  and high  $p_T$  trigger. The coincidence of hits in the innermost chambers allows for  
941 triggering of muons between 6 and 9 GeV, while the outermost layer allows the trigger to select high  
942 momentum tracks in the range of 9 to 35 GeV [7].

943 THIN GAP CHAMBERS (TGCs)

944 The thin gap chambers (TGCs) are multiwire proportional chambers where the wire to cathode dis-  
945 tance (1.4mm) is smaller than the wire-to-wire distance (1.8 mm). They contain a gas mixture of CO<sub>2</sub>  
946 and *n*-pentane and use a hih electric field to gain good time resolution. They serve two functions in the  
947 end-cap system. First, they serve as the trigger chambers. Second, they also provide azimuthal coordi-  
948 nate measurement which the MDTs do not. They sit on the inner and middle layers of the endcap. The  
949 outermost layer's azimuthal coordinate is determined by extrapolation [7].

950 2.2.5 MAGNET SYSTEM

951 As mentioned previously, there are two independent magnet systems in ATLAS. The first is a 2 T solenoid  
952 field in the inner detector which provides bending in the azimuthal plane. The second is an approxi-  
953 mately 0.5 T toroidal field in the muon system which provides bending in  $|\eta|$ . Figure 2.7 shows the pre-  
954 dicted field integral as a function of  $|\eta|$  [7].

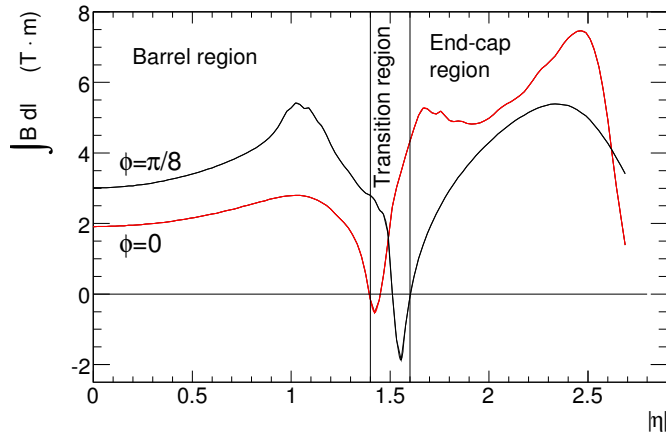


Figure 2.7: Predicted field integral as a function of  $|\eta|$  for the ATLAS magnet system [7]

955 2.2.6 TRIGGER SYSTEM

956 The ATLAS trigger system searches for signatures of muons, electrons, photons, hadronically decay-  
957 ing  $\tau$  leptons, and jets in order to save these events for further analysis. The trigger system in ATLAS

958 is designed to reduce the maximum LHC event rate of 40 MHz to a more reasonable rate that can be  
 959 recorded. The trigger first consists of a fast, hardware based system called the Level-1 (L1) trigger. The  
 960 L1 trigger consists of independent dedicated detector sub-components that can seed regions of in-  
 961 terest (RoIs) for further analysis downstream. For muons, the RPCs and TGCs are used, while in the  
 962 calorimeter coarsely grained sections of calorimeter cells called towers are used. Once regions of interest  
 963 are seeded, a software based system called the High Level Trigger (HLT) is used to reconstruct objects  
 964 and integrate information from different parts of the detector. In Run 1 of ATLAS, the HLT consisted  
 965 of two separate stages: the level 2 (L2) trigger and the event filter (EF).

966 The maximum trigger rate that the L1 trigger can handle is 75 kHz. In the HLT, the rate of events  
 967 written to disk is approximately 200 Hz. Figure 2.8 shows the trigger rates for different L1 triggers in  
 968 2012 and 2015 for ATLAS [9].

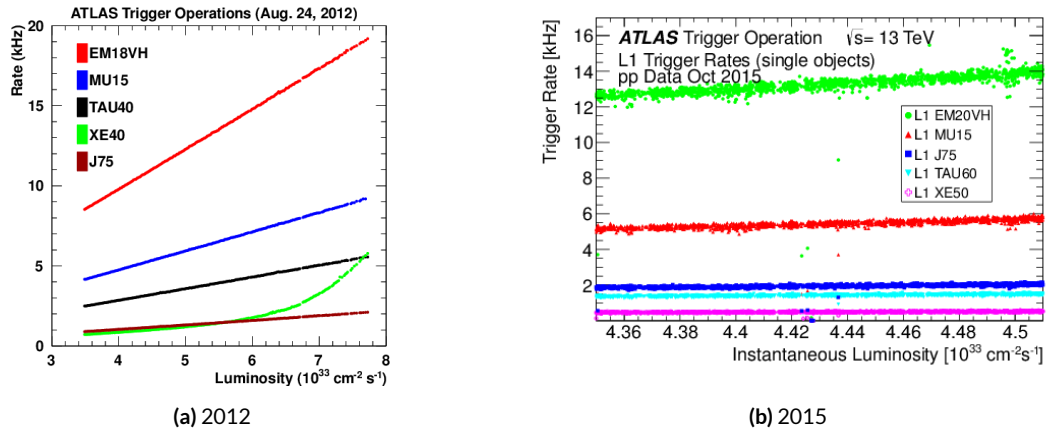


**Figure 2.8:** ATLAS trigger rates for Level-1 triggers as a function of instantaneous luminosity in 2012 and 2015 operation. These are single object triggers for electromagnetic clusters (EM), muons (MU), jets (J), missing energy (XE), and  $\tau$  leptons (TAU). The threshold of the trigger is given in the name in GeV. [9]

### 969 2.2.7 ATLAS DATASETS

970 ATLAS has collected data at center of mass energies of 7, 8, and 13 TeV. Figure 2.9 shows the integrated  
 971 luminosity as a function of time for each of the three collected datasets. At  $\sqrt{s} = 7$  TeV, ATLAS  
 972 recorded  $5.08 \text{ fb}^{-1}$ . Increased instantaneous luminosity in 2012 led to a larger dataset of  $21.3 \text{ fb}^{-1}$   
 973 recorded at  $\sqrt{s} = 8$  TeV. After Long Shutdown 1 (LS1) of the LHC and a restart in 2015, ATLAS

recorded  $3.9 \text{ fb}^{-1}$  of data at  $\sqrt{s} = 13 \text{ TeV}$ . [10, 11]

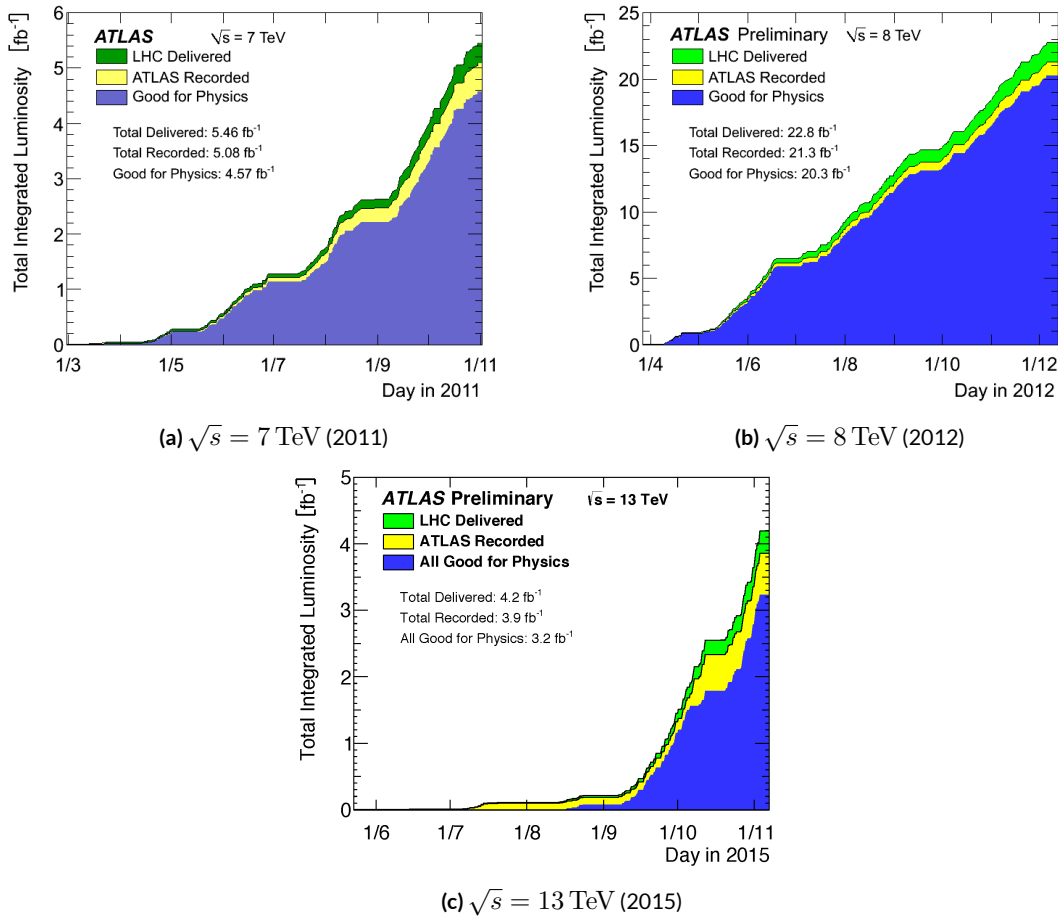


**Figure 2.9:** Instantaneous luminosity as a function of time for data recorded by ATLAS at different center of mass energies [10, 11]

## 2.2.8 DETECTOR PERFORMANCE

Table 2.2 summarizes the design requirements for each of the different sub-detectors. This table shows the energy and momentum resolution of each tracking, calorimetry, and muon measurements.

## 2.3 THE ATLAS MUON NEW SMALL WHEEL UPGRADE

As the LHC continues operation, it is scheduled to be upgraded in several phases to allow it to reach higher instantaneous luminosities and thus collect larger datasets. These conditions will open new doors

	Required resolution
Tracking	$\sigma_{p_T}/p_T = 0.05\% p_T \oplus 1\%$
EM calorimetry	$\sigma_E/E = 10\%/\sqrt{E} \oplus 0.7\%$
Hadronic calorimetry	
Barrel and end-cap	$\sigma_E/E = 50\%/\sqrt{E} \oplus 3\%$
Forward	$\sigma_E/E = 100\%/\sqrt{E} \oplus 10\%$
Muon spectrometer	$\sigma_{p_T}/p_T$ at $p_T = 1$ TeV

Table 2.2: Performance requirements for the ATLAS detector [7].

for study of rare physics processes but will also present interesting challenges that must be faced. ATLAS will require new detector technologies to cope with the increased background rates in the cavern in these high luminosity conditions. One such upgrade, scheduled to be installed during Long Shutdown 2 (LS2) of the LHC in 2018, is the ATLAS Muon New Small Wheel (NSW) upgrade [12]. The NSW will replace the innermost end-cap wheel of the muon system with new technologies, as this is the part of the muon detector closest to the beam and thus suffers from the highest rates.

### 2.3.1 MOTIVATION

The motivation of the NSW is two-fold. First, the objective is to alleviate the decreased tracking efficiency that comes in a high rate environment. As figure 2.10, at the LHC design luminosity both the efficiency of recording hits and reconstructing track segments in the MDTs decreases at the LHC design luminosity.

Second, the NSW will work to alleviate the rate of fake triggers arising in the endcap. Figure 2.11 shows the extrapolated trigger rates as a function of the  $p_T$  threshold with and without the NSW upgrade. As the figure shows, the NSW upgrade will reduce the trigger rate by an order of magnitude compared to the current endcap trigger system.

### 2.3.2 NSW DETECTOR TECHNOLOGIES

The NSW will use two new detector technologies - micromesh gaseous structure detectors (micromegas) and small-strip thin gap chambers (sTGCs) [12, 62]. Unlike the previous detectors, both of these detector technologies can be used for tracking or trigger. However, the micromegas is more suited to tracking

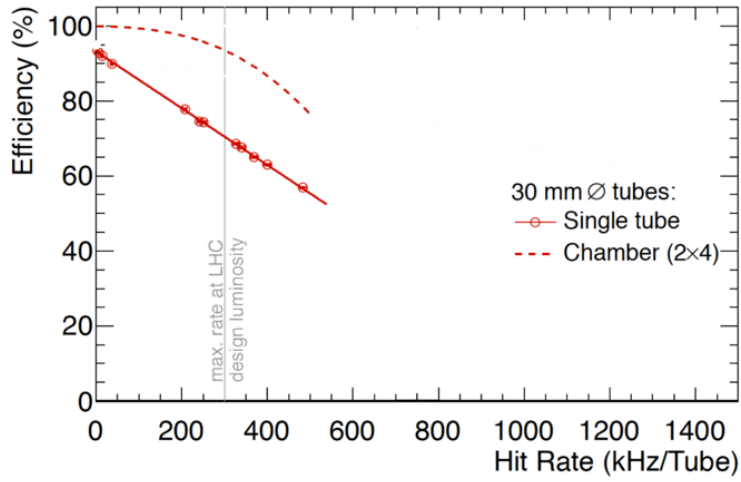


Figure 2.10: MDT tube hit (solid) and segment (dashed) efficiency as a function of hit rate per tube [12]

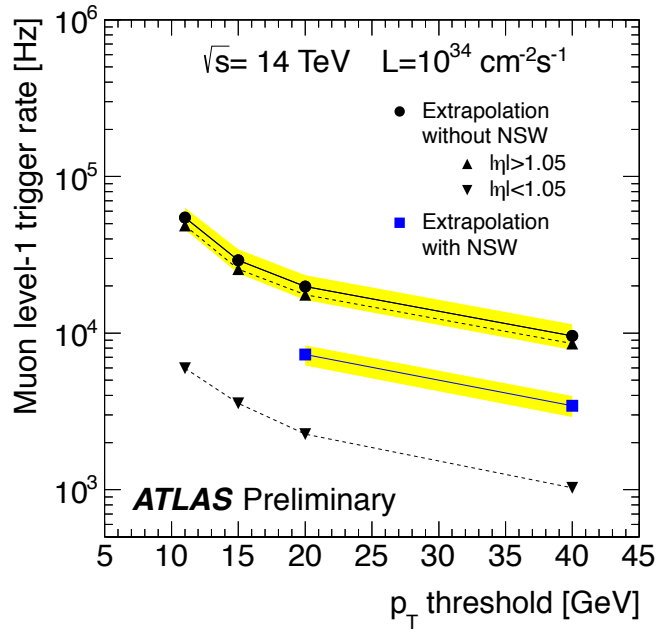


Figure 2.11: Trigger rate as a function of  $p_T$  threshold with and without the NSW upgrade [12]

because of its good spatial resolution, while the sTGCs have better time resolution and are more suited for the trigger. To maintain a fully redundant system, both technologies are used for both purposes.

1002 **MICROMEGAS**

1003 Micromegas detectors operate using a thin metallic mesh that sits approximately  $100 \mu\text{m}$  away from  
1004 the readout electrodes to create the amplification region. Above this mesh, there is a drift region on the  
1005 order of a few mm in length capped by a drift electrode. As a charged particle traverses the detector, it  
1006 ionizes gas and the electrons drift down towards readout strips. The timing of the drift can be used to  
1007 reconstruct the angle of traversal of the particle. This is illustrated in figure 2.12. The micromegas used in  
1008 ATLAS will be resistive micromegas, where the readout electrodes are topped with resistive strips [63].  
1009 This alleviates the risk of sparking in the large area detectors that ATLAS will use.

1010 In ATLAS, the micromegas drift gap will be 5 mm and the amplification gap will be  $128 \mu\text{m}$ . They  
1011 are filled with the same gas mixture as the MDTs. They will be stacked in an octuplet in an XXUV-  
1012 UVXX geometry, where X refers to straight strips and U and V refer to stero strips at an angle of  $\pm 1.5^\circ$ .  
1013 This arrangement allows for measurement of the azimuthal coordinate and gives a large lever arm be-  
1014 tween the straight strips for triggering purposes. Figure 2.12 shows the geometry of a single micromegas  
1015 detector as well as its operating principle [12].

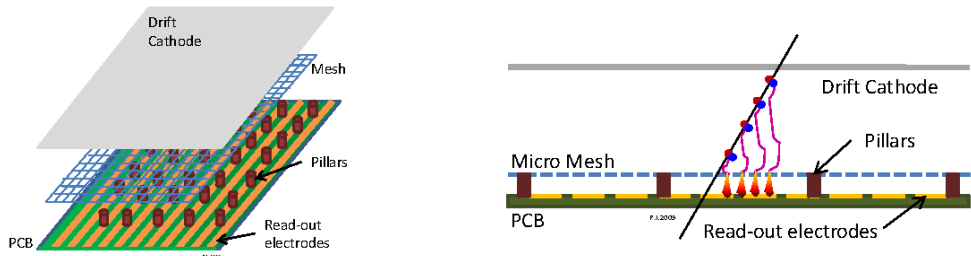
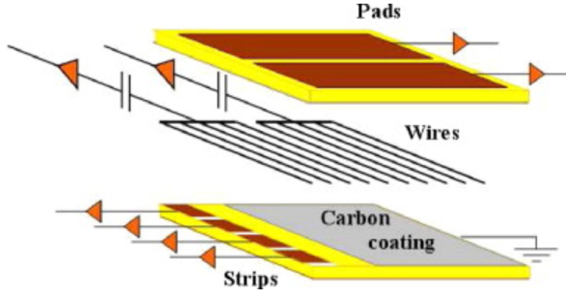


Figure 2.12: Illustrations of the geometry (left) and operating principle (right) of the micromegas detector [12]

1016 **sTGCs**

1017 The sTGCs are similar to the TGCs already described. They consist of gold-plated tungsten wires with  
1018 a 1.8 mm pitch between two cathode planes 1.4 mm away from the wire plane. One cathode plane  
1019 consists of strips with a 3.2 mm pitch (much smaller pitch than the TGCs), while the other consists  
1020 of coarser pads that are used for defining regions of interest in the sTGC trigger algorithm. Figure 2.13  
1021 shows the basic detector geometry.



**Figure 2.13:** Geometry of the sTGC detector [12]

### 2.3.3 PHYSICS IMPACT

Maintaining low  $p_T$  thresholds for muons while still staying within the trigger rate budget at Level 1 (20 kHz) for the muon system is crucial for physics analyses to be successful in high luminosity conditions. One realm where the lepton trigger threshold is especially important is in Higgs physics. In the  $H \rightarrow WW^*$  analysis, one of the  $W$  bosons is off shell and tends to decay to soft leptons. In associated production of a Higgs with a  $W$ , the lepton is also important because the lepton provides the main handle which allows the event to be triggered. Table 2.3 shows the impact of increasing the trigger thresholds on these analyses. It shows that either raising the threshold or using only the barrel both have significant impacts on the signal efficiency. With the NSW, the signal efficiency is largely maintained and the triggers can be unprescaled.

Threshold	$H \rightarrow b\bar{b}$ (%)	$H \rightarrow WW^*$ (%)
$p_T > 20$ GeV	93	94
$p_T > 40$ GeV	61	75
$p_T > 20$ GeV (barrel only)	43	72
$p_T > 20$ GeV (with NSW)	90	92

**Table 2.3:** Signal efficiencies for  $WH$  production with  $H \rightarrow b\bar{b}$  and  $H \rightarrow WW^* \rightarrow \mu\nu qq$  under different trigger configurations [12].

### 2.4 OBJECT RECONSTRUCTION IN ATLAS

ATLAS analyses first start by requiring the presence of certain reconstructed physics objects in the event. This section will present a brief overview of the algorithms used to reconstruct electrons, muons, jets

1035 (including  $b$ -jets), and missing energy<sup>\*</sup>. The performance of object reconstruction and measurement will  
1036 also be discussed as these are relevant to the analyses presented later. Figure 2.14 gives an overview of the  
1037 different sub-detectors that each type of particle will interact with in ATLAS.

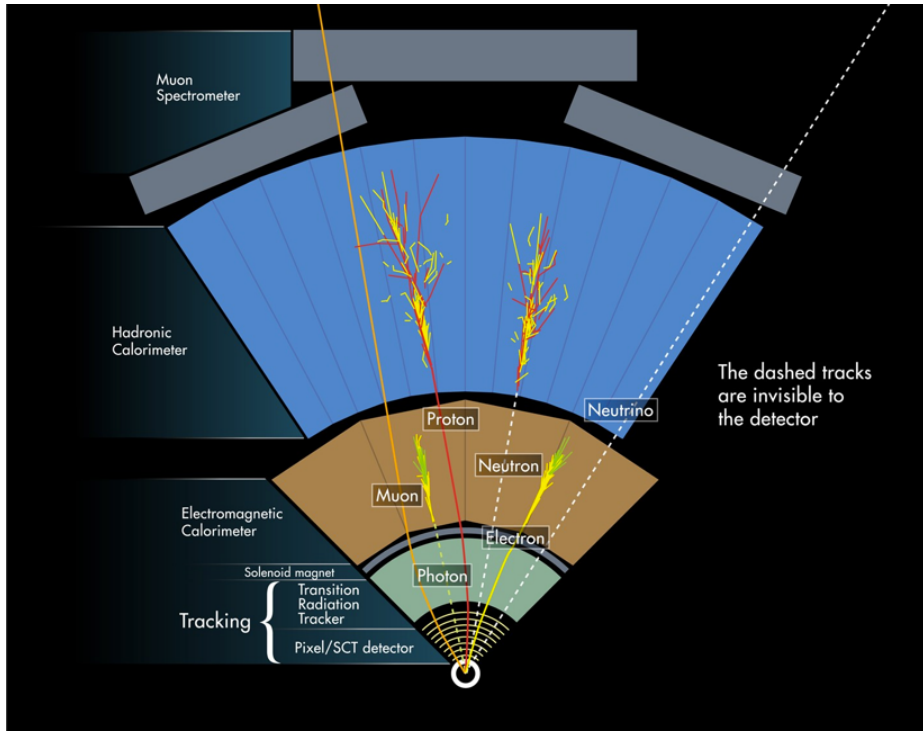


Figure 2.14: Illustration of particle interactions in ATLAS [13]

1038 2.4.I ELECTRONS

1039 Electrons in ATLAS will leave tracks in the inner detector and energy deposits in the electromagnetic  
1040 calorimeter. The algorithm for recognizing the signature of electrons proceeds in two steps: reconstruc-  
1041 tion and identification.

1042 In reconstruction, an electron candidate is formed by matching EM calorimeter deposits with ID  
1043 tracks. The algorithm first chooses seed clusters in the EM calorimeter by using a sliding window algo-  
1044 rithm that searches for towers with transverse energy larger than 2.5 GeV. In addition to seed clusters,  
1045 track candidates must be identified in the ID. The algorithm selects seed tracks with  $p_T > 1$  GeV that

---

\*Reconstruction algorithms for other objects, such as photons and  $\tau$  leptons, are not detailed here as these objects are not used in the presented studies.

1046 do not fit well with a pion hypothesis. Once candidate tracks are selected, they are re-fit with a Gaussian Sum Filter (GSF) algorithm to estimate electron parameters [64]. Finally, an electron candidate is  
 1047 formed if at least one track matches to a seed cluster in the calorimeter. The full details of the reconstruction  
 1048 algorithm can be found in reference [14].

1050 Once an electron candidate is present, identification criteria must be applied in order to reject fake  
 1051 electrons from background. Many different variables are used for this identification, most of them re-  
 1052 lated to the shower shape in the EM calorimeter and the amount of leakage into the hadronic calorime-  
 1053 ter, as well as information from the ID and in particular the TRT. There are both cut-based and likelihood-  
 1054 based criteria that range from “loose” to “very tight”. For details, see reference [14].

1055 Figure 2.15 shows the algorithm’s reconstruction efficiency of true electrons for different identification  
 1056 criteria as well as the electron energy resolution in simulation [14, 15]. The reconstruction efficiency is  
 1057 measured using both  $Z$  and  $J/\psi$  tag and probe techniques.

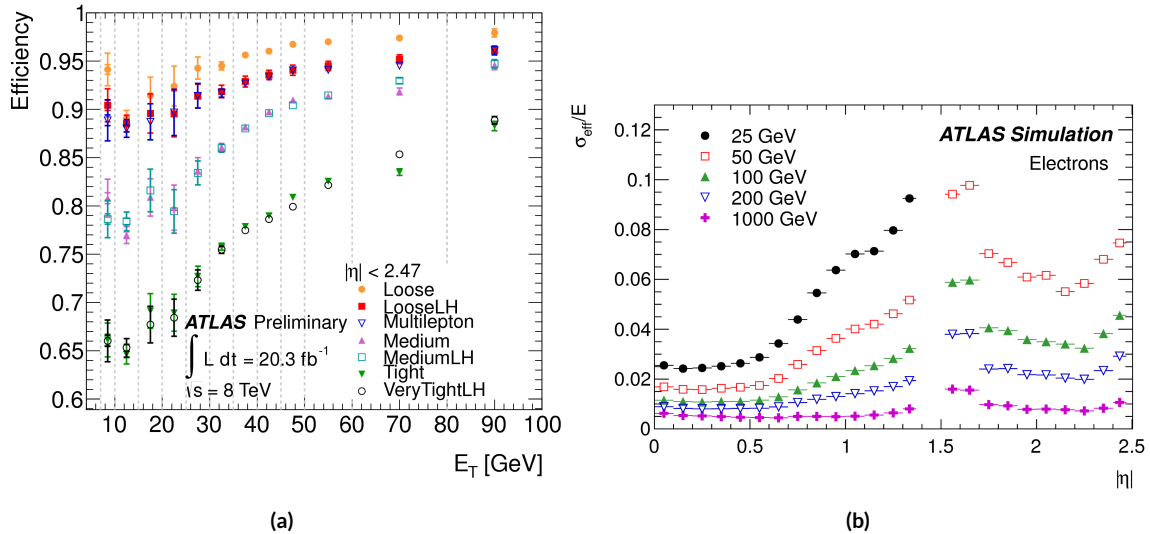


**Figure 2.15:** Electron performance: (a) reconstruction efficiency as a function of electron  $E_T$  [14] (b) energy resolution in simulation as a function of  $|\eta|$  for different energy electrons [15]

#### 1058 2.4.2 MUONS

1059 The ATLAS detector is designed to stop most particles before they reach the muon spectrometer. Muons,  
 1060 however, are minimum ionizing particles, meaning that they will not lose a significant amount of energy

1061 through interactions with the detector and will thus pass through. Therefore, the muon reconstruction  
1062 works to match tracks in the muon spectrometer with tracks in the inner detector.

1063 The first step of reconstruction is to reconstruct local straight line tracks, called segments, in each  
1064 muon chamber. Segments are then fit to larger tracks that traverse the entire muon spectrometer. Such  
1065 muon tracks are referred to as “standalone” tracks (SA) as they only use information from the muon  
1066 spectrometer. The standalone tracks are then matched to tracks in the inner detector to form “com-  
1067 bined” (CB) muons, where the combined ID and MS fit are used to determine the momentum and di-  
1068 rection of the muon. To improve acceptance, segment-tagged and calorimeter-tagged muons are also  
1069 reconstructed. In these cases, ID tracks are matched to segments in the MS and calorimeter deposits con-  
1070 sistent with a minimum ionizing particle, respectively. The details of the reconstruction can be found in  
1071 reference [16].

1072 As with electrons, once muon candidates are reconstructed they have identification criteria applied to  
1073 reduce background. These criteria include the  $\chi^2$  match between the ID and MS tracks, the number of  
1074 hits in the ID, overall ID and MS track fit quality, and additional variables [16]. The criteria range from  
1075 “loose” to “tight” as with electrons.

1076 Figure 2.16 shows the muon reconstruction efficiency (measured with  $Z$  and  $J/\psi$  tag and probe) and  
1077 invariant mass resolution [16].

#### 1078 2.4.3 JETS

1079 When a quark or gluon is produced in collisions, it is not measured directly in ATLAS. Rather, due to  
1080 QCD effects, it produces a collimated spray of hadrons in the direction of the original parton, which is  
1081 known as a jet. Jets are reconstructed in ATLAS using energy deposits in the hadronic calorimeter. The  
1082 first step is build “topological clusters” out of energy deposits in calorimeter cells [65, 66]. This is done  
1083 using strategy where seed cells are chosen by picking cells whose energy measurements are four times the  
1084 amount of noise expected for that cell. Adjacent cells with at least  $2\sigma$  energy measurements are added  
1085 to the cluster, then a final layer of clusters with energy above  $0\sigma$  are added. Once calorimeter clusters  
1086 are formed, they are clustered further into jet candidates using the anti- $k_T$  jet clustering algorithm [67].

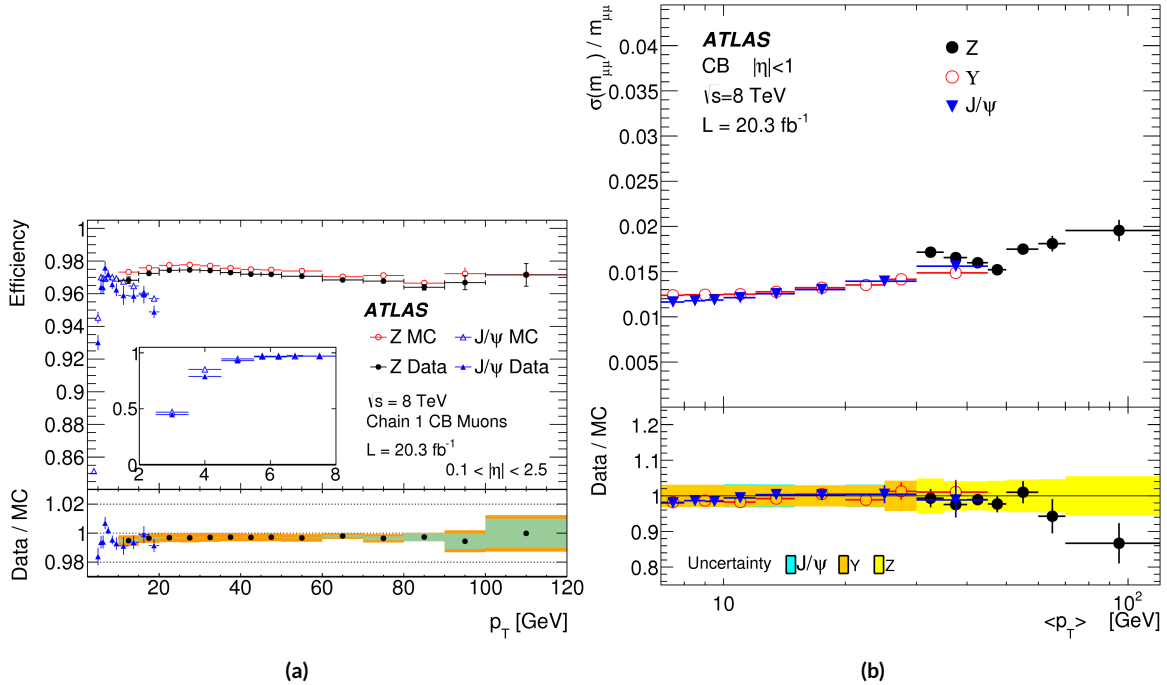


**Figure 2.16:** Muon performance: (a) reconstruction efficiency as a function of muon  $p_T$  (b) dimuon mass resolution as a function of average  $p_T$  [16]

This algorithm uses a parameter  $R$  that appears in the denominator of the clustering distance metric and defines the radial size of the jet in  $\eta$ - $\phi$  space.

The energy response of the calorimeter must be properly characterized in order to reconstruct jet energy. Calorimeter clusters can be calibrated either with the EM calibration, where each cluster is assumed to have come from the energy deposit of an electron or photon, or the LCW calibration, where local cluster weights are computed to allow for local calibration of clusters as hadronic or electromagnetic. The details of the jet energy calibration are not detailed here and are discussed in reference [17].

Figure 2.17 shows the jet energy response after calibration in Monte Carlo as a function of the true  $p_T$  of the jet [17].

#### 2.4.4 $b$ -TAGGING

One important aspect of jet physics is the task of identifying the flavor of parton that produced the measured jet. While in general this is very difficult, jets from  $b$ -quarks offer an interesting case where such identification is possible.  $B$  mesons have a lifetime on the order of  $10^{-12}$  seconds, which makes a  $c\tau$

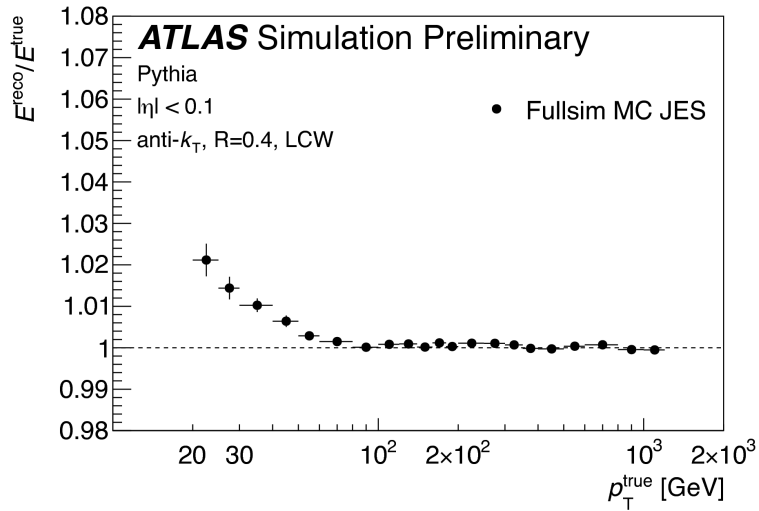


**Figure 2.17:** Jet energy response after calibration as a function of true  $p_T$  in simulation [17]

on the order of millimeters [1]. This type of displaced decay vertex can be identified in detectors like ATLAS and allows  $b$ -jets to be distinguished from other flavors of jets<sup>†</sup>.

ATLAS uses a multivariate machine learning algorithm to identify jets from  $b$ -quarks. The inputs to this algorithm are determined from lower level reconstruction algorithms. There are three distinct algorithms that reconstruct variables which are used as input to the multivariate technique.

The first family is referred to as IPxD (where the x can either be 2 or 3). These algorithms use the transverse and longitudinal impact parameters  $d_0$  and  $z_0$  of the tracks inside a jet to determine their consistency with the primary vertex. They two or three dimensional (hence the x) templates for light flavor, charm, and bottom jets and then evaluate the likelihood of the jet coming from each of these types. The likelihood ratios are used as inputs to the multivariate algorithm.

The next two algorithms used as input are referred to as the secondary vertex (SV) and JetFitter (JF) algorithms. The SV algorithm uses tracks inside the jet to fit for vertices that are displaced from the primary vertex. The JF algorithm attempts to reconstruct the full flight path of the  $b$  by looking for multiple displaced vertices along the same line (as  $B$  decays often result in subsequent  $c$  decays).

In Run 1, the multivariate  $b$ -tagging algorithm used a neural network and was referred to as MV1.

---

<sup>†</sup>Jets from charm quarks can also be detected in this way but they do not live quite as long so the displacement of the vertex is harder to distinguish

1115 The details of this algorithm and its inputs are given in reference [18]. In Run 2, the number of inputs  
 1116 was simplified and a boosted decision tree with 24 input variables was used, referred to as MV2. The  
 1117 details of this algorithm are in reference [19]. Figure 2.18 shows the performance of each of these algo-  
 1118 rithms.

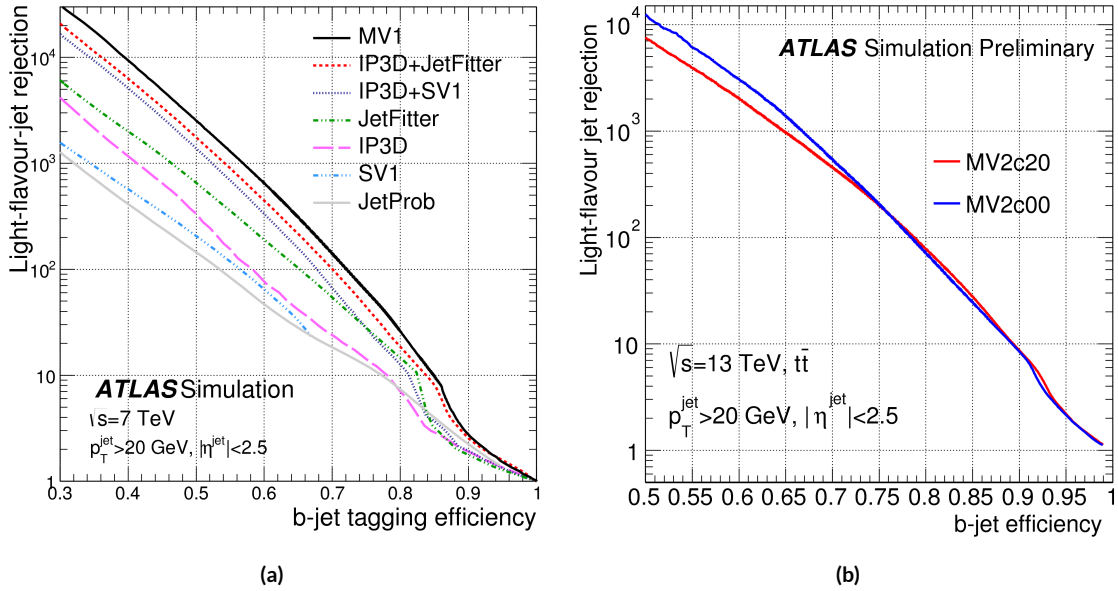


**Figure 2.18:** Light jet rejection ( $1/\text{efficiency}$ ) vs.  $b$ -jet efficiency for MV1 and its input algorithms (a) [18] and MV2 (b) [19] in simulated  $t\bar{t}$  events. The numbers in the algorithm names in (b) refer to the fraction of charm events used in the MV2 training.

#### 1119 2.4.5 MISSING TRANSVERSE ENERGY

1120 As noted in figure 2.14, neutrinos produced in ATLAS will pass through the detector without inter-  
 1121 acting. The only way of detecting the presence of particles like neutrinos (or BSM particles that are  
 1122 long-lived) is to use missing transverse momentum. The basic principle of missing transverse energy is  
 1123 to use the momentum balance of the incoming protons to infer the presence of missing particles. The  
 1124 net longitudinal momentum of the incoming partons that collide is not known (since each carries an un-  
 1125 known fraction of the proton's momentum). However, the protons (and thus incoming partons) have  
 1126 no net momentum in the plane transverse to the beam line (the  $x$ - $y$  plane). Therefore, if there are no  
 1127 un-measured particles in the final state, the transverse momenta of all of the final state particles should

1128 balance. The magnitude of this imbalance is known as missing transverse momentum ( $E_T^{\text{miss}}$ ).

1129 The basic calculation of missing transverse momentum from calorimeter cells is given in equation 2.4 [68].

$$\begin{aligned} E_x^{\text{miss}} &= -\sum_{i=1}^{N_{\text{cell}}} E_i \sin \theta_i \cos \phi_i \\ E_y^{\text{miss}} &= -\sum_{i=1}^{N_{\text{cell}}} E_i \sin \theta_i \sin \phi_i \end{aligned} \quad (2.4)$$

1130 The  $E_T^{\text{miss}}$  calculation is separated into different terms based on the objects that the calorimeter clusters are associated with. This way, each cell's contribution is calibrated appropriately according to the object. This separation of terms is shown in equation 2.5 [68].

$$\begin{aligned} E_{x(y)}^{\text{miss,calo}} &= E_{x(y)}^{\text{miss},e} + E_{x(y)}^{\text{miss},\gamma} + E_{x(y)}^{\text{miss},\tau} + E_{x(y)}^{\text{miss,jets}} \\ &\quad + E_{x(y)}^{\text{miss,softjets}} + E_{x(y)}^{\text{miss},\mu} + E_{x(y)}^{\text{miss,CellOut}} \end{aligned} \quad (2.5)$$

1133 The CellOut term of the above equation corresponds to calorimeter cells with energy deposits that are not associated with other objects. The soft jets term comes from cells associated to jets with  $p_T$  between 7 and 20 GeV, while the jets term comes from jets with  $p_T > 20$  GeV. Because muons do not deposit significant energy in the calorimeter, the muon momentum is used for the muon term [68]. The final  $E_T^{\text{miss}}$  is calculated using equation 2.6.

$$E_T^{\text{miss}} = \sqrt{(E_x^{\text{miss}})^2 + (E_y^{\text{miss}})^2} \quad (2.6)$$

1138 Figure 2.19 shows the resolution of the components of the  $E_T^{\text{miss}}$  under different pileup suppression techniques [20].

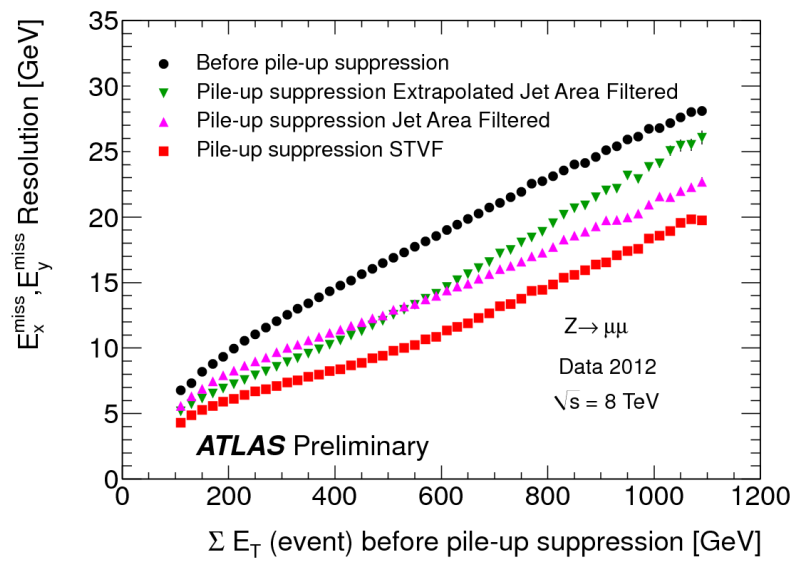


**Figure 2.19:** Resolution of  $E_T^{\text{miss}}$  components as a function of  $\sum E_T$  before pileup suppression with different pileup techniques [20]

1140

## Part II

1141

Observation and measurement of Higgs

1142

boson decays to  $WW^*$  in LHC Run I at

1143

$$\sqrt{s} = 7 \text{ and } 8 \text{ TeV}$$

*Basic research is what I am doing when I don't know  
what I am doing.*

Wernher von Braun

# 3

1144

## 1145 $H \rightarrow WW^* \rightarrow \ell\nu\ell\nu$ Analysis Strategy

### 1146 3.1 INTRODUCTION

1147 This chapter presents an overview of the strategy for searching for a Higgs boson in the  $H \rightarrow WW^* \rightarrow$   
1148  $\ell\nu\ell\nu$  decay topology. Its purpose is to define in broad terms how the search and measurement are un-  
1149 dertaken, before going into details on the specific sub-categories within the larger analysis. First, the  
1150 properties of the Higgs signal are discussed and the associated backgrounds are presented. Next, the ob-  
1151 servables used to enhance the signal to background ratio are defined. Finally, the parameters of interest  
1152 in the search and measurement will be shown, along with a brief overview of the statistical treatment of  
1153 the final Higgs candidates.

1154 Following this chapter, the results of three different studies within the  $H \rightarrow WW^* \rightarrow \ell\nu\ell\nu$  channel  
1155 are shown. Chapter 4 presents a search for Higgs boson production in gluon fusion mode and the role  
1156 of the  $H \rightarrow WW^*$  channel in its discovery. Chapter 5 shows the search and first observation in ATLAS  
1157 of the Vector Boson Fusion (VBF) production mode of the Higgs in the  $H \rightarrow WW^*$  decay channel.

1158 Finally, chapter 6 shows the combined Run 1  $H \rightarrow WW^*$  results for the measurement of the Higgs  
1159 cross section and relative coupling strengths to other SM particles.

## 1160 3.2 THE $H \rightarrow WW^* \rightarrow \ell\nu\ell\nu$ SIGNAL IN ATLAS

1161 The signal studied in this and subsequent chapters is the Higgs boson in the  $WW^*$  final state, where  
1162 each  $W$  boson subsequently decays into a charged lepton and a neutrino. In its simplest decay path, the  
1163 final state consists of two neutrinos and two charged leptons, each of which can be either an electron or  
1164 a muon. If one or both of the  $W$ s decay to  $\tau$  leptons, only leptonic decays of the  $\tau$  are considered. This  
1165 decay path produces additional neutrinos in the final state but still gives two charged leptons as before.  
1166 Neutrinos are not detected in ATLAS, so the final state ultimately consists of two reconstructed leptons  
1167 and missing transverse momentum (denoted as  $E_T^{\text{miss}}$ ). Final states where both of the charged leptons  
1168 are electrons or muons are referred to as the “same flavor” ( $ee/\mu\mu$ ) final states, while those with one  
1169 electron and one muon are referred to as “different flavor” ( $e\mu$  or  $\mu e$ ).

1170 While the basic final state consists of two leptons and  $E_T^{\text{miss}}$ , there can be additional objects depend-  
1171 ing on the production mode of the Higgs. As described in detail in Chapter 1, if the Higgs is produced  
1172 via vector boson fusion production, there will be two additional forward jets in the event. Even in gluon  
1173 fusion, one or more jets can be produced through initial state radiation from the incoming gluons. Be-  
1174 cause of the varying background composition as a function of jet multiplicity, each bin in this variable  
1175 has its own dedicated requirements applied in the search and measurement. The  $n_j = 0$  and  $n_j = 1$   
1176 bins are dedicated to gluon fusion production, while the  $n_j \geq 2$  bin has separate dedicated searches for  
1177 ggF and VBF production.

1178 Figure 3.1 shows the relative branching fractions for the  $H \rightarrow WW^*$  process, calculated from the  
1179 Particle Data Group values for the  $W$  and  $\tau$  branching ratios[?]. The largest branching ratio is both  
1180  $W$  bosons decaying to quark pairs at 45.44%. The next largest is one  $W$  decaying leptonically and the  
1181 other decaying to quarks, a branching ratio of 34.18%. In all cases,  $\ell$  denotes either an electron or muon,  
1182 and the leptonic branching ratios of the  $\tau$  are included. For example, the  $\ell\nu qq$  final state includes one  $W$   
1183 decaying to  $e\nu$ ,  $\mu\nu$ , or  $\tau\nu$ . In the case of the  $W \rightarrow \tau\nu$  decay, the  $\tau$  lepton then decays to an electron or

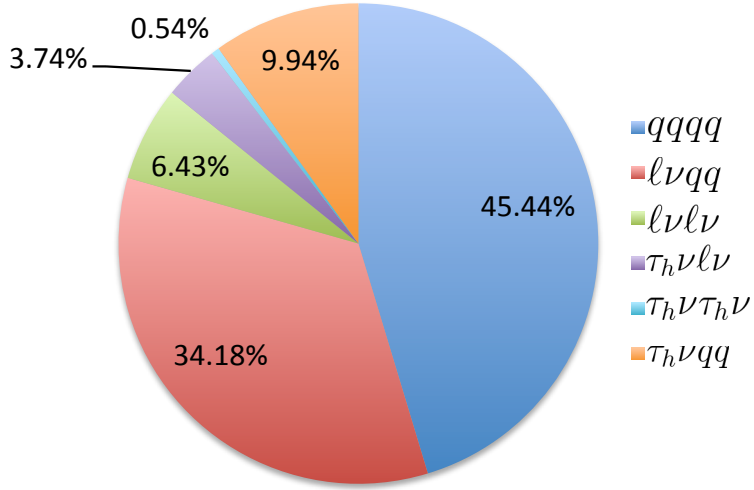


**Figure 3.1:** Branching ratios for a  $WW$  system.  $q$  refers to quarks.  $\ell$  can be either an electron or muon, and the leptonic branching ratios of the  $\tau$  are included. For example, the  $\ell\nu qq$  final state includes one  $W$  decaying to  $e\nu$ ,  $\mu\nu$ , or  $\tau\nu$ .  $\tau_h$  refer to hadronic decays of the  $\tau$ .

1184 muon via  $\tau \rightarrow \nu_\tau \ell \nu_\ell$ . Final states with a  $\tau_h$  refer to hadronic decays of the  $\tau$ . The branching ratio to the  
 1185  $\ell\nu\ell\nu$  final state is 6.43%.

1186 While the  $\ell\nu\ell\nu$  final state is not a large fraction of the branching ratio, there are significant advantages  
 1187 in this channel. First, both the  $qqqq$  and  $\ell\nu qq$  channels suffer from a large QCD multijet background,  
 1188 which is often difficult to model. Second, events in the the  $\ell\nu\ell\nu$  channel in data can be triggered more  
 1189 efficiently due to the presence of two leptons.

### 1190 3.3 BACKGROUND PROCESSES

1191 Many processes from the Standard Model can also produce a final state with two leptons and missing  
 1192 transverse momentum . This section lists the dominant backgrounds to Higgs production. It gives gen-  
 1193 eral descriptions of how the backgrounds mimic Higgs production and how they can be reduced. Ta-  
 1194 ble3.1 summarizes the different processes.

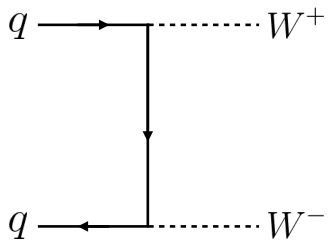


**Figure 3.2:** Feynman diagram for Standard Model WW production

### 1195 3.3.1 STANDARD MODEL WW PRODUCTION

1196 Non-resonant Standard Model diboson production, as shown in figure 3.2, is an irreducible background  
 1197 to Higgs boson production in the WW final state. It produces the same exact final state objects, namely  
 1198 leptonically decaying W bosons. There are no additional objects in the final state that allow for back-  
 1199 ground reduction. Therefore the analysis solely relies on the correlations between the leptons to reduce  
 1200 this background.

### 1201 3.3.2 TOP QUARK PRODUCTION

1202 Production of top quarks, either in pairs ( $t\bar{t}$  production) or singly (e.g.  $Wt$  production), can also mimic  
 1203 Higgs production. Because top quarks decay via  $t \rightarrow Wb$ , top pair production can produce a final state  
 1204 with two W bosons that then decay leptonically. In this case, however, there are two additional jets from  
 1205 the bottom quarks in the final state. This allows the analysis to veto on the presence of jets identified as  
 1206 originating from a  $b$  in order to reduce the size of the background.

1207 Single top production can occur via  $s$ -channel,  $t$ -channel, or associated production ( $Wt$ ). The mode  
 1208 which most closely resembles the Higgs final state is  $Wt$ . In this case, there are two real W bosons pro-  
 1209 duced, as with  $t\bar{t}$ . However, the decay of the single top quark will still also produce one  $b$ -jet, meaning a  
 1210  $b$  veto will reduce this background as well.

1211 Figure 3.3 shows the Feynman diagrams for  $t\bar{t}$  and  $Wt$  production.

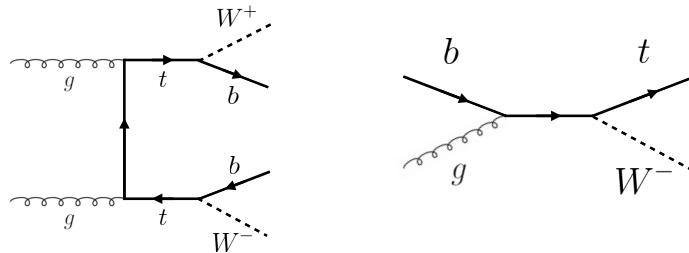


**Figure 3.3:** Feynman diagrams for top pair production (left) and  $Wt$  production (right)

### 1212 3.3.3 $W$ +JETS BACKGROUND

1213 Single  $W$  boson production, in association with jets, is a unique background. The other background  
 1214 considered so far have all included real leptons in the final state. In this case, however, only one real lep-  
 1215 ton from the decay of a  $W$  exists in the final state. The second reconstructed lepton can arise from two  
 1216 different cases. First, the lepton may truly be an algorithm “fake”, or a jet misidentified as a lepton by  
 1217 either the electron or muon reconstruction algorithms. Second, the lepton may be a real lepton but  
 1218 coming from semi-leptonic decays of particles inside the shower of the jet. This background can be re-  
 1219 duced by requiring that the reconstructed lepton have little activity surrounding it in the calorimeter  
 1220 (also known as an “isolated” lepton). Figure 3.4 shows the Feynman diagram for  $W$ +jets production.

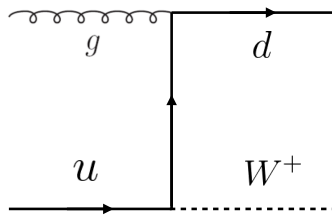


**Figure 3.4:** An example Feynman diagram of  $W$ +jets production

### 1221 3.3.4 $Z/\gamma^*$ +JETS BACKGROUND

1222 Production of a  $Z/\gamma^*$  in association with jets (also known as Drell-Yan) is also a background to Higgs  
 1223 production. In particular, the same flavor final states have a large  $Z$ +jets background, as the  $Z$  decays  
 1224 into two leptons of the same flavor. (This background also enters the different flavor final state through

the leptonic decays of  $Z \rightarrow \tau\tau$ ). Figure 3.5 shows the production of a  $Z$  in association with one jet. Because there are no neutrinos in this final state, variables like  $E_T^{\text{miss}}$  can be used to reduce the background.

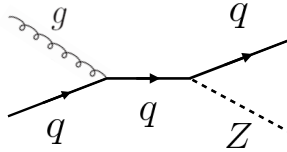


**Figure 3.5:** An example Feynman diagram of  $Z + \text{jets}$  production

### 3.3.5 OTHER (SUBDOMINANT) BACKGROUNDS

There are additional processes which contribute to the background composition but are not produced as frequently as those listed already. The first of these are referred to as  $VV$  or “Other diboson” processes and include multiple Standard Model diboson processes, including  $WZ$ ,  $ZZ$ ,  $W\gamma$ ,  $W\gamma^*$ , and  $Z\gamma$  production. Additionally, there is background from QCD multijet production, where two jets are misidentified as leptons.

Category	Process	Description
SM $WW$	$WW \rightarrow \ell\nu\ell\nu$	Real leptons and neutrinos
Top quark production	$t\bar{t} \rightarrow WbWb \rightarrow \ell\nu b\ell\nu b$ $tW \rightarrow WbW \rightarrow \ell\nu\ell\nu b$ $t\bar{b}, t\bar{q}\bar{b}$	Real leptons, untagged $b$ s Real leptons, untagged $b$ Untagged $b$ , jet misidentified as lepton
Drell-Yan	$Z/\gamma^* \rightarrow ee, \mu\mu$ $Z/\gamma^* \rightarrow \tau\tau \rightarrow \ell\nu\ell\nu$	“Fake” $E_T^{\text{miss}}$ Real leptons and neutrinos
Other dibosons	$ZZ \rightarrow \ell\ell\nu\nu$ $W\gamma^*, WZ \rightarrow \ell\nu\ell\ell, ZZ \rightarrow \ell\ell\ell\ell$ $W\gamma, Z\gamma$	Real leptons and neutrinos Unreconstructed leptons $\gamma$ reconstructed as $e$ , unreconstructed lepton
$W + \text{jets}$	$Wj \rightarrow \ell\nu j$	Jet reconstructed as lepton
QCD multijet	$jj$	Jets reconstructed as leptons

**Table 3.1:** A summary of backgrounds to the  $H \rightarrow WW^* \rightarrow \ell\nu\ell\nu$  signal

1233 3.4 SHARED SIGNAL REGION SELECTION REQUIREMENTS

1234 As presented in section 3.2, there are many different combinations of objects that can define a  $H \rightarrow$   
1235  $WW^* \rightarrow \ell\nu\ell\nu$  final state. The multiplicity of jets and the flavor combinations of the leptons both lead  
1236 to many potential signal regions. Additionally, signal regions can be optimized separately to be sensi-  
1237 tive to the distinct production modes of the Higgs. Gluon fusion, vector boson fusion, and associated  
1238 production of a Higgs all lead to unique final state topologies. Figure 3.6 delineates the different signal  
1239 regions used in the gluon fusion and vector boson fusion  $H \rightarrow WW^*$  analyses. While there are different  
1240 optimizations possible in each signal region, there are also some commonly shared selections that will be  
1241 described here.

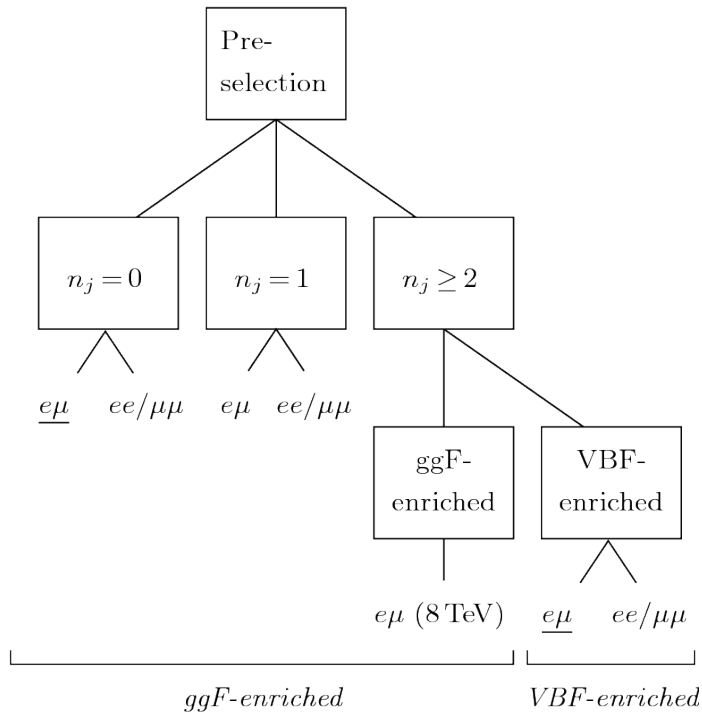


Figure 3.6: An illustration of the unique analysis signal regions[21]

1242 3.4.1 EVENT PRE-SELECTION

1243 Before being sorted into the distinct signal regions, basic requirements are applied on the reconstructed  
1244 objects in the event to select Higgs-like event candidates. First, two oppositely charged leptons are re-

1245 quired.

1246 Once the leptons are selected, the last requirement for event pre-selection is the presence of neutrinos.  
1247 As neutrinos cannot be detected directly in ATLAS,  $E_T^{\text{miss}}$  can be used as a proxy for the combined neu-  
1248 trino momentum in the transverse plane. In general, it is expected that the signal should have a harder  
1249  $E_T^{\text{miss}}$  spectrum than backgrounds, especially if those backgrounds did not contain neutrinos. One ad-  
1250 ditional consideration when using  $E_T^{\text{miss}}$  is the fact that mis-measurements of objects in the detector  
1251 can lead to imbalances in the transverse plane that are not due to real particles escaping the detector.  
1252 One indicator that this is the case is that the  $E_T^{\text{miss}}$  vector in the transverse plane will be pointing in the  
1253 same direction as the mis-measured object. Therefore, a new variable,  $E_{T,\text{rel}}^{\text{miss}}$ , is used in the pre-selection.  
1254  $E_{T,\text{rel}}^{\text{miss}}$  is defined in equation 3.1.

$$E_{T,\text{rel}}^{\text{miss}} = \begin{cases} E_T^{\text{miss}} \sin \Delta\phi_{\text{near}} & \text{if } \Delta\phi_{\text{near}} < \pi/2 \\ E_T^{\text{miss}} & \text{otherwise,} \end{cases} \quad (3.1)$$

1255 If the closest object to the  $E_T^{\text{miss}}$  vector is within  $\pi/2$  radians in the transverse plane, the  $E_T^{\text{miss}}$  is pro-  
1256 jected away from this object. Otherwise, the normal  $E_T^{\text{miss}}$  vector is used. Figure 3.7 shows a graphical  
1257 illustration of this concept.

1258 Once both the lepton and  $E_T^{\text{miss}}$  pre-selections are made, the analysis can be divided into different  
1259 regions according to jet multiplicity.

### 1260 3.4.2 JET MULTIPLICITY

1261 Jet multiplicity, denoted as  $n_j$ , is used to sub-divide the analysis into its distinct signal regions. The rea-  
1262 son for this is twofold. First, different jet multiplicity bins will be more or less sensitive to different Higgs  
1263 production modes. For example, the  $n_j \geq 2$  region is more sensitive to VBF production because of  
1264 the two high momentum jets produced at matrix element level. For gluon fusion production to enter  
1265 this bin, two initial state radiation jets must be emitted. Second, background composition varies greatly  
1266 in different bins of  $n_j$ . Figure 3.8 shows the jet multiplicity in both the different flavor and same flavor  
1267 regions. It also shows the background composition in the bins of  $n_b$ . There are a few clear trends from

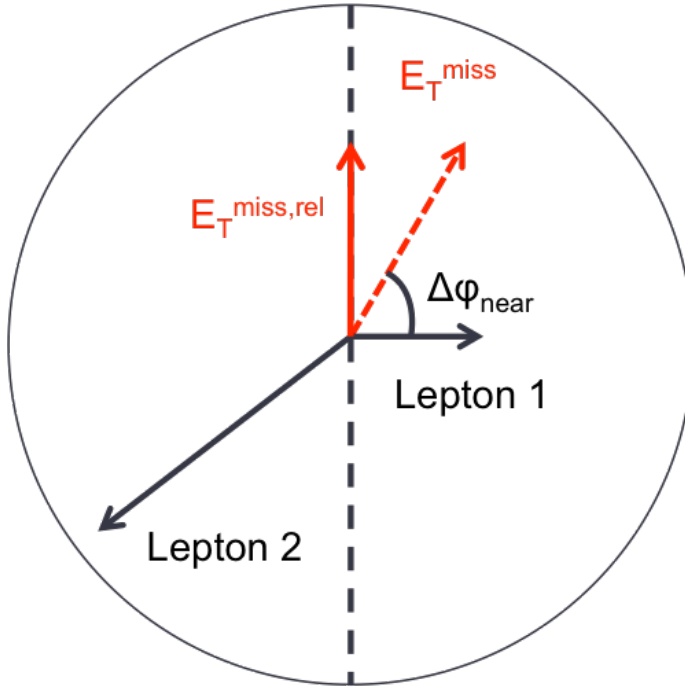


Figure 3.7: A graphical illustration of the  $E_{T,\text{rel}}^{\text{miss}}$  calculation

1268 this distribution. The first is that the Drell-Yan background dominates in the same flavor channels for  
 1269  $n_j \leq 1$ . Second, the top background becomes a clear contributor to the total background for  $n_j \geq 1$ .  
 1270 Lastly, the SM WW production dominates in the  $n_j = 0$  bin, as it is an irreducible background to  
 1271  $H \rightarrow WW^*$  production. Because of these distinct features, each jet multiplicity bin is treated separately.

### 1272 3.5 BACKGROUND REDUCTION IN SAME-FLAVOR FINAL STATES

1273 As described in section 3.4.2, the background composition of the same flavor final states is unique to that  
 1274 of the different flavor states. In particular, Drell Yan processes play a much larger role because the  $Z/\gamma^*$   
 1275 decays to same flavor leptons. Because real neutrinos are absent in the  $Z/\gamma^*$  decays to  $ee$  and  $\mu\mu$ , a re-  
 1276 quirement on  $E_T^{\text{miss}}$  should largely reduce the background. However, as this section will demonstrate,  
 1277 with increasing pileup conditions the resolution of the calorimeter-based  $E_T^{\text{miss}}$  degrades greatly. There-  
 1278 fore, two new variables for  $Z/\gamma^*$  background reduction are constructed and described in this section.

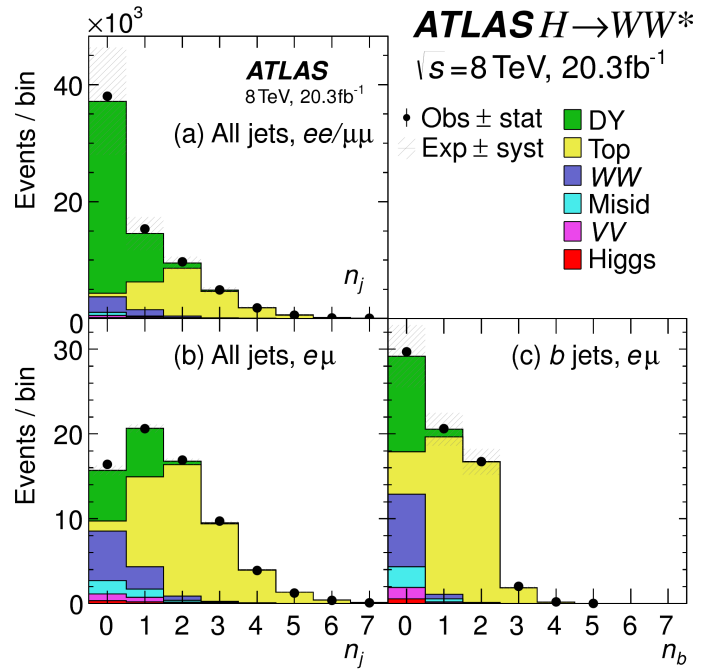


Figure 3.8: Predicted backgrounds (compared with data) as a function of  $n_j$  (a and b) and  $n_b$  (c)

### 1279 3.5.1 PILEUP AND $E_T^{\text{miss}}$ RESOLUTION

1280 Secondary interactions of protons in the colliding bunches of the LHC (known as pileup interactions,  
 1281 described in detail in Chapter 2) deposit energy into the ATLAS calorimeter on top of the energy that  
 1282 comes from the hard scatter process that is being searched for or analyzed. The calculation of  $E_T^{\text{miss}}$  is  
 1283 fundamentally Poissonian, as summing up all of the energy deposits in individual calorimeter cells or  
 1284 clusters is similar to a counting experiment. Thus, the energy resolution scales as  $\sqrt{E}$ , just as the error on  
 1285 a mean of  $N$  in a Poisson distribution is  $\sqrt{N}$ . As more energy is deposited in the calorimeter, the  $E_T^{\text{miss}}$   
 1286 resolution degrades, meaning that the  $E_T^{\text{miss}}$  resolution is particularly sensitive to LHC instantaneous  
 1287 luminosity conditions.

1288 Figure 3.9 shows an event display of a  $Z/\gamma^* + \text{jets}$  event candidate with the twenty-five reconstructed  
 1289 primary vertices. This display illustrates that while the interaction of interest only has tracks coming  
 1290 from the hardest primary vertex, all of the secondary interactions will deposit energy in the calorimeter as  
 1291 well.

1292 Figure 3.10 shows the RMS of the  $E_T^{\text{miss}}$  distribution in  $Z \rightarrow \mu\mu$  events (where there are no real neu-

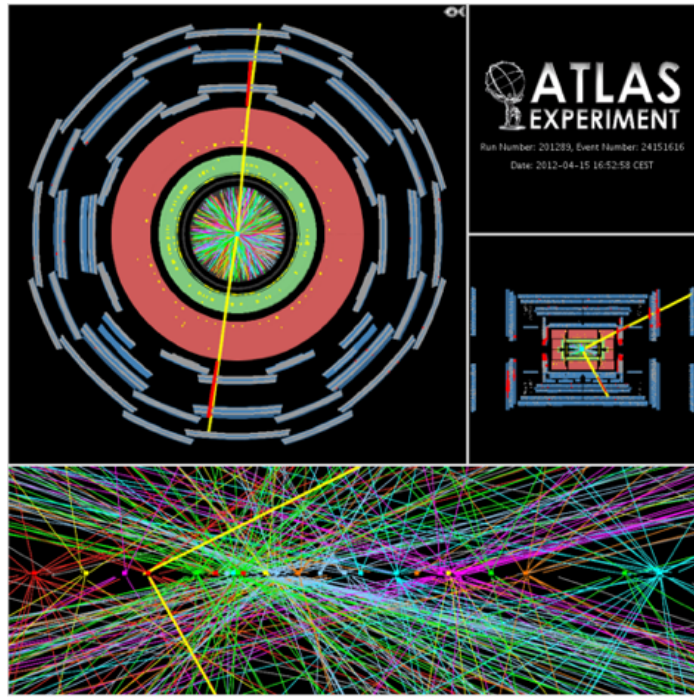


**Figure 3.9:** An event display of a  $Z/\gamma^*$  + jets event illustrating the effect of pileup interactions

trinos) as a function of the number of the average number of interactions. Under 2011 LHC conditions, this RMS was approximately 9 GeV, while under 2012 running conditions the resolution worsened to 12 GeV. This worsening dilutes the  $E_T^{\text{miss}}$  variable's ability to reduce the  $Z/\gamma^*$  background.

### 3.5.2 TRACK-BASED DEFINITIONS OF MISSING TRANSVERSE MOMENTUM

Because the increasing number of secondary proton-proton interactions degrades calorimeter-based  $E_T^{\text{miss}}$  resolution, a new variable using only contributions from the primary interaction vertex is necessary to further reduce the  $Z/\gamma^*$  background. While it is not possible to associate calorimeter energy deposits with a particular vertex, individual charged particle tracks in the Inner Detector are associated to unique vertices. Thus, two track-based definitions of missing transverse momentum , using only tracks coming from the primary vertex in the event, are used in the analysis. The simplest variable,  $p_T^{\text{miss}(\text{trk})}$ , is the vectorial sum of the  $p_T$  of all of the tracks from the primary vertex and the selected leptons (excluding the tracks associated with the selected leptons to avoid double counting). This is defined in equa-

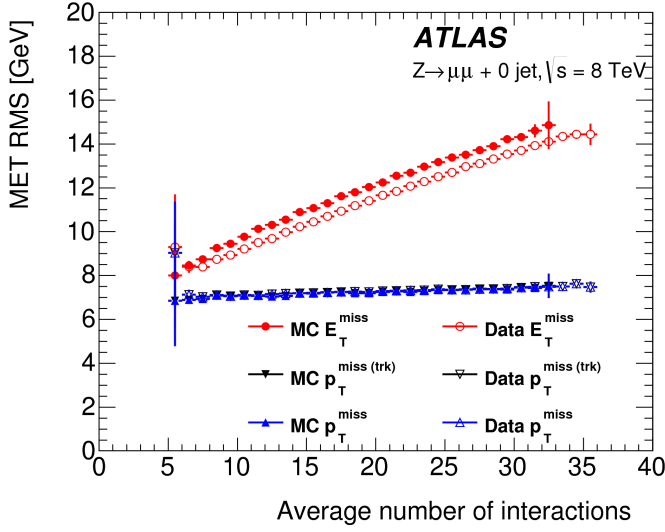


**Figure 3.10:** The RMS of different missing transverse momentum definitions as a function of the average number of interactions per bunch crossing

1305      tion 3.2.

$$p_T^{\text{miss}(\text{trk})} = - \left( \sum_{\text{selected leptons}} p_T + \sum_{\text{other tracks}} p_T \right), \quad (3.2)$$

1306      In events with hard jets, a better resolution on the missing transverse momentum is obtained by in-  
 1307      cluding the calorimeter based measurement of the hard jets rather than the track based measurements.  
 1308      Thus, another variable,  $p_T^{\text{miss}}$ , is defined, using the nominal measurements of  $p_T$  for the selected leptons  
 1309      and jets and using tracks rather than calorimeter clusters for the soft component of the missing transverse  
 1310      momentum . This is defined in equation 3.3.

$$p_T^{\text{miss}} = - \left( \sum_{\text{selected leptons}} p_T + \sum_{\text{selected jets}} p_T + \sum_{\text{other tracks}} p_T \right), \quad (3.3)$$

1311      Figure 3.10 illustrates that these two new variables accomplish their intended purpose. The resolution  
 1312      as a function of mean number of interactions for both  $p_T^{\text{miss}(\text{trk})}$  and  $p_T^{\text{miss}}$  is much flatter compared to  
 1313      the dependence for  $E_T^{\text{miss}}$ .

1314      Figure 3.11a shows the difference between the true and reconstructed values of missing transverse mo-

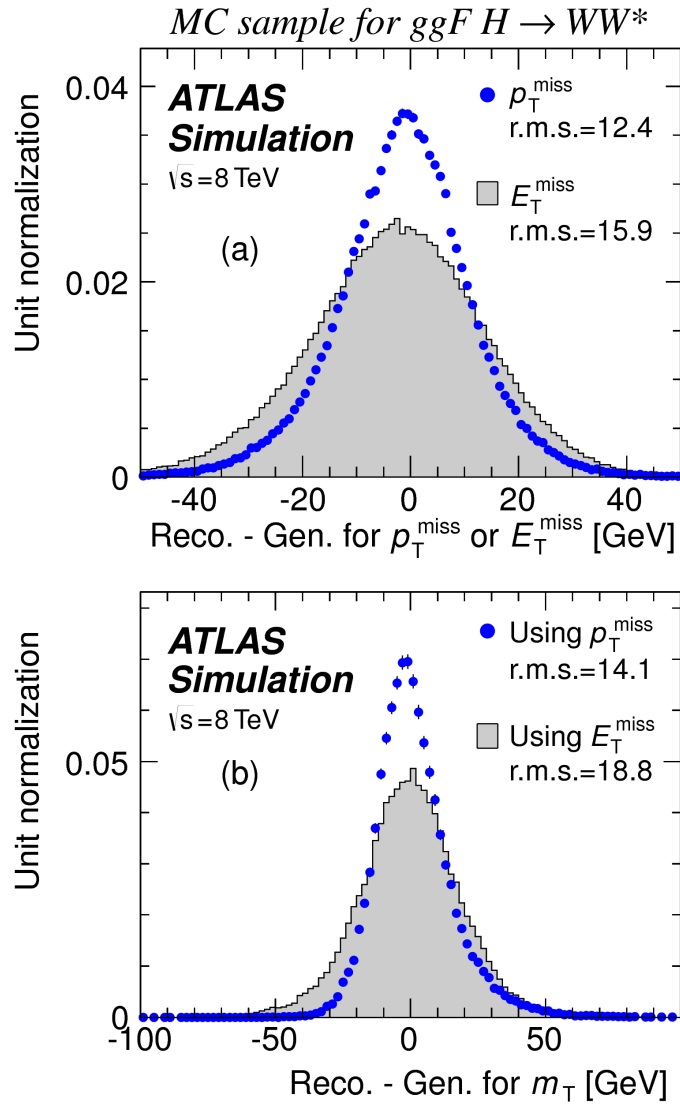


**Figure 3.11:** The difference between the true and reconstructed values of the missing transverse momentum (a) and  $m_T$  (b) in a gluon fusion signal sample

1315     mentum using both the track-based  $p_T^{\text{miss}}$  and calorimeter based  $E_T^{\text{miss}}$ . The RMS of the distribution

1316     improves by 3.5 GeV when using  $p_T^{\text{miss}}$ .

### 1317     3.5.3 Distinguishing $Z/\gamma^*$ +JETS AND $H \rightarrow WW^*$ TOPOLOGIES

1318     The track-based definitions of missing transverse momentum were constructed to mitigate degrading

1319     performance as a function of pileup. However, an additional variable can be constructed to exploit kine-

matic and topological differences between the  $Z/\gamma^*$  background and  $H \rightarrow WW^*$  signal. Because there  
 1320 are no real neutrinos in the final state (in the case of  $Z/\gamma^* \rightarrow ee, \mu\mu$  decays), the dilepton system of a  
 1321  $Z/\gamma^*$  will be balanced with the jets produced in the hard scatter. A new variable,  $f_{\text{recoil}}$ , is constructed  
 1322 to estimate the balance between the dilepton system and the jets in the quadrant opposite the dilepton  
 1323 vector in the transverse plane. It is defined in equation 3.4. The numerator of  $f_{\text{recoil}}$  is the magnitude of  
 1324 the vectorial sum of the  $p_T$  of jets in the quadrant opposite the dilepton system, weighted by each jet's Jet  
 1325 Vertex Fraction (JVF, described in chapter 2). The denominator is the magnitude of the dilepton  $p_T$ .  
 1326

$$f_{\text{recoil}} = \left| \sum_{\text{jets } j \text{ in } \wedge} \text{JVF}_j \cdot \mathbf{p}_T^j \right| / p_T^{\ell\ell}. \quad (3.4)$$

1327 Figure 3.12 shows a shape comparison of the distribution of  $f_{\text{recoil}}$  in a simulated  $Z/\gamma^* + \text{jets}$  sample,  
 1328 a  $H \rightarrow WW^*$  signal sample, and other backgrounds that contain real neutrinos. The  $Z/\gamma^* + \text{jets}$  events  
 1329 tend to be more balanced between the dilepton system and recoiling jets, while the processes containing  
 1330 real neutrinos are less balanced in the transverse plane. Thus, a requirement on  $f_{\text{recoil}}$  will also reduce  
 1331 the  $Z/\gamma^* + \text{jets}$  background while maintaining a good signal efficiency.

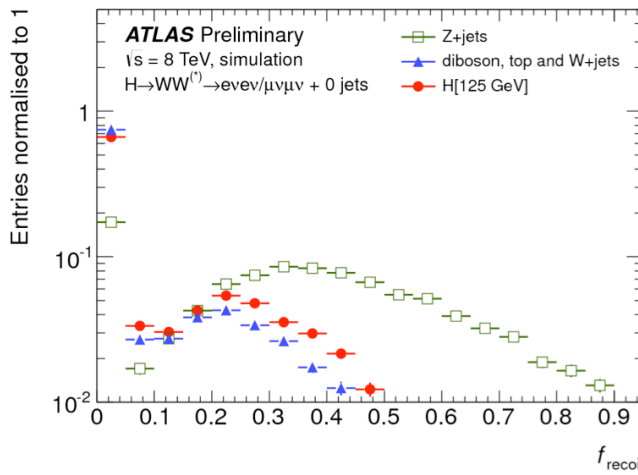


**Figure 3.12:** Comparison of  $f_{\text{recoil}}$  distributions for  $Z/\gamma^* + \text{jets}$ ,  $H \rightarrow WW^*$ , and other backgrounds with real neutrinos.

1332    3.5.4    OPTIMIZING BACKGROUND REDUCTION SELECTION REQUIREMENTS

1333    The requirements on  $p_T^{\text{miss(trk)}}$  and  $f_{\text{recoil}}$  used to reduce the Z+jets background must be optimized  
 1334    to maximize their efficacy. Figure 3.13 shows an early attempt to optimize the combination of the two  
 1335    requirements in the gluon fusion zero jet bin. Each bin shows the expected signal significance if the  
 1336     $p_{T,\text{rel}}^{\text{miss(trk)}}$  is required to be greater than the left edge of the bin and the  $f_{\text{recoil}}$  is required to be less than  
 1337    the top edge of the bin. The figure shows that the best signal significance comes from requiring low val-  
 1338    ues of  $f_{\text{recoil}} (< 0.05)$  and  $p_{T,\text{rel}}^{\text{miss(trk)}}$  values greater than 45 GeV.

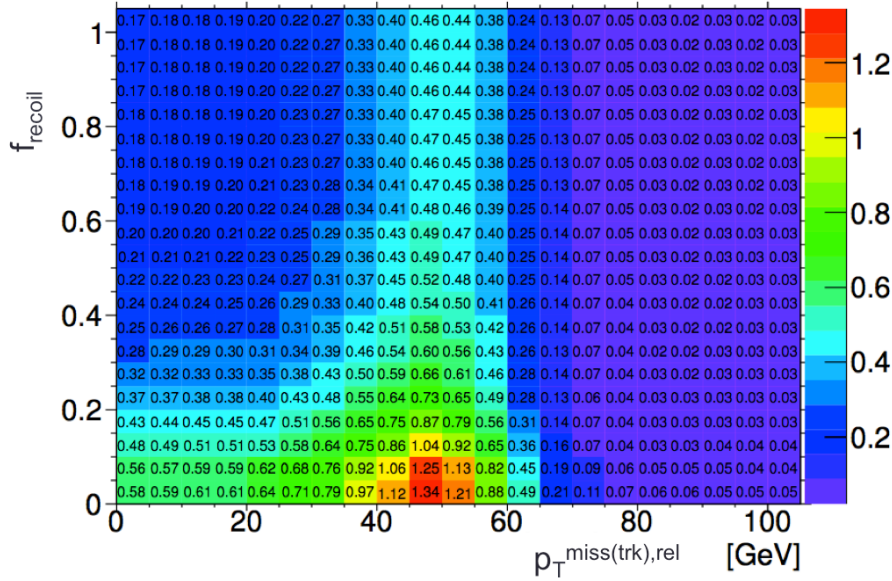


Figure 3.13: Signal significance as a function of required value for  $f_{\text{recoil}}$  and  $p_{T,\text{rel}}^{\text{miss(trk)}}$  in the ggF  $H \rightarrow WW^*$  with  $n_j = 0$

1339    3.6    PARAMETERS OF INTEREST AND STATISTICAL TREATMENT

1340    As with any search or measurement, there are particular parameters of the Higgs that the  $H \rightarrow WW^*$   
 1341    analysis is interested in measuring. In this case, the parameters of interest are the mass of the Higgs bo-  
 1342    son and its production cross section. Because the  $H \rightarrow WW^* \rightarrow \ell\nu\ell\nu$  process does not have a closed  
 1343    final state, it is not possible to measure the full invariant mass of the particle that may have produced  
 1344    the final state. However, a proxy for the invariant mass using transverse plane information can be de-

1345 fined. This is described in more detail in section 3.6.1. The second parameter of interest is the ratio of the  
 1346 measured cross section to that expected from the Standard Model Higgs, which is denoted a  $\mu$ . This is  
 1347 defined in equation 3.5.

$$\mu = \frac{\sigma}{\sigma_{\text{SM}}} \quad (3.5)$$

1348 All of the likelihoods used in the statistical analysis of the final signal region events are paramaterized  
 1349 as a function of  $\mu$ .  $\mu$  is a natural variable for hypothesis testing, as  $\mu = 0$  corresponds to a background  
 1350 only hypothesis and  $\mu = 1$  corresponds exactly to a Standard Model Higgs.

### 1351 3.6.1 TRANSVERSE MASS

1352 Because the longitudinal information about the neutrinos is not attainable, the  $H \rightarrow WW^* \rightarrow \ell\nu\ell\nu$   
 1353 analysis uses a mass variable, the transverse mass, that exploits information in the transverse plane as a  
 1354 proxy for the full invariant mass. The transverse mass is defined in equation 3.6.

$$m_T = \sqrt{(E_T^{\ell\ell} + p_T^{\text{miss}})^2 - |\mathbf{p}_T^{\ell\ell} + \mathbf{p}_T^{\text{miss}}|^2}, \quad (3.6)$$

1355 Here the  $E_T^{\ell\ell}$  and  $p_T^{\ell\ell}$  are the transverse energy and momentum of the dilepton system, while  $p_T^{\text{miss}}$  is  
 1356 a proxy for the transverse momentum of the di-neutrino system. The track-based  $p_T^{\text{miss}}$  is used in the  $m_T$   
 1357 rather than the calorimeter based  $E_T^{\text{miss}}$  because it has a better resolution on the true transverse mass.  
 1358 Figure 3.11b shows the improvement in the RMS of the difference between the true and reconstructed  
 1359 transverse mass in a ggF signal sample. The RMS improves by 4.7 GeV using  $p_T^{\text{miss}}$  in the  $m_T$  calcula-  
 1360 tion.

1361    3.6.2 STATISTICAL TREATMENT<sup>\*</sup>

1362    LIKELIHOOD FUNCTION

1363    The statistical analysis of final event candidates is framed as a hypothesis test, where the null hypothe-  
1364    sis is background-only (no Standard Model Higgs). The first step in the analysis is to form a likelihood  
1365    function for the data. In its simplest form, this likelihood is the probability of observing the number  
1366    of events seen in the final signal region given knowledge of the signal strength. Because observation of  
1367    events is fundamentally a Poisson counting experiment, this simple likelihood can be expressed as a Pois-  
1368    son probability of observing  $N$  events given a total number of predicted signal and background events.  
1369    This basic likelihood is shown in equation 3.7.

$$\mathcal{L}(\mu) = P(N|\mu S + B) \quad (3.7)$$

1370    Here,  $P$  is the Poisson probability density function,  $N$  is the total number of observed events,  $\mu$  is  
1371    the signal strength,  $S$  is the predicted number of signal events, and  $B$  is the predicted number of back-  
1372    ground events.

1373    In particle physics, certain background estimates are commonly normalized in so-called “control” re-  
1374    gions and those predictions are scaled by the same normalization factor in the signal region. This leads  
1375    to a slightly more complicated likelihood, which is a function of both the signal strength and the back-  
1376    ground normalization. This is shown in equation 3.8.

$$\mathcal{L}(\mu, \theta) = P(N|\mu S + \theta B) P(N_{\text{CR}}|\theta B_{\text{CR}}) \quad (3.8)$$

1377    Here,  $\theta$  is a so-called “nuisance parameter”, a parameter that is not a primary parameter of interest but  
1378    still enters the likelihood. The second Poisson term adds an extra term to the likelihood, enforcing the  
1379    fact that the background normalization must be consistent with the number of observed events in data  
1380    in the control region,  $N_{\text{CR}}$ .

1381    So far, these two formulations of likelihoods have assumed a single signal region and do not take into

---

\*Many thanks to Aaron Armbruster, whose thesis[69] inspired parts of this section.

1382 account any shape information of potential discriminating variables. The  $H \rightarrow WW^*$  analysis is di-  
 1383 vided into many different categories, and we can perform the same counting experiment described above  
 1384 in each individual category. As mentioned in section 3.6.1, the transverse mass is used as the primary dis-  
 1385 criminating variable in many of the  $H \rightarrow WW^*$  sub-analyses, so additionally we can perform the same  
 1386 counting experiment in each bin of the  $m_T$  distribution to incorporate some shape information. Thus,  
 1387 the total likelihood becomes a product over signal regions and bins of the  $m_T$  distribution. Finally, there  
 1388 are usually many backgrounds that are normalized in control regions, so the new formulation of the like-  
 1389 lihood takes this into account as well by including a product over control regions in the second Poisson  
 1390 term. All of these modifications are shown in equation 3.9.

$$\mathcal{L}(\mu, \theta) = \prod_{\substack{\text{SRs } i \\ \text{bins } b}} P\left(N_{ib} \middle| \mu S_{ib} + \sum_{\text{bkg } k} \theta_k B_{kib}\right) \prod_{\text{CRs } l} P\left(N_l \middle| \sum_{\text{bkg } k} \theta_k B_{kl}\right) \quad (3.9)$$

1391 The final step to get the full likelihood used in the analysis is to add nuisance parameters for the sys-  
 1392 tematic uncertainties. In cases where the uncertainty does not affect the shape of  $m_T$  bin-by-bin, each  
 1393 systematic uncertainty  $\epsilon$  is allowed to affect the expected event yields through a linear response function  
 1394 of the nuisance parameter, namely  $\nu(\theta) = (1 + \epsilon)^\theta$ . If instead the uncertainty does affect the shape,  
 1395 the effect is instead parameterized by  $\nu_b(\theta) = 1 + \epsilon_b \theta$ . The value of the nuisance parameters for the  
 1396 systematic uncertainty are constrained with a Gaussian term that is added to the likelihood as well. This  
 1397 is of the form  $g(\delta|\theta) = e^{-(\delta-\theta)^2/2}/\sqrt{2\pi}$ , where  $\delta$  is the central value and  $\theta$  is a nuisance parameter.  
 1398 Finally, a last term is added to account for the statistical uncertainty in the Monte Carlo samples used,  
 1399 which adds an additional poisson term. The full likelihood used in the final statistical analysis is defined

1400 in equation 3.10.

$$\begin{aligned} \mathcal{L}(\mu, \boldsymbol{\theta}) = & \prod_{\substack{\text{SRs i} \\ \text{bins b}}} P\left(N_{ib} \middle| \mu S_{ib} \cdot \prod_{\substack{\text{sig.} \\ r}} \nu_{br}(\theta_r) + \sum_{\text{bkg k}} \theta_k B_{kib} \cdot \prod_{\substack{\text{bkg.} \\ \text{syst.} \\ s}} \nu_{bs}(\theta_s)\right) \\ & \cdot \prod_{\text{CRs l}} P\left(N_l \middle| \sum_{\text{bkg k}} \theta_k B_{kl}\right) \\ & \cdot \prod_{\substack{\text{syst.} \\ t}} g(\delta_t | \theta_t) \cdot \prod_{\text{bkg k}} P(\xi_k | \zeta_k \theta_k) \end{aligned} \quad (3.10)$$

1401 In the fourth term of the equation, quantifying uncertainty due to finite Monte Carlo sample size,  $\xi$   
1402 represents the central value of the background prediction,  $\theta$  is the associated nuisance parameter,  $\zeta =$   
1403  $(B/\delta B)^2$ , where  $\delta B$  is the statistical uncertainty of  $B$ .

1404 The best fit value of the signal strength  $\mu$  is determined by finding the values of  $\mu$  and  $\boldsymbol{\theta}$  that maxi-  
1405 mize the likelihood, while setting  $\delta = 0$  and  $\xi = \zeta$ .

1406 Once the likelihood is defined, a test statistic must be built for use in hypothesis testing.

## 1407 TEST STATISTIC

1408 To distinguish whether the data match a background only or background and signal hypothesis, a test  
1409 statistic must be used. The  $H \rightarrow WW^*$  analysis used the profile likelihood technique[70]. The first step  
1410 in formulating this test statistic is to define the profile likelihood ratio, shown in equation 3.11.

$$\lambda(\mu) = \frac{\mathcal{L}(\mu, \hat{\theta}_\mu)}{\mathcal{L}(\hat{\mu}, \hat{\theta})} \quad (3.11)$$

1411 Here  $\hat{\theta}_\mu$  is the value of  $\theta$  that maximizes the likelihood for the choice of  $\mu$  being tested. Additionally,  
1412  $\hat{\theta}$  and  $\hat{\mu}$  represent the values of  $\theta$  and  $\mu$  that gives the overall maximum value of the likelihood.

1413 Once this is defined, a test statistic  $q_\mu$  is constructed. This is shown in equation 3.12.

$$q_\mu = -2 \ln \lambda(\mu) \quad (3.12)$$

<sub>1414</sub> A higher value of  $q_\mu$  means that the data are more incompatible with the hypothesized value of  $\mu$ , and  
<sub>1415</sub>  $q_0$  then corresponds to the value of the test statistic for the background only hypothesis. A  $p_0$  value is  
<sub>1416</sub> then defined to quantify the compatibility between the data and the null hypothesis. The  $p_0$  value is the  
<sub>1417</sub> probability of obtaining a value of  $q_0$  larger than the observed value, and this is shown in equation 3.13.

$$p_0 = \int_{q_0^{\text{obs}}}^{\infty} f(q_\mu | \mu = 0) dq_\mu \quad (3.13)$$

<sub>1418</sub> Here  $f(q_\mu)$  is the probability distribution function of the test statistic. Finally, the  $p_0$  value can be  
<sub>1419</sub> converted into a signal significance, using the formula in equation 3.14, or the one-sided tail of the Gaus-  
<sub>1420</sub> sian distribution.

$$Z_0 = \sqrt{2} \operatorname{erf}^{-1}(1 - 2p_0) \quad (3.14)$$

<sub>1421</sub> The threshold for discovery used in particle physics is  $Z_0 \geq 5$ , more commonly known as a value of  
<sub>1422</sub>  $5\sigma$ .

*The real voyage of discovery consists not in seeking new landscapes, but in having new eyes.*

Marcel Proust

# 4

1423

1424

1425

## The discovery of the Higgs boson and the role of the $H \rightarrow WW^* \rightarrow \ell\nu\ell\nu$ channel

1426 4.1 INTRODUCTION

1427 This chapter presents the results of the search for the Higgs boson in  $4.8 \text{ fb}^{-1}$  collected at  $\sqrt{s} = 7 \text{ TeV}$   
1428 and  $5.8 \text{ fb}^{-1}$  at  $\sqrt{s} = 8 \text{ TeV}$ . The results of three searches at  $\sqrt{s} = 8 \text{ TeV}$  in the  $H \rightarrow WW^* \rightarrow \ell\nu\ell\nu$   
1429 ,  $H \rightarrow \gamma\gamma$ , and  $H \rightarrow ZZ \rightarrow 4\ell$  channels are combined with results of searches at  $\sqrt{s} = 7 \text{ TeV}$   
1430 in the same search channels (as well as the  $H \rightarrow \tau\tau$  production and associated production searches for  
1431  $H \rightarrow b\bar{b}$ ). The results of this combination are a  $5.9\sigma$  detection of a new particle consistent with a Higgs  
1432 boson. Rather than going into detail for all of the different Higgs decay searches, this chapter will discuss  
1433 the three most sensitive channels and in particular focus on  $H \rightarrow WW^* \rightarrow \ell\nu\ell\nu$ . While the focus is  
1434 on  $WW^*$ , some of the  $ZZ^*$  and  $\gamma\gamma$  results are shown for completeness. The results not discussed here

1435 can be found in the ATLAS Higgs discovery publication[[22](#)].

1436 **4.2 DATA AND SIMULATION SAMPLES**

1437 The data sample used for the following results was taken in 2011 and 2012 at center of mass energies of 7  
1438 and 8 TeV, respectively, with  $4.8 \text{ fb}^{-1}$  collected at 7 TeV and  $5.8 \text{ fb}^{-1}$  collected at 8 TeV. Higgs pro-  
1439 duction in the gluon fusion and vector boson fusion modes is modeled with **POWHEG** for the hard scat-  
1440 tering event and **PYTHIA** for the showing and hadronization. Associated production of a Higgs with a  
1441 vector boson or top quarks is modeled via **PYTHIA**.

1442 Table 4.1 shows the Monte Carlo generators used for modeling the signal and background processes  
1443 relevant for the three analyses to be discussed.

Process	Generator
$\text{ggF}, \text{VBF } H$	<b>POWHEG + PYTHIA</b>
$WH, ZH, t\bar{t}H$	<b>PYTHIA</b>
$W + \text{jets}, Z/\gamma^* + \text{jets}$	<b>ALPGEN + HERWIG</b>
$t\bar{t}, tW, tb$	<b>MC@NLO + HERWIG</b>
$tqb$	<b>ACERMC + PYTHIA</b>
$q\bar{q} \rightarrow WW$	<b>MC@NLO + HERWIG</b>
$gg \rightarrow WW$	<b>GG2WW+ HERWIG</b>
$q\bar{q} \rightarrow ZZ$	<b>POWHEG + PYTHIA</b>
$gg \rightarrow ZZ$	<b>GG2ZZ+ HERWIG</b>
$WZ$	<b>MADGRAPH+ PYTHIA , HERWIG</b>
$W\gamma + \text{jets}$	<b>ALPGEN + HERWIG</b>
$W\gamma^*$	<b>MADGRAPH+ PYTHIA</b>
$q\bar{q}/gg \rightarrow \gamma\gamma$	<b>SHERPA</b>

**Table 4.1:** Monte carlo generators used to model signal and background for the Higgs search[[22](#)].

1444 **4.3  $H \rightarrow WW \rightarrow e\nu\mu\nu$  SEARCH**

1445 The  $H \rightarrow WW \rightarrow e\nu\mu\nu$  search is unique compared to the  $ZZ$  and  $\gamma\gamma$  channels. The Higgs mass can-  
1446 not be fully reconstructed due to the presence of neutrinos in the final state, so the transverse mass  $m_T$   
1447 is used as the final discriminating variable. Compared to the other channels, there are more backgrounds

1448 here as well, as discussed in chapter 3. The same flavor final states are excluded from this search due to  
1449 high pileup in the 8 TeV dataset.

1450 4.3.1 EVENT SELECTION

1451 The analysis requires two opposite charge isolated leptons, with the leading (sub-leading) lepton required  
1452 to have  $p_T > 25(15)$  GeV. The events are separated into different signal regions depending on which  
1453 flavor of lepton is leading ( $e\mu$  for leading electron,  $\mu e$  for leading muon). Strict lepton quality cuts are  
1454 applied to the sample to reduce backgrounds from fake leptons.

1455 Jets are reconstructed with the anti- $k_T$  algorithm with a radius parameter  $R = 0.4$ . The jets are  
1456 required to have  $p_T > 25$  GeV and  $|eta| < 4.5$ , with jets in the tracking volume required to have a  
1457 jet vertex fraction of 0.5 and jets in the forward region required to have  $p_T > 30$  GeV. The analysis is  
1458 separated into three different signal regions based on jet multiplicity:  $n_j = 0, 1, \geq 2$ .

1459 To indicate the presence of neutrinos in the event, a requirement of  $E_{T,\text{rel}}^{\text{miss}} > 25$  GeV is made\*. This  
1460 requirement significantly reduces the QCD multijet and  $Z/\gamma^*$  + jets backgrounds. Figure 4.1 shows the  
1461 distribution of  $n_j$  in data and simulation after applying these “pre-selection” requirements.

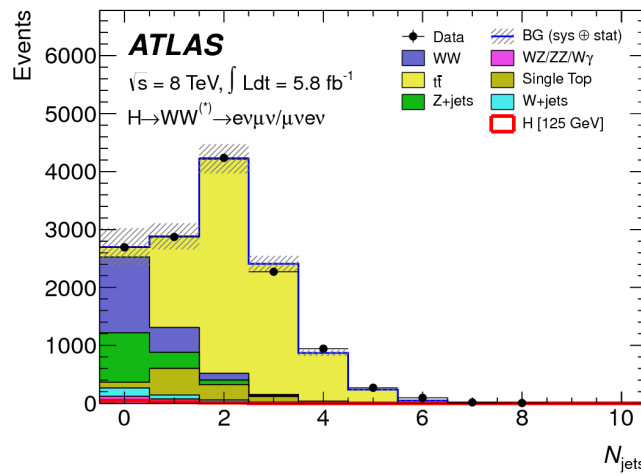


**Figure 4.1:** Jet multiplicity distribution in data and MC after applying lepton, jet, and  $E_{T,\text{rel}}^{\text{miss}}$  selections. The  $WW$  and top backgrounds have been normalized using control samples, and the hashed band indicates the total uncertainty on the prediction. [22]

\*For the definition of  $E_{T,\text{rel}}^{\text{miss}}$ , see chapter 3

1462     Additional selections are applied to require the dilepton topology to correspond to that of a SM  
1463     Higgs. The requirements are presented here - more detailed discussion on the motivation for each re-  
1464     quirement is saved for Chapter 5. In all of the jet multiplicity channels, the dilepton system is required to  
1465     have a small gap in azimuthal angle,  $\Delta\phi_{\ell\ell} < 1.8$ . Similarly, the  $m_{\ell\ell}$  is required to be less than 50 GeV  
1466     in the lower jet multiplicity channels and less than 80 GeV in the  $n_j \geq 2$  channel. In the  $n_j = 0$   
1467     channel, the magnitude of the dilepton  $p_T$ ,  $p_T^{\ell\ell}$ , is required to be greater than 30 GeV.

1468     In the higher jet multiplicity channels ( $n_j \geq 1$ ), the top background is a more important component  
1469     and must be reduced. The total transverse momentum  $p_T^{\text{sum}}$  is thus required to be less than 30 GeV.  
1470     Additionally, the di- $\tau$  invariant mass  $m_{\tau\tau}$  (dilepton mass computed under the assumption that the neu-  
1471     trinos from the  $\tau$  decay are emitted collinear to the charged leptons) is used to reject  $Z \rightarrow \tau\tau$  events by  
1472     requiring  $|m_{\tau\tau} - m_Z| > 25$  GeV. These variables are also discussed in more detail in Chapter 5.

1473     In the  $n_j \geq 2$  channel, requirements are made to isolate the VBF contribution to Higgs production.  
1474     The kinematics of the two leading jets are used to make these requirements. In particular, the event must  
1475     have  $\Delta y_{jj} > 3.8$  and  $m_{jj} > 500$  GeV, along with a veto on having any additional jets with rapidity  
1476     between the two leading jets.

#### 1477     4.3.2 BACKGROUND ESTIMATION

1478     The details of the background estimation techniques used in the  $H \rightarrow WW^* \rightarrow \ell\nu\ell\nu$  analysis are dis-  
1479     cussed in section 5.5. As that section refers to a later iteration of the analysis, a general discussion is given  
1480     here for completeness. The dominant backgrounds are SM  $WW$  production and top (both pair and  
1481     single) production, and these backgrounds have their normalizations estimated from dedicated control  
1482     regions while their shapes are taken from simulation.

1483     The control sample for the Standard Model  $WW$  background is defined by making the same require-  
1484     ments as the signal region with the  $m_{\ell\ell}$  requirement inverted (now requiring  $m_{\ell\ell} > 80$  GeV) and  
1485     removing the  $\Delta\phi_{\ell\ell}$  requirement. This creates a control sample that is 70% (40%) pure in the 0(1)-jet  
1486     region. The correction to the pure MC-based background estimate is quantified by defining a normal-  
1487     ization factor  $\beta$  which is the ratio of the data yield to the MC yield ( $N_{\text{data}}/N_{\text{MC}}$ ) in this control sample.

1488 Table 4.2 shows the  $WW$  normalization factors in the  $n_j = 0$  and  $n_j = 1$  bins (the  $n_j \geq 2$  estimate is  
 1489 taken directly from MC).

$n_j$	$\beta_{WW}$	$\beta_t$
= 0	$1.06 \pm 0.06$	$1.11 \pm 0.06$
= 1	$0.99 \pm 0.15$	$1.11 \pm 0.05$
$\geq 2$	-	$1.01 \pm 0.26$

**Table 4.2:** Normalization factors (ratio of data and MC yields in a control sample) for the Standard Model  $WW$  and top backgrounds in the  $H \rightarrow WW^* \rightarrow \ell\nu\ell\nu$  analysis [22]. Only statistical uncertainties are shown.

1490 The top background estimate is also computed separately in each jet multiplicity bin. In the  $n_j = 0$   
 1491 channel, the background is first normalized using data after pre-selection requirements with no selection  
 1492 on  $n_j$ . Then, a dedicated  $b$ -tagged control sample is used to evaluate the ratio of one-jet to two-jet events  
 1493 in data. The details of this technique are shown in reference [71]. In the  $n_j = 1$  and the  $n_j \geq 2$  regions,  
 1494 the top background is normalized in a control sample where the signal region selections are applied,  
 1495 but the  $b$ -jet veto is reversed and the Higgs topology requirements on  $m_{\ell\ell}$  and  $\Delta\phi_{\ell\ell}$  are removed. The  
 1496 resulting normalization factors for these techniques are shown in table 4.2.

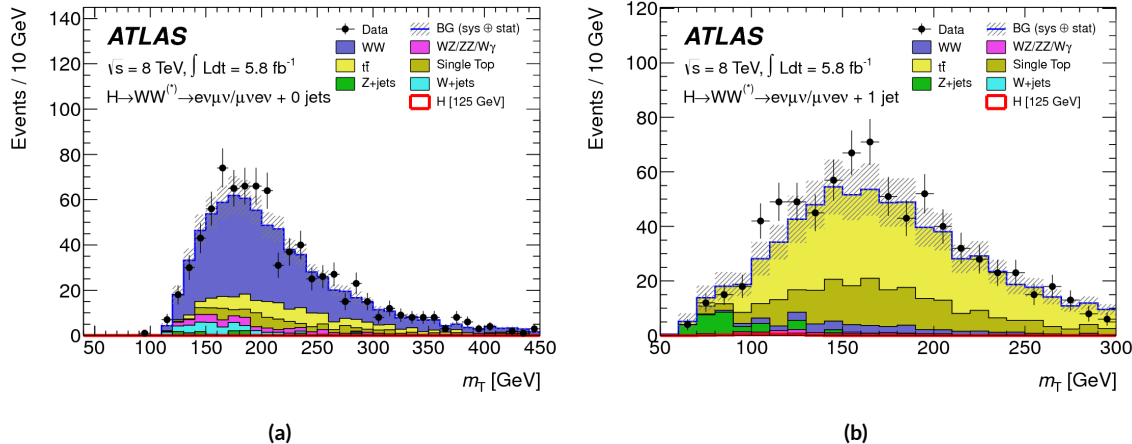


**Figure 4.2:** Comparison of  $m_T$  between data and simulation in the  $n_j = 0$   $WW$  (a) and  $n_j = 1$  top (b) control samples [22]

1497 The control samples which are used for background normalization can also be used to validate the  
 1498 modeling of the  $m_T$  distribution for each background. Figure 4.2 shows the comparison between data

1499 and MC for the  $m_T$  distribution after correcting the normalization of the backgrounds in the  $WW$  and  
1500 top control regions. Good agreement between data and simulation is seen in both cases.

1501 The  $W + \text{jets}$  background estimate is taken entirely from data using a control sample with one well  
1502 reconstructed lepton and one anti-identified lepton. All other backgrounds are taken purely from simu-  
1503 lation.

#### 1504 4.3.3 SYSTEMATIC UNCERTAINTIES

1505 The systematic uncertainties that have the largest impact on the analysis are the theoretical uncertainties  
1506 associated with the signal cross section, and these are shared with the  $ZZ^*$  and  $\gamma\gamma$  channels. The un-  
1507 certainties resulting from variations of the QCD scale are  $+7\% / -8\%$  on the final singal yield. Those  
1508 coming from variations of the parton distribution function (PDF) used in the simulation add a  $\pm 8\%$   
1509 uncertainty on the yield. The uncertainties on the branching ratios of the Higgs are  $\pm 5\%$ .

1510 The main experimental uncertainties come from variations of the jet energy scale (JES), jet energy  
1511 resolution, pile-up,  $E_T^{\text{miss}}$ ,  $b$ -tagging efficiency,  $W + \text{jets}$  background estimate, and integrated luminosity.  
1512 For more details, see reference [22].

#### 1513 4.3.4 RESULTS

1514 Table 4.3 shows the signal and background yields in the final signal region after normalizing the back-  
1515 grounds according to the methods described above.

	$n_j = 0$	$n_j = 1$	$n_j \geq 2$
Signal	$20 \pm 4$	$5 \pm 2$	$0.34 \pm 0.07$
$WW$	$101 \pm 13$	$12 \pm 5$	$0.10 \pm 0.14$
Other dibosons	$12 \pm 3$	$1.9 \pm 1.1$	$0.10 \pm 0.10$
$t\bar{t}$	$8 \pm 2$	$6 \pm 2$	$0.15 \pm 0.10$
Single top	$3.4 \pm 1.5$	$3.7 \pm 1.6$	-
$Z/\gamma^* + \text{jets}$	$1.9 \pm 1.3$	$0.10 \pm 0.10$	-
$W + \text{jets}$	$15 \pm 7$	$2 \pm 1$	-
Total background	$142 \pm 16$	$26 \pm 6$	$0.35 \pm 0.18$
Observed in data	185	38	0

**Table 4.3:** Data and expected yields for signal and background in the final  $H \rightarrow WW^* \rightarrow \ell\nu\ell\nu$  signal region.  
Uncertainties shown are both statistical and systematic. [22]

1516      Figure 4.3 shows the  $m_T$  distribution in the  $n_j \leq 1$  channels for 8 TeV data. (No events are observed  
 1517      in data in the  $n_j \geq 2$  channels in this dataset). The excess shown here relatively flat as a function of  
 1518      hypothesized Higgs mass. The combined 7 and 8 TeV data gives an excess with local significance of  $2.8\sigma$   
 1519      with an expected significance of  $2.3\sigma$ , corresponding to a  $\mu$  measurement of  $1.3 \pm 0.5$ .

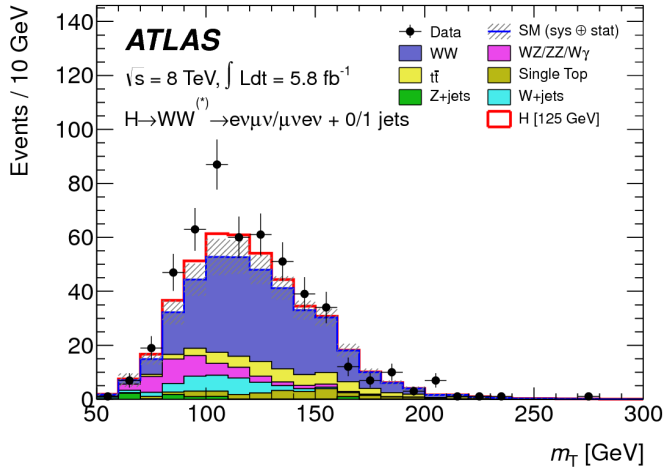


Figure 4.3:  $m_T$  distribution in the  $H \rightarrow WW \rightarrow e\nu\mu\nu$   $n_j \leq 1$  channels for 8 TeV data[22].

#### 1520    4.4    $H \rightarrow \gamma\gamma$ SEARCH

1521    The  $H \rightarrow \gamma\gamma$  search is in essence a search for a peaked excess above the falling SM diphoton mass spec-  
 1522    trum, with  $m_{\gamma\gamma}$  as the ultimate discriminating variable. Events are selected by requiring two isolated  
 1523    photons, with the leading (sub-leading) photon required to have  $E_T > 40(30)$  GeV. In the 8 TeV  
 1524    data, the photons are required to pass cut-based identification criteria consistent with a photon in the  
 1525    electromagnetic calorimeter and little leakage in the hadronic calorimeter.

1526    The main challenges for this analysis are accurate mass reconstruction and background estimation.  
 1527    In order to accurately reconstruct the invariant mass of the di-photon system, both the energy and di-  
 1528    rection of the photons must be measured well. Therefore, the identification of the primary vertex of the  
 1529    hard interaction is particularly important, and is done using a multivariate likelihood which combines  
 1530    information about the photon direction and vertex position. The background is modeled with a falling  
 1531    spectrum in  $m_{\gamma\gamma}$  that is parameterized by different functions depending on the category of the event.

1532 4.4.1 RESULTS

1533 The resulting diphoton mass spectrum is shown in figure 4.4. The best fit mass value in the  $\gamma\gamma$  channel  
 1534 alone in the combined 7 and 8 TeV data is 126.5 GeV. The local significance at this point is  $4.5\sigma$ , with  
 1535 an expected significance of  $2.5\sigma$ . Therefore, the measured signal strength  $\mu$  is  $1.8 \pm 0.5$  in this channel.

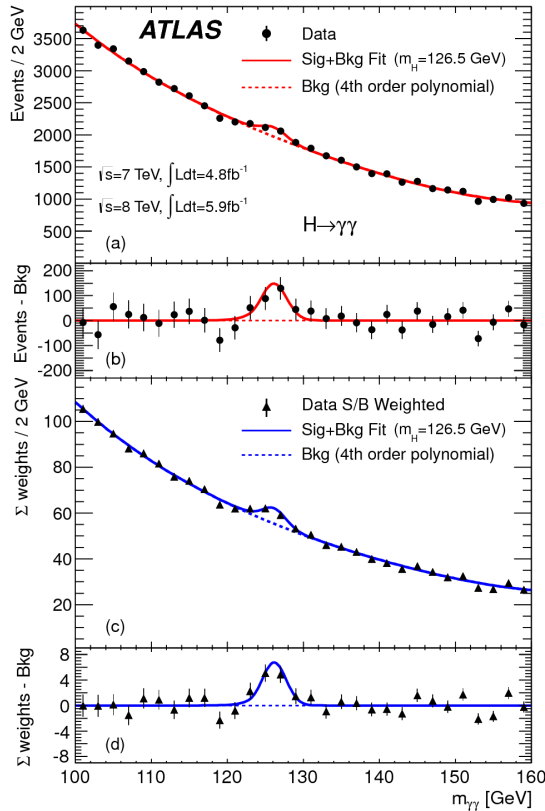


**Figure 4.4:** Diphoton mass spectrum in 7 and 8 TeV data. Panel a) shows the unweighted data distribution superimposed on the background fit, while panel c) shows the data where each event category is weighted by its signal to background ratio. Panels b) and d) show the respective distributions with background subtracted[22].

1536 4.5  $H \rightarrow ZZ \rightarrow 4\ell$  SEARCH

1537 The  $H \rightarrow ZZ \rightarrow 4\ell$  analysis searches for a Standard Model Higgs boson decaying to two  $Z$  bosons,  
 1538 each of which decays to a pair of same flavor, opposite charge isolated leptons. The ultimate discriminat-  
 1539 ing variable is  $m_{4\ell}$ , or the invariant mass of the four selected leptons. The  $\ell$  denotes an  $e$  or  $\mu$  as with the  
 1540  $H \rightarrow WW^* \rightarrow \ell\nu\ell\nu$  analysis.

1541 Four distinct signal regions are constructed depending on the flavors of the final state, additionally  
 1542 separated by the flavor of the leading lepton pair. These are referred to as  $4e$ ,  $2e2\mu$ ,  $2\mu2e$ ,  $4\mu$ .

1543 The main backgrounds in the  $H \rightarrow ZZ \rightarrow 4\ell$  search are continuum  $ZZ^*$  production,  $Z +$  jets pro-  
 1544 duction, and  $t\bar{t}$ . The  $m_{4\ell}$  distribution for background is estimated from simulation. The normalization  
 1545 of the SM  $ZZ^*$  background is also taken from MC simulation, while the  $Z +$  jets and  $t\bar{t}$  normalizations  
 1546 are taken from data-driven methods.

#### 1547 4.5.1 RESULTS

1548 Figure 4.5 shows the  $m_{4\ell}$  spectrum measured in the 7 and 8 TeV datasets. The total number of events  
 1549 observed in the window between 120 and 130 GeV is 13, with 6 events in the  $4\mu$  channel, 2 events in  
 1550 the  $4e$  channel, and 5 events in the  $2e2\mu/2\mu2e$ . The best fit  $\mu$  value in the combined 7 and 8 TeV data  
 1551 occurs at 125 GeV and is measured to be  $1.2 \pm 0.6$ . The observed significance at this mass is  $3.6\sigma$ , with  
 1552 an expected significance of  $2.7\sigma$ .

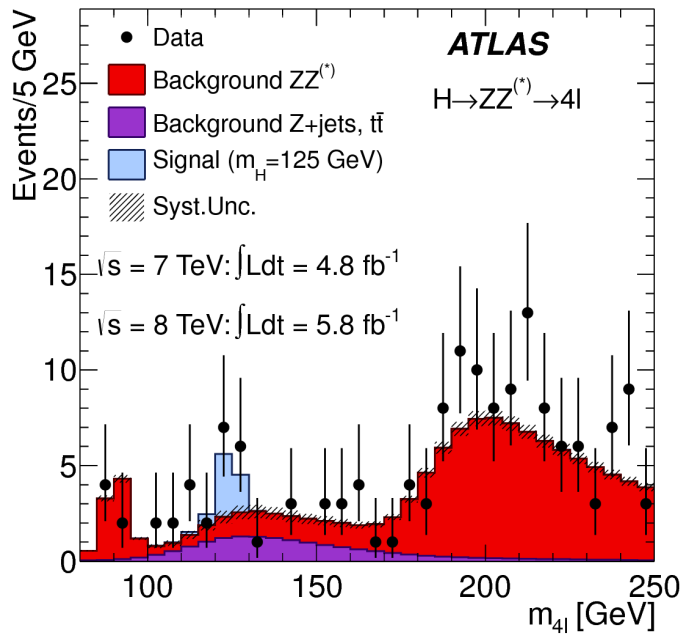


**Figure 4.5:** Four lepton invariant mass spectrum ( $m_{4\ell}$ ) in 7 and 8 TeV data compared to background estimate. A 125 GeV SM Higgs signal is shown in blue[22].

1553    4.6 COMBINED RESULTS

1554    The statistical interpretation of the combined results is undertaken as described in section 3.6.2, with a  
 1555    hypothesis test based on a likelihood ratio parameterized by the Higgs signal strength  $\mu$ . The null hy-  
 1556    pothesis corresponds to  $\mu = 0$ , while the SM Higgs corresponds to  $\mu = 1$ .

1557    Table 4.4 summarizes the properties of the individual channels as well as the significances of the ex-  
 1558    cesses seen. The most significant observed local excess comes from the  $\gamma\gamma$  channel. Figure 4.6 shows a  
 1559    comparison of the observed local  $p_0$  values as a function of hypothesized mass for the three different  
 1560    search channels. Both the  $ZZ^*$  and  $\gamma\gamma$  channels have very peaked excesses, while the  $WW^*$  excess can  
 1561    be seen as very broad because the  $m_T$  distribution does not provide detailed information about the true  
 1562    Higgs mass.

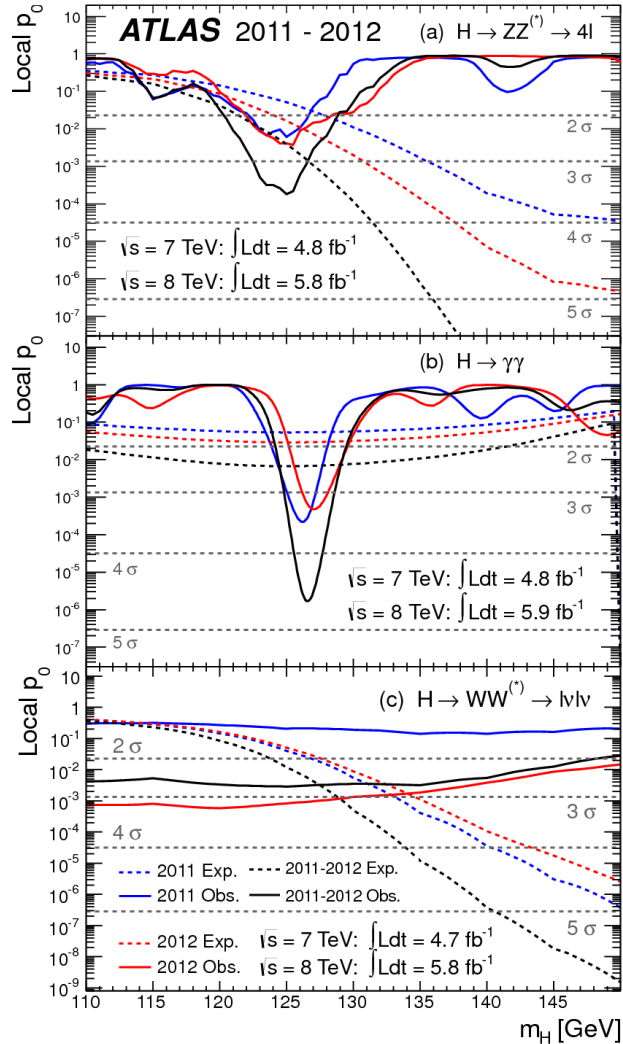
Channel	Fit var.	Observed $Z_l$	Expected $Z_l$	$\hat{\mu}$
$H \rightarrow ZZ^* \rightarrow 4\ell$	$m_{4\ell}$	3.6	2.7	$1.2 \pm 0.6$
$H \rightarrow \gamma\gamma$	$m_{\gamma\gamma}$	4.5	2.5	$1.8 \pm 0.5$
$H \rightarrow WW^* \rightarrow e\nu\mu\nu$	$m_T$	2.8	2.3	$1.3 \pm 0.5$
Combined	-	6.0	4.9	$1.4 \pm 0.3$

Table 4.4: Summary of the expected and observed significance and measured signal strengths in the combined 7 and 8 TeV datasets for the Higgs discovery analysis[22].

1563    Figure 4.7 shows the combined exclusion limit,  $p_0$ , and signal strength. The highest local excess comes  
 1564    at a value of 126.5 GeV and corresponds to a  $6.0\sigma$  observed excess.

1565    Figure 4.8 shows a comparison of the measured signal strengths between the different Higgs search  
 1566    channels. All measured  $\mu$  are consistent with unity within their uncertainty, and the combined  $\mu$  mea-  
 1567    surement is  $1.4 \pm 0.3$ .

1568    The likelihood can also be computed in a two-dimensional plane of  $m_H$  and  $\mu$ , and this is shown in  
 1569    figure 4.9. The figure shows that while the  $\gamma\gamma$  and  $ZZ^*$  channels have very good mass resolution, the  
 1570    excess in  $WW^*$  covers a broad mass range. The banana shape of the  $WW^*$  result is due to the fact that  
 1571    the excess in this channel can either be explained by increasing the signal strength or by changing the  
 1572    mass (and thus the cross section). The two parameters are correlated due to the lack of mass sensitivity in  
 1573    this channel.



**Figure 4.6:** Local  $p_0$  distribution as a function of hypothesized Higgs mass for the  $H \rightarrow ZZ^* \rightarrow 4\ell$  (a),  $H \rightarrow \gamma\gamma$  (b), and  $H \rightarrow WW^* \rightarrow \ell\nu\ell\nu$  (c) channels. Dashed curves show expected results, while solid curves show observed. Red curves are from 7 TeV data, blue curves from 8 TeV, and black curved combined[22].

Because multiple Higgs mass points are searched for, the local significance must be corrected for a look-elsewhere effect to compute a true global significance. The global significance for finding a Higgs anywhere in the mass range of 110 GeV to 600 GeV is  $5.1\sigma$ . This increases slightly to  $5.3\sigma$  if only mass range from 110 to 150 GeV.

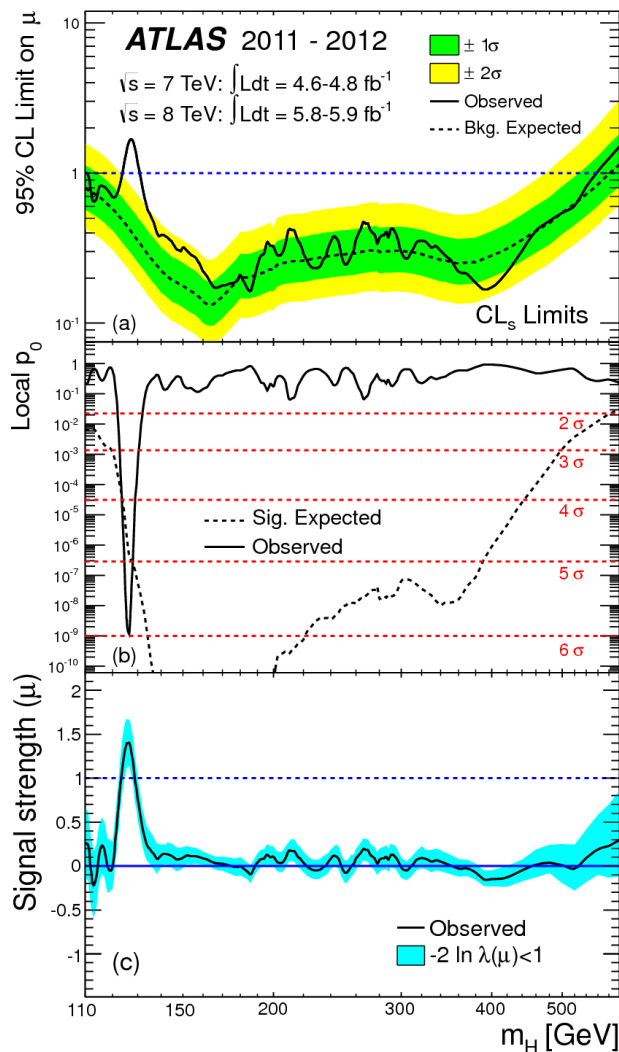


**Figure 4.7:** Combined 95% CL limits (a), local  $p_0$  values (b), and signal strength measurement (c) as a function of Higgs mass[22].

1578    4.7 CONCLUSION

1579    A search for the production of a Standard Model Higgs boson was conducted in  $4.8 \text{ fb}^{-1}$  collected at  
 1580     $\sqrt{s} = 7 \text{ TeV}$  and  $5.8 \text{ fb}^{-1}$  at  $\sqrt{s} = 8 \text{ TeV}$ . A new particle consistent with the Higgs boson was  
 1581    observed, with a mass of  $126.5 \text{ GeV}$  and a global (local) significance of  $5.1(6.0)\sigma$ . This is the first dis-  
 1582    covery level observation of a particle consistent with the Higgs.

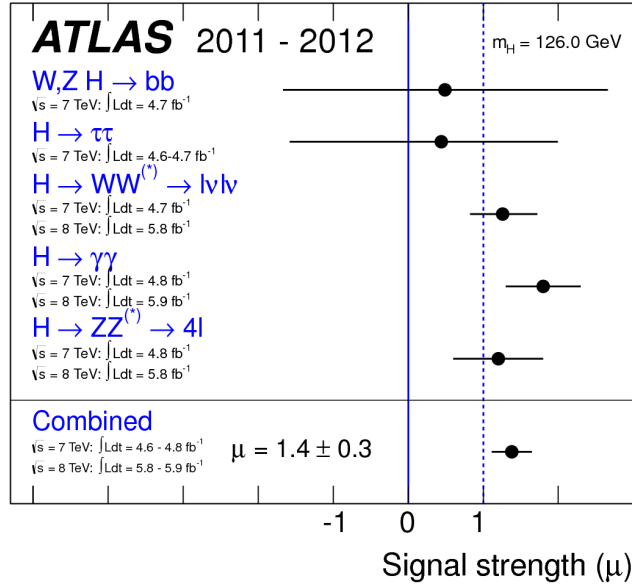


**Figure 4.8:** Comparison of measured signal strength  $\mu$  for a 126 GeV Higgs in the 7 and 8 TeV datasets[22].

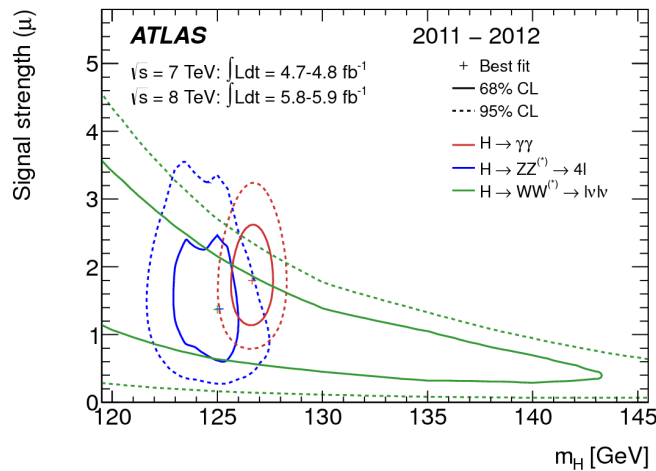


**Figure 4.9:** Two dimensional likelihood as a function of signal strength  $\mu$  and Higgs mass  $m_H$ [22].

*The imagination of nature is far, far greater than the  
imagination of man.*

Richard Feynman

# 5

1583

1584

## Observation of Vector Boson Fusion

1585

production of  $H \rightarrow WW^* \rightarrow \ell\nu\ell\nu$

1586 5.1 INTRODUCTION

1587 After the discovery of a particle consistent with the Higgs boson, the  $H \rightarrow WW^*$  analysis had two main  
1588 goals. The first goal was to increase the sensitivity of the analysis to fully confirm that the  $H \rightarrow WW^*$   
1589 process did indeed exist. The second goal was to characterize the particle as much as possible, including  
1590 searching for the lower cross-section production modes, in order to confirm that it was indeed a Higgs  
1591 boson. This chapter presents a dedicated search for Vector Boson Fusion (VBF) production of a Higgs  
1592 boson decaying via the  $H \rightarrow WW^* \rightarrow \ell\nu\ell\nu$  mode. First, basics of the topology of VBF production  
1593 are presented. Then, the details of the analysis are shown, including signal region definition, background  
1594 estimation techniques, and systematic uncertainties. Finally, the results of the analysis are presented. As

1595 will be shown, this analysis is the first and most sensitive observation of the VBF production mode of the  
1596 Higgs on ATLAS.

1597 In the VBF channel, there are both a selection requirement based signal region analysis (known as the  
1598 “cut-based”) and a multivariate analysis which uses a boosted decision tree (known as the BDT analysis).  
1599 The focus of this chapter will be on the cut-based signal region, as this is an important component of the  
1600 VBF analysis and in particular acts as strong validation for the final BDT result. Connections between  
1601 the cut-based and BDT analyses will be discussed where appropriate.

## 1602 5.2 DATA AND SIMULATION SAMPLES

1603 The results presented here are with  $20.3 \text{ fb}^{-1}$  taken at  $\sqrt{s} = 8 \text{ TeV}$  and  $4.5 \text{ fb}^{-1}$  taken at  $\sqrt{s} = 7 \text{ TeV}$ .  
1604 The details of the LHC and detector conditions during this period are given in Chapter 2. The trigger  
1605 selection defining the dataset is discussed in section 5.2.1. The simulation samples used for signal and  
1606 background modeling are given in section 5.2.2.

### 1607 5.2.1 TRIGGERS

1608 The analysis uses a combination of single lepton and dilepton triggers to allow lowering of the  $p_T$  thresh-  
1609 olds and increased signal acceptance. The  $p_T$  threshold on the leptons is a particularly important consid-  
1610 eration for this signal. Because the second  $W$  produced in the decay can be off-shell, it tends to pro-  
1611 duce lower momentum leptons. Thus, being able to lower the  $p_T$  threshold while still maintaining  
1612 a low background rate is critical. Figure 5.1 shows an example of the subleading lepton  $p_T$  for a VBF  
1613  $H \rightarrow WW^*$  signal compared to the corresponding  $t\bar{t}$  background. Note that the lepton  $p_T$  spectrum is  
1614 considerably softer in the signal sample.

1615 As discussed in Chapter 2, there are multiple levels in the ATLAS trigger system, and there are differ-  
1616 ent  $p_T$  thresholds imposed for the leptons at each level. Additionally, some triggers have a loose selection  
1617 on the isolation of the lepton (looser than that applied offline in the analysis object selection). Table 5.1  
1618 shows the thresholds used for single lepton triggers, while table 5.2 shows the thresholds coming from  
1619 di-lepton triggers. The single lepton trigger efficiency for muons that pass the analysis object selection is

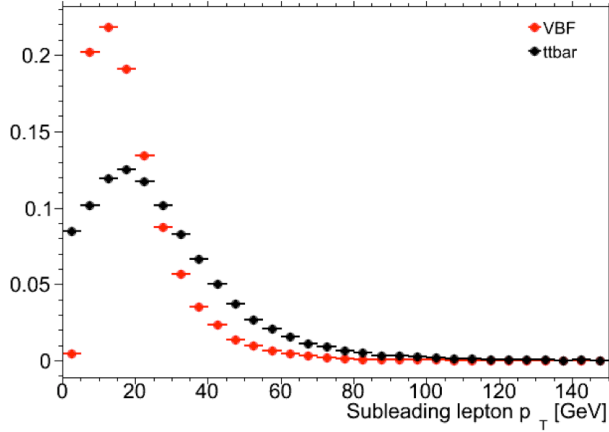


**Figure 5.1:** A comparison of the subleading lepton  $p_T$  spectrum between VBF  $H \rightarrow WW^*$  production and  $t\bar{t}$  background

1620 70% for muons in the barrel region ( $|\eta| < 1.05$ ) and 90% in the endcap region. The electron trigger ef-  
1621 ficiency increases with electron  $p_T$  but the average is approximately 90%. These efficiencies are measured  
1622 by combined performance and trigger signature groups[72, 73].

	Level-1 threshold	High-level threshold
Electron	18	$24i$
	30	60
Muon	15	$24i$
		36

**Table 5.1:** Single lepton triggers used for electrons and muons. A logical “or” of the triggers listed for each lepton type is taken. Units are in GeV, and the  $i$  denotes an isolation requirement in the trigger.

	Level-1 threshold	High-level threshold
$ee$	10 and 10	12 and 12
$\mu\mu$	15	18 and 8
$e\mu$	10 and 6	12 and 8

**Table 5.2:** Di-lepton triggers used for different flavor combinations. The two thresholds listed refer to leading and sub-leading leptons, respectively. The di-muon trigger only requires a single lepton at level-1.

1623 The combination of all triggers shown gives good efficiency for signal events. This efficiency is sum-  
1624 marized in table 5.3. The relative improvement in efficiency by adding the dilepton triggers is also shown  
1625 in the same table. The largest gain comes in the  $\mu\mu$  channel. Overall the trigger selection shows a good  
1626 efficiency for  $H \rightarrow WW^*$  signal events.

Channel	Trigger efficiency	Gain from $2\ell$ trigger
$ee$	97%	9.1%
$\mu\mu$	89%	18.5%
$e\mu$	95%	8.3%
$\mu e$	81%	8.2%

**Table 5.3:** Trigger efficiency for signal events and relative gain of adding a dilepton trigger on top of the single lepton trigger selection. The first lepton is the leading, while the second is the sub-leading. Efficiencies shown here are for the ggF signal in the  $n_j = 0$  category but are comparable for the VBF signal.

### 1627 5.2.2 MONTE CARLO SAMPLES

1628 Modeling of signal and background processes in the signal region, in particular for the  $m_T$  distribution,  
 1629 is an important consideration for the final interpretation of the analysis. Therefore, careful consideration  
 1630 must be paid to which Monte Carlo (MC) generators are used for specific processes. With the exception  
 1631 of the  $W + \text{jet}$  and multijet backgrounds, the  $m_T$  shape used as the final discriminant is taken from simu-  
 1632 lation. (Many backgrounds are normalized from data, as described in section 5.5).

1633 Table 5.4 shows the MC generators used for the signal and background processes, as well as their cross  
 1634 sections. In order to include corrections up to next-to-leading order (NLO) in the QCD coupling con-  
 1635 stant  $\alpha_s$ , the `POWHEG` [74] generator is often used. In some cases, only leading order generators like  
 1636 `ACERMC` [75] and `GG2VV` [76] are available for the process in question. If the process requires good  
 1637 modeling for very high parton multiplicities, the `SHERPA` [77] and `ALPGEN` [78] generators are used  
 1638 to provide merged calculations for five or fewer additional partons. These matrix element level calcula-  
 1639 tions must then be additionally matched to models of the underlying event, hadronization, and parton  
 1640 shower. There are four possible generators for this: `SHERPA`, `PYTHIA 6`[79], `PYTHIA 8`[80], or `HERWIG`  
 1641 [81] + `JIMMY` [82]. The simulation additionally requires an input parton distribution function (PDF).  
 1642 The `CT10`[83] PDFs are used for `SHERPA` and `POWHEG` simulated samples, while `CTEQ6Li`[84] is used  
 1643 for `ALPGEN + HERWIG` and `ACERMC` simulations. The Drell-Yan samples are reweighted to the `MRST`  
 1644 [85] PDFs, as these are found to give the best agreement between data and simulation.

1645 Once the basic hard scattering process is simulated, it must be passed through a detector simulation  
 1646 and additional pile-up events must be overlaid. The pile-up events are modeled with `PYTHIA 8`, and the

Process	MC generator	$\sigma \cdot \mathcal{B}$ (pb)
Signal		
ggF	$H \rightarrow WW^*$ POWHEG +PYTHIA 8	0.435
VBF	$H \rightarrow WW^*$ POWHEG +PYTHIA 8	0.0356
VH	$H \rightarrow WW^*$ PYTHIA 8	0.0253
$WW$		
$q\bar{q} \rightarrow WW$ and $qg \rightarrow WW$	POWHEG +PYTHIA 6	5.68
$gg \rightarrow WW$	GG2VV +HERWIG	0.196
$(q\bar{q} \rightarrow W) + (q\bar{q} \rightarrow W)$	PYTHIA 8	0.480
$q\bar{q} \rightarrow WW$	SHERPA	5.68
VBS $WW + 2$ jets	SHERPA	0.0397
Top quarks		
$t\bar{t}$	POWHEG +PYTHIA 6	26.6
$Wt$	POWHEG +PYTHIA 6	2.35
$tq\bar{b}$	ACERMC +PYTHIA 6	28.4
$t\bar{b}$	POWHEG +PYTHIA 6	1.82
Other dibosons ( $VV$ )		
$W\gamma$ ( $p_T^\gamma > 8$ GeV)	ALPGEN +HERWIG	369
$W\gamma^*$ ( $m_{\ell\ell} \leq 7$ GeV)	SHERPA	12.2
$WZ$ ( $m_{\ell\ell} > 7$ GeV)	POWHEG +PYTHIA 8	12.7
VBS $WZ + 2$ jets	SHERPA	0.0126
( $m_{\ell\ell} > 7$ GeV)		
$Z\gamma$ ( $p_T^\gamma > 8$ GeV)	SHERPA	163
$Z\gamma^*$ (min. $m_{\ell\ell} \leq 4$ GeV)	SHERPA	7.31
$ZZ$ ( $m_{\ell\ell} > 4$ GeV)	POWHEG +PYTHIA 8	0.733
$ZZ \rightarrow \ell\ell\nu\nu$ ( $m_{\ell\ell} > 4$ GeV)	POWHEG +PYTHIA 8	0.504
Drell-Yan		
$Z$ ( $m_{\ell\ell} > 10$ GeV)	ALPGEN +HERWIG	16500
VBF $Z + 2$ jets	SHERPA	5.36
( $m_{\ell\ell} > 7$ GeV)		

**Table 5.4:** Monte Carlo samples used to model the signal and background processes[21].

ATLAS detector is simulated with GEANT4[86]. Because of the unique phase space of the  $H \rightarrow WW^*$  analysis, events are sometimes filtered at generator level to allow for more efficient generation of relevant events. The efficiency of the trigger in MC simulation does not always match the measured efficiency in

1650 data, so trigger scale factors are applied to correct the MC efficiency to the data. These are derived by the  
1651 combined performance groups[72, 73].

1652 **5.3 OBJECT SELECTION**

1653 In order to define the signal region, the analysis must first select the objects to be considered. The de-  
1654 tails of the object reconstruction algorithms are discussed in Chapter 2, while this section gives specific  
1655 selection cuts used in the  $H \rightarrow WW^*$  analysis.

1656 The first step in this process is to select a primary vertex candidates. The event’s primary vertex is the  
1657 vertex with the largest sum of  $p_T^2$  for associated tracks and is required to have at least three tracks with  
1658  $p_T > 450$  MeV. Many of the object selection cuts are then made relative to this chosen primary vertex.

1659 **5.3.1 MUONS**

1660 The analysis uses combined muon candidates, where a track in the Inner Detector has been matched  
1661 to a standalone track in the Muon Spectrometer. The track parameters are combined statistically in the  
1662 muon reconstruction algorithm[16]. The muons are required to be within  $|\eta| < 2.5$  and have a  $p_T >$   
1663 10 GeV. To reduce backgrounds coming from mis-reconstructed leptons, there are requirements on  
1664 the impact parameter of the muon relative to the primary vertex. The transverse impact parameter  $d_0$   
1665 is required to be small relative to its estimated uncertainty, the exact cut value being  $d_0/\sigma_{d_0} < 3$ . The  
1666 longitudinal impact parameter  $z_0$  must satisfy  $|z_0 \sin \theta| < 1$  mm.

1667 As discussed previously, the muons must also be isolated. There are two types of lepton isolations  
1668 that are calculated: track-based and calorimeter-based. For muons, the track-based isolation is defined  
1669 using the scalar sum  $\sum p_T$  for tracks with  $p_T > 1$  GeV (excluding the muon’s track) within a cone of  
1670  $\Delta R = 0.3$  ( $0.4$ ) for muon with  $p_T > 15$  GeV ( $10 < p_T < 15$  GeV). The final isolation requirement  
1671 is made my requiring that this scalar sum be no more than a certain fraction of the muon’s  $p_T$ . This re-  
1672 quirement varies with muon  $p_T$  and the exact cuts are defined in table 5.5.

1673 The calorimeter-based muon isolation is defined using as a  $\sum E_T$  calculated from calorimeter cells  
1674 using the same cone size as the track-based isolation but excluding cells with  $\Delta R < 0.05$  around the

1675 muon. This requirement is also defined as a cut on the ratio of the sum to the muon  $p_T$  and varies with  
1676 muon  $p_T$ . The cut values are also given in table 5.5.

1677 The isolation requirements loosen as a function of  $p_T$  to allow for larger signal acceptance. At low  $p_T$ ,  
1678 the isolation is tightened to reduce the  $W + \text{jets}$  background which arises from a misidentified lepton.

$p_T$ range (GeV)	Calorimeter isolation	Track isolation
10 – 15	0.06	0.06
15 – 20	0.12	0.08
20 – 25	0.18	0.12
> 25	0.30	0.12

**Table 5.5:**  $p_T$  dependent isolation requirements for muons. Muons are required to have the amount of calorimeter or track based cone sums be less than this fraction of their  $p_T$ .

### 1679 5.3.2 ELECTRONS

1680 Electrons are identified by matching reconstructed clusters in the electromagnetic calorimeter with tracks  
1681 in the inner detector. The electrons are identified using a likelihood based method[14, 64] which takes  
1682 into account the shower shapes in the calorimeter, the matching of tracks to clusters, and the amount of  
1683 transition radiation in the TRT. The electrons are required to have  $|\eta| < 2.47$ , and candidates in the  
1684 transition region between the barrel and endcap ( $1.37 < |\eta| < 1.52$ ) are excluded. As the muons, the  
1685 electrons are required to have transverse impact parameter significance  $< 3$ , while in the longitudinal  
1686 direction they must have  $|z_0 \sin \theta| < 0.4$  mm. Some electron requirements also vary with electron  $E_T$ ,  
1687 and these requirements are summarized in table 5.6.

1688 The isolation for electrons are defined similarly to the muons but with unique cuts on the objects in-  
1689 cluded. The track-based isolation is defined using tracks with  $p_T > 400$  MeV with cone sizes as defined  
1690 previously. The calorimeter-based isolation also uses the same cone size as the muon, but here the cells  
1691 within a  $0.125 \times 0.175$  area in  $\eta \times \phi$  around the electron cluster's barycenter are excluded. The other  
1692 difference with respect to muons is that the denominator of the isolation ratio is the electron's  $E_T$  rather  
1693 than  $p_T$ . The isolation cuts very with electron  $E_T$  and are defined in table 5.6.

1694 The electron is also required to not be consistent with a vertex coming from a photon conversion.

$p_T$ range (GeV)	Quality cut	Calorimeter isolation	Track isolation
10 – 15	Very tight LH	0.20	0.06
15 – 20	Very tight LH	0.24	0.08
20 – 25	Very tight LH	0.28	0.10
> 25	Medium	0.28	0.10

**Table 5.6:**  $p_T$  dependent requirements for electrons. Electrons are required to have the amount of calorimeter or track based cone sums be less than this fraction of their  $E_T$ .

### 1695 5.3.3 JETS

1696 Jets are clustered with the anti- $k_T$  reconstruction algorithm using a radius parameter of  $R = 0.4$ . They  
 1697 are required to have a jet vertex fraction (JVF) of at least 50%, meaning that half of the tracks associated  
 1698 with the jet originated from the primary vertex. Jets with no tracks associated (i.e. those outside the ac-  
 1699 ceptance of the ID) do not have this requirement applied. Jets are required to have  $p_T > 25$  GeV if  
 1700 they are within the tracking acceptance ( $|\eta| < 2.4$ ). Jets with  $2.4 < |\eta| < 4.5$  are required to have  
 1701  $p_T > 30$  GeV. This tighter requirement reduces jets from pileup in the region where JVF requirements  
 1702 cannot be applied. The two highest  $p_T$  jets in the event are referred to as the “VBF” jets and used to com-  
 1703 pute various analysis selections later.

1704 Identification of  $b$ -jets is done using the MV1 algorithm and is limited to the acceptance of the ID  
 1705 ( $|\eta| < 2.5$ ). The operating point of MV1 that is used is the one that is 85% efficient for identifying true  
 1706  $b$ -jets. This operating point has a 10.3% of mis-tagging a light quark jet as a  $b$ -jet. In order to improve  
 1707 the rejection of  $b$ -jets, a lower threshold than the nominal  $p_T$  threshold described above is used. For the  
 1708 purposes of counting the number of  $b$ -jets, jets with  $p_T$  down to 20 GeV are used.

### 1709 5.3.4 OVERLAP REMOVAL

1710 There are some cases where certain reconstructed objects will overlap and one will have to be chosen  
 1711 (for example, an electron and a jet in the calorimeter). First, the case of lepton overlap is dealt with. If  
 1712 an electron candidate extends into the muon spectrometer, it is removed. If a muon or electron have a  
 1713  $\Delta R < 0.1$ , the electron is removed and the muon is kept. If two electron candidates overlap within  
 1714 the same radius, then the higher  $E_T$  electron is kept. Next, the overlap between leptons and jets is con-

1715 sidered. If an electron and jet are within  $\Delta R < 0.3$  of one another, the electron is kept and the jet is  
1716 removed. However, if a muon and jet overlap within  $\Delta R < 0.3$ , the jet is kept (as it is likely that the  
1717 muon is the result of a semileptonic decay inside the jet).

1718 Once the overlap removal is complete, the final set of objects used in the analysis is defined.

#### 1719 5.4 ANALYSIS SELECTION

1720 The VBF analysis uses two distinct selections. The first is a more standard selection, referred to as “cut-  
1721 based”, that applies requirements on the VBF variables and uses  $m_T$  as the final discriminating variable.  
1722 The second is a looser selection that uses a Boosted Decision Tree (BDT) score as the final discriminator  
1723 in order to take advantage of the detailed correlations between the VBF variables. While the BDT analy-  
1724 sis is ultimately more sensitive, the cut-based serves as an important component of the analysis. First, the  
1725 cut-based allows for confirming the modeling and validity of many variables used as input to the BDT.  
1726 Second, because this is the first use of such an MVA technique in the  $H \rightarrow WW^*$  analysis, the cut-based  
1727 selection allows confirmation of the final BDT result with a more traditional analysis. The cut-based  
1728 techniques are the focus of this chapter, but connections to the BDT result will be illustrated when ap-  
1729 propriate.

1730 One important note is that because this analysis is dedicated to the measurement of the VBF pro-  
1731 duction mode of the Higgs, events coming from gluon fusion production with the Higgs decaying via  
1732  $H \rightarrow WW^* \rightarrow \ell\nu\ell\nu$  are treated as background events. This will be seen throughout the various  
1733 predictions shown.

##### 1734 5.4.1 COMMON PRE-SELECTION

1735 Both the cut-based and BDT analyses have a common pre-selection that is applied before the main signal  
1736 region requirements. The requirements on leptons are common to all  $n_j$  bins. The analysis requires two  
1737 oppositely charged leptons, with the leading lepton required to have  $p_T > 22$  GeV while the subleading  
1738 lepton must have  $p_T > 10$  GeV. Next, to remove low mass  $Z/\gamma^*$  events, a cut on the dilepton mass  
1739  $m_{\ell\ell} > 10$  (12) GeV is applied in the different (same) flavor channel. In the same flavor channels, there is

1740 an additional veto placed on the region around the Z peak, requiring that  $|m_{\ell\ell} - m_Z| > 15$  GeV.

1741 There are also requirements on the amount of missing transverse momentum in the event. These  
1742 are only applied in the same flavor channels, as in the different flavor channels  $t\bar{t}$  is the dominant back-  
1743 ground in  $n_j \geq 2$ . The BDT analysis requires  $p_T^{\text{miss}} > 40$  GeV and  $E_T^{\text{miss}} > 45$  GeV. The cut-  
1744 based analysis must select more tightly on these variables to have maximal sensitivity and thus requires  
1745  $p_T^{\text{miss}} > 50$  GeV and  $E_T^{\text{miss}} > 55$  GeV.

1746 Finally, because this analysis is focused on VBF, a requirement on the jet multiplicity is placed, with  
1747  $n_j \geq 2$ . Additionally, the analysis requires that there are no jets identified as b-quarks in the event, or  
1748  $n_b = 0$ .

#### 1749 5.4.2 CUT-BASED SELECTION

1750 The cut-based selection places sequential requirements on variables reconstructed from the VBF jets in  
1751 order to increase the signal to background ratio.

#### 1752 GENERAL BACKGROUND REDUCTION

1753 Top pair production is the primary background in the  $n_j \geq 2$  bin. Even though  $n_b = 0$  is required,  
1754 an additional variable is constructed to further suppress the top background. There is often additional  
1755 QCD radiation that accompanies the  $t\bar{t}$  system when it is produced. Therefore, a variable which tests for  
1756 the presence of this additional radiation,  $p_T^{\text{sum}}$ , is constructed. It is defined in equation 5.1.

$$p_T^{\text{sum}} = p_T^{\ell\ell} + p_T^{\text{miss}} + \sum p_T^j \quad (5.1)$$

1757 The first cut after pre-selection in the cut-based analysis requires  $p_T^{\text{sum}} < 15$  GeV to further suppress  
1758  $t\bar{t}$  production.

1759 In the different flavor channels, a cut is made to reduce the contamination from  $Z \rightarrow \tau\tau$  decays. The  
1760 di- $\tau$  invariant mass,  $m_{\tau\tau}$ , is constructed by assuming that the neutrinos from the  $\tau$  decays were collinear  
1761 with the leptons[? ]. The analysis requires that this mass not be consistent with a  $Z$  by requiring  $m_{\tau\tau} <$   
1762  $m_Z - 25$  GeV.

1763 VBF TOPOLOGICAL CUTS

1764 The characteristic feature of VBF production of the Higgs is the presence of two additional forward jets  
1765 coming from the incoming partons which radiate the vector bosons that make the Higgs. These jets are  
1766 forward because the outgoing partons still carry the longitudinal momentum of the incoming partons.  
1767 Figure 5.2 shows the distribution of the  $\eta$  for the leading jet in a VBF event compared to a background  
1768 top pair production event. As can be seen, the VBF jets tend to be more forward in  $\eta$ , while the  $t\bar{t}$  jets are  
1769 more central.

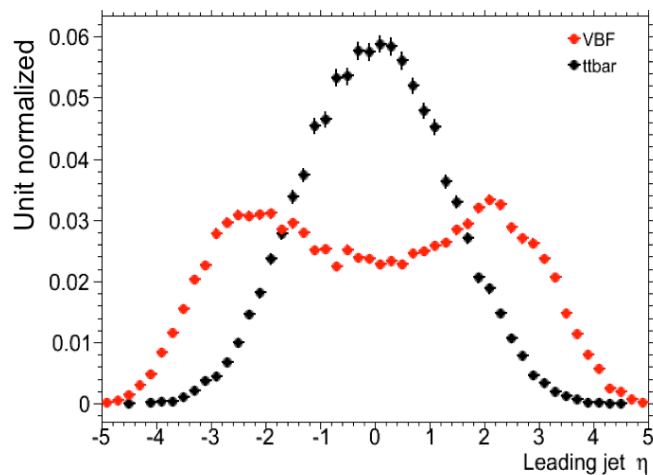


Figure 5.2: Leading jet  $\eta$  in VBF  $H \rightarrow WW^*$  (red) and  $t\bar{t}$  (black)

1770 Because the cross section for VBF production is an order of magnitude smaller than gluon fusion pro-  
1771 duction, these forward jets must be used in order to better reduce background and achieve a good signal  
1772 to background ratio. The dedicated VBF search selection requirements are constructed to maximally  
1773 exploit the features of the unique VBF topology.

1774 Requirements on the VBF jets are collectively referred to as the “VBF topological cuts”. First, a re-  
1775 quirement on the dijet invariant mass of the VBF jets,  $m_{jj}$ , is placed, requiring  $m_{jj} > 600$  GeV. Next,  
1776 the event is required to have a large gap in rapidity between the two VBF jets, or  $\Delta y_{jj} > 3.6$ . Both  
1777 of these cuts put tight requirements on the presence of two forward, high  $p_T$  jets moving in opposite

1778 directions in the longitudinal plane.

1779 Beyond requiring the presence of the two forward VBF jets, the analysis also vetoes on the presence  
1780 of any additional jets that fall between the two VBF jets. This cut is referred to as the central jet veto, or  
1781 CJV. Any events with a third jet with  $p_T > 20$  GeV whose rapidity is between the region defined by the  
1782 two VBF jets are vetoed. This can be expressed in terms of a variable called the jet centrality, defined in  
1783 equation 5.2.

$$C_{j3} = \left| \eta_{j3} - \frac{\eta_{j1} + \eta_{j2}}{2} \right| / \frac{|\eta_{j1} - \eta_{j2}|}{2}, \quad (5.2)$$

1784 Here,  $\eta_{j1}$  and  $\eta_{j2}$  are the pseudorapidities of the leading and subleading jets, respectively, while  $\eta_{j3}$  is  
1785 the pseudorapidity of the extra jet in the event (if one exists). Intuitively,  $C_{j3}$  is zero when  $\eta_{j3}$  is directly  
1786 centered between the two jets and unity when  $\eta_{j3}$  is aligned with either of the VBF jets. Thus, the CJV  
1787 can be expressed as a requirement that  $C_{j3} > 1$ .

1788 The decay products of the Higgs tend to be central as well. Thus, the analysis also requires that both  
1789 leptons in the analysis fall within the rapidity gap defined by the jets. This cut is referred to as the outside  
1790 lepton veto, or OLV. A quantitative way to define the cut is to require that the centrality of each lepton  
1791 (defined analogously to that of the third jet in equation 5.2) correspond to the lepton being within the jet  
1792 rapidity gap, or  $C_\ell < 1$  for both leptons.

1793 Figure 5.3a-c shows the  $m_{jj}$ ,  $\Delta y_{jj}$ , and  $C_{\ell 1}$  variables at the stage where all previous cuts in the se-  
1794 quence have been made. The agreement between data and Monte Carlo is good, and the bottom panels  
1795 show their power in discriminating the VBF signal from the background processes.

1796 The final signal region is also split into two bins of  $m_{jj}$ , with the first bin corresponding to  $600 \text{ GeV} <$   
1797  $m_{jj} < 1 \text{ TeV}$  and the second bin corresponding to  $m_{jj} > 1 \text{ TeV}$ . The first bin has more statistics but  
1798 also a larger contribution from background, while the second bin has lower statistics but a 1:1 signal to  
1799 background ratio.

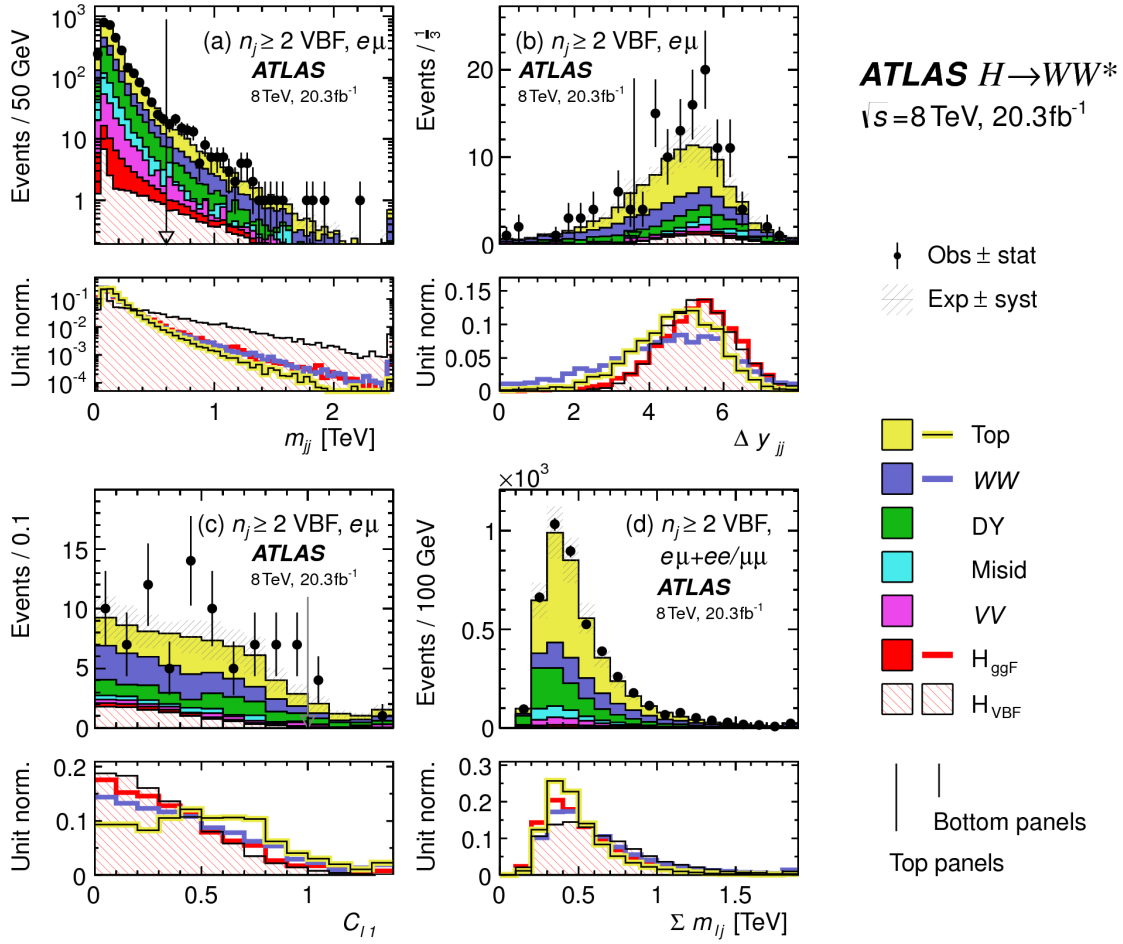


**Figure 5.3:** Distributions of (a)  $m_{jj}$ , (b)  $\Delta y_{jj}$ , (c)  $C_{\ell 1}$ , and (d)  $\sum m_{ij}$ , for the VBF analysis. The top panels compare simulation and data, while the bottom panels show normalized distributions for all background processes and signal[21].

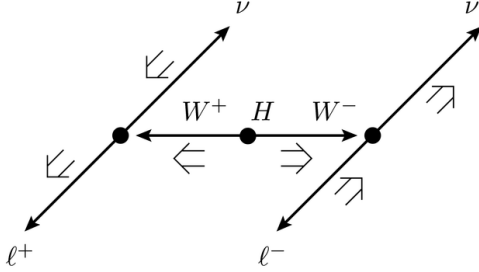


**Figure 5.4:** A cartoon of the WW final state. Momenta are represented with thin arrows, spins with thick arrows. [21]

#### 1800 HIGGS TOPOLOGICAL CUTS

1801 The final state leptons will exhibit unique correlations due to the fact that they are arising from the decay  
 1802 of a spin zero resonance. In particular, the spins of the final state leptons and neutrinos must all cancel,  
 1803 as shown in figure 5.4. Because the neutrino has a left handed chirality and the anti-neutrino has a right  
 1804 handed chirality (in the massless neutrino approximation), the spin and momentum of the particles  
 1805 will be anti-aligned and aligned, respectively. In the transverse plane, the momenta of all four final state  
 1806 objects must cancel as well. With the constraint of having both the momenta and the spin alignments  
 1807 cancel, the final state kinematics strongly prefer having a small angle between the leptons in the trans-  
 1808 verse plane (low  $\Delta\phi_{\ell\ell}$ ). This angular correlation will also lead to low values of the di-lepton invariant  
 1809 mass  $m_{\ell\ell}$ . These unique signal final state kinematic correlations will be exploited to define the ultimate  
 1810 signal region.

1811 The analysis places additional requirements on the final state leptons. Two requirements on dilepton  
 1812 kinematics are made that are common with lower multiplicity jet bins as well. The angle between leptons  
 1813 in the transverse plane,  $\Delta\phi_{\ell\ell}$ , is required to be less than 1.8 radians. Additionally, the dilepton mass  $m_{\ell\ell}$   
 1814 is required to be less than 50 GeV.

1815 The cut-based analysis uses  $m_T$  as the final discriminating variable as in the ggF focused analysis. The  
 1816 optimal number of bins in  $m_T$  was found to be three bins, with the bin boundaries at 80 and 130 GeV.

1817 Table 5.7 shows the data and estimated signal and background yields from simulation as each cut de-  
 1818 scribed above is made. The table shows how each cut reduces specific backgrounds and how the overall

1819 signal to background ratio grows through the cutflow.

1820 Figure 5.5 shows an ATLAS event display of a candidate event in the final signal region.

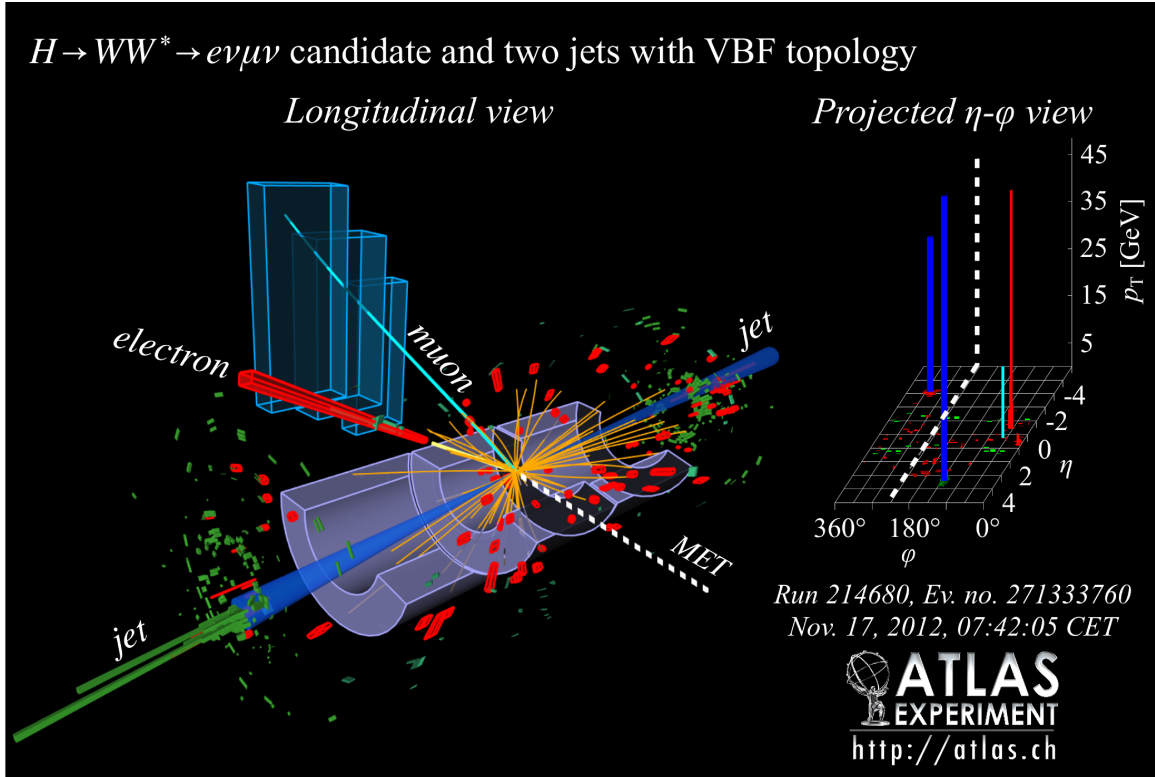


Figure 5.5: Event display of a VBF candidate event[21].

1821 5.4.3 BDT-BASED SELECTION

1822 The boosted decision tree based analysis takes a different philosophy compared to the cut-based. Rather  
1823 than cutting sequentially on many variables, the BDT analysis uses many of these variables as inputs  
1824 to the BDT and the output BDT score ( $O_{\text{BDT}}$ ) as the final discriminant. The BDT is trained with the  
1825 VBF  $H \rightarrow WW^*$  simulation as the signal samples and all other processes as background, including ggF  
1826  $H \rightarrow WW^*$  production. While the BDT based analysis is treated as a separate result, it has significant  
1827 overlap with the cut-based selection.

**Table 5.7:** Event selection for the  $n_j \geq 2$  VBF analysis in the 8 TeV cut-based analysis[21].

Selection	Summary										Composition of $N_{\text{bkg}}$							
	$N_{\text{obs}}/N_{\text{bkg}}$	$N_{\text{obs}}$	$N_{\text{bkg}}$	$N_{\text{signal}}$	$N_{\text{ggF}}$	$N_{\text{VBF}}$	$N_{\text{VH}}$	$N_{WW}^{\text{QCD}}$	$N_{WW}^{\text{EW}}$	$N_{t\bar{t}}$	$N_t$	$N_{\text{top}}$	$N_{Wj}$	$N_{jj}$	$N_{VV}$	$N_{\text{misid}}$	$N_{\text{Drell-Yan}}$	$N_{ee/\mu\mu} N_{\tau\tau}^{\text{QCD}}$
$e\mu$ sample	1.00 ± 0.00	61434	61180	85	32	26	1350	68	51810	2970	847	308	380	51	3260	46		
$n_b = 0$	1.02 ± 0.01	7818	7700	63	26	16	993	43	3000	367	313	193	273	35	2400	29		
$p_T^{\text{sum}} < 15$	1.03 ± 0.01	5787	5630	46	23	13	781	38	1910	270	216	107	201	27	2010	23		
$m_{\tau\tau} < m_Z - 25$	1.05 ± 0.02	3129	2970	40	20	9.9	484	22	1270	177	141	66	132	7.6	627	5.8		
$m_{jj} > 600$	1.31 ± 0.12	131	100	2.3	8.2	—	18	8.9	40	5.3	1.8	2.4	5.1	0.1	15	1.0		
$\Delta y_{jj} > 3.6$	1.33 ± 0.13	107	80	2.1	7.9	—	11.7	6.9	35	5.0	1.6	2.3	3.3	—	11.6	0.8		
$C_{j3} > 1$	1.36 ± 0.18	58	43	1.3	6.6	—	6.9	5.6	14	3.0	1.3	1.3	2.0	—	6.8	0.6		
$C_{\ell 1} < 1, C_{\ell 2} < 1$	1.42 ± 0.20	51	36	1.2	6.4	—	5.9	5.2	10.8	2.5	1.3	1.3	1.6	—	5.7	0.6		
$m_{\ell\ell}, \Delta\phi_{\ell\ell}, m_\tau$	2.53 ± 0.71	14	5.5	0.8	4.7	—	1.0	0.5	1.1	0.3	0.3	0.3	0.6	—	0.5	0.2		
<hr/>																		
$ee/\mu\mu$ sample	0.99 ± 0.01	26949	27190	31	14	10.1	594	37	23440	1320	230	8.6	137	690	679	16		
$n_b, p_T^{\text{sum}}, m_{\tau\tau}$	1.03 ± 0.03	1344	1310	13	8.0	4.0	229	12.0	633	86	26	0.9	45	187	76	1.5		
$m_{jj}, \Delta y_{jj}, C_{j3}, C_\ell$	1.39 ± 0.28	26	19	0.4	2.9	0.0	3.1	3.1	5.5	1.0	0.2	0.0	0.7	3.8	0.7	0.1		
$m_{\ell\ell}, \Delta\phi_{\ell\ell}, m_\tau$	1.63 ± 0.69	6	3.7	0.3	2.2	0.0	0.4	0.2	0.6	0.2	0.2	0.0	0.1	1.5	0.3	0.1		

1828 PRE-TRAINING SELECTION AND BDT INPUTS

1829 Before training, the common preselection cuts described in section 5.4.1 are applied. Additionally, the  
1830 central jet veto and outside lepton veto described in section 5.4.2 are applied. The BDT has eight input  
1831 variables, six of which are also variables that are used in the cut-based analysis. The six shared variables  
1832 are  $p_T^{\text{sum}}$ ,  $m_{jj}$ ,  $\Delta y_{jj}$ ,  $m_{\ell\ell}$ ,  $\Delta\phi_{\ell\ell}$ , and  $m_T$ . The seventh variable input in the BDT is a combination of  
1833 the variables used to do the OLV in the cut-based analysis. The BDT uses as input the sum of lepton  
1834 centralities, or  $\sum C_\ell = C_{\ell 1} + C_{\ell 2}$ . The final BDT input variable,  $\Sigma m_{\ell j}$ , is constructed to account for  
1835 the correlations between the jets and leptons in the event. It is the sum of the invariant masses of all four  
1836 possible lepton-jet combinations.

1837 Figure 5.3d shows the agreement between data and simulation for the  $\Sigma m_{\ell j}$  variable, as well as show-  
1838 ing its discriminating power. Figure 5.6 shows the distributions of the Higgs topological variables that  
1839 are shared between the cut-based and BDT analyses. Figure 5.7 shows the distributions of the VBF topo-  
1840 logical variables shared between the cut-based and BDT analyses. In both cases, the VBF yield has been  
1841 scaled by a factor of 50 to better show the shape difference compared to the backgrounds.

1842 Table ?? summarizes the cuts applied for the cut-based and analyses, as well as which variables are used  
1843 as input to the BDT.

1844 5.5 BACKGROUND ESTIMATION

1845 This section describes the procedures used to estimate backgrounds for the VBF analysis in both the  
1846 cut-based and BDT analyses.

1847 5.5.1 GENERAL STRATEGY

1848 Most of the backgrounds in the VBF analysis have shapes estimated from Monte Carlo simulation but  
1849 normalizations derived from control regions in data. In essence, a normalization factor (denoted with  
1850  $\beta$  or abbreviated as NF) is derived by scaling the MC yield in the control region to the corresponding  
1851 yield in data. Once this factor is derived, it can be used to scale the MC estimate of the background in the

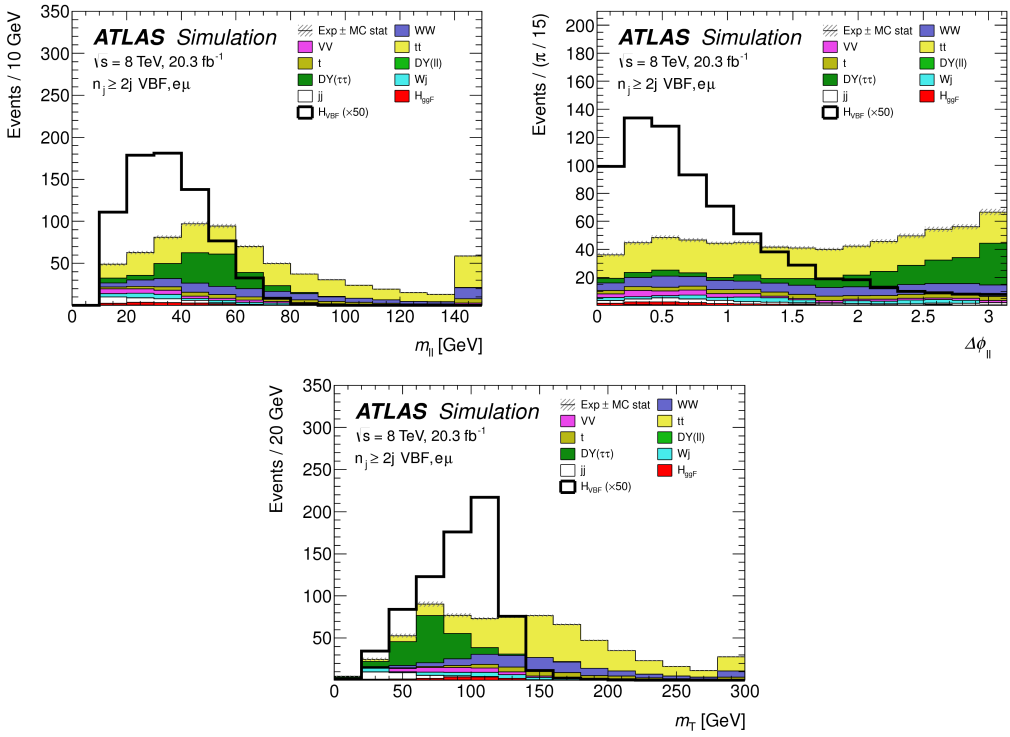


**Figure 5.6:** Distributions of  $m_{\ell\ell}$  (top left),  $\Delta\phi_{\ell\ell}$  (top right), and  $m_T$  (bottom), Higgs topology variables used in the selection requirements of the cut-based signal region and as inputs to the BDT result. These are plotted after all of the BDT pre-training selection cuts[21].

1852 signal region. This is illustrated in equation 5.3.

$$B_{\text{SR}}^{\text{est}} = B_{\text{SR}} \times \frac{N_{\text{CR}}}{B_{\text{CR}}} \equiv B_{\text{SR}} \times \beta \quad (5.3)$$

1853 Here,  $B$  denotes the MC yield prediction in the denoted region, while  $N$  denotes the observed number of events in data in the denoted region.

1854 Another way of writing the same equation, in terms of an extrapolation factor  $\alpha$  rather than a normalization factor  $\beta$ . The overall calculation is exactly the same. However, when phrased in this way, it  
1855 shows how the uncertainty on the background estimation can be reduced. This is shown in equation 5.4.

$$B_{\text{SR}}^{\text{est}} = N_{\text{CR}} \times \frac{B_{\text{SR}}}{B_{\text{CR}}} \equiv N_{\text{CR}} \times \alpha \quad (5.4)$$

1856 Phrased this way, the equation shows that with enough statistics in the control region, a large theoret-

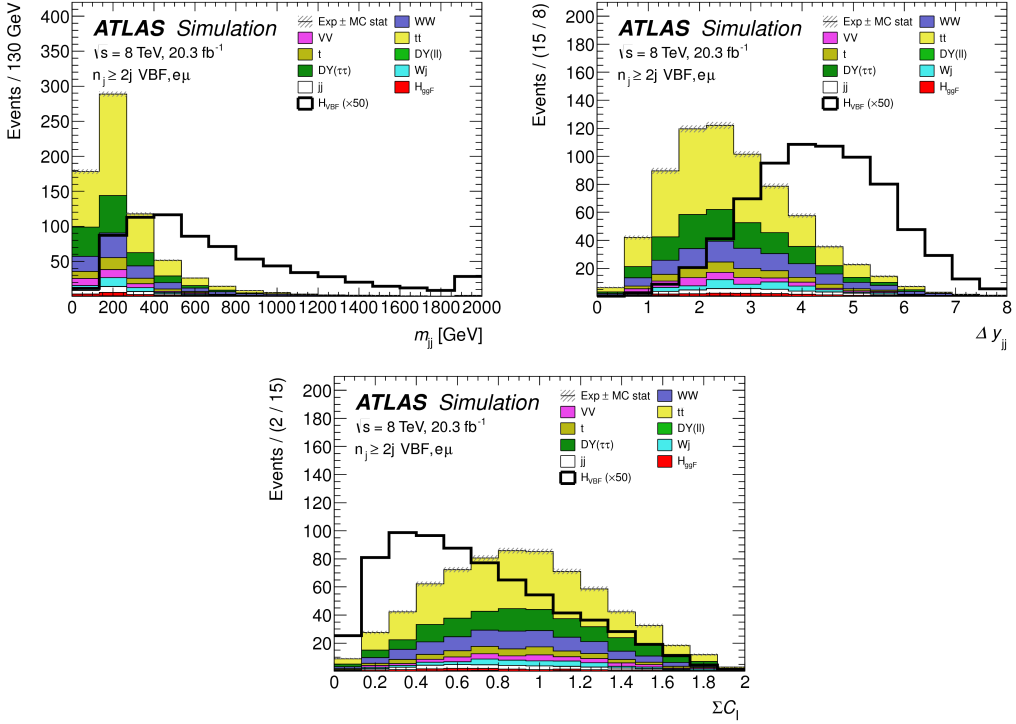


**Figure 5.7:** Distributions of  $m_{jj}$  (top left),  $\Delta y_{jj}$  (top right),  $\sum C_\ell$  (bottom), VBF topology variables used in the selection requirements of the cut-based signal region and as inputs to the BDT result. These are plotted after all of the BDT pre-training selection cuts[21].

ical uncertainty on the overall background yield in the signal region can be replaced by a small statistical uncertainty coming from the number of data events in the CR and a smaller theoretical uncertainty on the extrapolation from the control region to the signal region.

### 5.5.2 TOP BACKGROUND

The normalization factor  $\beta_t$  for the top background in the VBF analysis is derived in a region required to have one b-tagged jet, or  $n_b = 1$ . In the cut-based analysis, normalization factors are computed at every stage of the cutflow by applying the appropriate cuts in the CR. These NF are then applied to the  $t\bar{t}$  and single top event yields in the SR. In the BDT analysis, a single normalization factor is computed for each bin of  $O_{\text{BDT}}$  after applying the BDT pre-training cuts described previously. The computed normalization factors are derived with all flavor combinations combined in order to decrease statistical uncertainty. Additionally, in the BDT analysis, BDT bins 2 and 3 are merged for the same reason.

1870 Table 5.8 shows the evolution of the  $\beta_t$  through the cut-based selection. Table 5.9 shows the value  
 1871 of the  $\beta_t$  in each bin of  $O_{\text{BDT}}$ . In all cases, the computed factors are relatively consistent with unity,  
 1872 with the largest discrepancy coming in bin 1 of  $O_{\text{BDT}}$ . The normalization factors in the bins of  $O_{\text{BDT}}$   
 1873 are also consistent with those derived in the cut-based signal region, increasing confidence in the BDT  
 1874 estimation.

Cut	$\beta_t$
$p_T^{\text{sum}} < 15 \text{ GeV}$	$1.03 \pm 0.01$
$m_{\tau\tau} < m_Z - 25$	$1.05 \pm 0.01$
$m_{jj} > 600 \text{ GeV}$	$0.96 \pm 0.06$
$\Delta y_{jj} > 3.6$	$1.02 \pm 0.08$
CJV	$1.13 \pm 0.16$
OLV	$1.01 \pm 0.19$
$m_{jj} < 1 \text{ TeV}$	$0.94 \pm 0.19$
$m_{jj} > 1 \text{ TeV}$	$1.48 \pm 0.66$

**Table 5.8:** Top normalization factors computed at each stage of the cut-based selection. Uncertainties are statistical only.

$O_{\text{BDT}}$	$\beta_t$
Bin0	$1.09 \pm 0.02$
Bin1	$1.58 \pm 0.15$
Bin2	$0.95 \pm 0.31$
Bin3	$0.95 \pm 0.31$

**Table 5.9:** Top normalization factors computed for each bin of  $O_{\text{BDT}}$ . Uncertainties are statistical only.

1875 Figure 5.8 shows the  $m_{jj}$  and  $O_{\text{BDT}}$  distributions in the top control region. Overall the modeling  
 1876 looks consistent with the data.

1877 While these normalization factors can be computed and applied to the expected background yields  
 1878 listed in tables like table 5.7, in the end the normalization of the top background is profiled (meaning  
 1879 there is a dedicated Poisson constraint) and allowed to float in the final statistical fit.

### 1880 5.5.3 $Z/\gamma^* \rightarrow \tau\tau$ BACKGROUND

1881 In the different flavor channels, the  $Z/\gamma^* \rightarrow \tau\tau$  background is an important one. Di-tau production  
 1882 can produce an  $e\mu$  final state if each  $\tau$  lepton decays to a different flavor lepton.

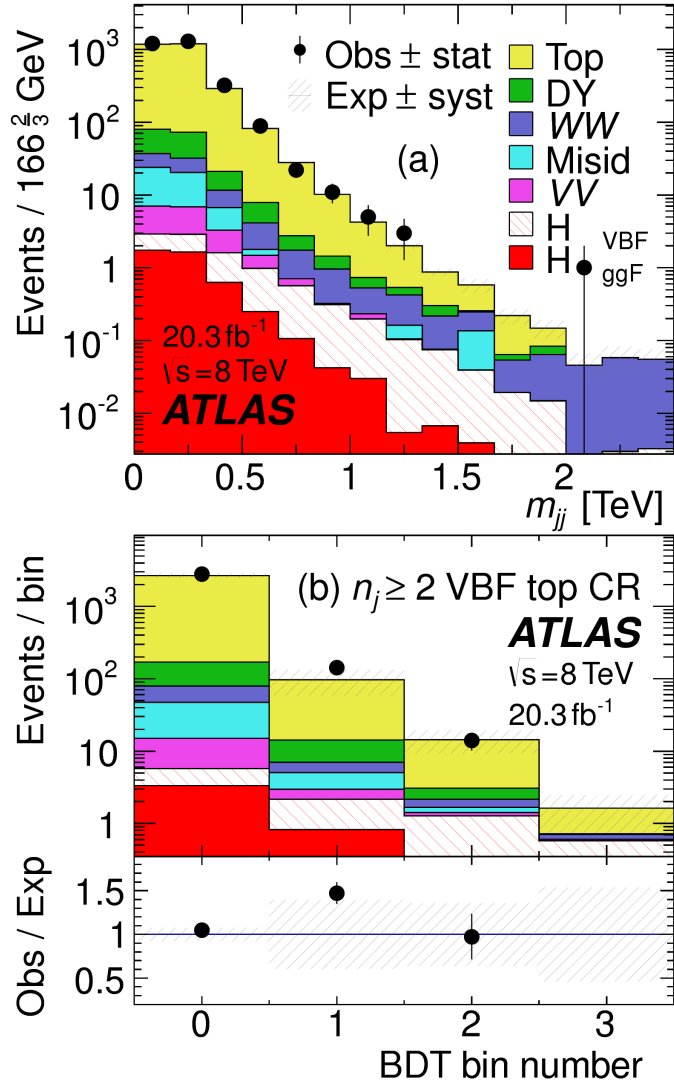


**Figure 5.8:** Distributions of  $m_{jj}$  (a) and  $O_{\text{BDT}}$  (b) in the VBF  $n_b = 1$  top CR [21].

In the BDT analysis, a single normalization factor for the background is derived. A control region is defined using the pre-training selection cuts, except requiring that  $|m_{\tau\tau} - m_Z| < 25 \text{ GeV}$  so that the region is enriched in  $Z/\gamma^* \rightarrow \tau\tau$  background. Additional requirements of  $m_{\ell\ell} < 80(75) \text{ GeV}$  in the different (same) flavor channel, as well as  $O_{\text{BDT}} > -0.48$  are applied to increase the purity of the region. The final  $\beta_{Z/\gamma^* \rightarrow \tau\tau}$  is calculated to be  $0.9 \pm 0.3$  (statistical uncertainty only). Because of the small contribution of this background in the BDT analysis and the large statistical uncertainty, no additional systematics are calculated. The final SR estimate is scaled by this  $\beta$  and not allowed to float in

1890 the fit.

1891 The cut-based corrections are a bit more involved because they need to be applied cut by cut through  
1892 the cutflow, as well as in the final signal region for the fit. The region is defined including all SR cuts  
1893 up to the  $Z/\gamma^* \rightarrow \tau\tau$  veto, which is instead made into a Z mass peak requirement as for the BDT  
1894 region. The  $m_{\ell\ell}$  cut from the BDT region is included as well. The cut-based approach aims to correct  
1895 the normalization of the  $Z/\gamma^* \rightarrow \tau\tau$  background in two ways. First, an overall normalization factor is  
1896 computed from the control region. However, the VBF topological cuts are not included in this region,  
1897 and applying them as is done in the top CR is not feasible due to limited statistics. So, instead, correction  
1898 factors (CF) to the cut efficiencies of the VBF cuts are derived in a same flavor  $Z \rightarrow \ell\ell$  control region,  
1899 which has significantly more statistics. The CF is simply the ratio of the cut efficiencies in data and MC  
1900 derived in this region. In the end, the overall background estimate is given by equation 5.5.

$$N_{Z/\gamma^* \rightarrow \tau\tau}^{\text{est}} = B_{Z/\gamma^* \rightarrow \tau\tau}^{\text{SR}} \times \beta_{\tau\tau} \times \frac{\epsilon_{\text{VBF cuts}}^{\text{data}}}{\epsilon_{\text{VBF cuts}}^{\text{MC}}} \quad (5.5)$$

1901 The hypothesis is that while the normalization correction must be derived in a dedicated region, the  
1902 efficiency of the VBF cuts should not be sensitive to the type of  $Z/\gamma^*$  process and thus the larger control  
1903 region can be exploited to derive the CF. Figure 5.9 shows a shape comparison for the  $m_{jj}$  variable in  
1904  $Z \rightarrow \tau\tau$  events in the signal region and  $Z \rightarrow \ell\ell$  events in the control region. The figure shows that the  
1905 shapes are indeed comparable and thus any CF derived in the same flavor control region can reliably be  
1906 applied in the signal region.

1907 Table 5.10 shows the overall normalization factor  $\beta_{\tau\tau}$  and the efficiency correction factors for the var-  
1908 ious VBF topological cuts. In general, the statistical uncertainties on the cut efficiency corrections are  
1909 quite good, and the MC tends to underestimate the efficiency of the VBF cuts for the  $Z/\gamma^* \rightarrow \tau\tau$  back-  
1910 ground. The overall normalization factor is also consistent with that calculated for the BDT analysis.

#### 1911 5.5.4 $Z/\gamma^* \rightarrow \ell\ell$ BACKGROUND

1912 In the same flavor channels, the  $Z/\gamma^* \rightarrow \ell\ell$  background is dominant and thus must be estimated  
1913 correctly. In both the BDT and cut-based analyses, the background is estimated using the so-called

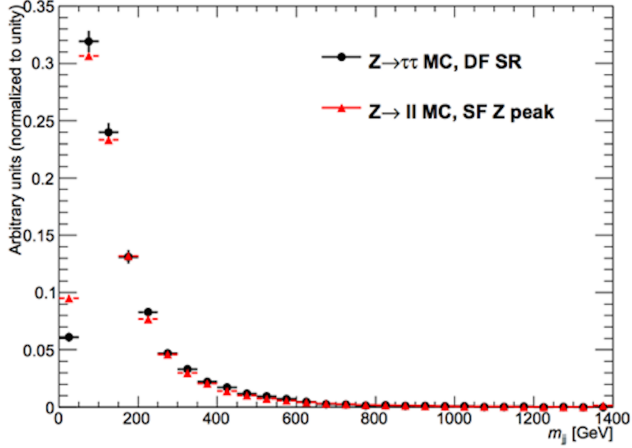


**Figure 5.9:** Comparison of  $m_{jj}$  shape in a same flavor  $Z \rightarrow \ell\ell$  control region and the VBF cut-based signal region.

$\beta_{\tau\tau}$	$0.97 \pm 0.04$
Cut	Correction factors
$m_{jj} > 600 \text{ GeV}$	$1.09 \pm 0.01$
$\Delta y_{jj} > 3.6$	$1.14 \pm 0.02$
CJV	$1.20 \pm 0.02$
OLV	$1.17 \pm 0.03$
$m_{jj} < 1 \text{ TeV}$	$1.17 \pm 0.06$
$m_{jj} > 1 \text{ TeV}$	$1.18 \pm 0.13$

**Table 5.10:**  $Z/\gamma^* \rightarrow \tau\tau$  correction factors for the VBF cut-based analysis. Uncertainties are statistical only.

“ABCD” method. The ABCD method creates four different regions by defining cuts on two variables. One of the regions (A) is the signal region, while the other regions are defined by inverting one of both of the cuts. in this case, the two variables used are  $m_{\ell\ell}$  and  $E_T^{\text{miss}}$ , because inverting either of the SR cuts on these variables will give regions rich in the  $Z/\gamma^* \rightarrow \ell\ell$  background. Figure 5.10 illustrates the general strategy for each region.

In both of the cut-based and BDT analyses, the  $Z$  peak region is defined with  $|m_{\ell\ell} - m_Z| < 15 \text{ GeV}$ . In the cut-based analysis, low  $m_{\ell\ell}$  corresponds to  $m_{\ell\ell} < 50 \text{ GeV}$  (this defines the cut-based SR) while in the BDT it is  $m_{\ell\ell} < 75 \text{ GeV}$ . In the cut-based, high and low  $E_T^{\text{miss}}$  are defined as opposite ends of the 55 GeV cut applied for the signal region definition. The BDT low  $E_T^{\text{miss}}$  region is between 25 and 45 GeV, while the high  $E_T^{\text{miss}}$  region is  $E_T^{\text{miss}} > 45 \text{ GeV}$ .

Once the regions are defined, the final signal region background estimate is done by taking the esti-

<b>Region A (SR)</b>	<b>Region C</b>
High $E_T^{\text{miss}}$	High $E_T^{\text{miss}}$
Low $m_{\ell\ell}$	Z peak
<b>Region B</b>	<b>Region D</b>
Low $E_T^{\text{miss}}$	Low $E_T^{\text{miss}}$
Low $m_{\ell\ell}$	Z peak

**Figure 5.10:** General illustration of the ABCD region definitions for  $Z/\gamma^* \rightarrow \ell\ell$  background estimation.

1925 mate in region B and extrapolating it to the signal region (A) by multiplying it by the ratio of regions  
 1926 C and D. Effectively, the  $Z$  peak region is used to estimate the efficiency of the  $E_T^{\text{miss}}$  cut in data, and  
 1927 then this efficiency is applied in the low  $m_{\ell\ell}$  region. An additional correction is also applied for the non-  
 1928 closure of the method in MC. This is summarized in equations 5.6 and 5.7.

$$N_{Z/\gamma^* \rightarrow \ell\ell}^{\text{SR}} = N_{Z/\gamma^* \rightarrow \ell\ell}^{\text{B}} \times \frac{N_{Z/\gamma^* \rightarrow \ell\ell}^{\text{C}}}{N_{Z/\gamma^* \rightarrow \ell\ell}^{\text{D}}} \times f_{\text{corr}} \quad (5.6)$$

$$f_{\text{corr}} = \frac{B_{\text{MC}}^{\text{A}}/B_{\text{MC}}^{\text{B}}}{B_{\text{MC}}^{\text{C}}/B_{\text{MC}}^{\text{D}}} \quad (5.7)$$

1929 Here, the  $N$  refer to data yields in each region with the non  $Z/\gamma^*$  backgrounds subtracted, while  $B$   
 1930 refer to the  $Z/\gamma^*$  yields in MC in each region.

1931 A normalization factor  $\beta_{\ell\ell}$  is computed for each analysis as the ratio of the predicted data yield to  
 1932 the MC yield in the SR. The shape of the BDT distribution is taken from data region B, while the shape  
 1933 of the  $m_T$  distribution in the cut-based analysis is taken from  $Z/\gamma^*$  MC in the SR. The values of the  
 1934  $\beta_{\ell\ell}$  in the cut-based and BDT analyses from this method are summarized in table 5.11. They are quite  
 1935 consistent with one another within the statistical uncertainties. In the cut-based analysis, the same cut  
 1936 efficiency correction factors shown in table 5.10 are also applied (in product with the  $\beta_{\ell\ell}$ ) in the same  
 1937 flavor channels to this background, as they were derived in the  $Z$  peak region.

	$\beta_t$
BDT Bin 1	$1.01 \pm 0.15$
BDT Bin 2	$0.89 \pm 0.28$
Cut-based	$0.81 \pm 0.21$

**Table 5.11:**  $Z/\gamma^* \rightarrow \ell\ell$  normalization factors for cut-based and BDT analyses. Uncertainties are statistical only.

### 1938 5.5.5 $WW$ AND OTHER DIBOSON BACKGROUNDS

1939 The  $WW$  and other diboson backgrounds have both their shape and normalization taken from MC  
 1940 simulation. They are validated in dedicated control regions and found to agree with data well.

1941 As  $WW$  is the largest of these backgrounds and is irreducible, validating the estimate is of particular  
 1942 importance. The validation region is constructed by requiring the pre-selection cuts on leptons and  $m_{\ell\ell}$ ,  
 1943  $n_b = 0$ , and  $m_T > 100$  GeV. The  $m_{T2}$  variable[?] is an additional discriminant that will isolate  
 1944 the  $WW$  background, and a requirement of  $m_{T2} > 160$  GeV is placed to define the  $WW$  validation  
 1945 region. This cut gives a 60% purity for the validation region. The derived normalization factor in the  
 1946 region is  $1.15 \pm 0.19$  and is thus consistent with unity. Figure 5.11 shows the  $m_{T2}$  distribution and how  
 1947 it distinguishes the  $WW$  background.

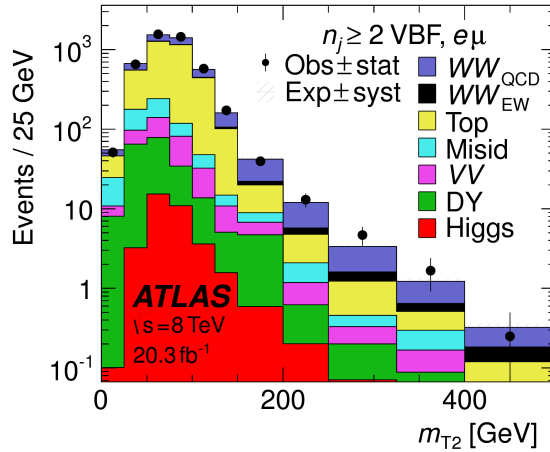


**Figure 5.11:** Distribution of  $m_{T2}$  in the  $WW$  validation region of the VBF analysis[21].

1948 5.5.6 HIGGS PRODUCTION VIA GLUON-GLUON FUSION

1949 Because this analysis is dedicated to measuring the VBF contribution to Higgs production, the com-  
1950 ponent of Higgs production from gluon-gluon fusion is treated as a background. The shape is taken  
1951 directly from simulation, using the generators described in table 5.4. In the final combined fit of all dif-  
1952 ferent signal regions, the normalization is controlled by either a combined signal strength parameter  $\mu$ ,  
1953 which controls the normalization of both ggF and VBF production, or a separate parameter  $\mu_{\text{ggF}}$  de-  
1954 pending on the interpretation being presented in the final results.

1955 5.5.7 BACKGROUNDS WITH MISIDENTIFIED LEPTONS

1956 As discussed previously, the  $W + \text{jets}$  and QCD multijet backgrounds are derived with fully data-driven  
1957 methods. These backgrounds do not make a large contribution to the final VBF signal region but their  
1958 estimation methods are discussed briefly here.

1959  $W + \text{jets}$  BACKGROUND

1960 The  $W + \text{jets}$  background enters the signal region by having one of the jets mis-reconstructed as a lep-  
1961 ton. The background is estimated by constructing a control sample with two leptons, where one lepton  
1962 passes the usual lepton quality cuts but the second lepton fails one of those cuts (also known as the “anti-  
1963 identified” lepton). This control region is rich in the  $W + \text{jets}$  contribution because if a second lepton is  
1964 reconstructed in a  $W + \text{jets}$  event it is likely to be poor quality. The purity of this  $W + \text{jets}$  control sample  
1965 is 85% to 90% depending on the exact configuration of leptons in the final state.

1966 The signal region estimate of  $W + \text{jets}$  is estimated by extrapolation from the control sample to the sig-  
1967 nal region using extrapolation factors derived in a  $Z + \text{jets}$  control sample in data. The extrapolation fac-  
1968 tor is the ratio of the number of lepton candidates satisfying all quality criteria to the number of lepton  
1969 candidates anti-identified. This ratio is measured in bins of  $p_T$  and  $\eta$ . Thus, the final signal region esti-  
1970 mate (binned as the extrapolation factor is binned) is simply the number of events in the anti-identified  
1971 lepton control sample multiplied by the extrapolation factor derived from the  $Z + \text{jets}$  control sample.  
1972 Figure 5.12 shows the extrapolation factors derived for electrons and muons.

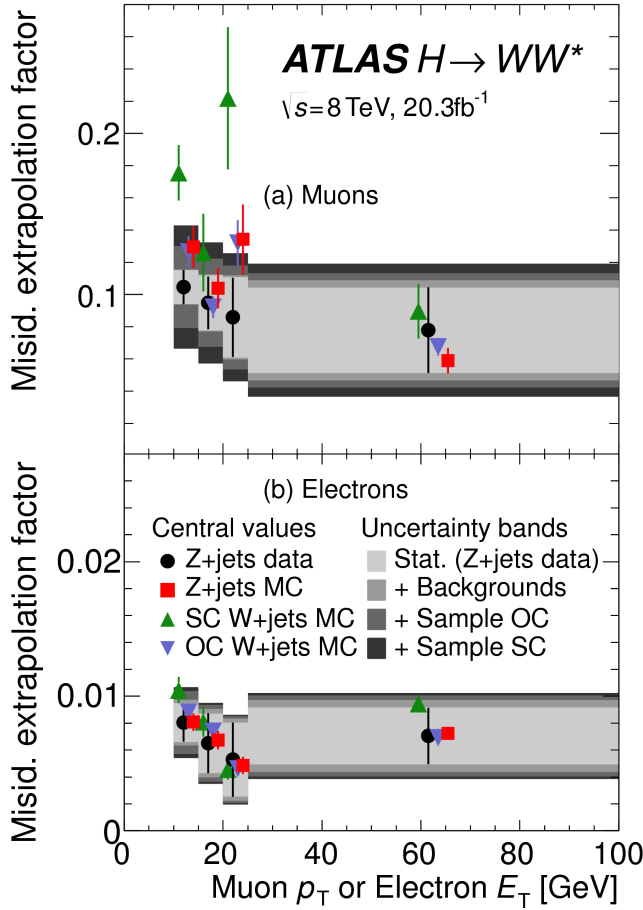


**Figure 5.12:** Extrapolation factors for the  $W$ +jets estimate derived for muons (a) and electrons (b) as a function of lepton  $p_T$ [21].

1973      QCD MULTIJET BACKGROUND

1974      The method for estimating the multijet background is very similar to the  $W$ +jets estimation method.  
 1975      The control sample in this case has two anti-identified leptons but otherwise satisfies all signal region  
 1976      requirements. The extrapolation factor is estimated from a multijet sample and applied twice to the  
 1977      control sample.

1978      **5.5.8 BACKGROUND COMPOSITION IN FINAL SIGNAL REGION**

1979      After all of these estimation procedures, the final signal region composition can be calculated. The esti-  
 1980      mated yields are all shown in table 5.7. Figure 5.13 shows the relative percentages of the different back-

1981 ground for the different flavor and same flavor final states. In  $e\mu$ , the leading backgrounds are top back-  
 1982 grounds, ggF Higgs, and SM  $WW$  production. In  $ee/\mu\mu$ , the leading background is Drell-Yan, fol-  
 1983 lowed by top and ggF Higgs.

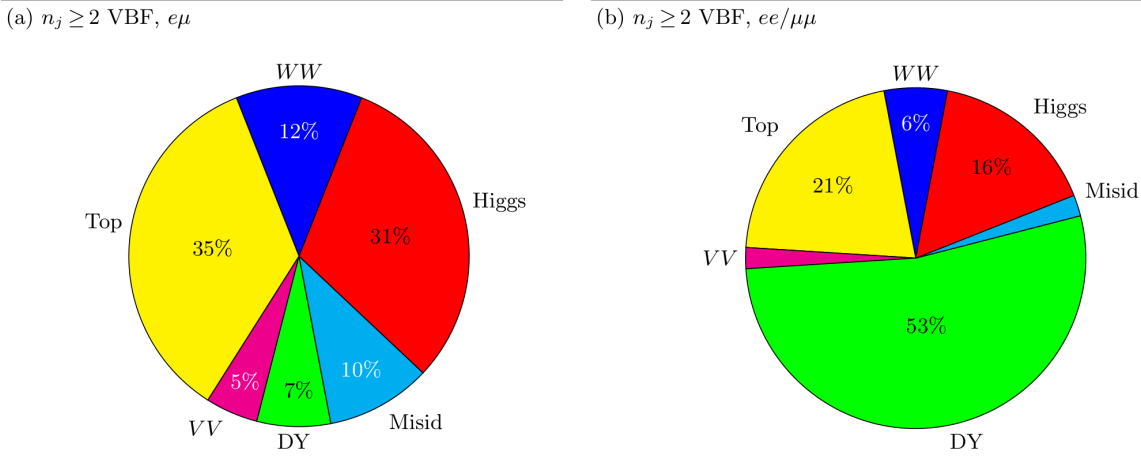


Figure 5.13: Background composition in final VBF signal region[21].

## 1984 5.6 SYSTEMATIC UNCERTAINTIES

1985 There are two main types of systematic uncertainties that are assessed for the analysis. First, theoreti-  
 1986 cal uncertainties associated with the various signal and background yield estimates are discussed. Then,  
 1987 experimental uncertainties due to detector effects are shown. Normalization uncertainties refer to uncer-  
 1988 tainties that affect the cross section of the process in question in the signal region being probed. Shape  
 1989 uncertainties refer to systematic uncertainties that affect the shape of the final discriminating variable  
 1990 (either  $m_T$  or  $O_{BDT}$ ).

### 1991 5.6.1 THEORETICAL UNCERTAINTIES

1992 There are four main components to theoretical uncertainties assigned to signal and background pro-  
 1993 cesses taken from Monte Carlo. Each one is a different source of variation in the overall acceptance for  
 1994 that process. The first involves variation of the QCD renormalization and factorization scales used in  
 1995 the calculation. In this case, the two scales are varied independently and simultaneously by factors of  
 1996 two high or low and quantifying the resulting variation in normalization and shape for the process. This

approximates the correction to the cross section that would come from including the next order of the QCD calculation (referred to as scale uncertainty). Next, there is an uncertainty associated with the PDF set used in generating the events. The uncertainty eigenvectors for the given PDF set are studied, and the envelope of maximal variation is taken as an uncertainty. Finally, there are two uncertainties associated with the choice of MC software (referred to as PDF uncertainty). An uncertainty associated with the generator chosen for the hard scattering process is evaluated by keeping the parton showering software constant but varying the matrix element generator and taking the maximal variation as an uncertainty (referred to as the generator uncertainty). The converse variation can also be done, where the matrix element generator remains constant and the generator used for the underlying event/parton shower modeling is varied (referred to as the UE/PS uncertainty). In cases where the background is normalized in a control region, the systematic uncertainty arises from variations of the extrapolation factor  $\alpha$  between the CR and the SR, which can affect the normalization of the background in the SR.

There are two additional uncertainties that are applied to the Higgs processes as well. First, there are uncertainties assigned to the Higgs total production cross section. Then, there are uncertainties assigned based on the fact that the analysis is done in exclusive jet bins and it is possible for signal events to migrate from one bin to the next depending on the presence or absence of jets. These are assigned using the Jet Veto Efficiency (JVE) procedure[?] for ggF events and the Stewart-Tackmann (ST) method[87] for VBF production.

Table 5.12 shows the total theory uncertainties on the backgrounds in the cut-based analysis. These are the sum in quadrature of the uncertainties from each of the variations described above.

Process	Theory syst. (%)
ggF $H$	48
Top	26
QCD $WW$	37
$Z/\gamma^* \rightarrow \tau\tau$	6.1

**Table 5.12:** Systematic uncertainties for various processes in the cut-based VBF analysis, given in units of % change in yield.  
Values are given for the low  $m_{jj}$  signal region.

Figures 5.14 and 5.15 show the variations in the extrapolation factor from the PDF and QCD uncertainties on the top background estimate, binned in  $m_T$ , for the cut-based analysis. In both cases, there

2019 was no significant shape uncertainty but normalization uncertainties were assigned according to the  
 2020 maximal variation. These uncertainties enter into the 26% total uncertainty on top quoted in table 5.12.  
 2021 While the estimate for the same-flavor  $Z/\gamma^* \rightarrow \ell\ell$  background is data-driven, there is still a sys-  
 2022 tematic uncertainty taken for the non-closure of the method in Monte Carlo. This is taken as the max-  
 2023 imum of the deviation of the non-closure factor  $f_{\text{corr}}$  from unity and its uncertainty, or  $\max(|1 -$   
 2024  $f_{\text{corr}}|, \delta f_{\text{corr}})$ . For the cut-based analysis this non-closure uncertainty 23%, while for the BDT analy-  
 2025 sis it is 17%.

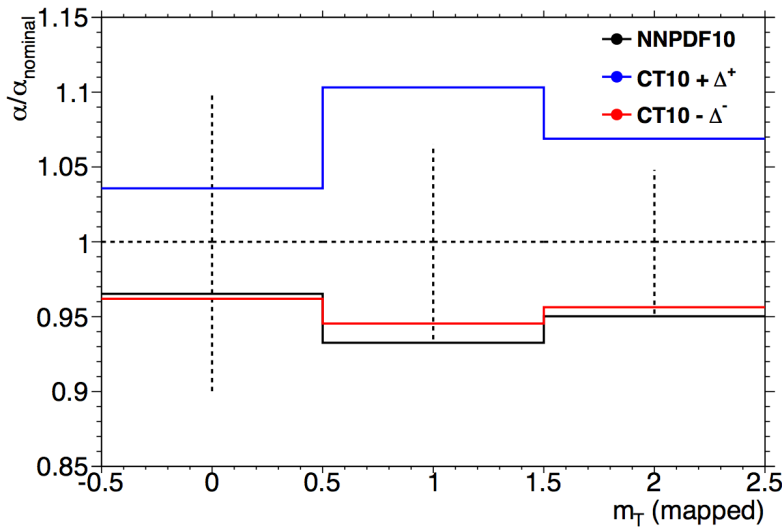
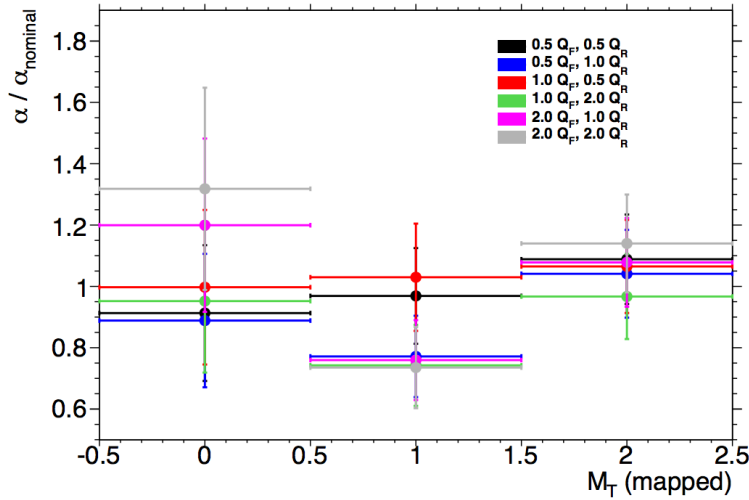


Figure 5.14: Variations in the top background extrapolation factor in the cut-based analysis due to PDF uncertainties, binned in  $m_T$ .

### 2026 5.6.2 EXPERIMENTAL UNCERTAINTIES

2027 In this analysis, the theoretical uncertainties end up being the most dominant, but there are some ex-  
 2028 perimental uncertainties that make a contribution as well. The first is the uncertainty on the measured  
 2029 integrated luminosity, which affects backgrounds whose normalization is taken from MC and is mea-  
 2030 sured to be 2.8% in the 8 TeV dataset [88]. The dominant sources of uncertainty overall are uncertainties  
 2031 on the jet energy scale and resolution and the  $b$ -tagging efficiency. Additional sources include lepton  
 2032 uncertainties on identification, resolution, and trigger efficiency, as well as uncertainties on the missing  
 2033 transverse momentum .



**Figure 5.15:** Variations in the top background extrapolation factor in the cut-based analysis due to QCD scale uncertainties, binned in  $m_T$ .

2034     The jet energy scale uncertainty is split into several independent components, including jet-flavor  
 2035     dependent calorimeter response uncertainties, uncertainties on modeling of pile-up interactions, uncer-  
 2036     tainties on extrapolation from the central to forward detector regions, and MC non-closure [89]. The  
 2037     uncertainty on energy scale for jets used in this analysis ranges from 1% to 7% depending on the jet  $p_T$   
 2038     and  $\eta$ . The jet energy resolution varies from 5% to 20%, with uncertainties ranging from 2% to 40%  
 2039     (the largest uncertainties occurring at the selection threshold).

2040     The b-tagging efficiency is independently measured in data samples enriched in dileptonic decays of  
 2041      $t\bar{t}$  events or in events where a muon is reconstructed in the vicinity of a jet[90, 91]. The efficiencies and  
 2042     their uncertainties are binned in  $p_T$  and decomposed into uncorrelated components using an eigenvec-  
 2043     tor method[? ]. Uncertainties on the efficiency range from 1% to 7.8%. The uncertainty on the rate of  
 2044     misidentification of  $c$ -jets as  $b$ -jets ranges from 6-14%, while the uncertainty on the rate of light jet mis-  
 2045     tagging ranges from 9-19% depending on  $p_T$  and  $\eta$ .

2046     The total experimental uncertainties on different signal and background components are summa-  
 2047     rized in table 5.13. They are compared to the level of other statistical and systematic uncertainties as well.  
 2048     Overall, the experimental uncertainties are sub-dominant compared to the statistical and theoretical  
 2049     uncertainties.

Sample	Total error	Stat. error	Expt. syst. err.	Theo. syst. err.
$n_j \geq 2$ VBF-enriched				
$N_{\text{sig}}$	13	-	6.8	12
$N_{\text{bkg}}$	9.2	4.7	6.4	4.5
$N_{WW}$	32	-	14	28
$N_{\text{top}}$	15	9.6	7.6	8.5
$N_{\text{misid}}$	22	-	12	19
$N_{VV}$	20	-	12	15
$N_{\tau\tau} (\text{DY})$	40	25	31	2.9
$N_{ee/\mu\mu} (\text{DY})$	19	11	15	-

**Table 5.13:** Composition of the post-fit uncertainties (in %) on the total signal ( $N_{\text{sig}}$ ), total background ( $N_{\text{bkg}}$ ), and individual background yields in the VBF analysis[21].

## 2050 5.7 RESULTS

2051 While the combined results of all the  $H \rightarrow WW^*$  sub-analyses will be discussed in the next chapter, this  
 2052 section presents the results of the VBF specific analysis and interpretations.

2053 As table 5.7 shows, the final cut-based signal region contains 20 events in data with  $m_T < 150$  GeV,  
 2054 14 coming from the  $e\mu$  channel and 6 coming from the  $ee + \mu\mu$  channel. The BDT analysis has many  
 2055 more candidates due to its looser selection, and the yields in each bin of  $O_{\text{BDT}}$  are shown in table 5.14.

2056 Figure 5.16(a) shows the final distribution of data candidates compared to the expected  $m_T$  distri-  
 2057 bution for signal and background. The data are very consistent with a VBF Higgs hypothesis. Fig-  
 2058 ure 5.16(b) shows where the data candidates fall in the two-dimensional binning of  $m_T$  and  $m_{jj}$  used  
 2059 in the fit for the cut-based analysis.

2060 Figure 5.17 shows the distributions of  $O_{\text{BDT}}$  and  $m_T$  in the VBF BDT analysis. Again the data are  
 2061 quite consistent with a VBF Higgs hypothesis.

2062 Because the cut-based result is used as a validation for the BDT analysis and the two signal regions are  
 2063 not fully orthogonal, it is interesting to explore which events overlap between the two analyses. Of the  
 2064 twenty events in the cut-based signal region, only seven were not selected by the BDT analysis, while the  
 2065 other thirteen also enter the BDT signal region. Figure ?? shows where the different analysis candidates  
 2066 lie in the  $m_{jj}$ - $m_T$  plane. This shows clearly that the advantage of the BDT analysis is that it can extract

(a) Before the BDT classification

Selection	Summary						Composition of $N_{\text{bkg}}$											
	$N_{\text{obs}}/N_{\text{bkg}}$	$N_{\text{obs}}$	$N_{\text{bkg}}$	$N_{\text{signal}}$	$N_{\text{ggF}}$	$N_{\text{VBF}}$	$N_{\text{VH}}$	$N_{\text{WW}}$	$N_{\text{WW}}^{\text{NEW}}$	$N_{\text{WW}}^{\text{QCD}}$	$N_t$	$N_{\text{Wj}}$	$N_{\text{misid}}$	$N_{ij}$	$N_{VV}$	$N_{\text{Drell-Yan}}$	$N_{\tau\tau}^{\text{QCD}}$	$N_{\tau\tau}^{\text{NEW}}$
$e\mu$ sample	$1.04 \pm 0.04$	718	689	13	15	2.0	90	II	327	42	29	23	31	—	2.2	130	2	—
$ee/\mu\mu$ sample	$1.18 \pm 0.08$	469	397	6.0	7.7	0.9	37	3	132	17	5.2	1.2	10.1	168	23	1	—	—

(b) Bins in  $O_{\text{BDT}}$ 

$e\mu$ sample	Bins in $O_{\text{BDT}}$																	
	Bin 0 (not used)	Bin 1	Bin 2	Bin 3	Bin 4	Bin 5	Bin 6	Bin 7	Bin 8	Bin 9	Bin 10	Bin 11	Bin 12	Bin 13	Bin 14	Bin 15	Bin 16	Bin 17
$ee/\mu\mu$ sample	$1.91 \pm 0.08$	396	345	3.8	1.3	0.8	33	2	123	16	4.1	1.1	8.8	137	20.5	0.5	—	—
Bin 0 (not used)	$0.82 \pm 0.14$	53	45	1.5	2.2	0.1	3.0	0.5	10.4	1.8	0.8	0.2	0.9	26	1.7	0.1	—	—
Bin 1	$1.77 \pm 0.49$	14	7.9	0.6	2.5	—	0.8	0.3	1.1	0.2	0.2	—	0.3	4.4	0.3	0.1	—	—
Bin 2	$6.52 \pm 2.87$	6	0.9	0.2	1.7	—	0.1	0.2	0.2	—	—	—	—	0.7	—	—	—	—

**Table 5.14:** Event selection for the VBF BDT analysis. The event yields in (a) are shown after the preselection and the additional requirements applied before the BDT classification (see text). The event yields in (b) are given in bins in  $O_{\text{BDT}}$  after the classification[21].

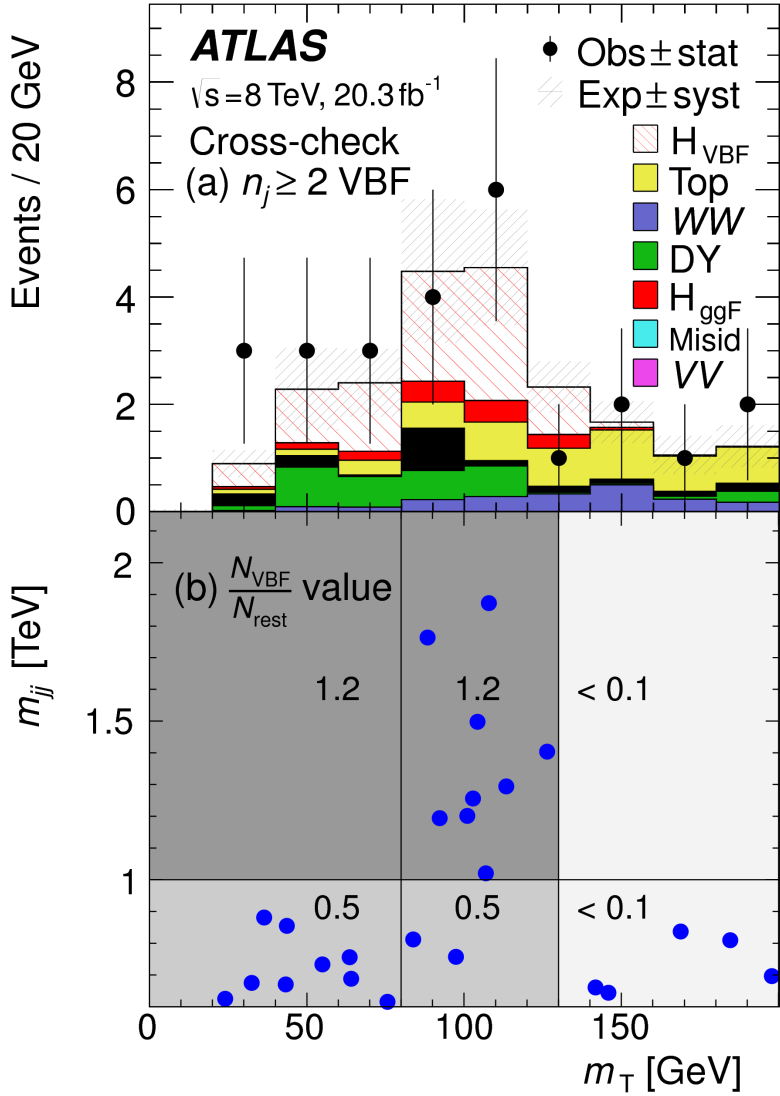


**Figure 5.16:** Postfit distributions in the cut-based VBF analysis. Panel (a) shows the one-dimensional  $m_T$  distribution, while (b) shows the data candidates split into the bins of  $m_T$  and  $m_{jj}$  used in the final fit[21].

signal candidates lower  $m_{jj}$  region due to its ability to recognize correlations with other variables.  
 While the context of these results in the broader  $H \rightarrow WW^*$  statistical analysis will be presented in the next chapter, the significance of the VBF observation can be shown here. In the BDT analysis, the expected signal significance was  $2.7\sigma$ , while the observed significance was  $3.1\sigma$ . In the cut-based analysis, the expected significance was  $2.1\sigma$  and the observed significance was  $3.0\sigma$ . The compatibility between these two results can be evaluated by computing the probability of observing a larger difference

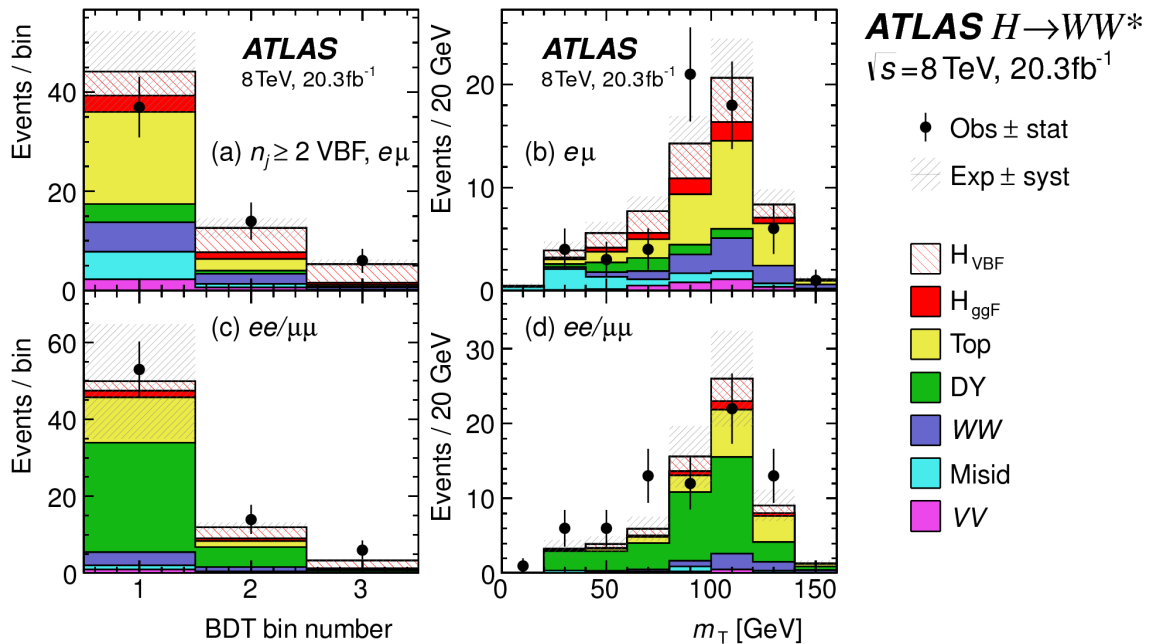


Figure 5.17: Postfit distributions in the BDT VBF analysis[21].

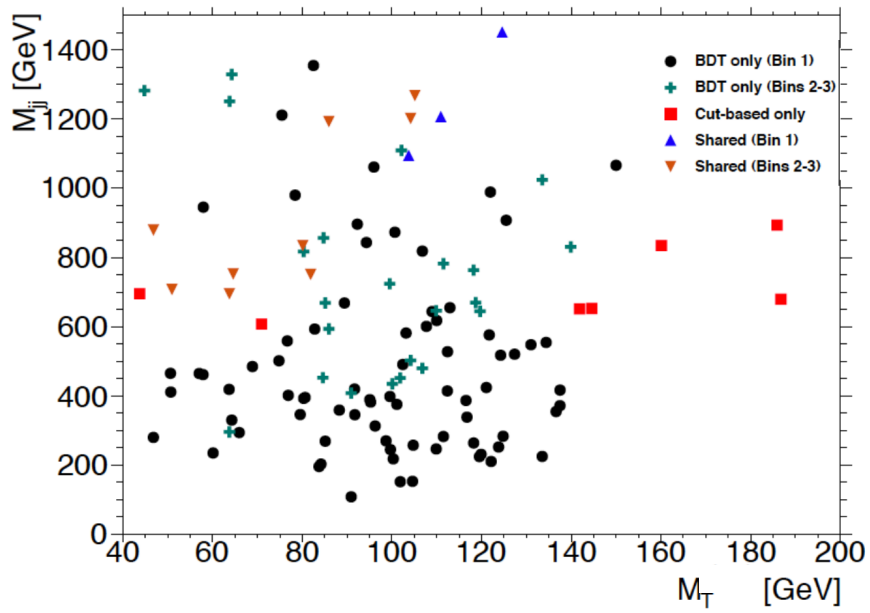


Figure 5.18: Overlap between cut-based and BDT VBF signal region candidates in the  $m_{jj}$ - $m_T$  plane.

2073 in  $Z_0$  values than the one measured. Using toy Monte Carlo with the ggF signal strength fixed to unity  
2074 and considering only statistical uncertainties, this probability is computed to be 79%, indicating good  
2075 agreement between the analyses.

2076 This result represents the first observation of the vector boson fusion production of a Higgs boson.

*The feeling is less like an ending than just another  
starting point.*

Chuck Palahniuk

# 6

2077

2078

## Combined Run I $H \rightarrow WW^* \rightarrow \ell\nu\ell\nu$

2079

## results

2080 6.1 INTRODUCTION

2081 In the final statistical analysis of  $H \rightarrow WW^* \rightarrow \ell\nu\ell\nu$ , the dedicated gluon-gluon fusion and vector  
2082 boson fusion sensitive signal regions are all combined into a single fit to determine the main parameters  
2083 of interest, the Higgs signal strength  $\mu$  and mass  $m_H$ . Therefore, while the specific requirements applied  
2084 for the VBF sensitive analysis are discussed in chapter 5, the final measurement of these parameters can  
2085 only be discussed in combination with the results of the ggF dedicated analysis. For example, because  
2086 ggF Higgs production is considered a background in the VBF analysis, the ggF dedicated signal regions  
2087 can actually constrain the normalization of this background in the VBF dedicated region.

2088 This chapter presents the combined interpretation of results in the  $H \rightarrow WW^* \rightarrow \ell\nu\ell\nu$  analysis

SR category $i$			Fit var.
$n_j$ , flavor	$\otimes m_{\ell\ell}$	$\otimes p_T^{\ell 2}$	
$n_j = 0$			
$e\mu$	$\otimes [10, 30, 55]$	$\otimes [10, 15, 20, \infty]$	$\otimes [e, \mu]$
$ee/\mu\mu$	$\otimes [12, 55]$	$\otimes [10, \infty]$	$m_T$
$n_j = 1$			
$e\mu$	$\otimes [10, 30, 55]$	$\otimes [10, 15, 20, \infty]$	$\otimes [e, \mu]$
$ee/\mu\mu$	$\otimes [12, 55]$	$\otimes [10, \infty]$	$m_T$
$n_j \geq 2$ ggF			
$e\mu$	$\otimes [10, 55]$	$\otimes [10, \infty]$	$m_T$
$n_j \geq 2$ VBF			
$e\mu$	$\otimes [10, 50]$	$\otimes [10, \infty]$	$O_{BDT}$
$ee/\mu\mu$	$\otimes [12, 50]$	$\otimes [10, \infty]$	$O_{BDT}$

**Table 6.1:** All signal regions definitions input into final statistical fit[21].

for gluon fusion and vector boson fusion Higgs production. First, the results of the dedicated gluon fusion search are presented. Then, a comparison of the individual production mode signal strengths ( $\mu_{ggF}$  and  $\mu_{VBF}$  and a measurement of the combined signal strength ( $\mu$ ) are shown. Subsequently, the measured values of the Higgs couplings to fermions and vector bosons is presented. Finally, the cross section measurement for ggF and VBF production are shown.

## 6.2 RESULTS OF DEDICATION GLUON FUSION $H \rightarrow WW^* \rightarrow \ell\nu\ell\nu$ SEARCH

The details of the dedicated gluon fusion  $H \rightarrow WW^* \rightarrow \ell\nu\ell\nu$  search are not discussed in this thesis and instead left to more comprehensive sources[21]. However, a brief summary of the results are essential for describing the results of the full analysis and interpreting the results of the dedicated VBF search in this broader context.

Table 6.1 shows the individual signal regions that were input into the final statistical fit. The ggF dedicated bins use  $m_T$  as their discriminating variable and are separated into bins of  $p_T$  of the subleading lepton as well. The VBF dedicated bin uses the  $O_{BDT}$  distribution as its final discriminant.

Table 6.2 shows the yields in the various signal regions in both data and expected signal and back-

2103 grounds. The yields for signal and background are all scaled according to the final normalizations calcu-  
2104 lated in the fit.

	$N_{\text{obs}}$	$N_{\text{bkg}}$	$N_{\text{ggF}}$	$N_{\text{VBF}}$
$n_j = 0$	3750	$3430 \pm 90$	$300 \pm 50$	$8 \pm 4$
$n_j = 1$	1596	$1470 \pm 40$	$102 \pm 26$	$17 \pm 5$
$n_j \geq 2, \text{ggF } e\mu$	1017	$960 \pm 40$	$37 \pm 11$	$13 \pm 1.4$
$n_j \geq 2, \text{VBF}$	130	$99 \pm 9$	$7.7 \pm 2.6$	$21 \pm 3$

**Table 6.2:** Post-fit yields in the different ggF and VBF dedicated signal regions[21].

2105 Figure 6.1 shows the final post-fit  $m_T$  distribution in the  $n_j \leq 1$  regions. The data are very consistent  
2106 with the hypothesis of ggF Higgs production.

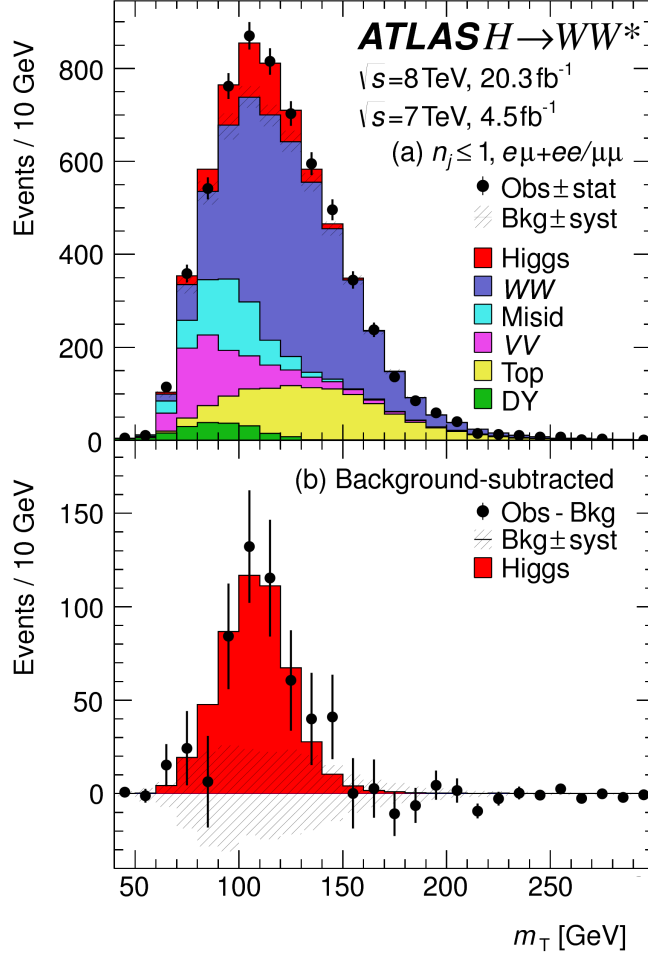


**Figure 6.1:** Post-fit  $m_T$  distribution in the  $n_j \leq 1$  regions[21].

2107 These yields are used as input, along with the VBF results in chapter 5, for the physical interpretation  
2108 of results presented in subsequent sections.

2109 **6.3 SIGNAL STRENGTH MEASUREMENTS IN ggF AND VBF PRODUCTION**

2110 When all of the signal regions are combined in the fit, there can be a combined measurement of the sig-  
2111 nal strength as well as the individual ggF and VBF signal strengths. The combined signal strength is the  
2112 ratio of the sum of the gluon fusion and VBF cross sections to the theory prediction, or a singal strength  
2113 for the total Higgs production cross section that this analysis is sensitive to. The final measured com-  
2114 bined signal strength  $\mu$  is measured shown in equation 6.1.

$$\begin{aligned} \mu &= 1.09 \quad {}^{+0.16}_{-0.15} \text{ (stat.)} \quad {}^{+0.08}_{-0.07} \left( \begin{array}{l} \text{expt} \\ \text{syst} \end{array} \right) \quad {}^{+0.15}_{-0.12} \left( \begin{array}{l} \text{theo} \\ \text{syst} \end{array} \right) \quad \pm 0.03 \left( \begin{array}{l} \text{lumi} \\ \text{syst} \end{array} \right) \\ &= 1.09 \quad {}^{+0.16}_{-0.15} \text{ (stat)} \quad {}^{+0.17}_{-0.14} \text{ (syst)} \\ &= 1.09 \quad {}^{+0.23}_{-0.21}. \end{aligned} \tag{6.1}$$

2115 Figure 6.2 gives the best fit signal strength  $\hat{\mu}$  as a function of hte hypothesized Higgs mass. The value  
2116 at 125.36 GeVcorresponds to the  $\mu$  quoted in equation 6.1. This value of the Higgs mass is used because  
2117 it is the most precise mass measurement from ATLAS, a result of the combined  $\gamma\gamma$  and  $ZZ$  mass mea-  
2118 surements[? ].

2119 As explained in chapter 3, a probability  $p_0$  can be computed using the test statistic  $q_0$  to quantify the  
2120 probability that the background could fluctuate to produce an excess at least as large as the one observed  
2121 in the data. The local  $p_0$  value is shown in figure 6.3 as a function of  $m_H$ . The minimum  $p_0$  value is  
2122 at  $m_H = 130$  GeV and coresponds to a significance of  $6.1\sigma$ . The curve is relatively flat and the sig-  
2123 nificance is the same at 125.36 GeVwithin the quoted precision. The expected significance for a signal  
2124 with strength  $\mu = 1.0$  is  $5.8\sigma$ . This represents the first discovery level significance measurement in the  
2125  $H \rightarrow WW^* \rightarrow \ell\nu\ell\nu$  analysis.

2126 All the results presented so far in this section have been for the combined gluon fusion and VBF pro-  
2127 duction modes. However, each signal strength can be calculated separately in the likelihood as well.  
2128 There are two ways to do this. First, the likelihood can be parameterized in terms of a single parameter,

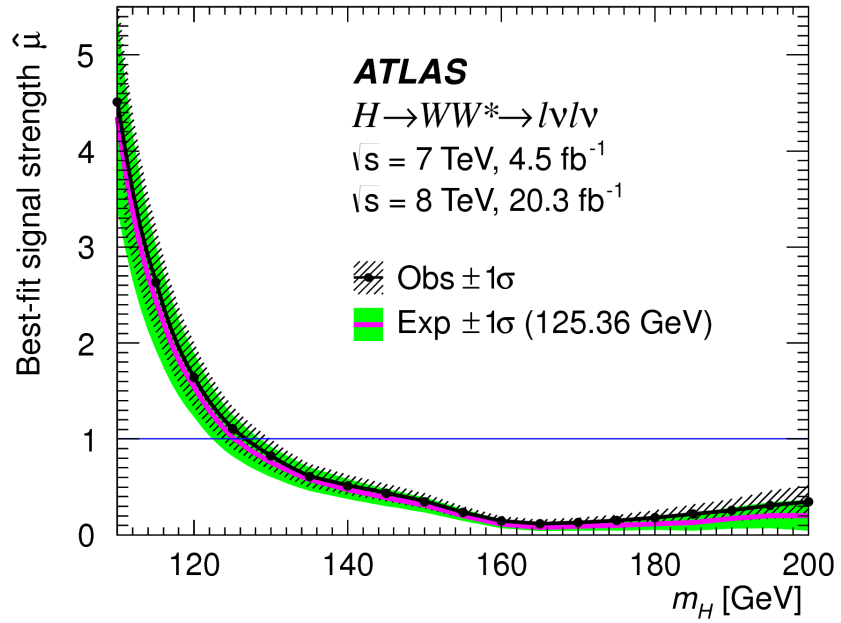


Figure 6.2: Best fit signal strength  $\hat{\mu}$  as a function of hypothesized  $m_H$ [21].

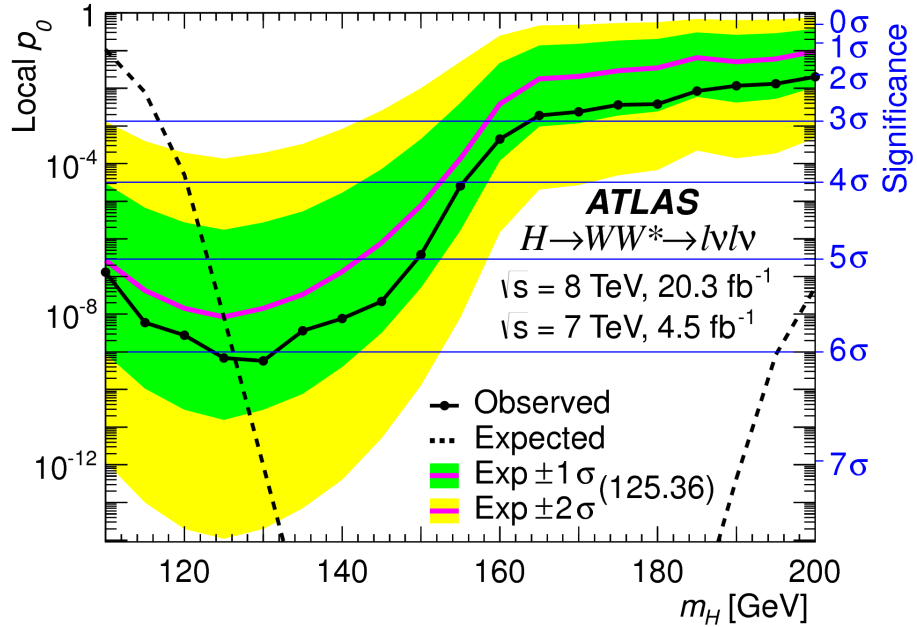
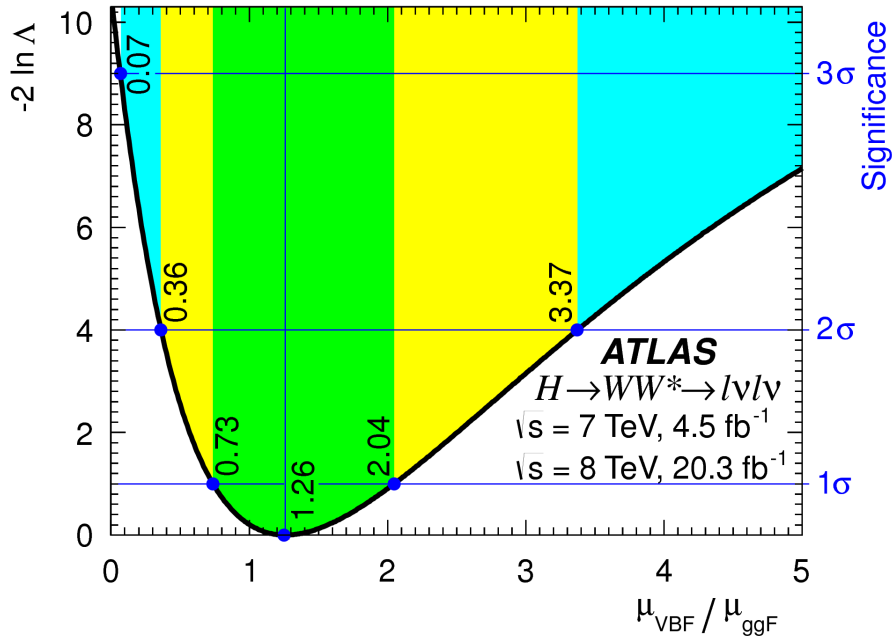


Figure 6.3: Local  $p_0$  as a function of  $m_H$ [21].

<sup>2129</sup> the ratio of the VBF and gluon fusion signal strengths. With this method, the significance of the VBF  
<sup>2130</sup> observation can be evaluated. Figure 6.4 shows the likelihood as a function of the ratio  $\mu_{\text{VBF}}/\mu_{\text{ggF}}$ .



**Figure 6.4:** Likelihood as a function of  $\mu_{\text{VBF}} / \mu_{\text{ggF}}$ [21].

2131 The best fit value of the ratio of signal strengths is shown in equation 6.2. Within the quoted uncer-  
 2132 tainties, it is consistent with a ratio of unity.

$$\frac{\mu_{\text{VBF}}}{\mu_{\text{ggF}}} = 1.26^{+0.61}_{-0.45} (\text{stat.})^{+0.50}_{-0.26} (\text{syst.}) = 1.26^{+0.79}_{-0.53} \quad (6.2)$$

2133 The null hypothesis for VBF production corresponds to a ratio of  $\mu_{\text{VBF}} / \mu_{\text{ggF}} = 0$ . The likelihood  
 2134 in figure 6.4 gives a significance of  $3.2\sigma$  at  $\mu_{\text{VBF}} / \mu_{\text{ggF}} = 0$ , as quoted in chapter 5.

2135 In addition to the ratio of signal strengths, each signal strength can be varied independently in the  
 2136 likelihood as well. Figure 6.5 shows the two dimensional likelihood scan in the  $\mu_{\text{ggF}}-\mu_{\text{VBF}}$  plane. The  
 2137 best fit values of the two signal strengths are shown in equation 6.3. Both are consistent with unity  
 2138 within their uncertainties.

$$\begin{aligned} \mu_{\text{ggF}} &= 1.02 \pm 0.19^{+0.22}_{-0.18} = 1.02^{+0.29}_{-0.26} \\ \mu_{\text{VBF}} &= 1.27 \pm 0.40^{+0.44}_{-0.40} \pm 0.21^{+0.29}_{-0.21} = 1.27^{+0.53}_{-0.45}. \end{aligned} \quad (6.3)$$

(stat.) (syst.)

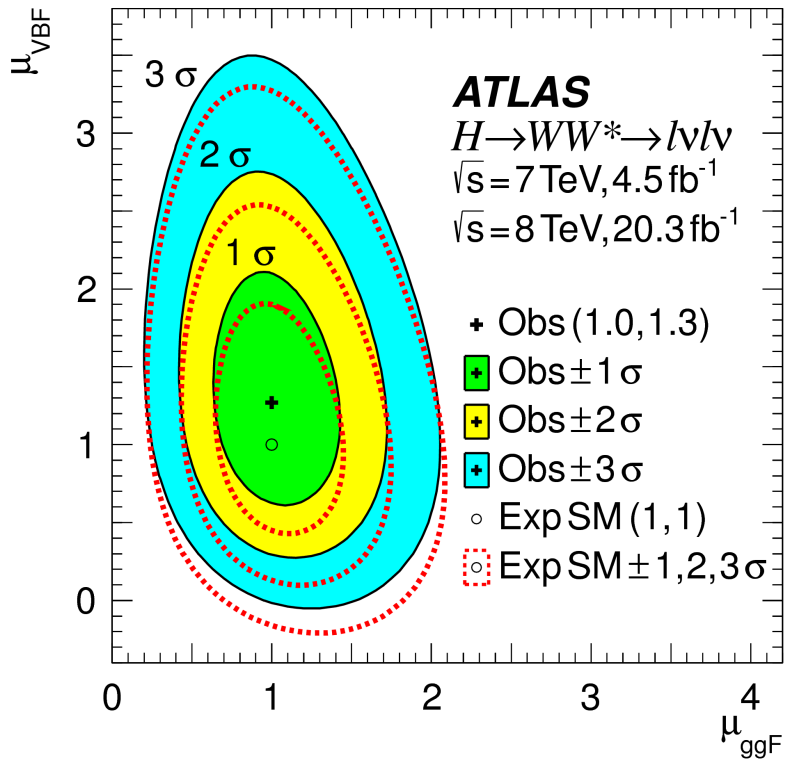


**Figure 6.5:** Likelihood scan as a function of  $\mu_{\text{VBF}}$  and  $\mu_{\text{ggF}}$ [21].

## 2139 6.4 MEASUREMENT OF HIGGS COUPLINGS TO VECTOR BOSONS AND FERMIONS

2140 Similar to the parameterization of signal strength, the couplings of the Higgs to fermions and bosons can  
 2141 also be parameterized. The parameter of interest in this case is  $\kappa$ , or the ratio of the measured coupling  
 2142 to the standard model expectation. Both the fermion and boson couplings have these so-called scale fac-  
 2143 tors,  $\kappa_F$  for fermions and  $\kappa_V$  for bosons. Gluon fusion production is sensitive to the fermion couplings  
 2144 through the top quark loops in its production, while VBF production is sensitive to the vector boson  
 2145 couplings in its production. Both modes are sensitive to the vector boson couplings in their decays. The  
 2146 signal strengths will have dependence on the coupling scale factors as described in equation 6.4[2].

$$\begin{aligned} \mu_{\text{ggF}} &\propto \frac{\kappa_F^2 \cdot \kappa_V^2}{(\mathcal{B}_{H \rightarrow f\bar{f}} + \mathcal{B}_{H \rightarrow gg}) \kappa_F^2 + (\mathcal{B}_{H \rightarrow VV}) \kappa_V^2} \\ \mu_{\text{VBF}} &\propto \frac{\kappa_V^4}{(\mathcal{B}_{H \rightarrow f\bar{f}} + \mathcal{B}_{H \rightarrow gg}) \kappa_F^2 + (\mathcal{B}_{H \rightarrow VV}) \kappa_V^2}. \end{aligned} \quad (6.4)$$

2147 Figure 6.6 shows the two-dimensional likelihood scan of  $\kappa_F$  and  $\kappa_V$ . The best-fit values are given in  
2148 equation 6.5. The best-fit values are consistent with unity within their uncertainties.

$$\begin{aligned} \kappa_F &= 0.93 & +0.24 & +0.21 & = 0.93 & +0.32 \\ && -0.18 & -0.14 && -0.23 \\ \kappa_V &= 1.04 & +0.07 & +0.07 & = 1.04 & \pm 0.11. \end{aligned} \quad (6.5)$$

(stat.) (syst.)

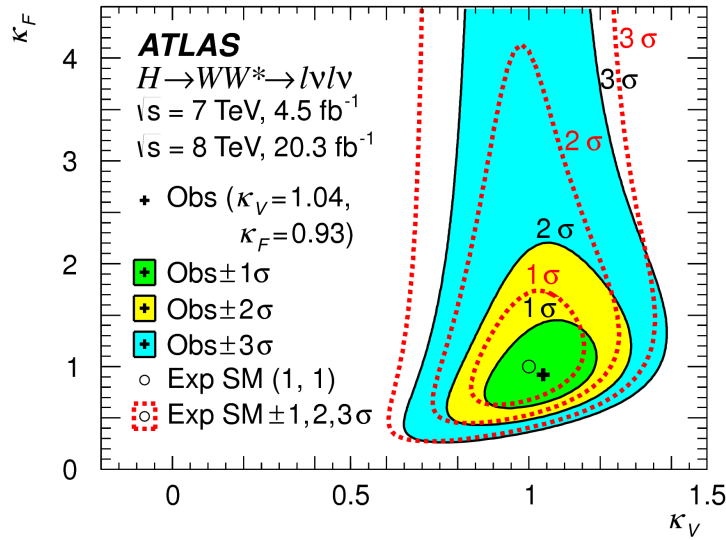


**Figure 6.6:** Likelihood scan as a function of  $\kappa_F$  and  $\kappa_V$ [21].

2149 **6.5 HIGGS PRODUCTION CROSS SECTION MEASUREMENT**

2150 Another measurement that comes naturally from the signal strength numbers quoted earlier is the pro-  
2151 duction cross section and 7 and 8 TeV for both gluon fusion and VBF production. The general equa-  
2152 tion for calculating the cross section is given in equation 6.6.

$$\begin{aligned} (\sigma \cdot \mathcal{B}_{H \rightarrow WW^*})_{\text{obs}} &= \frac{(N_{\text{sig}})_{\text{obs}}}{\mathcal{A} \cdot \mathcal{C} \cdot \mathcal{B}_{WW \rightarrow \ell\nu\ell\nu}} \cdot \frac{1}{\int L dt} \\ &= \hat{\mu} \cdot (\sigma \cdot \mathcal{B}_{H \rightarrow WW^*})_{\text{exp}} \end{aligned} \quad (6.6)$$

2153  $(N_{\text{sig}})_{\text{obs}}$  is the number of events observed in data.  $\mathcal{A}$  is the geometric and kinematic acceptance of  
 2154 the detector, while  $\mathcal{C}$  is the efficiency of the signal region selection for events that are reconstructed in the  
 2155 detector. The branching ratio of a  $WW$  system to leptons must also be divided out. The production  
 2156 cross section depends on the center of mass energy and the production mode desired (gluon fusion or  
 2157 VBF), and so three separate cross section measurements are quoted in equation 6.7.

$$\begin{aligned}
 \sigma_{\text{ggF}}^{\text{7TeV}} \cdot \mathcal{B}_{H \rightarrow WW^*} &= 2.0 \pm 1.7 {}^{+1.2}_{-1.1} = 2.0 {}^{+2.1}_{-2.0} \text{ pb} \\
 \sigma_{\text{ggF}}^{\text{8TeV}} \cdot \mathcal{B}_{H \rightarrow WW^*} &= 4.6 \pm 0.9 {}^{+0.8}_{-0.7} = 4.6 {}^{+1.2}_{-1.1} \text{ pb} \\
 \sigma_{\text{VBF}}^{\text{8TeV}} \cdot \mathcal{B}_{H \rightarrow WW^*} &= 0.51 {}^{+0.17}_{-0.15} {}^{+0.13}_{-0.08} = 0.51 {}^{+0.22}_{-0.17} \text{ pb.}
 \end{aligned} \tag{6.7}$$

(stat.) (syst.)

2158 The predicted cross section values for gluon fusion are  $3.3 \pm 0.4$  pb at 7 TeV and  $4.2 \pm 0.5$  pb  
 2159 at 8 TeV, consistent with the measured values within their uncertainties. For vector boson fusion, the  
 2160 predicted cross section is  $0.35 \pm 0.02$  pb, again consistent with the measured value.

## 2161 6.6 CONCLUSION

2162 The combined analysis of the gluon fusion and vector boson fusion processes in  $H \rightarrow WW^* \rightarrow \ell\nu\ell\nu$   
 2163 in the 7 and 8 TeV datasets has yielded the first discovery level significance for Higgs production in this  
 2164 decay channel. Additionally, precise measurements of the couplings to vector bosons and fermions are  
 2165 given. Finally, signal strengths and cross sections for each production mode are measured. Figure 6.7  
 2166 shows the  $H \rightarrow WW^* \rightarrow \ell\nu\ell\nu$  measurements in comparison with other Higgs decay channels in  
 2167 ATLAS. The measurement of signal strength from this channel remains the most sensitive in both the  
 2168 gluon fusion and VBF production modes for the Run 1 dataset.

**ATLAS**

### Individual analysis

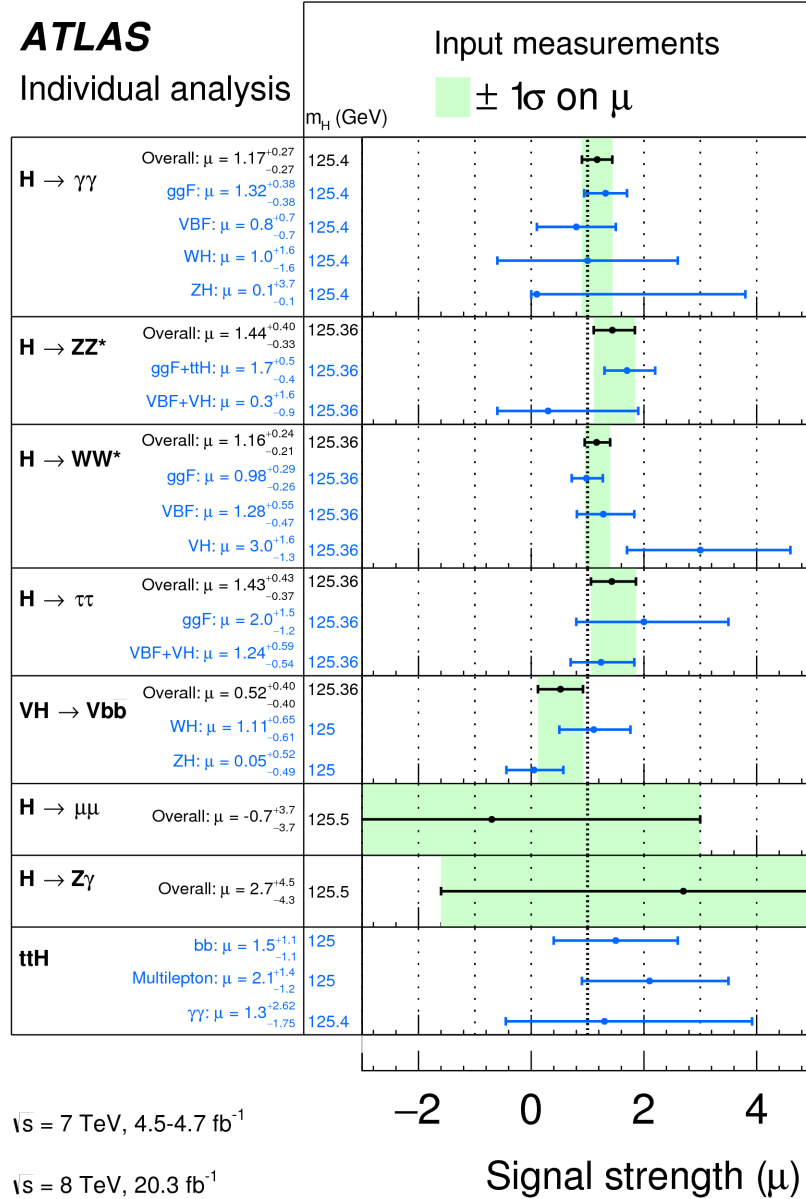


Figure 6.7: Comparison of signal strength measurements in different Higgs decay channels on ATLAS[23].

## Part III

2169

2170

2171

2172

Search for Higgs pair production in the

$HH \rightarrow b\bar{b}b\bar{b}$  channel in LHC Run 2 at  $\sqrt{s} =$

13 TeV

*Passion is in all great searches and is necessary to all  
creative endeavors.*

W. Eugene Smith

# 7

2173

## 2174 Search for Higgs pair production in boosted 2175 $b\bar{b}b\bar{b}$ final states

### 2176 7.1 INTRODUCTION

2177 After the discovery of the Higgs boson in the ATLAS Run 1 dataset and the subsequent measurements  
2178 of its properties, the Higgs transformed into a potential tool in searches for physics beyond the Stan-  
2179 dard Model. The pair production cross section of the Higgs can be enhanced through BSM physics.  
2180 Studying di-Higgs production also probes the Higgs self-coupling, shedding light on the structure  
2181 of the Higgs potential. This chapter presents a search for resonant production of a Higgs pair in the  
2182  $X \rightarrow HH \rightarrow b\bar{b}b\bar{b}$  final state in  $3.2 \text{ fb}^{-1}$  of data collected at  $\sqrt{s} = 13 \text{ TeV}$ . In particular, this  
2183 chapter focuses on a search for this final state in the regime where  $m_X$  is large ( $\gtrsim 1 \text{ TeV}$ ) and the Higgs  
2184 bosons in the decay are significantly boosted. A tailored selection for this boosted selection, using novel

2185 techniques in jet substructure and  $b$ -tagging, is discussed. Then, the data-driven background estimate is  
 2186 presented. Finally, the results of the search are shown. The signal models used as benchmarks are a spin-  
 2187 2 Randall Sundrum graviton (RSG) and a narrow width spin-0 resonance. These models are described  
 2188 in more detail in Chapter 1. Limits on signal models are reserved for the next chapter where the results of  
 2189 this chapter are combined with the results of a separate selection dedicated to the lower  $m_X$  regime.

## 2190 7.2 MOTIVATION

2191 With the center of mass energy increase from  $\sqrt{s} = 8$  TeV to  $\sqrt{s} = 13$  TeV, the LHC and ATLAS  
 2192 are able to probe new resonances at higher mass scales than previously accessible in Run 1. This is a  
 2193 powerful motivator for searching for a new resonance in the early 13 TeV data. Figure 7.1 shows the  
 2194 ratios of parton luminosities between 8 and 13 TeV for different resonance masses. For a resonance of  
 2195  $M_X = 2$  TeV, the cross section at  $\sqrt{s} = 13$  TeV is roughly a factor of 10 larger than at  $\sqrt{s} = 8$  TeV.

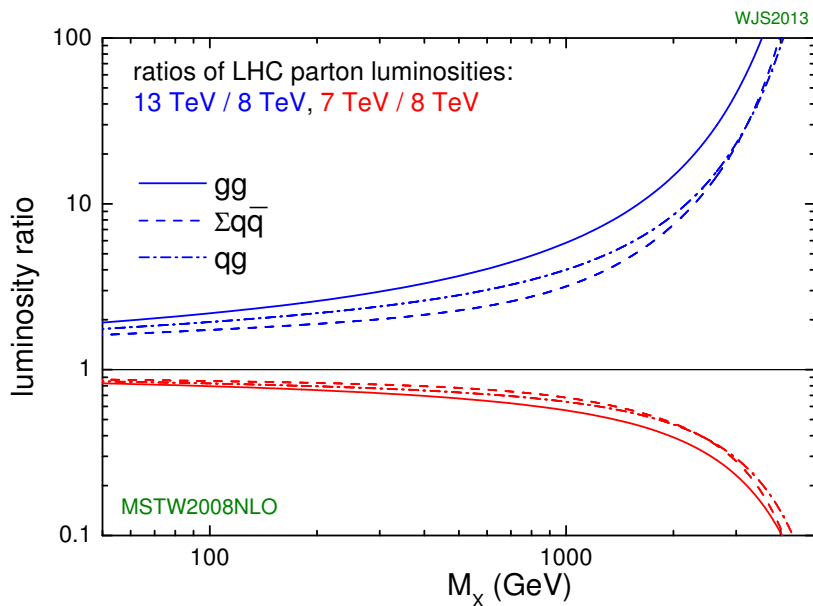


**Figure 7.1:** Parton luminosity ratios as a function of resonance mass  $M_X$  for 13/8 TeV and 7/8 TeV [24].

2196 Higgs pair production offers a vast array of unprobed regions of phase space where searches for BSM  
 2197 physics can be made. Chapter 1 discusses some possibilities for both resonant and non-resonant enhance-

ment of the di-Higgs production cross section. Given the increased mass reach of the LHC in Run 2, it is particularly important to focus on resonant searches at high  $m_X$ . One consideration when conducting a search in the  $HH$  final state is which decay modes of the Higgs to consider. Figure 7.2 shows the branching ratio of the  $HH$  final state for different combinations of decays of each individual Higgs. As the largest branching ratio for the 125 GeV Higgs is  $H \rightarrow b\bar{b}$ , the  $HH \rightarrow b\bar{b}b\bar{b}$  branching ratio is also the largest at 33%.

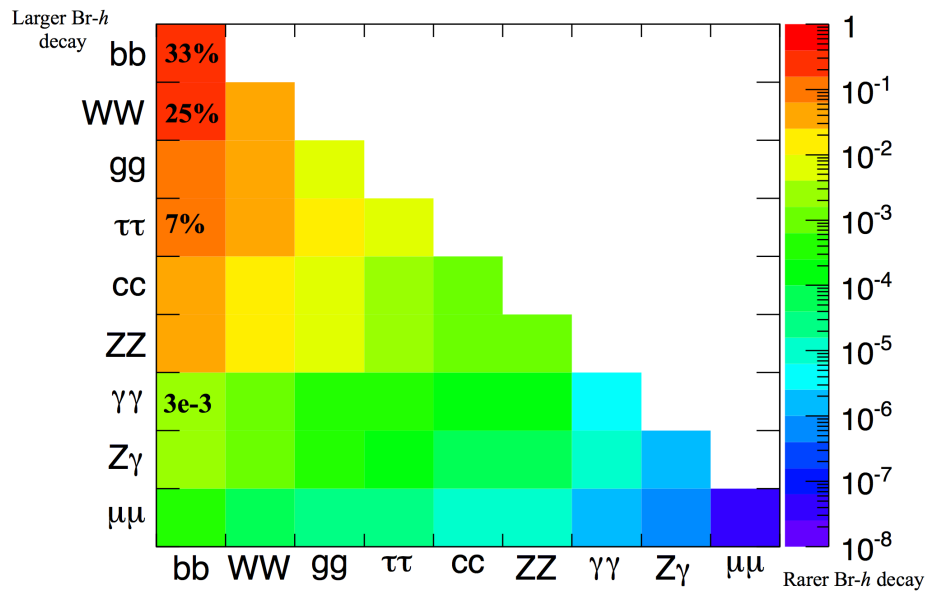


Figure 7.2: Summary of  $HH$  branching ratios [25].

At high  $m_X$ , the Higgs bosons resulting from the decay of a heavy resonance will have large  $p_T^*$ . The  $\Delta R$  between the decay products of the Higgs is inversely proportional to the Higgs  $p_T$ , as shown in equation ??.

$$\Delta R \approx \frac{2m}{p_T} \quad (7.1)$$

Figure 7.3 shows the minimum  $\Delta R$  between truth level  $B$  decay vertices in simulation samples for Randall-Sundrum gravitons of different masses. The figure shows that as the mass of the graviton increases, the  $\Delta R$  distribution between the  $b$  quarks in the Higgs decay tends to shift to lower values. Be-

\*In the limit that  $m_H \ell \ell m_X$ , the Higgs  $p_T$  is roughly  $m_X/2$ .

cause of this effect, it is necessary to tailor a selection to target these merged  $b$ -jets.

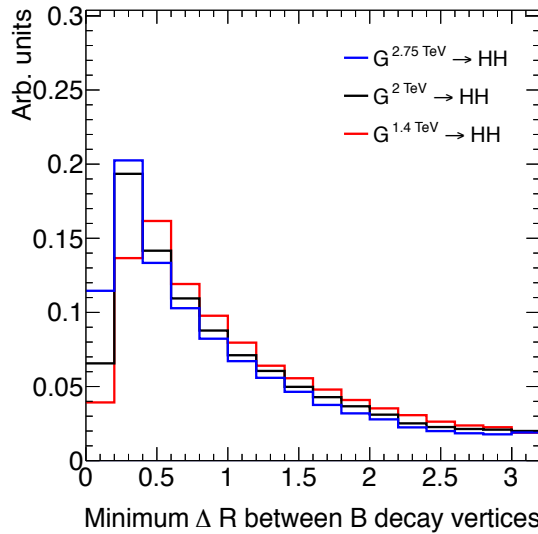


**Figure 7.3:** Minimum  $\Delta R$  between  $B$  decay vertices for different RSG masses in a  $G_{KK}^* \rightarrow HH \rightarrow 4b$  sample with  $c = 1$

## 7.3 DATA AND SIMULATION SAMPLES

### 7.3.1 SIGNAL MODELS

While the resonance search is by its nature generic (as it is a simple search for a peak in the  $4b$  invariant mass spectrum), there are two signal models that the selection requirements have been optimized for. The first is Randall-Sundrum (RSG) model, where a tower of massive spin-2 Kaluza-Klein gravitons is predicted. The second is a heavy narrow spin-0 resonance, the so-called “heavy Higgs”. This type of resonance arises, for example, in the two Higgs doublet model (2HDM). More details about the physics of these models and their motivation is given in chapter 1.

Signal graviton ( $G_{KK}^*$ ) events are generated at leading order (LO) with **MADGRAPH5 v2.2.2** [92]. The PDF set used is the **NNPDF2.3 LO** set [93]. For modeling parton shower and hadronization in jets, **PYTHIA 8.186** is used with the A14 tune [80, 94]. The free parameters in the RSG model are the graviton mass and the coupling constant  $c \equiv k/\bar{M}_{\text{Pl}}$ <sup>†</sup>. Both the production cross section and width of the

<sup>†</sup> $k$  is the curvature constant for the warped extra dimension and  $\bar{M}_{\text{Pl}}$  is the Planck mass divided by  $8\pi$

graviton are proportional to  $c^2$ . Samples are generated at both  $c = 1$  and  $c = 2$  for a variety of mass points between 300 GeV and 3 TeV.

The second signal sample is a heavy spin-0 resonance  $H$  with a fixed width of  $\Gamma_H = 1$  GeV. This is generated with **MADGRAPH5** and uses the **CT10** PDF set [83]. The parton shower and hadronization are handled by **HERWIG ++** with the **CTEQ6L1** PDF set and the **UEEE5** event tune [84, 95, 96]. Because the width and branching ratios depend on 2HDM parameters, each mass point generated with this fixed width corresponds to a different point in the 2HDM parameter phase space. Mass points are generated between 300 GeV and 1 TeV as with the RSG signal samples.

### 7.3.2 BACKGROUND SAMPLES

While the dominant **QCD** multijet background is estimated with a fully data-driven method, the sub-dominant backgrounds  $t\bar{t}$  and  $Z + \text{jets}$  are modeled with some input from simulation.

$t\bar{t}$  events are simulated at next-to-leading order (NLO) with the **POWHEG-BOX** version 1 generator using the **CT10** PDF set [97]. The parton shower, hadronization, and underlying event are simulated with **PYTHIA 6.428** with the **CTEQ6L1** PDF set [79]. The Perugia 2012 tune is used [98]. NNLO **QCD** corrections to the cross sections are computed in **Top++ 2.0** [99]. The top quark mass is set to 172.5 GeV. The shapes of distributions in  $t\bar{t}$  are taken from MC while the normalization is taken from data.

Finally, the  $Z + \text{jets}$  background is simulated with **PYTHIA 8.186** and the **NNPDF2.3** LO PDF set. This background is negligible compared to the others and is taken fully from MC.

### 7.3.3 DATA SAMPLE AND TRIGGER

This analysis is done on  $3.2 \text{ fb}^{-1}$  of data taken in 2015 at  $\sqrt{s} = 13$  TeV. The details of the machine conditions during this time can be found in Chapter 2. Only data which was taken during stable beam conditions with all detectors functioning is used. Events must pass a trigger which requires a single 360 GeV large radius ( $R = 1.0$ ) jet to be reconstructed in the HLT. Figure 7.4 shows the trigger efficiency for various trigger options as a function of graviton mass. Above  $m_G > 1$  TeV, the single large radius jet trigger is 99% efficient for events passing the signal selection.

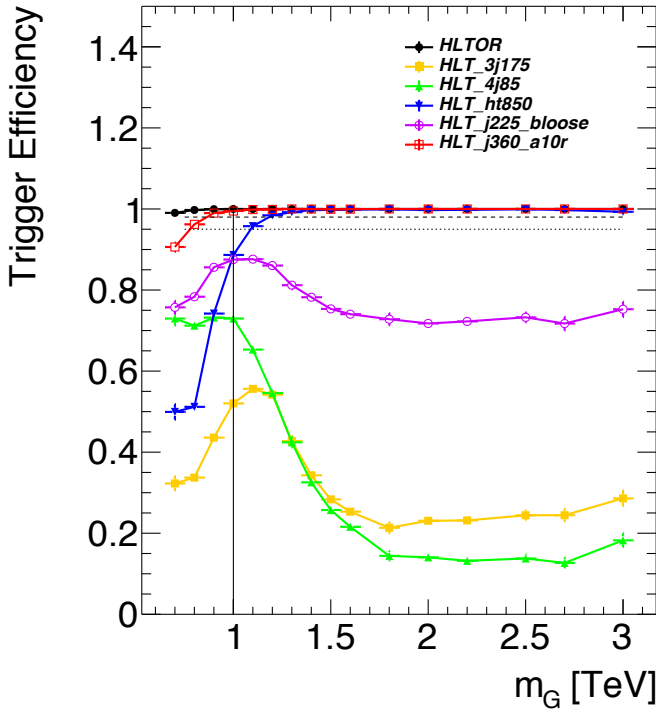


**Figure 7.4:** Trigger efficiency for events passing all signal region selections as a function of mass in  $G_{\text{KK}}^* \rightarrow HH \rightarrow 4b$  samples with  $c = 1$  [26]. In the trigger names, “j” refers to a jet or jets. “ht” refers to  $H_T$ , the scalar sum of transverse momenta in the event. “bloose” refers to a loose  $b$ -tagging requirement applied to the jet. “a10r” refers to anti- $k_T$  jets with  $R = 1.0$ . The numbers at the end are the thresholds on the given quantity in GeV.

## 2248 7.4 EVENT RECONSTRUCTION AND OBJECT SELECTION

2249 The boosted selection first begins by defining a unique set of objects that can be exploited to increase  
 2250 signal efficiency in the kinematic regime where the final state  $b$ -jets are very merged.

### 2251 7.4.1 LARGE RADIUS ( $R = 1.0$ ) JETS

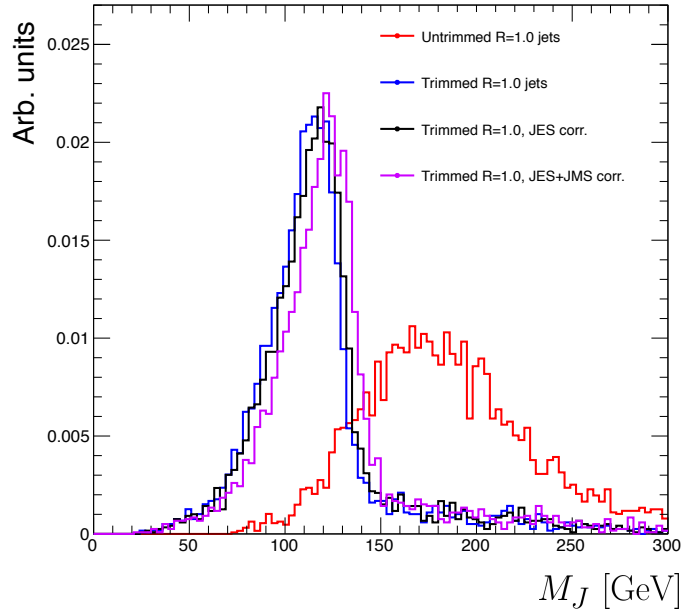
2252 The first step towards reconstructing the final state is to define objects that can be used to measure the  
 2253 kinematics of the Higgs bosons. In the boosted selection anti- $k_T$  jets with a radius parameter of 1.0  
 2254 are used. These jets are much larger in angular size than the typical  $R = 0.4$  jets and are intended to  
 2255 encompass both jets resulting from the Higgs decay<sup>‡</sup>. The jets are built from clusters in the calorimeter

---

<sup>‡</sup>This is in contrast to the resolved selection, which uses two  $R = 0.4$  anti- $k_T$  jets for each Higgs

2256 calibrated with local calibration weighting [17].

2257 Because of the large extent of these jets, great care must be taken to remove potential contributions of  
2258 calorimeter clusters from pile-up. This is done using a technique called jet trimming [100]. With trim-  
2259 ming, the constituents of the large radius jet are re-clustered with a smaller radius with the  $k_T$  algorithm.  
2260 Then, these so-called subjets are removed from the larger jet if  $p_T^{\text{subjet}}/p_T^{\text{jet}} < f_{\text{cut}}$ . In this analysis, the  
2261 subjet radius is  $R = 0.2$  and  $f_{\text{cut}} = 0.05$ . Trimming has been shown to improve the mass resolution  
2262 of large radius jets. Figure 7.5 shows the effect of trimming on the large radius jet mass ( $M_J$ ). Because  
2263 the large radius jet fully contains the higgs decay products, its invariant mass should correspond to the  
2264 125 GeV mass of the Higgs. The trimming algorithm brings the jet mass much closer to the expected  
2265 Higgs mass and improves the mass resolution.



2266 **Figure 7.5:** Comparison of untrimmed and trimmed jet masses for large radius jets in a RSG sample with  $m_{G_{\text{KK}}^*} = 1 \text{ TeV}$ .  
2267 JES (JMS) refers to the standard jet energy (mass) scale calibration for ATLAS [17].

2268 The large radius jets are required to satisfy  $250 < p_T < 1500 \text{ GeV}$ . They must also be within  
2269  $|\eta| < 2.0$  in order to ensure that the full jet is within the inner detector tracking volume. Finally, they  
2270 are required to have  $M_J > 50 \text{ GeV}$ . The upper  $p_T$  cut and lower threshold on mass are applied to  
2271 correspond to the kinematic range where uncertainties are available in ATLAS calibrations [101, 102].

2270 7.4.2 TRACK JETS AND  $b$ -TAGGING

2271 Because the  $b$ -jets from boosted Higgs decays are so close together (as illustrated in figure 7.3), narrow ra-  
 2272 dius jets are required to fully resolve both  $b$ -jets. The minimum radius feasible for jets based on calorime-  
 2273 ter deposits is determined by the calorimeter granularity. However, because  $b$ -tagging relies on informa-  
 2274 tion from the inner detector, it is possible to define another type of jet that can have a smaller radius and  
 2275 better  $b$ -tagging resolution. These jets are called “track jets” [27, 102].

2276 Track jets are formed by applying the usual anti- $k_T$  clustering algorithm to tracks that are required  
 2277 to be consistent with the primary vertex. After the jet axis has been determined using these tracks, a sec-  
 2278 ond step of track association is also performed to add tracks that can be useful for  $b$ -tagging [27]. In this  
 2279 analysis, the tracks are clustered with a radius parameter of  $R = 0.2$ . This radius has been shown to  
 2280 give good performance in boosted Higgs tagging [27, 102]. Figure 7.6 shows a comparison among dif-  
 2281 ferent track jet radii of the efficiency for reconstructing two  $b$ -jets from each Higgs in a RSG sample as a  
 2282 function of mass. Track jets with radius of 0.2 give the best performance, especially at high mass.

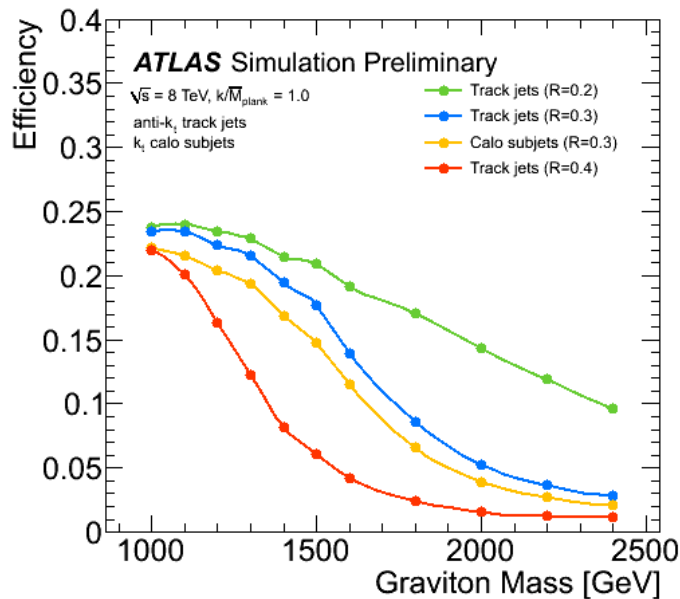


Figure 7.6: Efficiency of finding two  $b$ -jets from each Higgs in an RSG event using calorimeter jets with  $R = 0.3$  or different track jet radii [27]

2283 In this analysis, track jets are required to have  $p_T > 10 \text{ GeV}$  and  $|\eta| < 2.5$ . They must also have at

2284 least two tracks.

2285 **7.4.3 MUONS**

2286 Muons are used in this study to correct the four-momenta of calorimeter jets by accounting for semi-  
2287 leptonic  $b$  decays. The muons used are combined ID and MS muons which must satisfy tight identifica-  
2288 tion requirements [16]. The muons must have  $p_T > 4 \text{ GeV}$  and  $|\eta| < 2.5$ . Table 7.1 summarizes the  
2289 object requirements described in this section.

	$R$	$p_T$	$ \eta $	$M$
Calorimeter jets	1.0	$250 < p_T < 1500 \text{ GeV}$	$< 2.0$	$> 50 \text{ GeV}$
Track jets	0.2	$> 10 \text{ GeV}$	$< 2.5$	-
Muons	-	$4 \text{ GeV}$	$< 2.5$	-

Table 7.1: Summary of requirements on objects used in the  $X \rightarrow HH \rightarrow b\bar{b}b\bar{b}$  search

2290 **7.5 EVENT SELECTION**

2291 The first requirement in the boosted selection is for  $\geq 2$  large radius jets satisfying the selections outlined  
2292 above. The two highest momentum large-R jets in the event are referred to as “Higgs candidates”. The  
2293 leading jet is required to have  $p_T > 350 \text{ GeV}$ .

2294 Track jets satisfying the object selections are matched to Higgs candidate jets via ghost association [103].  
2295 Each Higgs candidate must have at least 2 track jets associated with it. These basic requirements are illus-  
2296 trated in figure 7.7

2297 The QCD multijet background produces less central jets than high mass resonances, so there is an ad-  
2298 ditional requirement that the two Higgs candidates be close together in  $\eta$ . The large-R jets are required  
2299 to satisfy  $|\Delta\eta(JJ)| < 1.7$ .

2300 The final set of requirements ensures that the Higgs candidates are consistent with expected proper-  
2301 ties of the 125.0 GeV Higgs. First, a variable ( $X_{hh}$ ) is defined to measure the consistency of both of the

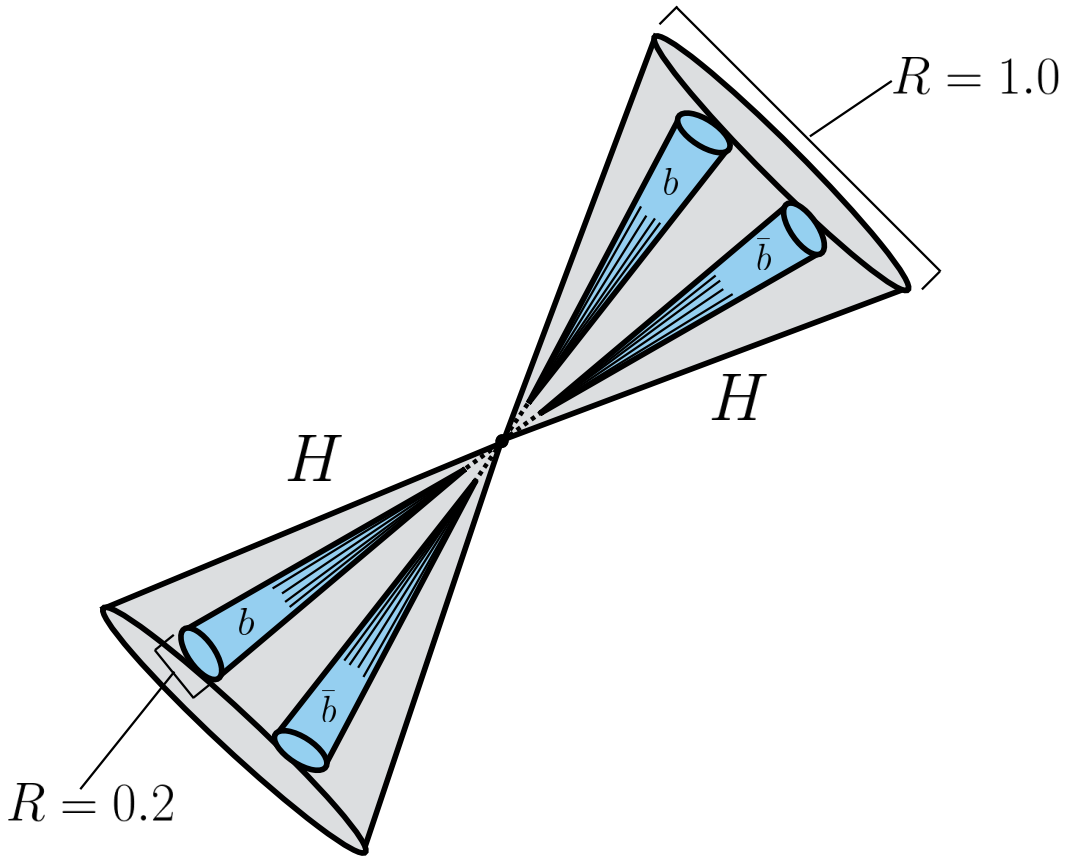


**Figure 7.7:** Illustration of the boosted selection requirements on Higgs candidates. Each large-radius calorimeter jet (Higgs candidate) must contain two track jets

2302     Higgs candidate jets with the SM Higgs mass. This is shown in equation 7.2.

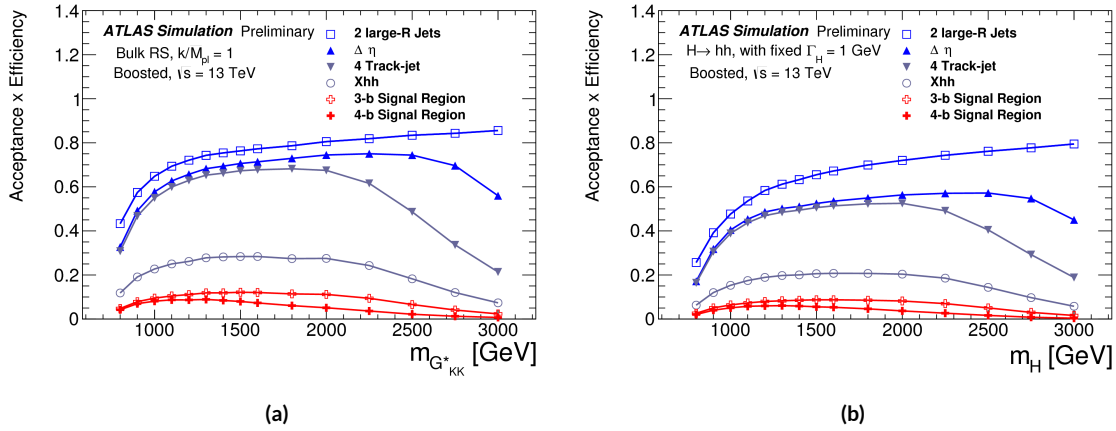
$$X_{hh} = \sqrt{\left(\frac{M_J^{\text{lead}} - 124 \text{ GeV}}{0.1 M_J^{\text{lead}}}\right)^2 + \left(\frac{M_J^{\text{sublead}} - 115 \text{ GeV}}{0.1 M_J^{\text{sublead}}}\right)^2} \quad (7.2)$$

2303     The mass values in the  $X_{hh}$  formula are optimized to maximize signal efficiency. The sub-leading jet  
 2304     typically has a lower mass due to semi-leptonic  $b$  decays and final state radiation.  $X_{hh}$  effectively acts as  
 2305     a  $\chi^2$  measurement of the consistency of the two Higgs candidate masses with the signal hypothesis. The  
 2306     denominators of each term ( $0.1 M$ ) give the uncertainty on the mass measurement for the large radius  
 2307     jets. Events are required to satisfy  $X_{hh} < 1.6$ .

2308     The last requirement applied is on the number of  $b$ -tagged track jets. There are two signal regions de-

fined. The first requires exactly four  $b$ -tagged track jets, two in each Higgs candidate (known as the 4b signal region). At high resonance masses, this requirement is inefficient, so an additional signal region requiring only three  $b$ -tagged track jets is also defined (known as the 3b signal region). While this has a larger background it is also more efficient for high resonance masses. For both signal regions, threshold on MV<sub>2</sub> score is chosen such that the algorithm is 77% efficiency in finding true  $b$ -jets<sup>§</sup>. Different working points were tested and this was found to be optimal. Appendix A has more details on this optimization.

Before making the requirement on  $X_{hh}$ , the masses of the Higgs candidates are corrected for semi-leptonic  $b$  decays using muons with the criteria outlined in the previous section. Any muons within a  $\Delta R < 0.2$  of a  $b$ -tagged track jet have their four-momenta added to the four-momentum of the Higgs candidate. This correction does not affect the pre-selection requirements but does affect the  $X_{hh}$  requirement and the final invariant mass distribution used.



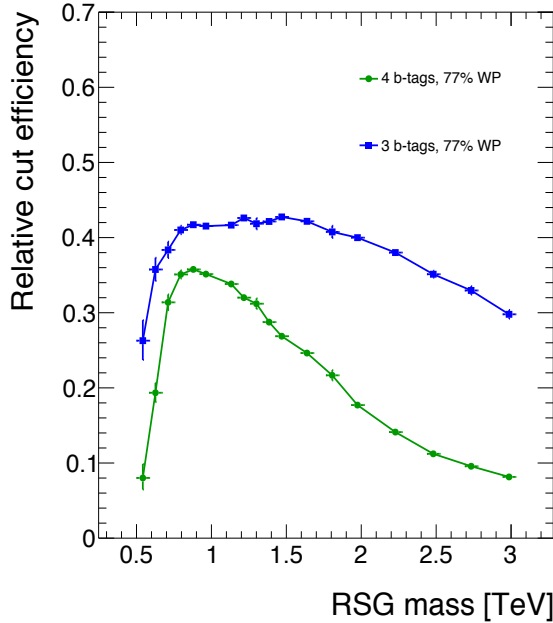
**Figure 7.8:** Acceptance  $\times$  efficiency as a function of mass for (a) RSG and (b) narrow heavy scalar signal models [28].

Figure 7.8 shows the product of acceptance and efficiency as a function of mass for both the RSG and narrow heavy scalar resonance signal models. After  $m_X > 1$  TeV, the efficiency of the 4b requirement begins to decline. After  $m_X > 2$  TeV, the efficiency of requiring two track jets in each Higgs candidate begins to decline as well. Both of these behaviors illustrate the difficulty of resolving the merged decay

<sup>§</sup>The specific MV<sub>2</sub> algorithm chosen is MV<sub>2c20</sub>, where the fraction of charm events used in the training is 20%

2325 products at high mass. More details on the degradation of the  $b$ -tagging efficiency at high masses are  
2326 shown in appendix B.

2327 Figure 7.9 shows a more detailed comparison of the signal efficiency in the  $3b$  vs  $4b$  signal regions for  
2328 the RSG model. The efficiencies shown here are relative to all prior selection requirements.



2329 **Figure 7.9:** Efficiency of requiring 3 or 4  $b$ -tagged track jets vs. RSG mass. The efficiency quoted is relative to the previous  
2330 selection requirements (rather than an absolute efficiency).

2329 The final discriminating variable used in the boosted analysis is  $M_{2J}$ , the invariant mass of the two  
2330 Higgs candidates. In order to improve the mass resolution, the four-momenta of each Higgs candidate  
2331 are scaled by  $m_h/M_J$ . The effect of this correction is small in the boosted analysis but is done for consis-  
2332 tency with the resolved selection.

2333 Table 7.2 shows the effect of the selection requirements on signal and background simulations as well  
2334 as data.

## 2335 7.6 DATA-DRIVEN BACKGROUND ESTIMATION

2336 The largest background to this final state is QCD multijet production, constituting 80-90% of the total  
2337 background. Because of the difficulties in modeling higher order QCD processes, this background is

Selection	Data	$m_{G_{KK}^*} = 1\text{TeV}$	$m_{G_{KK}^*} = 2\text{TeV}$	$t\bar{t}$	$Z+\text{jets}$
N(fiducial large-R jets) $\geq 2$	2202396	23.3	0.48	32345.2	4255.7
leading large-R jet $p_T > 350\text{ GeV}$	1873741	22.9	0.48	26511.7	3649.9
Both large-R jet $m > 50\text{ GeV}$	1854625	21.2	0.47	24369.8	3575.8
Both large-R jet $p_T < 1500\text{ GeV}$	1853601	21.2	0.46	24346.5	3572.9
$ \Delta\eta(JJ)  < 1.7$	1435273	20.8	0.44	20751.0	3265.8
$\geq 2$ track-jets per large-R jet	1224727	19.8	0.40	18234.5	2692.6
$3 b\text{-tags}, X_{hh} < 1.6$	316	3.4	0.067	46.7	2.0
$4 b\text{-tags}, X_{hh} < 1.6$	20	2.9	0.030	1.4	0.0

**Table 7.2:** Effect of boosted selection on data, RSG signal models,  $t\bar{t}$ , and  $Z+\text{jets}$ . The numbers from simulation are normalized with the MC generator cross section and do not take into account the data driven estimates described in section 7.6 [33].

estimated with a fully data-driven method. The only other non-negligible background is  $t\bar{t}$ , constituting the other 10-20%. Due to the presence of  $t\bar{t}$  in the sideband region where the QCD background will be estimated, the normalization of the QCD and  $t\bar{t}$  backgrounds are simultaneously estimated.

### 7.6.1 MASS REGION DEFINITIONS

The first step in the data-driven background estimate is to define a sideband mass region where the background normalization can be derived. Additionally, a control region is defined where the background estimate can be validated. The control (CR) and sideband (SB) regions are defined using a radial distance in the two-dimensional large-R jet mass plane,  $R_{hh}$ , which is defined in equation 7.3.

$$R_{hh} = \sqrt{(M_J^{\text{lead}} - 124\text{ GeV})^2 + (M_J^{\text{sublead}} - 115\text{ GeV})^2} \quad (7.3)$$

Events in the sideband region are required to fail the signal region  $X_{hh} < 1.6$  requirement and have  $R_{hh} > 35.8\text{ GeV}$ . The control region consists of those events which are not in the signal or sideband regions. Figure 7.10 shows the definition of the signal, control, and sideband mass regions.

Table 7.3 summarizes the mass region selections for the three different regions used in the analysis.

---

\*The  $Z+\text{jets}$  background is a sub-percent level contribution

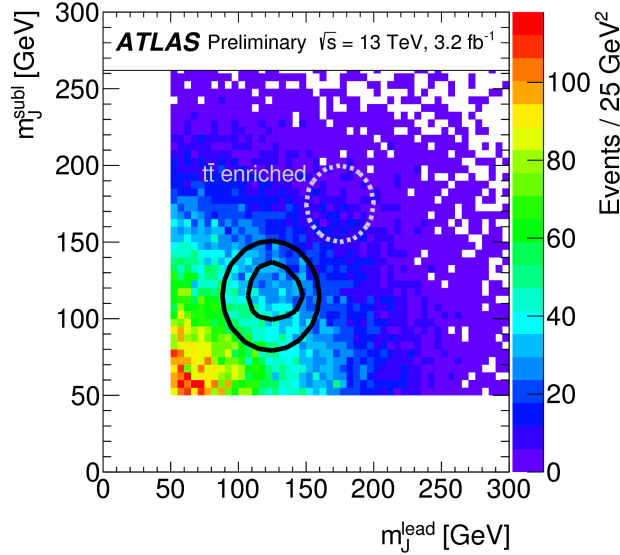


**Figure 7.10:**  $M_J^{\text{sublead}}$  vs.  $M_J^{\text{lead}}$  in a 2  $b$ -tag data sample. The signal region is defined by the inner black contour ( $X_{hh} < 1.6$ ) and the sideband region is defined by the outer contour ( $R_{hh} > 35.8 \text{ GeV}$ ). The region between the black contours is the control region. The mass region which is enriched in  $t\bar{t}$  background is also shown for illustration. [28]

Region	Requirement	Notes
Signal Region (SR)	$X_{hh} < 1.6$	-
Control Region (CR)	$R_{hh} < 35.8 \text{ GeV}$ and $X_{hh} > 1.6$	Used for validation of background estimates
Sideband Region (SB)	$R_{hh} > 35.8 \text{ GeV}$	Used to derive background normalization

**Table 7.3:** Mass region definitions used for background estimation

### 2350 7.6.2 BACKGROUND ESTIMATION

2351 The method for estimating the background in this analysis is similar to the ABCD method presented in  
 2352 Chapter 5. In this case, the two handles used to define different regions for the estimate are the number  
 2353 of  $b$ -tagged track jets and the mass regions. A region requiring exactly two  $b$ -tagged track jets in one large-  
 2354 R jet (referred to as the 2-tag or 2 $b$  region) is defined for use in the background estimate. The number of  
 2355 expected background events in the 3 $b$  and 4 $b$  signal regions is then given by equation 7.4.

$$N_{\text{bkg}}^{3(4)-\text{tag},\text{SR}} = \mu_{\text{Multijet}} N_{\text{Multijet}}^{2-\text{tag},\text{SR}} + \beta_{t\bar{t}} N_{t\bar{t}}^{3(4)-\text{tag},\text{SR}} + N_{Z+\text{jets}}^{3(4)-\text{tag},\text{SR}} \quad (7.4)$$

2356 In this equation,  $N_{\text{bkg}}^{3(4)\text{-tag}}$  is the expected number of background events in the  $3b$  or  $4b$  signal re-  
 2357 gions.  $N_{\text{Multijet}}^{2\text{-tag}}$  is the number of multijet events in the 2-tag region.  $N_{t\bar{t}}^{3(4)\text{-tag}}$  is the number of  $t\bar{t}$   
 2358 events predicted in the MC for the  $3b$  or  $4b$  signal region, and the variable is similarly defined for the  
 2359  $Z+\text{jets}$  background. The  $\beta_{t\bar{t}}$  parameter is a scale factor used to correct the normalization of the  $t\bar{t}$  esti-  
 2360 mate in the signal region.  $\mu_{\text{Multijet}}$  is an extrapolation factor that is derived in the sideband region and  
 2361 used to estimate the ratio of 2-tag events to 3(4)-tag events in the signal region. It is defined in equa-  
 2362 tion 7.5.

$$\mu_{\text{Multijet}} = \frac{N_{\text{Multijet}}^{3(4)\text{-tag,SB}}}{N_{\text{Multijet}}^{2\text{-tag,SB}}} = \frac{N_{\text{data}}^{3(4)\text{-tag,SB}} - \beta_{t\bar{t}} N_{t\bar{t}}^{3(4)\text{-tag,SB}} - N_{Z+\text{jets}}^{3(4)\text{-tag,SB}}}{N_{\text{data}}^{2\text{-tag,SB}} - \beta_{t\bar{t}} N_{t\bar{t}}^{2\text{-tag,SB}} - N_{Z+\text{jets}}^{2\text{-tag,SB}}} \quad (7.5)$$

2363 The  $t\bar{t}$  scale factor ( $\beta_{t\bar{t}}$ ) and the QCD multijet extrapolation factor ( $\mu_{\text{Multijet}}$ ) are estimated together  
 2364 in a simultaneous fit in the sideband region. Then, the number of events in the 2-tag signal region is  
 2365 used, along with the  $t\bar{t}$  estimate in the  $3b$  and  $4b$  signal regions and  $\mu_{\text{Multijet}}$ , to estimate the total num-  
 2366 ber of background events in the two final signal regions. The shape of the final discriminant  $M_{2J}$  is also  
 2367 taken from the 2-tag signal region where there are more statistics. This method is illustrated graphically  
 2368 in figure 7.11.

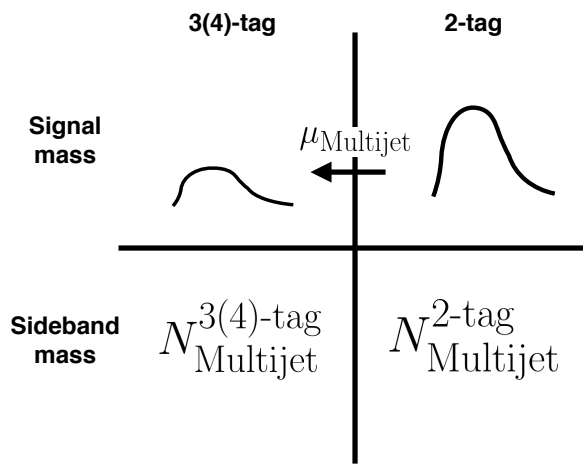


**Figure 7.11:** An illustration of the data-driven background estimation technique for the boosted analysis

2369 In the  $3b$  region, the fit yields values of  $\mu_{\text{Multijet}} = 0.160 \pm 0.03$  and  $\beta_{t\bar{t}} = 1.02 \pm 0.09$ . In the  $4b$

region, the fit gives  $\mu_{\text{Multijet}} = 0.0091 \pm 0.0007$  and  $\beta_{t\bar{t}} = 0.82 \pm 0.39$ . The uncertainties quoted are statistical only. The larger uncertainties in the  $4b$  values indicate the lower statistics available in that region.

Figure 7.12 shows the distributions of data and background estimates in the  $3b$  and  $4b$  sideband regions after the background fit has been done. The normalizations are constrained from the fit to match that of the data, but good modeling of the shape of the mass of the leading large-R jet is seen as well. The shapes of the kinematic distributions in the  $4b$  region are taken from the  $3b$  region due to the better MC statistics in that region.

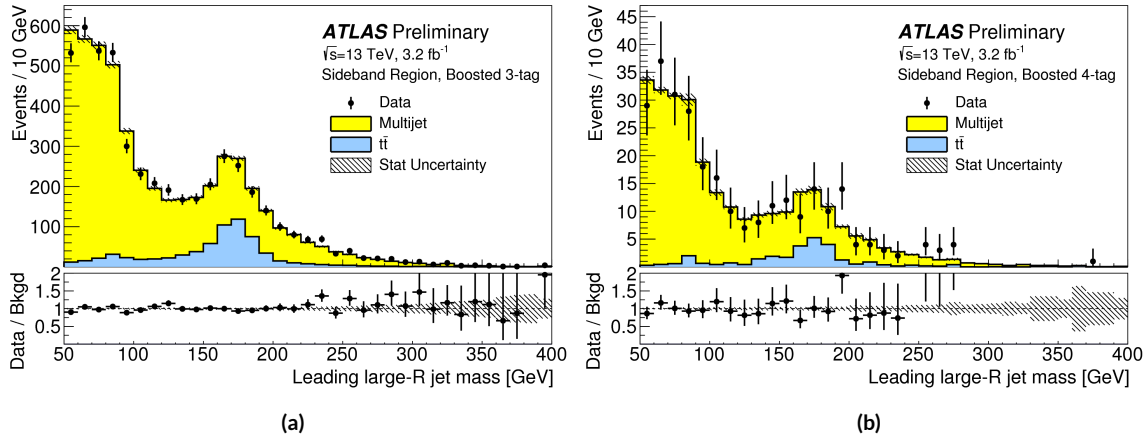


**Figure 7.12:** Leading large-R jet mass in the  $3b$  (a) and  $4b$  (b) sideband regions. The multijet and  $t\bar{t}$  backgrounds are estimated using the data-driven methods described above. Because their normalizations are derived in the sideband region, the total background normalization is constrained by default to match the normalization of the data [28].

### 7.6.3 BACKGROUND SHAPE FIT

As mentioned in the previous section, the background shape in the 3-tag and 4-tag signal regions is taken from the 2-tag signal mass region. Due to the limited statistics available, the background shapes are additionally smoothed after being extrapolated to the 3-tag and 4-tag signal regions. Only the data in the range  $900 < M_{2J} < 2000$  GeV is included in the fit due to the limited statistics available above 2 TeV. Both the  $t\bar{t}$  and QCD multijet background are independently fit with an exponential shape,  $y = e^{ax+b}$ . Other shapes are considered and used for the systematic uncertainties. Table 7.4 shows the fit values for

the parameters. Because both the  $3b$  and  $4b$  QCD shapes come from the 2-tag region, the slopes derived are very similar.

	$a$	$b$
QCD ( $4b$ )	$0.00545 \pm 0.00021$	$5.44 \pm 0.24$
$t\bar{t}$ ( $4b$ )	$0.00746 \pm 0.00021$	$4.88 \pm 0.36$
QCD ( $3b$ )	$0.00545 \pm 0.00021$	$8.30 \pm 0.24$
$t\bar{t}$ ( $3b$ )	$0.00746 \pm 0.00021$	$8.58 \pm 0.36$

**Table 7.4:** Parameters derived for exponential fit to background  $M_{2J}$  shape in the  $3b$  and  $4b$  signal regions [33]

#### 7.6.4 VALIDATION OF BACKGROUND ESTIMATE

The background estimate can be validated by using the method to estimate the number of events in the control mass region rather than the signal mass region. Figure 7.13 shows the  $M_{2J}$  distribution in the  $3b$  and  $4b$  control regions, comparing data and background estimates. In both cases, both the background shape and normalization are consistent with the data, indicating good agreement. The ratio of data to the background estimates is also fit to a line in the figure to test for any shape difference. The slope of the line is within  $1\sigma$  (from the fit uncertainties) of flat, further indicating that the data is consistent with the background estimate in the control region.

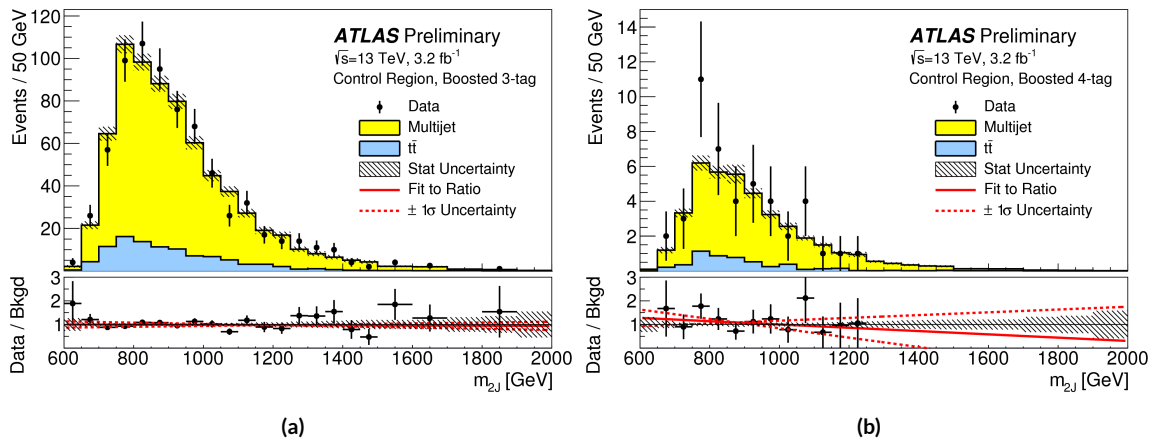


**Figure 7.13:** Di-jet invariant mass ( $M_{2J}$ ) in the  $3b$  (a) and  $4b$  (b) control regions. The multijet and  $t\bar{t}$  backgrounds are estimated using the data-driven methods described above [28].

Table 7.5 shows the yields in data and background estimates in the 3-tag and 4-tag sideband and con-

2396 trol regions. Again, here, it can be seen that the total number of predicted background events from the  
 2397 data driven method is consistent with the number of data events in the region.

Sample (3-tag)	Sideband Region	Control Region
Multijet	$4328 \pm 27$	$607 \pm 10$
$t\bar{t}$	$683.5 \pm 8.1$	$99.6 \pm 3.1$
$Z+jets$	$31.8 \pm 3.7$	$7.7 \pm 1.8$
Total	$5043 \pm 28$	$715 \pm 11$
Data	5043	724
Sample (4-tag)	Sideband Region	Control Region
Multijet	$247.4 \pm 1.5$	$34.7 \pm 0.6$
$t\bar{t}$	$28.4 \pm 1.5$	$5.1 \pm 0.7$
$Z+jets$	$3.4 \pm 1.2$	$0.6 \pm 0.5$
Total	$279.2 \pm 2.5$	$40.3 \pm 1.0$
Data	279	45

Table 7.5: The number of events in data and predicted background events in the boosted 3-tag and 4-tag sideband and control regions. The uncertainties shown are statistical only. [28]

## 2398 7.7 SYSTEMATIC UNCERTAINTIES

2399 The systematic uncertainties in this analysis can be divided into two broad categories. The first type is  
 2400 uncertainties associated with the modeling of the signal processes. The second type of uncertainty is  
 2401 associated with both the shape and normalization of the background prediction.

### 2402 7.7.1 SIGNAL MODELING UNCERTAINTIES

2403 The signal modeling uncertainty has three main components: theoretical uncertainty on the acceptance,  
 2404 experimental uncertainties on the large-R jets, and experimental uncertainties on the track jets related to  
 2405  $b$ -tagging. In this analysis the experimental uncertainties are the most significant.

2406 The first uncertainty on signal modeling is the theoretical uncertainty on the acceptance. As explained  
 2407 in section 5.6.1, there are four components to this uncertainty. The first is related to missing higher order  
 2408 terms from the matrix element calculations which is estimated by varying the QCD renormalization and

2409 factorization scales. The second is uncertainty due to the PDF set used. The third is a generator uncer-  
2410 tainty which is estimated by modifying the generator used to model the underlying event and hadroniza-  
2411 tion. Finally, there is an uncertainty associated with the modeling of the initial state and final state radia-  
2412 tion (ISR/FSR). The total theoretical uncertainty on the signal yield is 3%, and this is dominated by the  
2413 ISR/FSR modeling.

2414 There are uncertainties on the large-R jets in both the jet energy scale (JES) and jet energy resolution  
2415 (JER) as well as the jet mass scale (JMS) and jet mass resolution (JMR). These are evaluated using  $\sqrt{s} =$   
2416 8 TeV data from Run 1 of ATLAS and extrapolated to the Run 2 beam and detector conditions using  
2417 MC<sup>¶</sup>. The details of these uncertainties can be found in reference [104].

2418 Uncertainties on the track jets are related to the  $b$ -tagging efficiency. The total uncertainty on the sig-  
2419 nal yield due to  $b$ -tagging is evaluated by propagating variations of the  $b$ -tagging efficiency through the  
2420 boosted selection requirements. The uncertainties are calculated jet-by-jet and parameterized as a func-  
2421 tion of  $b$ -jet  $p_T$  and  $\eta$  [105]. For high  $p_T$   $b$ -jets (with  $p_T > 300$  GeV), the uncertainties are extrapolated  
2422 using MC simulation from the lower  $p_T$   $b$ -jets [106].

2423 Table 7.6 shows the systematic uncertainties on the signal normalization for models with  $m_{G_{KK}^*} =$   
2424 1.5 TeV and both  $c = 1$  and  $c = 2$  as well as a narrow width heavy scalar. The dominant uncertainty  
2425 comes from  $b$ -tagging and this uncertainty is larger in the 4-tag region than the 3-tag region.

### 2426 7.7.2 BACKGROUND UNCERTAINTIES

2427 Uncertainties on the QCD multijet background normalization and shape are estimated using the control  
2428 mass region. As shown previously, the background predictions in the control region match with the  
2429 data yields within the statistical uncertainty in both the 3-tag and 4-tag control regions. As an additional  
2430 protection, the statistical uncertainty on the background prediction in the control region is assigned as a  
2431 systematic uncertainty on the normalization of the QCD background.

2432 Additional robustness tests are done by varying the definition of the control mass region and the  $b$ -  
2433 tagging requirements used to define the 2-tag sample. In all cases, the effect of the variations is found to

---

<sup>¶</sup>The uncertainties are correspondingly larger due to the uncertainty of this extrapolation.

Source	Background		$G_{KK}^*$	$H$
	$c = 1$	$c = 2$		
Luminosity	-	5.0	5.0	5.0
3-tag				
JER	< 1	< 1	< 1	< 1
JES	2	< 1	< 1	< 1
JMR	1	12	12	11
JMS	5	14	13	17
$b$ -tagging	1	23	22	23
Theoretical	-	3	3	3
Multijet Normalization	3	-	-	-
Statistical	2	1	1	1
Total	7	31	30	33
4-tag				
JER	< 1	< 1	< 1	< 1
JES	< 1	< 1	< 1	< 1
JMR	4	12	13	13
JMS	5	13	13	14
$b$ -tagging	2	36	36	36
Theoretical	-	3	3	3
Multijet Normalization	14	-	-	-
Statistical	3	1	1	1
Total	15	42	42	43

**Table 7.6:** Summary of systematic uncertainties in the total background and signal event yields (expressed in %) in the boosted 3-tag and 4-tag signal regions. Systematic uncertainties on the signal normalization are shown for models with  $m_{G_{KK}^*} = 1.5$  TeV and both  $c = 1$  and  $c = 2$  as well as a narrow width heavy scalar.

<sup>2434</sup> be within the statistical uncertainties on the background normalization in the control region.

<sup>2435</sup> Shape uncertainties on the background are evaluated using two techniques. First, as shown in figure 7.13, the ratio between the data and background prediction is fit with a linear function. The uncertainties on the slope of this fit are assigned as shape uncertainties. An additional uncertainty is assigned <sup>2436</sup> by using alternate power law fit functions for the smoothing of the background shape. Table 7.7 shows <sup>2437</sup> the alternate shapes used. The largest difference between the nominal fit function and the alternates, <sup>2438</sup> taking into account the  $1\sigma$  uncertainty band on each fit as well, is taken as a shape uncertainty. <sup>2439</sup>

Functional Form
$f_1(x) = p_0(1-x)^{p_1}x^{p_2}$
$f_2(x) = p_0(1-x)^{p_1}e^{p_2 x^2}$
$f_3(x) = p_0(1-x)^{p_1}x^{p_2} x$
$f_4(x) = p_0(1-x)^{p_1}x^{p_2} \ln x$
$f_5(x) = p_0(1-x)^{p_1}(1+x)^{p_2} x$
$f_6(x) = p_0(1-x)^{p_1}(1+x)^{p_2} \ln x$
$f_7(x) = \frac{p_0}{x}(1-x)^{p_1-p_2} \ln x$
$f_8(x) = \frac{p_0}{x^2}(1-x)^{p_1-p_2} \ln x$

**Table 7.7:** Alternate fit functions used to model the  $M_{JJ}$  distribution in the QCD multijet background. In the equations,  $x = M_{JJ}/\sqrt{s}$ .

2441     The uncertainties on the  $t\bar{t}$  background are obtained by propagating the various experimental varia-  
 2442     tions (JES, JER, JMS, JMR,  $b$ -tagging) through the analysis selection requirements. Table 7.6 summarizes  
 2443     the background uncertainties in the 3-tag and 4-tag regions.

2444     7.8 RESULTS

2445     Table 7.8 shows the observed yields in the 3-tag and 4-tag signal regions for the boosted analysis com-  
 2446     pared to the predicted number of background events. In the 3-tag region, 316 events are observed with  
 2447     a predicted background of  $285 \pm 19$ . In the 4-tag region, 20 events are observed with a predicted back-  
 2448     ground of  $14.6 \pm 2.4$ . Figure 7.14 shows the  $M_{JJ}$  distribution in the 3-tag and 4-tag regions. There are  
 2449     some small excesses in the data, in particular in the 3-tag region around  $M_{JJ} \approx 900$  GeV and in the  
 2450     region of  $1.6 < M_{JJ} < 2.0$  TeV. The significance of these excesses will be evaluated in the next chapter  
 2451     in the statistical combination with the resolved results.

Sample	Signal Region (3-tag)	Signal Region (4-tag)
Multijet	$235 \pm 14$	$13.5 \pm 2.4$
$t\bar{t}$	$48 \pm 22$	$1.2 \pm 1.0$
$Z+jets$	$2.0 \pm 2.2$	-
Total	$285 \pm 19$	$14.6 \pm 2.4$
Data	316	20
$G_{KK}^*(1000 \text{ GeV}), c = 1$	$3.4 \pm 0.9$	$2.9 \pm 1.1$

**Table 7.8:** Observed yields in the 3-tag and 4-tag signal regions for the boosted analysis compared to the predicted number of background events Errors correspond to the total uncertainties in the predicted event yields. The yields for a graviton with  $m_{G_{KK}^*} = 1 \text{ TeV}$  and  $c = 1$  are also shown. [28]

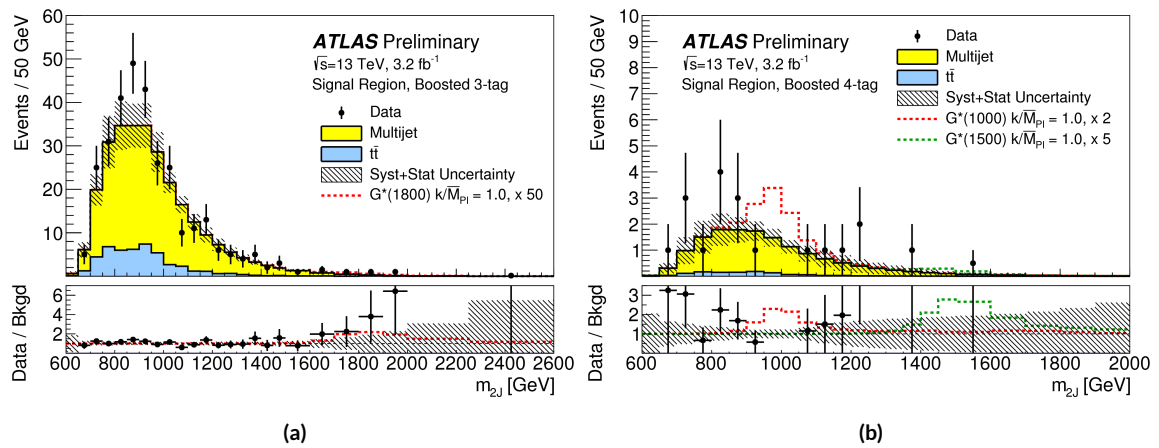


**Figure 7.14:** Di-jet invariant mass ( $M_{2J}$ ) in the  $3b$  (a) and  $4b$  (b) signal regions. The multijet and  $t\bar{t}$  backgrounds are estimated using the data-driven methods described above. In the  $3b$  region, a graviton signal with  $m_{G_{KK}^*} = 1.8 \text{ TeV}$  and  $c = 1$  is overlaid, with the cross section multiplied by a factor of 50 so that the signal is visible. In the  $4b$  region, signals with  $m_{G_{KK}^*} = 1.0 \text{ TeV}$  and  $m_{G_{KK}^*} = 1.5 \text{ TeV}$  are overlaid, both with  $c = 1$  and the yields multiplied by factors of 2 and 5 respectively [28].

*This is a really enlightening quote.*

Tomo Lazovich

# 8

2452

2453

## Combined limits from boosted and resolved searches

2454

2455 8.1 INTRODUCTION

2456 In order to cover the full mass range of possible resonances decaying to di-Higgs final states, two distinct  
2457 tailored selections were produced. The resolved selection is more sensitive in the mass range of  $400 < m_X < 1100$  GeV while the boosted selection is more sensitive to masses in the range  $1100 < m_X <$   
2458  $3000$  GeV. Chapter 7 presents the details of the boosted selection and results. In setting limits on spin-2  
2459 Randall-Sundrum graviton (RSG) and narrow width heavy scalar ( $H$ ) models, the results of the boosted  
2460 selection are combined with the results of the resolved selection to cover the full mass range.  
2461

2462 This chapter presents limits on signal models resulting from the  $X \rightarrow HH \rightarrow b\bar{b}b\bar{b}$  search in both  
2463 the resolved and boosted selections. It first presents a brief overview of the resolved results that go into

2464 the limit setting. Then, an overview of the statistical methods used for the search and limit setting is  
2465 given. Finally, limits on the RSG and heavy scalar models are presented.

2466 **8.2 RESOLVED RESULTS**

2467 The details of the resolved selection will not be presented here and can be found in reference [28]. In  
2468 basic terms, the selection searches for four  $R = 0.4$  b-tagged calorimeter jets (where each pair of jets is  
2469 one Higgs candidate). This is distinct from the boosted methodology which searches for merged decay  
2470 products. The backgrounds to the resolved selection are the same as those presented in Chapter 7 for the  
2471 boosted analysis.

2472 Table 8.1 shows the results for data yields and expected background in the resolved signal region. Fig-  
2473 ure 8.1 shows the  $M_{2J}$  distribution in the resolved signal region. The total number of events is consis-  
2474 tent with the prediction and no significant excess is seen. One event in the boosted 4-tag signal is shared  
2475 with the resolved signal region and has a mass of 852 GeV.

Sample	Signal Region Yield
Multijet	$43.3 \pm 2.3$
$t\bar{t}$	$4.3 \pm 3.0$
$Z + \text{jets}$	-
Total	$47.6 \pm 3.8$
Data	46
SM $hh$	$0.25 \pm 0.07$
$G_{\text{KK}}^*(800 \text{ GeV}), c = 1$	$5.7 \pm 1.5$

**Table 8.1:** Observed yields in the resolve selection 4-tag signal region compared to the predicted number of background events Errors correspond to the total uncertainties in the predicted event yields. The yields for a graviton with  $m_{G_{\text{KK}}^*} = 800 \text{ GeV}$  and  $c = 1$  are also shown. [28]

2476 **8.3 SEARCH TECHNIQUE AND RESULTS**

2477 The statistical technique used for the search in this analysis is the same as that used in the  $H \rightarrow WW^*$   
2478 analysis presented in section 3.6.2. The test statistic  $q_0$  is used to define the  $p$ -values which measure the

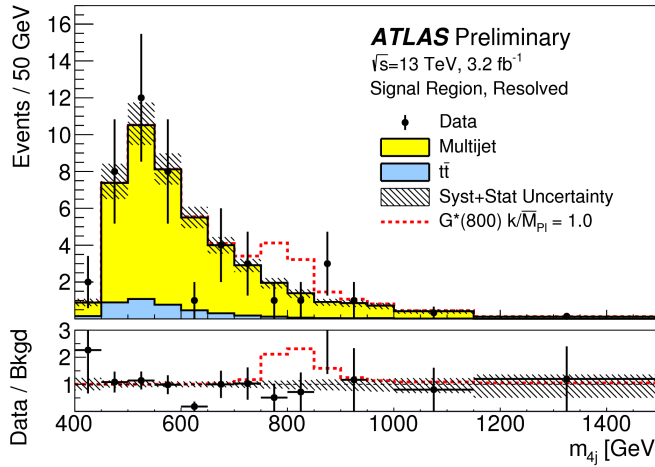


**Figure 8.1:** Di-jet invariant mass ( $M_{2J}$ ) in the resolved signal region. Agraviton signal with  $m_{G_{KK}^*} = 800$  GeV and  $c = 1$  is overlaid. [28].

compatibility of the data with the background-only hypothesis corresponding to a signal strength  $\mu = 0$ .

Local  $p_0$  values are computed to quantify the probability that the background could produce a fluctuation greater than or equal to the one observed in the data. In the resolved analysis, no significant excesses are observed. The largest discrepancy with respect to the background only hypothesis occurs near a resonance mass of 900 GeV and is found to be less than  $2\sigma$  in significance.

In the boosted selection, the largest local excess is a broad excess in the  $3b$  signal region that begins near  $M_{2J} \approx 1.7$  GeV. Assuming a  $G_{KK}^*$  with this mass and  $c = 1.0$ , the local significance of this excess is  $2.0\sigma$ .

#### 8.4 LIMIT SETTING

In the absence of any significant excess observed in the data, limits on different signal models can be set. This section describes the limit setting procedure and presents combined results of the resolved and boosted analyses.

2492 8.4.1 LIMIT SETTING PROCEDURE

2493 The procedure used for setting exclusion limits in this analysis is the  $\text{CL}_s$  method [107]. The first step in  
 2494 setting the limits is to define a test statistic which will be used. For limit setting, the test statistic is shown  
 2495 in equation 8.1.

$$\tilde{q}_\mu = \begin{cases} -2 \ln \frac{L(\mu, \hat{\theta}(\mu))}{L(0, \hat{\theta}(0))} & \hat{\mu} < 0 \\ -2 \ln \frac{L(\mu, \hat{\theta}(\mu))}{L(\hat{\mu}, \hat{\theta})} & 0 \leq \hat{\mu} < \mu \\ 0 & \hat{\mu} > \mu \end{cases} \quad (8.1)$$

2496 In the above equation,  $\mu$  is the value of the signal strength under test,  $\hat{\mu}$  is the best fit  $\mu$ ,  $\hat{\theta}$  is the  
 2497 best fit value of the nuisance parameters,  $\hat{\theta}$  is the best fit value of the nuisance parameters under the fixed  
 2498  $\mu$  value, and  $L$  is the Poisson likelihood of the data (as described in section 3.6.2).

2499 The test statistic  $\tilde{q}_\mu$  is constructed to protect against two interesting corner cases when setting the  
 2500 upper limit on the cross section. First, it protects against negative signal strengths  $\mu$  which are unphys-  
 2501 ical. Second, it does not count excesses in the data larger than those expected by a signal strength  $\mu$  as  
 2502 evidence against the  $\mu$  hypothesis.

2503 The  $\text{CL}_s$  statistic is constructed by taking a ratio of two probabilities.  $\text{CL}_{s+b}$  is the probability that  
 2504 the signal+background hypothesis would produce a value of the test statistic that is less than or equal  
 2505 to the observed value\*.  $\text{CL}_b$  is the probability that the background only hypothesis will pro-  
 2506 duce a value of the test statistics less than or equal to the observed. The  $\text{CL}_s$  statistic is then the ratio  
 2507  $\text{CL}_{s+b}/\text{CL}_b$ . A 95% upper limit on the cross section is set at the value of  $\mu$  that makes the  $\text{CL}_s$  statistic  
 2508 less than 5%.

2509 In practice, the limits are computed numerically within an asymptotic approximation for the distri-  
 2510 bution of the test statistic  $\tilde{q}_\mu$ . The details of this approximation can be found in reference [70].

2511 The resolved and boosted analyses are combined using a very simple procedure rather than a full sta-  
 2512 tistical combination. For each mass point tested, the limit which gives the most stringent constraint is

---

\*Lower values of  $\tilde{q}_\mu$  mean better compatibility

used. This means that for mass points below 1.1 TeV the resolved signal region is used, while at and above this point the combination of the orthogonal  $3b$  and  $4b$  boosted signal regions is used.

#### 8.4.2 LIMIT SETTING RESULTS

Figure 8.2 shows the combined 95% upper bounds as a function of mass for three different models:

$G_{\text{KK}}^*$  with  $c = 1$ ,  $G_{\text{KK}}^*$  with  $c = 2$ , and a narrow heavy scalar  $H$ .

The cross section of  $\sigma(pp \rightarrow G_{\text{KK}}^* \rightarrow hh \rightarrow b\bar{b}b\bar{b})$  with  $c = 1$  is constrained to be less than 70 fb for masses in the range  $600 < m_{G_{\text{KK}}^*} < 3000$  GeV. For the RSG model with  $c = 2$ , cross sections limits between 40 fb and 200 fb are set for the mass range of  $500 < m_{G_{\text{KK}}^*} < 3000$  GeV. Masses in the range of  $475 < m_{G_{\text{KK}}^*} < 785$  GeV are excluded with  $c = 1$  (with an exclusion of the range 465 to 745 GeV expected). Masses less than 980 GeV are excluded with  $c = 2$  (with an exclusion for masses less than 1 TeV expected).

In the heavy Higgs model, the cross section upper limits for  $\sigma(pp \rightarrow H \rightarrow hh \rightarrow b\bar{b}b\bar{b})$  ranges from 30 to 300 fb in the mass range of  $500 < m_H < 3000$  GeV.

The resolved analysis can also set an upper limit on the Standard Model di-Higgs production cross section discussed in chapter 3. The upper limit on  $\sigma(pp \rightarrow hh \rightarrow b\bar{b}b\bar{b})$  in the Standard Model is constrained to be less than 1.22 pb.

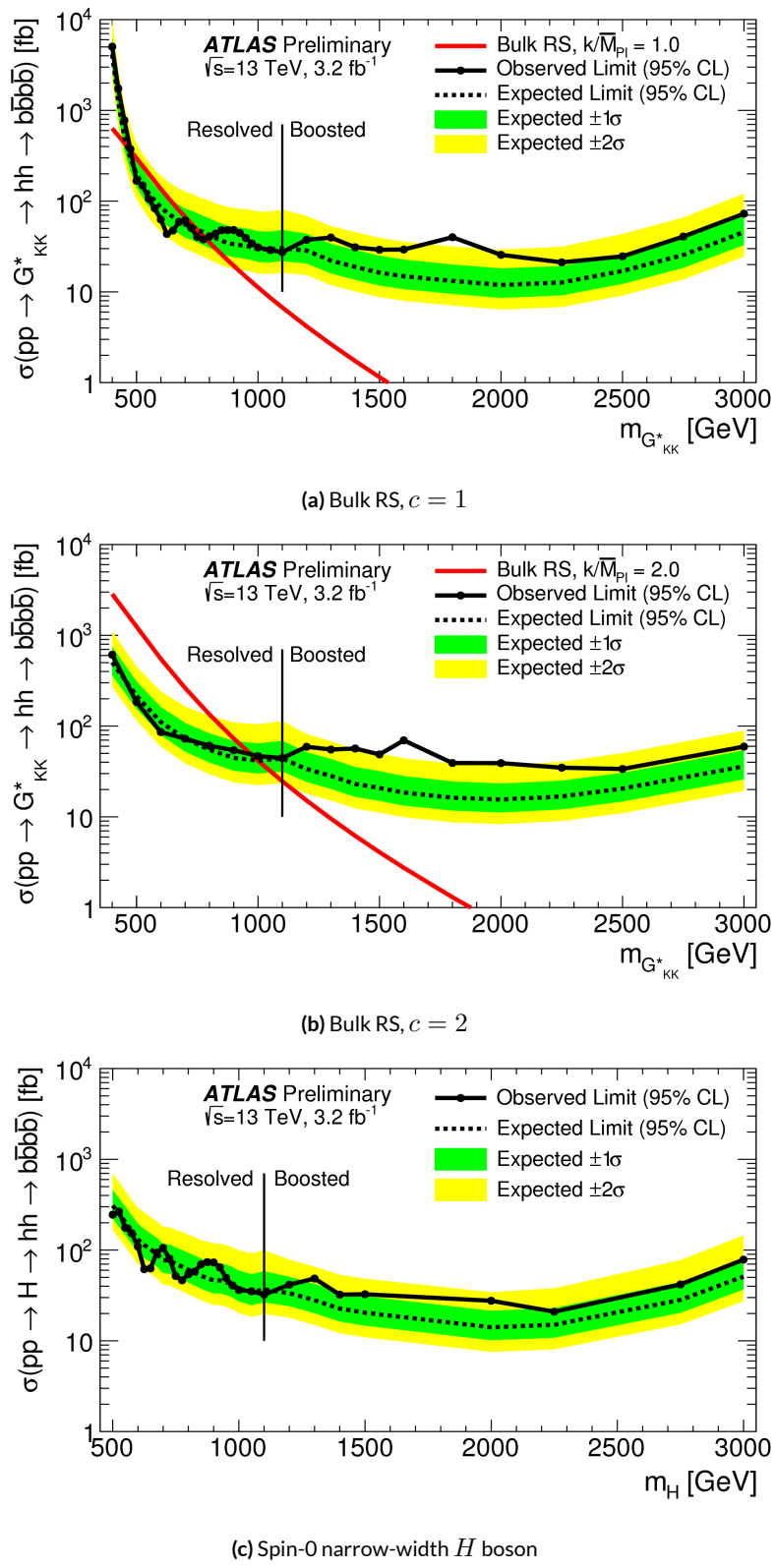


**Figure 8.2:** Expected and observed upper limit as a function of mass for  $G^*_{KK}$  in the RSG model with (a)  $c = 1$  and (b)  $c = 2$ , as well as (c)  $H$  with fixed  $\Gamma_H = 1$  GeV, at the 95% confidence level in the  $CL_s$  method. [28]

2529

## Part IV

2530

## Looking ahead

# 9

2531

2532

## Conclusion

2533 This dissertation presented two distinct studies: the observation and measurement of the Higgs boson  
2534 in the  $H \rightarrow WW^* \rightarrow \ell\nu\ell\nu$  channel at  $\sqrt{s} = 7$  TeV and  $\sqrt{s} = 8$  TeV and a search for Higgs pair  
2535 production in the  $HH \rightarrow b\bar{b}b\bar{b}$  channel at  $\sqrt{s} = 13$  TeV with the ATLAS detector in  $pp$  collisions at  
2536 the Large Hadron Collider.

2537 In the  $H \rightarrow WW^* \rightarrow \ell\nu\ell\nu$ , results from both the discovery of the Higgs boson and the full  
2538 ATLAS Run 1 dataset were presented. With the full  $20.3 \text{ fb}^{-1}$  at  $\sqrt{s} = 8$  TeV and  $4.2 \text{ fb}^{-1}$  at  $\sqrt{s} =$   
2539 7 TeV, ATLAS achieved discovery level significance in the  $H \rightarrow WW^*$  channel alone and obtained  
2540 the first observation of vector boson fusion production in that channel. The combined signal strength  
2541 is measured to be  $\mu = 1.09^{+0.23}_{-0.21}$ . The total observed significance of the  $H \rightarrow WW^*$  process is ob-  
2542 served to be  $6.1\sigma$  (with  $5.8\sigma$  expected). Advanced methods for background reduction and estimation,  
2543 particularly in same-flavor lepton final states, are shown. The VBF signal strength is measured to be  
2544  $\mu_{\text{VBF}} = 1.27^{+0.53}_{-0.45}$  with an observed significance of  $3.2\sigma$  (with  $2.7\sigma$  expected).

2545 These results required many novel innovations. The increase of pileup interactions in the higher in-  
2546 stantaneous luminosity LHC conditions of 2012 led to a degradation of missing transverse momentum  
2547 resolution. As a result, the prominent  $Z/\gamma^*$ +jets background of the same flavor  $H \rightarrow WW^* \rightarrow \ell\nu\ell\nu$   
2548 final states increased greatly. New variables, including a track-based missing transverse momentum and  
2549 a measurement of the balance between the dilepton system and recoiling jets, allowed for significant re-  
2550 duction of this background. In the VBF channel, selections were optimized to exploit the unique VBF  
2551 final state topology. Incorporating these variables into a boosted decision tree technique allowed the  
2552 analysis to exceed the  $3\sigma$  observation threshold.

2553 At  $\sqrt{s} = 13$  TeV, a search for Higgs pair production in the  $b\bar{b}b\bar{b}$  final state with  $3.2 \text{ fb}^{-1}$  was con-  
2554 ducted. A signal region optimized for the boosted final states arising from high mass resonances was  
2555 constructed. This signal region utilized large-radius calorimeter jets and  $b$ -tagging with small radius track  
2556 jets to maximize the signal acceptance. No significant excesses were observed, and upper limits on cross  
2557 sections are placed for spin-2 Randall Sundrum gravitons (RSG) and narrow spin-0 resonances. The  
2558 cross section of  $\sigma(pp \rightarrow G_{\text{KK}}^* \rightarrow hh \rightarrow b\bar{b}b\bar{b})$  with  $k/\bar{M}_{\text{Pl}} = 1$  is constrained to be less than  $70 \text{ fb}$  for  
2559 masses in the range  $600 < m_{G_{\text{KK}}^*} < 3000 \text{ GeV}$ . For the RSG model with  $k/\bar{M}_{\text{Pl}} = 2$ , cross sections  
2560 limits between  $40 \text{ fb}$  and  $200 \text{ fb}$  are set for the mass range of  $500 < m_{G_{\text{KK}}^*} < 3000 \text{ GeV}$ . The cross  
2561 section upper limits for  $\sigma(pp \rightarrow H \rightarrow hh \rightarrow b\bar{b}b\bar{b})$  ranges from  $30$  to  $300 \text{ fb}$  in the mass range of  
2562  $500 < m_H < 3000 \text{ GeV}$ .

# A

2563

2564

## Optimization of $b$ -tagging working point in

2565

$$X \rightarrow HH \rightarrow b\bar{b}b\bar{b} \text{ search}$$

2566 To the  $3b$  and  $4b$  signal regions in the boosted  $X \rightarrow HH \rightarrow b\bar{b}b\bar{b}$  search, the MV<sub>2</sub> algorithm with a  
2567 20% fraction of charm events in training is used (MV<sub>2c20</sub>). Once the algorith is selected, an efficiency  
2568 working point must also be chosen. This working point defines the efficiency with which true  $b$ -jets  
2569 are tagged and also fixes the overall background rejection of the algorithm. Higher efficiency working  
2570 points accept more true  $b$ -jets but also allow for more background. Five different working points (70%,  
2571 77%, 80%, 85%, 90%) are tested. With each working point, the full data driven background estimation  
2572 method is run to quantify the amount of background that will be present in the final signal region. The  
2573 significance is quantified using the median discovery significance for signal and background with Poisson

2574 errors, given in equation A.1 [108].

$$Z = \sqrt{2 \left( (s + b) \ln \left( 1 + \frac{s}{b} \right) - s \right)} \quad (\text{A.1})$$

2575 Note that in the limit where  $s$  is much smaller than  $b$ , this equation reduces to the more well known

2576  $s/\sqrt{b}$ .

2577 Figure A.1 shows the estimated significance as a function of signal mass in RSG  $c = 1$  models for  
 2578 the  $3b$  and  $4b$  signal regions. The 77% working point gives the best performance over a wide range of  
 2579 masses in the  $4b$  signal region. As this is the region which contributes the most to the total discovery  
 2580 significance, the 77% efficiency working point is chosen for the analysis.

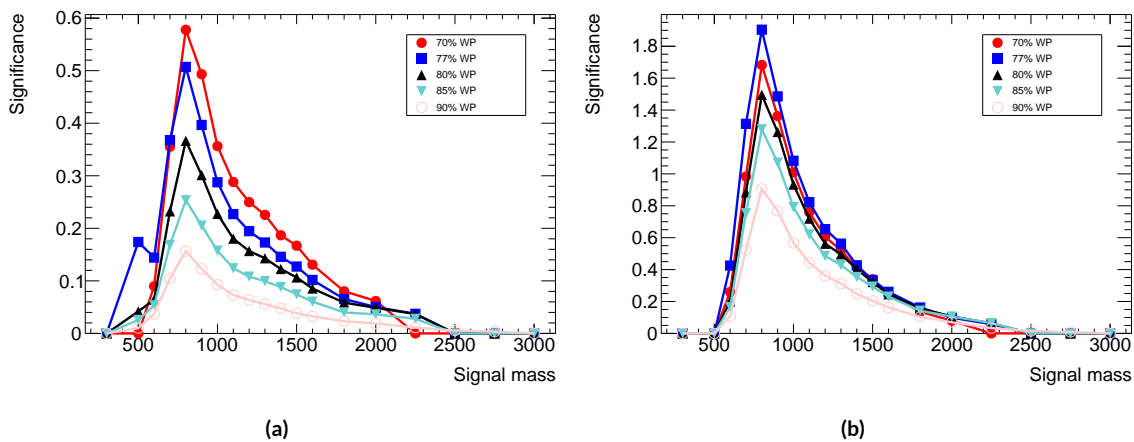


**Figure A.1:** Estimated significance as a function of signal mass for RSG  $c = 1$  models in the  $3b$  (a) and  $4b$  (b) regions for different  $b$ -tagging efficiency working points

2581

# B

2582

*b*-tagging efficiency at high  $p_{\tau}$

# References

2583

- 2584 [1] K. A. Olive et al. Review of Particle Physics. *Chin. Phys.*, C38:090001, 2014. doi: 10.1088/1674-1137/38/9/090001.
- 2585
- 2586 [2] LHC Higgs Cross Section Working Group, S. Heinemeyer, C. Mariotti, G. Passarino, and  
2587 R. Tanaka (Eds.). Handbook of LHC Higgs Cross Sections: 3, Higgs Properties. 2013.
- 2588 [3] Kaustubh Agashe, Hooman Davoudiasl, Gilad Perez, and Amarjit Soni. Warped Gravitons at the  
2589 LHC and Beyond. *Phys. Rev.*, D76:036006, 2007. doi: 10.1103/PhysRevD.76.036006.
- 2590 [4] Johan Alwall, Michel Herquet, Fabio Maltoni, Olivier Mattelaer, and Tim Stelzer. MadGraph  
2591 5:Going Beyond. *JHEP*, 1106:128, 2011. doi: 10.1007/JHEP06(2011)128.
- 2592 [5] Howard E. Haber and Oscar Stål. New LHC benchmarks for the  $\mathcal{CP}$ -conserving two-Higgs-  
2593 doublet model. *Eur. Phys. J.*, C75(10):491, 2015. doi: 10.1140/epjc/s10052-015-3697-x.
- 2594 [6] Lyndon Evans. The Large Hadron Collider. In Holstein, BR and Haxton, WC and Jawahery,  
2595 A, editor, *ANNUAL REVIEW OF NUCLEAR AND PARTICLE SCIENCE, VOL 61*,  
2596 volume 61 of *Annual Review of Nuclear and Particle Science*, pages 435–466. 2011. doi: {10.1146/annurev-nucl-102010-130438}.
- 2598 [7] ATLAS Collaboration. The ATLAS experiment at the CERN Large Hadron Collider. *JINST*, 3:  
2599 So8003, 2008. doi: 10.1088/1748-0221/3/08/S08003.
- 2600 [8] Track Reconstruction Performance of the ATLAS Inner Detector at  $\sqrt{s} = 13$  TeV. Technical  
2601 Report ATL-PHYS-PUB-2015-018, CERN, Geneva, Jul 2015. URL <http://cds.cern.ch/record/2037683>.
- 2603 [9] ATLAS Collaboration. ATLAS Trigger Operations Public Results. 2015. URL <https://twiki.cern.ch/twiki/bin/view/AtlasPublic/TriggerOperationPublicResults>.
- 2604
- 2605 [10] ATLAS Collaboration. ATLAS Luminosity Public Results, Run 1. 2012. URL <https://twiki.cern.ch/twiki/bin/view/AtlasPublic/LuminosityPublicResults>.
- 2606
- 2607 [11] ATLAS Collaboration. ATLAS Luminosity Public Results, Run 2. 2015. URL <https://twiki.cern.ch/twiki/bin/view/AtlasPublic/LuminosityPublicResultsRun2>.
- 2608

- 2609 [12] T Kawamoto, S Vlachos, L Pontecorvo, J Dubbert, G Mikenberg, P Iengo, C Dallapiccola,  
2610 C Amelung, L Levinson, R Richter, and D Lellouch. New Small Wheel Technical Design Re-  
2611 port. Technical Report CERN-LHCC-2013-006. ATLAS-TDR-020, CERN, Geneva, Jun 2013.  
2612 URL <https://cds.cern.ch/record/1552862>. ATLAS New Small Wheel Technical Design  
2613 Report.
- 2614 [13] Joao Pequenao and Paul Schaffner. An computer generated image representing how ATLAS  
2615 detects particles. Jan 2013. URL <https://cds.cern.ch/record/1505342>.
- 2616 [14] Electron efficiency measurements with the ATLAS detector using the 2012 LHC proton-proton  
2617 collision data. Technical Report ATLAS-CONF-2014-032, CERN, Geneva, Jun 2014. URL  
2618 <https://cds.cern.ch/record/1706245>.
- 2619 [15] Georges Aad et al. Electron and photon energy calibration with the ATLAS detector using LHC  
2620 Run 1 data. *Eur. Phys. J.*, C74(10):3071, 2014. doi: 10.1140/epjc/s10052-014-3071-4.
- 2621 [16] Georges Aad et al. Measurement of the muon reconstruction performance of the ATLAS detec-  
2622 tor using 2011 and 2012 LHC proton–proton collision data. *Eur. Phys. J.*, C74(11):3130, 2014. doi:  
2623 10.1140/epjc/s10052-014-3130-x.
- 2624 [17] Monte Carlo Calibration and Combination of In-situ Measurements of Jet Energy Scale, Jet En-  
2625 ergy Resolution and Jet Mass in ATLAS. Technical Report ATLAS-CONF-2015-037, CERN,  
2626 Geneva, Aug 2015. URL <http://cds.cern.ch/record/2044941>.
- 2627 [18] Georges Aad et al. Performance of *b*-Jet Identification in the ATLAS Experiment. 2015.
- 2628 [19] Expected performance of the ATLAS *b*-tagging algorithms in Run-2. Technical Report ATL-  
2629 PHYS-PUB-2015-022, CERN, Geneva, Jul 2015. URL <http://cds.cern.ch/record/2037697>.
- 2630 [20] Performance of Missing Transverse Momentum Reconstruction in ATLAS studied in Proton-  
2631 Proton Collisions recorded in 2012 at 8 TeV. Technical Report ATLAS-CONF-2013-082, CERN,  
2632 Geneva, Aug 2013. URL <http://cds.cern.ch/record/1570993>.
- 2633 [21] ATLAS Collaboration. Observation and measurement of Higgs boson decays to WW\* with the  
2634 ATLAS detector. *Phys. Rev. D*, 92(012006), 2015.
- 2635 [22] Georges Aad et al. Observation of a new particle in the search for the Standard Model Higgs  
2636 boson with the ATLAS detector at the LHC. *Phys. Lett.*, B716:1–29, 2012. doi: 10.1016/j.physletb.  
2637 2012.08.020.
- 2638 [23] Georges Aad et al. Measurements of the Higgs boson production and decay rates and coupling  
2639 strengths using pp collision data at  $\sqrt{s} = 7$  and 8 TeV in the ATLAS experiment. *Eur. Phys. J.*,  
2640 C76(1):6, 2016. doi: 10.1140/epjc/s10052-015-3769-y.

- 2642 [24] W.J. Stirling. 7/8 and 13/8 TeV LHC luminosity ratios. 2013. URL [http://www.hep.ph.ic.ac.uk/~wstirlin/plots/lhclumi7813\\_2013\\_v0.pdf](http://www.hep.ph.ic.ac.uk/~wstirlin/plots/lhclumi7813_2013_v0.pdf).
- 2643
- 2644 [25] J Alison. Experimental Studies of hh. Oct 2014. URL <http://cds.cern.ch/record/1952581>.
- 2645
- 2646 [26] Baojia (Tony) Tong. Private communication.
- 2647 [27] Flavor Tagging with Track Jets in Boosted Topologies with the ATLAS Detector. Technical Report ATL-PHYS-PUB-2014-013, CERN, Geneva, Aug 2014. URL <https://cds.cern.ch/record/1750681>.
- 2648
- 2649
- 2650 [28] Search for pair production of Higgs bosons in the  $b\bar{b}b\bar{b}$  final state using proton-proton collisions at  $\sqrt{s} = 13$  TeV with the ATLAS detector. Technical Report ATLAS-CONF-2016-017, CERN, Geneva, Mar 2016. URL <https://cds.cern.ch/record/2141006>.
- 2651
- 2652
- 2653 [29] Christopher G. Tully. *Elementary particle physics in a nutshell*. 2011.
- 2654 [30]
- 2655 [31] Mike Lamont for the LHC team. The First Years of LHC Operation for Luminosity Production. International Particle Accelerator Conference, 2013. URL [https://accelconf.web.cern.ch/accelconf/IPAC2013/talks/moyab101\\_talk.pdf](https://accelconf.web.cern.ch/accelconf/IPAC2013/talks/moyab101_talk.pdf).
- 2656
- 2657
- 2658 [32] Paul Collier for the LHC team. LHC Machine Status. CERN Resource Review Board, 2015.
- 2659 URL <https://cds.cern.ch/record/2063924/files/CERN-RRB-2015-119.PDF>.
- 2660
- 2661 [33] Qi Zeng. Private communication.
- 2662
- 2663 [34] Serguei Chatrchyan et al. Observation of a new boson at a mass of 125 GeV with the CMS experiment at the LHC. *Phys. Lett.*, B716:30–61, 2012. doi: 10.1016/j.physletb.2012.08.021.
- 2664
- 2665
- 2666 [35] David Griffiths. *Introduction to elementary particles*. 2008.
- 2667
- 2668 [36] F. Halzen and Alan D. Martin. *QUARKS AND LEPTONS: AN INTRODUCTORY COURSE IN MODERN PARTICLE PHYSICS*. 1984. ISBN 0471887412, 9780471887416.
- 2669
- 2670 [37] Matthew D. Schwartz. *Quantum Field Theory and the Standard Model*. Cambridge University Press, 2014. ISBN 1107034736, 9781107034730. URL <http://www.cambridge.org/us/academic/subjects/physics/theoretical-physics-and-mathematical-physics/quantum-field-theory-and-standard-model>.
- 2671
- 2672 [38] S. Dawson. Introduction to electroweak symmetry breaking. In *High energy physics and cosmology. Proceedings, Summer School, Trieste, Italy, June 29-July 17, 1998*, pages 1–83, 1998. URL <http://alice.cern.ch/format/showfull?sysnb=0301862>.

- 2673 [39] S. L. Glashow. Partial Symmetries of Weak Interactions. *Nucl. Phys.*, 22:579–588, 1961. doi:  
2674 10.1016/0029-5582(61)90469-2.
- 2675 [40] Steven Weinberg. A Model of Leptons. *Phys. Rev. Lett.*, 19:1264–1266, 1967. doi: 10.1103/  
2676 PhysRevLett.19.1264.
- 2677 [41] A. Salam. *Elementary Particle Theory*. Almqvist and Wiksell, Stockholm, 1968.
- 2678 [42] J. Iliopoulos S.L. Glashow and L. Maiani. D2:1285, 1970.
- 2679 [43] R. Keith Ellis, W. James Stirling, and B. R. Webber. QCD and collider physics. *Camb. Monogr.  
2680 Part. Phys. Nucl. Phys. Cosmol.*, 8:1–435, 1996.
- 2681 [44] P. W. Higgs. Broken symmetries and the masses of gauge bosons. 13:508, 1964.
- 2682 [45] P. W. Higgs. Spontaneous symmetry breakdown without massless bosons. 145:1156, 1966.
- 2683 [46] F. Englert and R. Brout. Broken symmetry and the mass of gauge vector mesons. 13:321, 1964.
- 2684 [47] G. S. Guralnik, C. R. Hagen, and T. W. .B. Kibble. Global conservation laws and massless parti-  
2685 cles. *Phys. Rev. Lett.*, 13:585, 1964. doi: 10.1103/PhysRevLett.13.585.
- 2686 [48] Matthew J. Dolan, Christoph Englert, and Michael Spannowsky. New Physics in LHC Higgs  
2687 boson pair production. *Phys. Rev.*, D87(5):055002, 2013. doi: 10.1103/PhysRevD.87.055002.
- 2688 [49] Roberto Contino, Margherita Ghezzi, Mauro Moretti, Giuliano Panico, Fulvio Piccinini, and  
2689 Andrea Wulzer. Anomalous Couplings in Double Higgs Production. *JHEP*, 08:154, 2012. doi:  
2690 10.1007/JHEP08(2012)154.
- 2691 [50] R. Grober and M. Muhlleitner. Composite Higgs Boson Pair Production at the LHC. *JHEP*, 06:  
2692 020, 2011. doi: 10.1007/JHEP06(2011)020.
- 2693 [51] Lisa Randall and Raman Sundrum. A Large mass hierarchy from a small extra dimension. *Phys.  
2694 Rev. Lett.*, 83:3370–3373, 1999. doi: 10.1103/PhysRevLett.83.3370.
- 2695 [52] A. Liam Fitzpatrick, Jared Kaplan, Lisa Randall, and Lian-Tao Wang. Searching for the Kaluza-  
2696 Klein Graviton in Bulk RS Models. *JHEP*, 09:013, 2007. doi: 10.1088/1126-6708/2007/09/013.
- 2697 [53] Julien Baglio, Otto Eberhardt, Ulrich Nierste, and Martin Wiebusch. Benchmarks for Higgs Pair  
2698 Production and Heavy Higgs boson Searches in the Two-Higgs-Doublet Model of Type II. *Phys.  
2699 Rev.*, D90(1):015008, 2014. doi: 10.1103/PhysRevD.90.015008.
- 2700 [54] G. C. Branco, P. M. Ferreira, L. Lavoura, M. N. Rebelo, Marc Sher, and Joao P. Silva. Theory  
2701 and phenomenology of two-Higgs-doublet models. *Phys. Rept.*, 516:1–102, 2012. doi: 10.1016/j.  
2702 physrep.2012.02.002.

- 2703 [55] Jose M. No and Michael Ramsey-Musolf. Probing the Higgs Portal at the LHC Through Reso-  
2704 nant di-Higgs Production. *Phys. Rev.*, D89(9):095031, 2014. doi: 10.1103/PhysRevD.89.095031.
- 2705 [56] Lyndon R Evans and Philip Bryant. LHC Machine. *J. Instrum.*, 3:S08001, 164 p, 2008. URL  
2706 <https://cds.cern.ch/record/1129806>. This report is an abridged version of the LHC  
2707 Design Report (CERN-2004-003).
- 2708 [57] CMS Collaboration. The cms experiment at the cern lhc. *Journal of Instrumentation*, 3(08):  
2709 S08004, 2008. URL <http://stacks.iop.org/1748-0221/3/i=08/a=S08004>.
- 2710 [58] LHCb Collaoration. The LHCb Detector at the LHC. *JINST*, 3:S08005, 2008. doi: 10.1088/  
2711 1748-0221/3/08/S08005.
- 2712 [59] ALICE Collaboration. The alice experiment at the cern lhc. *Journal of Instrumentation*, 3(08):  
2713 S08002, 2008. URL <http://stacks.iop.org/1748-0221/3/i=08/a=S08002>.
- 2714 [60] ATLAS Collaboration. Luminosity Determination in  $pp$  Collisions at  $\sqrt{s} = 7$  TeV Using the  
2715 ATLAS Detector at the LHC. *Eur. Phys. J.*, C 71:1630, 2011. doi: 10.1140/epjc/s10052-011-1630-5.
- 2716 [61] M Capeans, G Darbo, K Einsweiller, M Elsing, T Flick, M Garcia-Sciveres, C Gemme, H Perneg-  
2717 ger, O Rohne, and R Vuillermet. ATLAS Insertable B-Layer Technical Design Report. Tech-  
2718 nical Report CERN-LHCC-2010-013, ATLAS-TDR-19, CERN, Geneva, Sep 2010. URL  
2719 <https://cds.cern.ch/record/1291633>.
- 2720 [62] Y Giomataris, Ph. Rebourgeard, J.P. Robert, and G. Charpak. Micromegas: a high-granularity  
2721 position-sensitive gaseous detector for high particle-flux environments. *Nuclear Instruments  
2722 and Methods in Physics Research Section A: Accelerators, Spectrometers, Detectors and As-  
2723 sociated Equipment*, 376(1):29 – 35, 1996. ISSN 0168-9002. doi: [http://dx.doi.org/10.1016/0168-9002\(96\)00175-1](http://dx.doi.org/10.1016/0168-9002(96)00175-1). URL <http://www.sciencedirect.com/science/article/pii/0168900296001751>.
- 2726 [63] T Alexopoulos, J. Burnens, R. de Oliveira, G. Glonti, O. Pizzirusso, V. Polychronakos,  
2727 G. Sekhniaidze, G. Tsipolitis, and J. Wotschack. A spark-resistant bulk-micromegas chamber for  
2728 high-rate applications. *Nuclear Instruments and Methods in Physics Research Section A: Acceler-  
2729 ators, Spectrometers, Detectors and Associated Equipment*, 640(1):110 – 118, 2011. ISSN 0168-9002.  
2730 doi: <http://dx.doi.org/10.1016/j.nima.2011.03.025>. URL <http://www.sciencedirect.com/science/article/pii/S0168900211005869>.
- 2732 [64] Improved electron reconstruction in ATLAS using the Gaussian Sum Filter-based model for  
2733 bremsstrahlung. Technical Report ATLAS-CONF-2012-047, CERN, Geneva, May 2012. URL  
2734 <https://cds.cern.ch/record/1449796>.

- 2735 [65] W Lampl, S Laplace, D Lelas, P Loch, H Ma, S Menke, S Rajagopalan, D Rousseau, S Snyder,  
 2736 and G Unal. Calorimeter Clustering Algorithms: Description and Performance. Technical  
 2737 Report ATL-LARG-PUB-2008-002, ATL-COM-LARG-2008-003, CERN, Geneva, Apr 2008.  
 2738 URL <https://cds.cern.ch/record/1099735>.
- 2739 [66] Georges Aad et al. Topological cell clustering in the ATLAS calorimeters and its performance in  
 2740 LHC Run 1. 2016.
- 2741 [67] Matteo Cacciari, Gavin P. Salam, and Gregory Soyez. The Anti-k(t) jet clustering algorithm.  
 2742 *JHEP*, 04:063, 2008. doi: 10.1088/1126-6708/2008/04/063.
- 2743 [68] Georges Aad et al. Performance of Missing Transverse Momentum Reconstruction in Proton-  
 2744 Proton Collisions at 7 TeV with ATLAS. *Eur. Phys. J.*, C72:1844, 2012. doi: 10.1140/epjc/  
 2745 s10052-011-1844-6.
- 2746 [69] Aaron James Armbruster. Discovery of a Higgs Boson with the ATLAS detector. 2013. CERN-  
 2747 THESIS-2013-047.
- 2748 [70] G. Cowan, K. Cranmer, E. Gross, and O. Vitells. Asymptotic formulae for likelihood-based tests  
 2749 of new physics. *Eur. Phys. J.*, C 71:1554, 2011. doi: 10.1140/epjc/s10052-011-1554-0.
- 2750 [71] ATLAS Collaboration. Limits on the production of the Standard Model Higgs Boson in  $pp$   
 2751 collisions at  $\sqrt{s} = 7$  TeV with the ATLAS detector. *Eur. Phys. J.*, C 71:1728, 2011. doi: 10.1140/  
 2752 epjc/s10052-011-1728-9.
- 2753 [72] ATLAS Collaboration. Performance of the ATLAS muon trigger in  $pp$  collisions at  $\sqrt{s} = 8$   
 2754 TeV. *Eur. Phys. J. C*, (arXiv:1408.3179. CERN-PH-EP-2014-154):75, 19 p, Aug 2014. URL <https://cds.cern.ch/record/1749694>.
- 2755
- 2756 [73] ATLAS collaboration. Electron trigger performance in 2012 ATLAS data, 2015. ATLAS-COM-  
 2757 DAQ-2015-091.
- 2758 [74] Paolo Nason. A new method for combining NLO QCD with shower Monte Carlo algorithms.  
 2759 *JHEP*, 11:040, 2004.
- 2760 [75] B. P. Kersevan and E. Richter-Was. The Monte Carlo event generator AcerMC version 2.0 with  
 2761 interfaces to PYTHIA 6.2 and HERWIG 6.5. 2004.
- 2762 [76] Nikolas Kauer and Giampiero Passarino. Inadequacy of zero-width approximation for a light  
 2763 Higgs boson signal. 2012.
- 2764 [77] T. Gleisberg, Stefan. Hoeche, F. Krauss, M. Schonherr, S. Schumann, et al. Event generation with  
 2765 SHERPA 1.1. *JHEP*, 0902:007, 2009. doi: 10.1088/1126-6708/2009/02/007.

- 2766 [78] Michelangelo L. Mangano et al. ALPGEN, a generator for hard multiparton processes in  
 2767 hadronic collisions. *JHEP*, 0307:001, 2003. doi: 10.1088/1126-6708/2003/07/001.
- 2768 [79] Torbjorn Sjostrand, Stephen Mrenna, and Peter Z. Skands. PYTHIA 6.4 Physics and Manual.  
 2769 *JHEP*, 0605:026, 2006. doi: 10.1088/1126-6708/2006/05/026.
- 2770 [80] Torbjorn Sjostrand, Stephen Mrenna, and Peter Z. Skands. A Brief Introduction to PYTHIA 8.1.  
 2771 *Comput.Phys.Commun.*, 178:852–867, 2008. doi: 10.1016/j.cpc.2008.01.036.
- 2772 [81] G. Corcella et al. HERWIG 6: An event generator for hadron emission reactions with interfering  
 2773 gluons (including super-symmetric processes) . *JHEP*, 01:010, 2001. doi: 10.1088/1126-6708/2001/  
 2774 01/010.
- 2775 [82] J. M. Butterworth, Jeffrey R. Forshaw, and M. H. Seymour. Multiparton interactions in photo-  
 2776 production at HERA. *Z. Phys.*, C 72:637, 1996. doi: 10.1007/s002880050286.
- 2777 [83] Jun Gao, Marco Guzzi, Joey Huston, Hung-Liang Lai, Zhao Li, et al. The CT10 NNLO Global  
 2778 Analysis of QCD. *Phys.Rev.*, D89:033009, 2014. doi: 10.1103/PhysRevD.89.033009.
- 2779 [84] P. M. Nadolsky. Implications of CTEQ global analysis for collider observables. *Phys. Rev.*, D 78:  
 2780 013004, 2008. doi: 10.1103/PhysRevD.78.013004.
- 2781 [85] A. Sherstnev and R. S. Thorne. Parton distributions for the LHC. *Eur. Phys. J.*, C 55:553, 2009.  
 2782 doi: 10.1140/epjc/s10052-008-0610-x.
- 2783 [86] S. Agostinelli et al. GEANT4, a simulation toolkit. *Nucl. Instrum. Meth.*, A 506:250, 2003. doi:  
 2784 10.1016/S0168-9002(03)01368-8.
- 2785 [87] I. Stewart and F. Tackmann. Theory uncertainties for Higgs mass and other searches using jet  
 2786 bins. *Phys. Rev.*, D 85:034011, 2012. doi: 10.1103/PhysRevD.85.034011.
- 2787 [88] ATLAS Collaboration. Luminosity Determination in  $pp$  Collisions at  $\sqrt{s} = 7$  TeV Using the  
 2788 ATLAS Detector at the LHC. *Eur. Phys. J.*, C 71:1630, 2011. doi: 10.1140/epjc/s10052-011-1630-5.
- 2789 [89] Jet energy scale and its systematic uncertainty in proton-proton collisions at  $\sqrt{s} = 7$  tev with  
 2790 atlas 2011 data. *ATLAS-CONF-2013-004*, 2013.
- 2791 [90] Calibrating the  $b$ -tag efficiency and mistag rate in  $35 \text{ pb}^{-1}$  of data with the atlas detector.  
 2792 *ATLAS-CONF-2011-089*, 2011.
- 2793 [91] ATLAS Collaboration. Measurement of the  $b$ -tag Efficiency in a Sample of Jets Containing  
 2794 Muons with  $5 \text{ fb}^{-1}$  of Data from the ATLAS Detector. *ATLAS-CONF-2012-043*, 2012. URL  
 2795 <http://cdsweb.cern.ch/record/1435197>.

- 2796 [92] J. Alwall et al. The automated computation of tree-level and next-to-leading order differential  
 2797 cross sections, and their matching to parton shower simulations. *JHEP*, 07:079, 2014.
- 2798 [93] Richard D. Ball et al. Parton distributions with LHC data. *Nucl. Phys. B*, 867:244, 2013.
- 2799 [94] ATLAS Collaboration. ATLAS Run 1 Pythia8 tunes. (ATL-PHYS-PUB-2014-021), Nov 2014.  
 2800 URL <https://cds.cern.ch/record/1966419>.
- 2801 [95] M. Bahr et al. Herwig++ Physics and Manual. *Eur. Phys. J. C*, 58:639–707, 2008. doi: 10.1140/  
 2802 epjc/s10052-008-0798-9.
- 2803 [96] Stefan Gieseke, Christian Rohr, and Andrzej Siódak. Colour reconnections in Herwig++. *Eur.*  
 2804 *Phys. J. C*, 72:2225, 2012. doi: 10.1140/epjc/s10052-012-2225-5.
- 2805 [97] Simone Alioli, Paolo Nason, Carlo Oleari, and Emanuele Re. A general framework for imple-  
 2806 menting NLO calculations in shower Monte Carlo programs: the POWHEG BOX. *JHEP*, 06:  
 2807 043, 2010.
- 2808 [98] Peter Zeiler Skands. Tuning Monte Carlo Generators: The Perugia Tunes. *Phys. Rev. D*, 82:  
 2809 074018, 2010. doi: 10.1103/PhysRevD.82.074018.
- 2810 [99] Michal Czakon and Alexander Mitov. Top++: A Program for the Calculation of the Top-Pair  
 2811 Cross-Section at Hadron Colliders. 2011.
- 2812 [100] D. Krohn, J. Thaler, and L.-T. Wang. Jet Trimming. *JHEP*, 02:084, 2010. doi: 10.1007/  
 2813 JHEP02(2010)084.
- 2814 [101] ATLAS Collaboration. Identification of Boosted, Hadronically Decaying W Bosons and Com-  
 2815 parisons with ATLAS Data Taken at  $\sqrt{s} = 8$  TeV. 2015.
- 2816 [102] Expected Performance of Boosted Higgs ( $\rightarrow b\bar{b}$ ) Boson Identification with the ATLAS Detector  
 2817 at  $\sqrt{s} = 13$  TeV. Technical Report ATL-PHYS-PUB-2015-035, CERN, Geneva, Aug 2015. URL  
 2818 <https://cds.cern.ch/record/2042155>.
- 2819 [103] Matteo Cacciari and Gavin P. Salam. Pileup subtraction using jet areas. *Phys. Lett. B*, 659:119,  
 2820 2008. doi: 10.1016/j.physletb.2007.09.077.
- 2821 [104] ATLAS Collaboration. Identification of boosted, hadronically-decaying  $W$  and  $Z$  bosons in  
 2822  $\sqrt{s} = 13$  TeV Monte Carlo Simulations for ATLAS. (ATL-PHYS-PUB-2015-033), Aug 2015.  
 2823 URL <https://cds.cern.ch/record/2041461>.
- 2824 [105] ATLAS Collaboration. Calibration of  $b$ -tagging using dileptonic top pair events in a combina-  
 2825 torial likelihood approach with the ATLAS experiment. (ATLAS-CONF-2014-004), 2014. URL  
 2826 <http://cds.cern.ch/record/1664335>.

- 2827 [106] ATLAS Collaboration. Performance of  $b$ -Jet Identification in the ATLAS Experiment. 2015.
- 2828 [107] Alexander L. Read. Presentation of search results: The CL(s) technique. *J. Phys. G*, 28:2693,  
2829 2002. doi: 10.1088/0954-3899/28/10/313.
- 2830 [108] Glen Cowan, Eilam Gross. Discovery significance with statistical uncertainty in the background  
2831 estimate. 2008. URL <http://www.pp.rhul.ac.uk/~cowan/stat/notes/SigCalcNote.pdf>.
- 2832



**T**HIS THESIS WAS TYPESET using L<sup>A</sup>T<sub>E</sub>X, originally developed by Leslie Lamport and based on Donald Knuth's T<sub>E</sub>X.

The body text is set in 11 point Egenolff-Berner Garamond, a revival of Claude Garamont's humanist typeface. The above illustration, *Science Experiment 02*, was created by Ben Schlitter and released under CC BY-NC-ND 3.0. A template that can be used to format a PhD dissertation with this look & feel has been released under the permissive AGPL license, and can be found online at [github.com/asm-products/Dissertate](https://github.com/asm-products/Dissertate) or from its lead author, Jordan Suchow, at [suchow@post.harvard.edu](mailto:suchow@post.harvard.edu).